



12th European conference on RADar in meteorology and hydrology (ERAD 2024)

Book of Extended Abstracts



9-13 September 2024

Città Universitaria Sapienza
University of Rome, Rome, Italy

Since 2000, the biennial ERAD (European conference on RADar in meteorology and hydrology) conference is an awaited occasion, within the radar community, to connect academia, industry, and weather services, in an international and dynamic environment, fostering collaboration among scientists, engineers, and operational stakeholders. This journey keeps going thanks to the dedicated effort and collaboration of the international weather radar community.

The Institute of Atmospheric Sciences and Climate of Italian National Research Council (CNR-ISAC) and the Sapienza University of Rome had the honour to host the 12th edition in Rome, Italy.

Each ERAD conference, while sharing common goals, offers something unique that reflects the characteristics of its host venue and organizers. In Rome, we had the privilege of holding the conference on the vibrant main campus of Italy's largest university, Sapienza University of Rome, which provided ERAD 2024 with access to the monumental Aula Magna auditorium and the fascinating Museum of Classical Art.

Continuing the tradition of ERAD conferences, students and early-stage researchers had the opportunity to attend the event and trainings, present their studies, and most importantly, network within a diverse community that fosters knowledge in the areas of scientific and technological research related to radar in meteorology and other environmental applications. Some of them received support for their participation, and poster competitions and oral presentations were organized to stimulate quality research.

Finally, ERAD 2024 also provided a valuable platform for scientists and weather services to interact with manufacturers to stay informed about the latest product offerings related to weather radar.

As many other conferences, after the experience of COVID 19 pandemic, ERAD 2024 offered the flexibility of attendance, allowing participants to be physically present at the Sapienza venue or to join remotely.

At the conference, seven keynotes were presented, including one by the winner of the Gutta Aurea award, dedicated to the late Prof. Frank S. Marzano. A total of 154 oral presentations and 217 poster presentations were delivered in sessions organized according to the following topics:

- Clouds and precipitation physics
- Operational aspects
- Weather radar and climate
- Weather Radar technologies
- Radar hydrometeorological applications
- Radar and society
- Space borne clouds and precipitation radar

The collection of all the abstracts presented at the 12th edition of the European Conference on Radar in Meteorology and Hydrology are published in ERAD2024 Book of Abstract. Here we have the pleasure to present the extended abstracts submitted to the conference. A total of 26 extended abstracts have been provided and published in this book under Creative Commons Attribution 4.0 International licence. To view a copy of this license, visit <https://creativecommons.org/licenses/by/4.0/>

Enjoy the reading!

The Organizing Committee of ERAD 2024



SAPIENZA
UNIVERSITÀ DI ROMA

Cover image by Giacomo Roversi/Marco Petracca, licensed under CC BY 4.0
DOI 10.5281/zenodo.14170845

ERAD 2024 Committees

Internation ProgramCommittee

Aurora Bell, Australian Bureau of Meteorology,
Chair ERAD 2010

Alexis Berne, École polytechnique fédérale de
Lausanne, Switzerland, co-chair of ERAD 2022

Chandrasekar V., Colorado State University, US

Urs Germann, MeteoSwiss, Switzerland, co-chair
of ERAD 2022

Hidde Leijnse, KNMI, Netherlands, co-chair of
ERAD 2018

Dmitri Moisseev, University of Helsinki, Finland

Efrat Morin, The Hebrew University of Jerusalem

Daniel Michelson; Environment and Climate
Change Canada, chair of ERAD 2004, chair of
WMO Joint Expert Team on Operational Weather
Radar, JET-OWR

Djordje Mirkovic, NOAA, US

James Kurdzo; Massachusetts Institute of
Technology, Lincoln Laboratory. US

Kurtuluş Öztürk; Turkish State Meteorological
Service, Turkey, co-chair of ERAD 2016

Daniel Sempere Torres; Universitat Politècnica de
Catalunya, Spain, chair of ERAD 2006.

Remko Uijlenhoet; Delft University of
Technology, Netherlands, co-chair of ERAD 2018)

Miguel Rico-Ramirez; University of Bristol, UK

Silke Troemel; Universität Bonn, Germany

Annakaisa Von Lerber; Finnish Meteorological
Institute, Finland, chair of EUMETNET-OPERA

Organizing committee

Luca Baldini, CNR-ISAC, Co-chair

Nazzareno Pierdicca, Sapienza
University of Rome, Co-chair

Mario Montopoli, CNR-ISAC, Co-chair

Francesco Napolitano, Sapienza
University of Rome

Elisa Adirosi, CNR-ISAC,

Alessandro Bracci, CNR-ISAC

Technical partner:

Island of meetings, by ER srls , via Marcantoni 16
06061 Castiglione del Lago, Perugia, Italy

Sponsors



Contents

ERAD 2024 Committees	3
Sponsors	4
Clouds and precipitation physics	7
T-MATRIX SIMULATIONS OF SPECTRAL POLARIMETRIC VARIABLES FROM A CLOUD-RADAR	8
POSITIVE AND NEGATIVE DIFFERENTIAL PHASE UPON SCATTERING: OBSERVATIONS AND UTILIZATION IN MICROPHYSICAL RETRIEVALS	13
INVESTIGATING THE SPATIOTEMPORAL CHARACTERISTICS OF MOTION FIELDS USING THREE-DIMENSIONAL RADAR ECHOES TO CONSTRUCT AN ENSEMBLE NOWCASTING SYSTEM.....	18
Operational aspects	23
RADAR-BASED STUDIES OF TERRAIN-INDUCED WINDSHEAR AND MICROBURSTS NEAR THE HONG KONG INTERNATIONAL AIRPORT DURING THE PASSAGE OF SUPER TYPHOON SAOLA IN SEPTEMBER 2023	24
AN INTER-RADAR INTERFERENCE SUPPRESSION METHOD FOR WEATHER RADAR DATA WITHOUT MODIFYING THE RADAR'S INTERNAL SIGNAL PROCESSING.....	29
AN INNOVATIVE APPROACH FOR REAL-TIME HAIL SIZE ESTIMATION.....	32
REAL-TIME TORNADO VORTEX DETECTION SYSTEM USING DEEP LEARNING - TOWARDS MITIGATION OF LOCALIZED AND SUDDEN METEOROLOGICAL DISASTERS.....	37
IMPLEMENTATION OF OPEN-SOURCE SOFTWARE IN AN OPERATIONAL RADAR PROCESSING CHAIN USING RAINBOW.....	42
COMPUTING ECHO TOP PRODUCTS WITH FAST QUALITY-WEIGHTED SLIDING WINDOWS .	45
Weather radar and climate.....	50
CLASSIFICATION OF CONVECTIVE SYSTEMS YIELDING TORNADOES IN JAPAN	51
Weather Radar technologies.....	56
A STUDY ON MISSING DATA CORRECTION TECHNIQUE FOR WEATHER RADAR DATA USING MACHINE LEARNING.....	57
POSTPROCESSING METHODS TO CHARACTERIZE MULTIMODAL PRECIPITATION IN DOPPLER SPECTRA FROM DWD'S C-BAND RADAR BIRDBATH SCAN	62
VERIFYING THE CLUTTER SUPPRESSION CAPABILITY OF X- AND C-BAND WEATHER RADARS EQUIPPED WITH SOLID STATE POWER AMPLIFIER TRANSMITTERS.....	67
COMPARING THE SENSITIVITY OF WEATHER RADARS WITH CONVENTIONAL MAGNETRON AND MODERN SOLID STATE POWER AMPLIFIER TRANSMITTER TECHNOLOGIES	72
A PHYSICS-INFORMED MACHINE-LEARNING ALGORITHM TO RECOVER CORRUPTED OR BLANKED DATA IN WEATHER RADAR VELOCITY MEASUREMENTS	77
OBSERVATIONS USING AN X-BAND PHASED-ARRAY BISTATIC RADAR NETWORK	82
Radar hydrometeorological applications	87
HYDROLOGICAL MODELING OF PROBABILISTIC RAINFALL FORECASTS FOR IMPACT-BASED FLOOD WARNING SYSTEM.....	88
A HYDROMETEOR CLASSIFICATION METHOD FOR DUAL POLARIZATION WEATHER RADAR BASED ON GAUSSIAN MIXTURE MODEL USING BAYESIAN INFERENCE	93
RAINFALL RUNOFF ANALYSIS USING RAINFALL PRODUCT WITH TEMPORAL AND SPATIAL INTERPOLATION OF PUBLICLY ACCESSIBLE WEATHER RADAR DATA IN THAILAND	98

RAINCELL PROJECT: COMMERCIAL MICROWAVE LINKS TO ESTIMATE RAINFALL AT MÉTÉO-FRANCE	103
A STRAIGHTFORWARD ATMOSPHERIC-RADAR SIMULATOR FOR VERTICAL-AIR MOTION ANALYSIS FROM FREQUENCY-MODULATED CONTINUOUS-WAVE-RADAR RAIN MEASUREMENTS	108
RAINFALL ESTIMATION FOR WINTER EVENTS WITH POLARIMETRIC VPR APPLIED TO THE GERMAN RADAR NETWORK	114
THE MEAN DIAMETER UPDATE APPROACH FOR ENSEMBLE-BASED DUAL-POLARIMETRIC RADAR DATA ASSIMILATION	119
ASSIMILATION OF RADAR DATA IN ICON AT VERY HIGHRESOLUTION - THE GLORI PROJECT.....	124
IMPACT OF LATENT HEAT NUDGING ON ICON MODEL FORECASTS	128
Radar and society	133
PROPOSAL OF HAIL FORECAST METHOD AND PERFORMANCE EVALUATION UTILIZING SNS POST DATA	134

Clouds and precipitation physics

T-matrix simulations of Spectral Polarimetric Variables from a cloud-radar

I. Tsikoudi^{1,2}, A. Battaglia³, C. Unal⁴, K.-A. Voudouri^{1,5}, and E. Marinou^{1,2}

¹Institute for Astronomy, Astrophysics, Space Applications and Remote Sensing, National Observatory of Athens, 15236 Athens, Greece

²Department of Physics, National and Kapodistrian University of Athens, 15772 Athens, Greece

³Department of Environment, Land and Infrastructure Engineering, Politecnico di Torino, 10129 Turin, Italy

⁴Department of Geoscience and Remote Sensing, Delft University of Technology, Delft, the Netherlands

⁵Department of Physics, Aristotle University of Thessaloniki, 54124 Thessaloniki, Greece

1 Introduction

Cloud radar observations and spectral polarimetry are crucial for understanding cloud microphysics. The overall purpose of this study is two-fold: (a) to describe the methodology for simulating polarimetric spectral variables including white and stochastic noise of a real radar spectrum, as well as the impact of atmospheric turbulence and (b) to compare simulations with observed spectra for rain observations. Rain electromagnetic scattering properties have been historically computed by assuming spheroidal shapes via the T-matrix method (Mishchenko et al., 2000). Such models have been found satisfactory to explain radar and radiometric measurements. However, raindrops generally change due to oscillations, which cause departure from rotationally symmetric shape, and make T-matrix tools impractical since they hinge upon the assumption of rotationally symmetric particles.

This work focuses on generating simulations of a 94 GHz cloud radar observations in rain conditions, pointing at 45 degrees and comparing with real observations. The spectral differential reflectivity (sZ_{DR}) and spectral differential phase ($s\delta_{hv}$) are the variables of interest. They are produced with the T-matrix method, by computing the electromagnetic scattering properties and simulating the radar response.

The simulation tool is described in section 2 and explores diverse conditions, allowing for the modification of rain rate, white and spectral noise, and turbulence parameters. The effect of atmospheric turbulence introduces an increased spread of velocities within the radar volume and contributes to the blurring of the spectral features, such as smearing out the distinct features (Mie scattering notches) in the Doppler spectrum. Incorporating the impact of turbulence in the simulations for spectral polarimetric variables is a complex task and the attempt is discussed in this study.

2 Methodology

The simulations are generated by using a Python package for computing the electromagnetic scattering properties of nonspherical particles using the T-matrix method (Leinonen, 2014), exclusively targeting in rain conditions. The backscattering amplitude matrix, S , and the phase matrix, Z , are calculated for drops of different diameters D , with axis ratios parameterized as following: Very small droplets are conceived as perfect spheres (axis ratio = 1), and as their size increases, they are modelled as spheroidal particles and an oblate shape is assumed (axis ratio > 1). The scattering geometry of the simulation corresponds to a radar pointing at a 45-degree elevation angle. Raindrops are assumed to be partially aligned with their maximum dimension preferentially on the horizontal plane: scattering properties are averaged over Gaussian distributions of canting angles with different standard deviations.

Firstly, the single-particle Polarimetric Variables are computed: the backscattering cross sections for Vertically and Horizontally polarized radiation (σ_{VV} , σ_{HH}), the differential scattering phase δ_{hv} and the co-polar correlation coefficient ρ_{hv} .

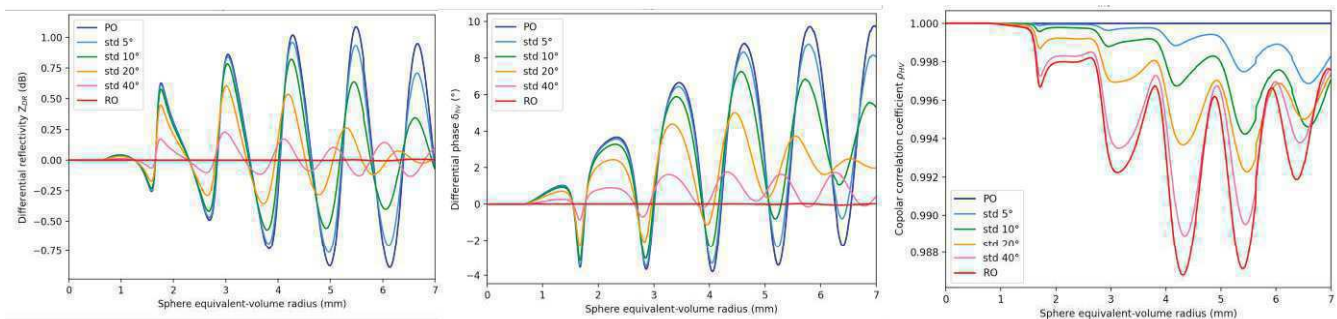


Figure 1: *Left:* Differential reflectivity Z_{DR} , *Middle:* Differential phase δ_{hv} , *Right:* Copolar correlation coefficient ρ_{hv} as a function of sphere equivalent-volume diameters, for a 94 GHz radar pointing at 45°. For the T-matrix method, a complex refractive index of water at 10°C temperature is assumed. PO, RO stand for Perfect Orientation and Random Orientation, respectively.

Then, an ideal spectrum S_{VV} (1) for the V-channel is independently generated for each diameter D . A Gamma distribution is used to represent the variability of a natural rainfall Drop Size Distribution $N(D)$.

$$S_{VV}(D) = \frac{\lambda^4}{\pi^5 |K|^2} N(D) \sigma_{VV}(D) \frac{dD}{du} \quad (1)$$

λ is the radar wavelength, $|K|^2$ is derived from the dielectric factor of water, $N(D)$ is the drop size distribution, σ_{VV} is the backscattering cross section for V channel and u is the velocity of droplets along the line of sight of the radar beam. Following Yu et al. (2012), the complex voltage signal in the V channel in the velocity domain can be written as:

$$V_V(u) = \sqrt{S_{VV}(u) \text{In}g^{[1]}} e^{i\theta^{[1]}} \quad (2)$$

where $g^{[1]}$ and $\theta^{[1]}$ are independent, identically distributed random variables with uniform distribution between 0 and 1 and between $-\pi$ and π , respectively. The time series of complex voltage signal can be obtained via an inverse FFT of V_V . This process can be repeated iteratively to generate independent stochastic realizations of the same spectrum. Similarly, for the H channel in the velocity domain:

$$V_H(u) = \sqrt{sZ_{DR}(u)} [s\rho_{HV}(u)V_V^{[1]}(u) + \sqrt{1 - s\rho_{HV}^2(u)}V_V^{[2]}(u)]e^{i\delta_{HV}(u)} \quad (3)$$

where the spectral variables $s\rho_{HV}$, $s\delta_{HV}$ and sZ_{DR} are presented in Figure 1, for each velocity bin, but also hold the prefix s in the notation to differentiate them from the commonly used integral polarimetric variables. $V_V^{[2]}$ is generated according to (2) with the same model spectrum S_{VV} , but with a second independent sequence of random numbers ($u^{[2]}$ and $\theta^{[2]}$). This process is repeated for each velocity bin for the total of the FFT spectral points within the Nyquist interval. The inverse Fourier transform of V_V and V_H represent simulated time series of complex signals for the V and H channels.

For the implementation of white noise, an approach similar to Eq. (2) is used:

$$N_V(u) = \sqrt{-\aleph_V \text{In}g^{[3]}} e^{i\theta^{[3]}} \quad \text{and} \quad N_H(u) = \sqrt{-\aleph_H \text{In}g^{[4]}} e^{i\theta^{[4]}} \quad (4)$$

where \aleph_V and \aleph_H are the noise level values for the V and H channel corresponding to the prescribed values of signal-to-noise ratios (SNR), and $u^{[3]}$, $\theta^{[3]}$, $u^{[4]}$, $\theta^{[4]}$ are again generated independently. The complex numbers that represent the simulation of the noisy I and Qs in the frequency domain for the V and H channels are calculated from:

$$S_V(u) = V_V(u) + N_V(u) \quad \text{and} \quad S_H(u) = V_H(u) + N_H(u) \quad (5)$$

To introduce the turbulent motions of drops in the simulations, the Doppler spectra must be convolved with a turbulence term S_{air} (6), that accounts for the turbulent motions within the atmosphere.

$$S_{air}(u) = \frac{1}{\sqrt{2\pi}\sigma_t} e^{-\frac{u^2}{2\sigma_t^2}} \quad (6)$$

$$S_{VV}^{turb} = \int_{-\infty}^{\infty} S_{VV}(u - \xi) S_{air}(\xi) d\xi \quad (7)$$

where ξ is the convolution variable and S_{air} accounts for the turbulent motions within the atmosphere. Atmospheric turbulence causes random fluctuations in the velocity of hydrometeors, thus broadening the Doppler spectrum. All droplets are here assumed to have no inertial effects and therefore acting like perfect tracers (Figure 2).

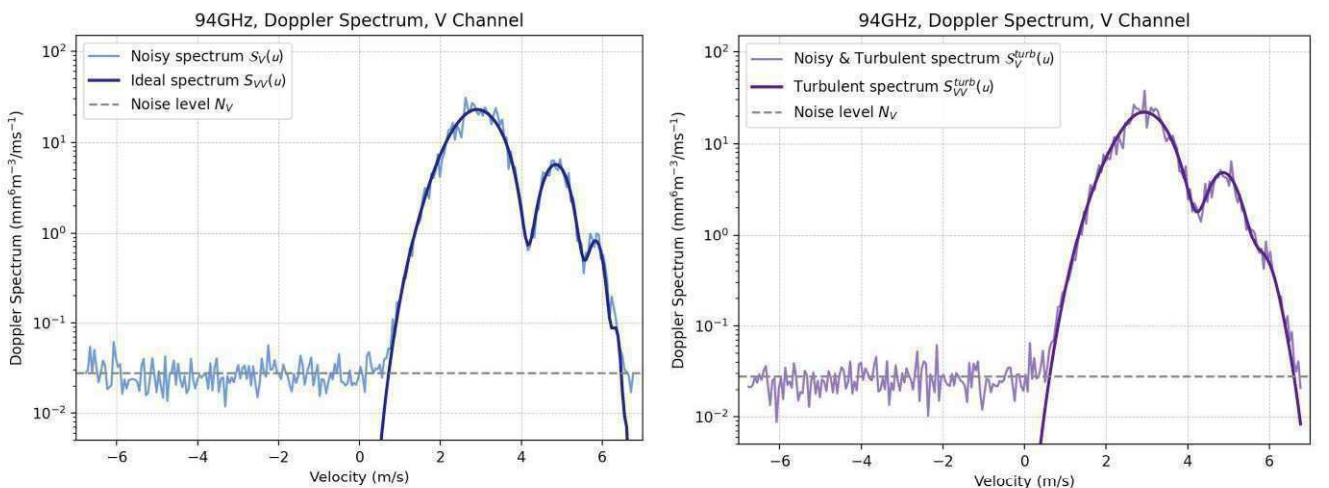


Figure 2: Left: Ideal Spectrum S_{VV} (eq. 1) – dark blue line, Noisy spectrum S_V (eq. 5) – light blue line, Right: Turbulent spectrum without noise effect (eq. 7) – dark purple line, Turbulent and noisy spectrum – light purple line. The grey dashed line, represents the noise level \aleph_V .

Then the broadened sZ_{DR} can be computed as the ratio of $S_{HH}^{turb}(v)$ to $S_{VV}^{turb}(v)$ whereas the turbulent-broadened parameters ρ_{HV}^{turb} and δ_{HV}^{turb} are then calculated respectively as the amplitude and the phase of the variable:

$$\rho_{hv}(u)e^{i\delta_{hv}(u)} = \frac{\langle S_H(u)S_V^*(u) \rangle}{\sqrt{\langle |S_H(u)|^2 \rangle \langle |S_V(u)|^2 \rangle}} \quad (8)$$

3 Results

To assess the accuracy of the cloud radar simulation methods, we compare the measurements with the simulated data. This comparison aims to validate the performance of the simulations and identify any discrepancies that may arise from the model assumptions or parameter settings. The cloud radar measurements were obtained using an RPG Frequency Modulated Continuous Wave (FMCW) Dual Polarization W-band Cloud Doppler Radar, operating at 94 GHz.

One case study from 3 February 2021, is presented in Figure 3. The rainfall is moderate, with rain rate approximately between 6 and 7 mm/h. The spectrum is acquired at an altitude of 484 meters above ground level. At this altitude, there is significantly less turbulence relatively to lower levels, due to the influence of surface effects diminishes, leading to generally more stable and less turbulent atmospheric conditions.

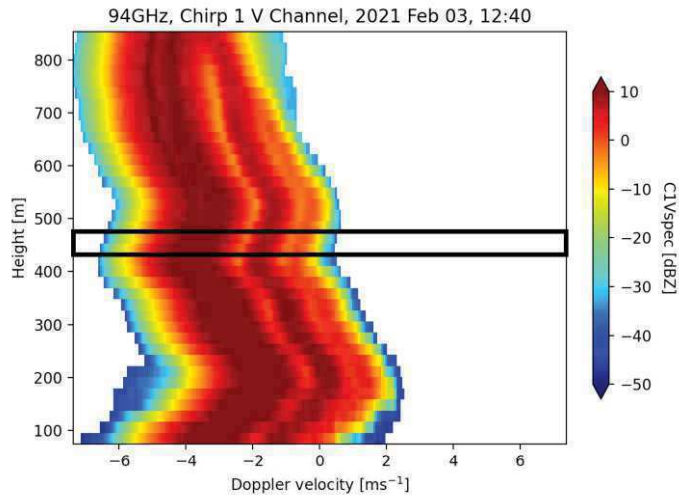


Figure 3: 03 Feb 2021, 12:40z with vertical profiles for reflectivity. The level that is used for case studies are marked by the black rectangle.

For the generation of the simulation of the spectral polarimetric variables, the optimal fit for the drop size distribution must be identified in order to apply equation 1. Therefore, the Least Squares Method was employed to minimize the sum of the squared differences between the measured and simulated spectra, ensuring that the best-fitting gamma DSD is selected. The best fit is presented in Figure 4.

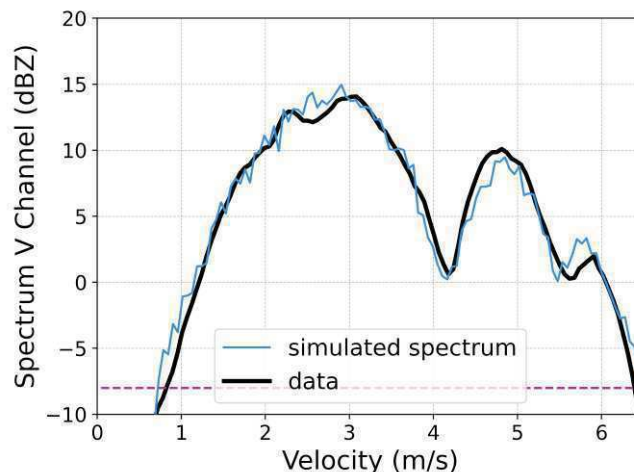


Figure 4: Measured Doppler Spectrum (black line) and optimum-fitted Gamma DSD (blue line). The purple dashed line indicates the threshold for applying the Least Squares Method in order to find the optimum fit.

The simulated variables as calculated from equation 8, are represented in figure 5. The black lines represent the measured sZ_{DR} (left) and $s\delta_{HV}$ (right), while the blue line is the simulation. The comparison between cloud radar simulations and measurements exhibits some correlation; however, there are notable discrepancies that indicate limitations in the current simulation model.

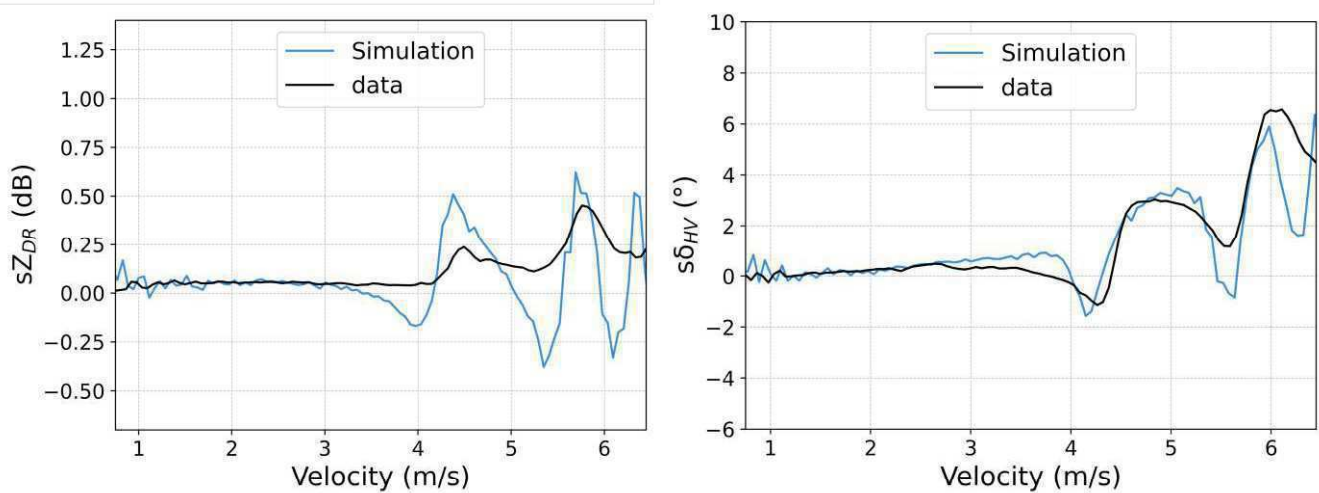


Figure 5: Spectral polarimetric variables of case study. Left panel: Spectral Differential reflectivity sZ_{DR} , Right panel: Spectral Differential phase $s\delta_{HV}$. The black lines represent the measured data, the blue lines represent the simulations from the above-described method.

We observe notable discrepancies in the simulations (blue lines) when compared to observational data. Specifically, the expected minima, as predicted by theoretical models, are not well-represented in the data, especially for Z_{DR} . For δ_{HV} , there is better agreement, though this deteriorates with larger drops. The simulations tend to produce more pronounced minima than those observed, suggesting potential issues in the microphysical assumptions, such as the parameterization of the drop shape. In our study, all drops are modelled as spheroids. In these cases, this T-matrix approach may fail at high frequencies, like 94 GHz.

4 Conclusions

This study compares simulated spectral polarimetric variables with real measurements from a 94 GHz cloud radar under moderate rain conditions. The results show that the simulations closely match observations within a specific spectrum range, particularly for Doppler velocities up to 5 m/s, where the polarimetric signal is minimal due to the predominantly spherical shape of raindrops. The simulations more accurately represent the maxima than the minima, specifically for the differential phase $s\delta_{HV}$. While the minima of the observed data for both sZ_{DR} and $s\delta_{HV}$ appear truncated, the simulated minima are significantly deeper. Despite these discrepancies, the overall trends in both simulations and measurements remain consistent. A potential explanation for these discrepancies may be found in the assumptions of the T-matrix approach, which models all drops as spheroidal or rotationally symmetric particles. Since raindrops oscillate and lack rotational symmetry, traditional methods like the T-matrix may produce inaccurate scattering parameters, particularly for resonant particles, where radar wavelengths are comparable to or smaller than raindrop size. More accurate methods should be explored. Future research should investigate whether more advanced scattering models can account for the observed variability, or alternatively, data from low turbulence conditions could be used to create look-up tables of polarimetric scattering properties based on incidence angle in a data-driven approach. This work contributes to the broader scientific effort to improve cloud radar simulations and advance the understanding of cloud processes and their impact on atmospheric dynamics.

5 Acknowledgements

I.T. and K.A.V. acknowledges the financial support by PANGAEA4CalVal (Grant Agreement 101079201) funded by the European Union. E.M. acknowledges support by the Hellenic Foundation for Research and Innovation (H.F.R.I.) under the “2nd Call for H.F.R.I. Research Projects to support Post-Doctoral Researchers” (Project Acronym: REVEAL, Project Number: 07222). This project was partially funded by the Horizon Europe programme under Grant Agreement No 101137680 via project CERTAINTY (Cloud-aERosol inTeractions & their impActs IN The earth sYstem and the European Space Agency under Contract No. 4000142902/23/I-NS via project AIRSENSE (Aerosol and aerosol-cloud Interaction from Remote SENSing Enhancement).

6 References

- Mishchenko, M. I., et al. (2000). Light scattering by nonspherical particles: Theory, measurements, and applications. San Diego: Academic Press
- Leinonen, J. (2014). High-level interface to t-matrix scattering calculations: architecture, capabilities and limitations. *Opt. Express*, 22 (2), 1655–1660. doi: 10.1364/OE.22.001655
- Yu, T., et al. (2012). Statistical quality of spectral polarimetric variables for weather radar. *Journal of Atmospheric and Oceanic Technology*, 29(9), 1221–1235. doi: <https://doi.org/10.1175/JTECH-D-11-00090.1>

Unal, C., and Y. van den Brule, 2024: Exploring Millimeter-Wavelength Radar Capabilities for Raindrop Size Distribution Retrieval: Estimating Mass-Weighted Mean Diameter from the Differential Backscatter Phase. *J. Atmos. Oceanic Technol.*, 41, 583–603, <https://doi.org/10.1175/JTECH-D-23-0094.1>.

Positive and Negative Differential Phase upon Scattering: Observations and Utilization in Microphysical Retrievals

Valery Melnikov^{1,2}, Dusan S. Zrnica², and Arthur Witt²

¹ University of Oklahoma, CIWRO, Norman, OK, USA.

² NOAA/OAR National Severe Storms Laboratory, Norman, OK, USA.

Abstract: The impact of the radar differential phase upon transmission (DPT) on measured differential phase (DP) is demonstrated using data from collocated S-band weather radars employing simultaneous transmission and reception of orthogonally polarized waves. It is shown that measured DPs from the radars are of opposite signs depending on the DPTs. These observations are the first evidence of DP dependence on the radar parameter DPT. The measured radar variables can be used to retrieve the microphysical hydrometeors' parameters.

1. Radar data

It is well known that reflectivity (Z) and differential reflectivity (ZDR) values in the melting layers (ML) are larger than those in areas just above and below. The correlation coefficient (CC) values drop in the ML. Increased values of differential phase (DP) in ML are reported (for instance, [1-3]). Such dependencies can be observed in the top panels of Fig. 1 collected with S-band WSR-88D KCRI located at Norman, OK, USA. The data were collected on 28 January 2024 at 180344 UTC at an antenna elevation angle of 10° . The ML is easily observed in the Z , ZDR , DP , and CC panels.

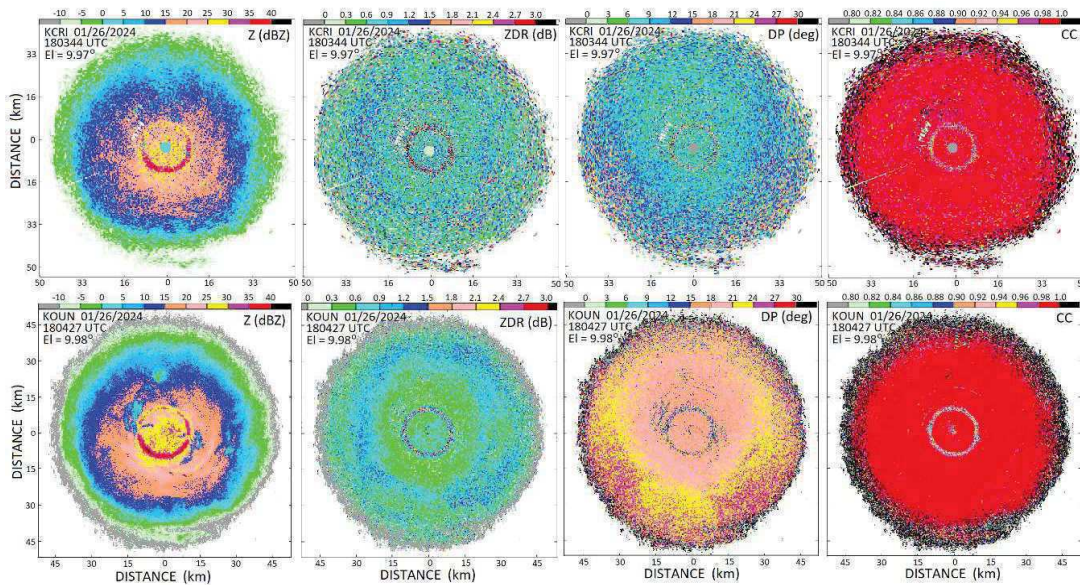


Fig. 1. (top): PPIs from KCRI collected 26 Jan 2024 at 180344 UTC at an elevation of 10° . (bottom): As in top, but from KOUN at 180427 UTC.

KCRI radar is a test system of the NWS Radar Operations Center. The radar is located 234 m apart from WSR-88D KOUN operated by the NOAA/OAR National Severe Storms Laboratory. The radars employ simultaneous transmission and reception of orthogonally polarized waves and operate at the wavelengths of 10.0 cm (KCRI) and 11.1 cm (KOUN). It can be noticed from panel (g) in Fig. 1 that the color of the ML is greenish, indicating that the KOUN's DP values in the ML are lower than those above and below it (in light blue). Fig. 2 depicts range profiles of the radar variables obtained by averaging over 360° . KCRI was running VCP-12 at the time, while KOUN was running an experimental VCP with a dwell time of 128 ms at the pulse repetition frequency of 1000 Hz, i.e., the number of averaged samples was 128. The elevation of 10° was common for both radars at 1803-1804 UTC.

Fig. 3 presents KOUN's observation of the CC and DP for four cases. In all KOUN's cases, the scattering differential phases from melting layers were negative.

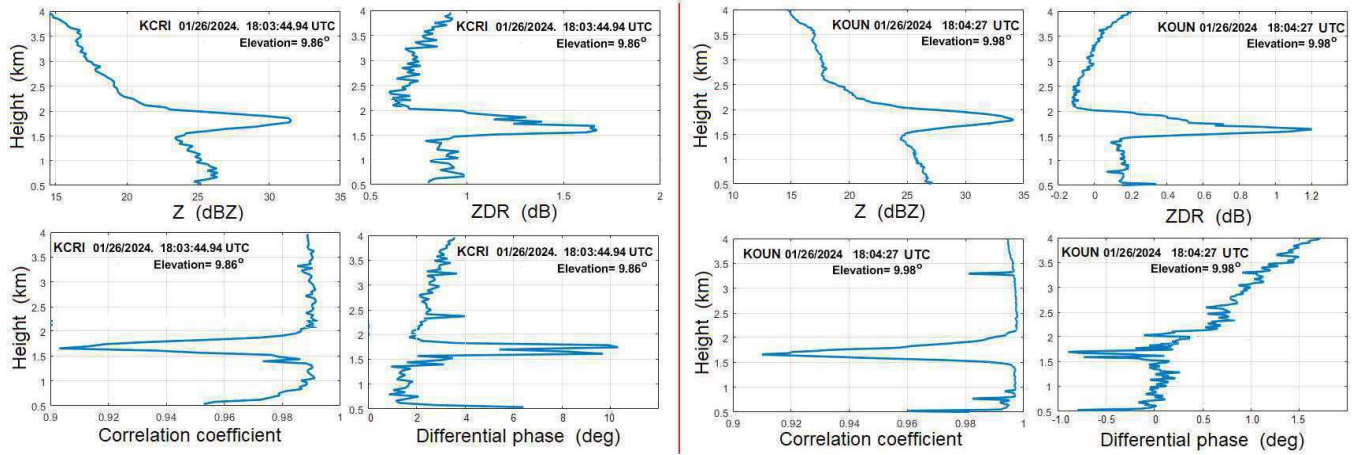


Fig. 2. (top): Range profiles of the KCRI's radar variables obtained by averaging the data in Fig. 1 (top) over azimuth. The height of maximum ZDR values is shown with the red horizontal line. (bottom): As in the top, but from KOUN.

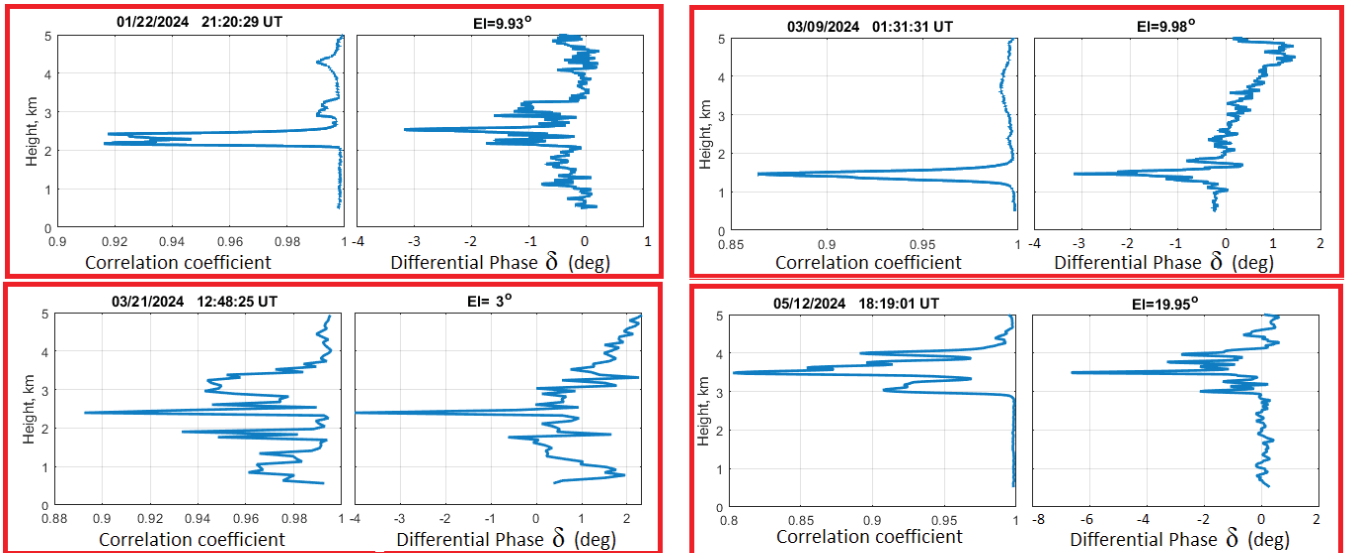


Fig. 3. KOUN's range profiles collected on the indicated dates.

2. Interpretation

Hydrometeors in MLs are wet ice particles in a plate-like shape. This representation comes from models of particles as a collection of stitched ice crystals (e.g., [4]) with water inclusions (see also Fig. 4) or a mixture of ice and water as in [5]. Due to water surface tension, the shape of water inclusions is close to a plate.

The scattering geometry of a wet crystal is shown in Fig. 4, where an ice dendrite (in yellow) holds a plate-like water droplet (in blue). The frame OXYZ has the Z axis oriented vertically. OM is oriented along the minor droplet's axis, so the angle between the Z axis and OM is the canting angle θ .

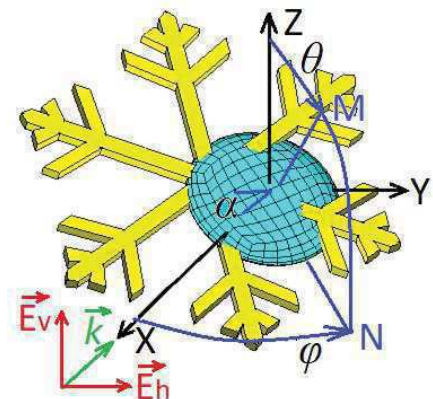


Fig. 4. Geometry of scattering off a wet snowflake.

The second and third orientation angles are φ and α . The latter shows the rotation of the droplet around the axis OM. Point N lies in the OXY horizontal plane and point M in the OZN plane. The angles θ , φ , and α are Euler's angles. The vector \mathbf{k} shows the direction of propagation of the impinging waves E_h and E_v , where the subscripts mean horizontal and vertical polarizations at horizontal incidence. The particles flutter in the air and the angles θ , φ , and α vary over time.

The amplitudes of scattering fields e_{hr} and e_{vr} from a single particle are described by the following matrix equation (e.g. [6]):

$$\begin{pmatrix} e_{hr} \\ e_{vr} \end{pmatrix} = \begin{pmatrix} C_{Rh} & 0 \\ 0 & C_{Rv} \end{pmatrix} \begin{pmatrix} 1 & 0 \\ 0 & e^{j\gamma} \end{pmatrix} \begin{pmatrix} S_{hh} & S_{hv} \\ S_{hv} & S_{vv} \end{pmatrix} \begin{pmatrix} 1 & 0 \\ 0 & e^{j\beta} \end{pmatrix} \begin{pmatrix} E_h \\ E_v \end{pmatrix}, \quad (1)$$

where C_{Rh} and C_{Rv} are the radar constants (the range dependence is included) for the horizontal and vertical radar channels, $\beta = \varphi_{dp} + \psi_t$ is the impinging phase with φ_{dp} being the one-way propagation differential phase and ψ_t is the differential phase upon transmission, $\gamma = \varphi_{dp} + \psi_r$ with ψ_r being the receiver differential phase. Phases ψ_r and ψ_t may differ because the signal paths in a radar transmitter and a receiver are different. The S_{hh} , S_{vv} , and S_{hv} are the scattering matrix coefficients.

The measured differential phase Φ_{DP} is

$$\Phi_{DP} = 2\varphi_{dp} + \psi_t + \psi_r + \delta = \beta + \gamma + \delta, \quad (2)$$

where δ is the differential phase upon scattering. The constants $C_{Rh,v}$ in (1) are obtained from radar calibration and are important in the reflectivity and ZDR measurements; all other radar variables are independent of these constants. We consider calibrated radar and known $C_{Rh,v}$, hence the constants can be omitted in further discussion. Then (1) simplifies to

$$e_{hr} = S_{hh} + S_{hv} e^{j\beta} \quad \text{and} \quad e_{vr} = (S_{vv} e^{j\beta} + S_{hv}) e^{j\gamma}. \quad (3)$$

Radar receives waves from all scatterers in the resolution volume and resulting voltage is

$$E_{hr} = \sum_n e_{hr}^{(n)} \exp(ikr_n), \quad (4)$$

where n numerates the scatterers and $\exp(ikr_n)$ accounts for the range r_n from radar to the n^{th} scatterer. The correlation function in the channel with the horizontally polarized wave is

$$R_{hv} = \langle E_{hr}^* E_{vr} \rangle, \quad (5)$$

where the brackets stand for ensemble averaging and the asterisk indicates complex conjugate. The averaging is performed over the sizes, shapes, orientations, and distances r_n . Assuming that the scattering amplitudes do not depend on the distance between scatterers, the averaging over distances can be separated from other averaging. Then range reshuffling of the scatterers leads to

$$R_{hv} = \langle N(D) e_{hr}^*(\theta, \varphi, \alpha, D) e_{vr}(\theta, \varphi, \alpha, D) \rangle. \quad (6)$$

where $N(D)$ is the size distribution of the scatterers with D being a characteristic size of the scatterer (e.g., its maximal diameter) and the sum in (4) is replaced with the mean product and the brackets stand for averaging over the sizes, shapes, and orientation angles θ , φ , and α .

Hydrometeors in MLs can be considered Rayleigh scatterers at S band. The scattering matrix elements for Rayleigh scatterers and an antenna elevation angle ν can be written as (e.g., eq. (2.53) in [7]),

$$S_{hh} = \alpha_a + \Delta\alpha \sin^2\theta \sin^2\varphi, \quad (7a)$$

$$S_{vv} = \alpha_a + \Delta\alpha (\sin^2\nu \sin^2\theta \cos^2\varphi + \cos^2\nu \cos^2\theta + \sin 2\nu \sin\theta \cos\theta \cos\varphi), \quad (7b)$$

$$S_{hv} = \Delta\alpha (\sin\nu \sin^2\theta \sin\varphi \cos\varphi + \cos\nu \sin\theta \cos\theta \sin\varphi). \quad (7c)$$

where α_a and α_b are polarizabilities along the major and minor spheroid axes and $\Delta\alpha = \alpha_b - \alpha_a$.

Cloud particles in MLs change their orientation angles θ , φ and α over time. The angles φ and α can be considered uniformly distributed in the interval $0 - 360^\circ$. Variations in the canting angle θ (Fig. 2) can be characterized with some distribution in the interval $0-180^\circ$. The orientation angles are described by the Fisher distribution $P(\theta, \varphi)$. For the uniform distribution in φ and α ,

$$P(\theta) = \frac{\mu}{2 \sinh(\mu)} \exp(\mu \cos\theta), \quad \mu \geq 0, \quad (8)$$

where the parameter μ can be represented via the mean canting angle $\langle \theta \rangle$ or the width σ_θ of the distribution of canting angles:

$$\langle \theta \rangle = \int_0^\pi \theta \sin\theta P(\theta) d\theta,$$

$$\langle \theta^2 \rangle = \int_0^\pi \theta^2 \sin\theta P(\theta) d\theta, \quad \sigma_\theta = (\langle \theta^2 \rangle - \langle \theta \rangle^2)^{1/2}.$$

The matrix coefficients (7) should be inserted into (6) and averaged to obtain the radar variables. The results for R_{hv} is

$$R_{\text{hv}} = \left\{ |\alpha_a|^2 + \alpha_a^* \Delta\alpha \left[1 - J_1 - \sin^2 \nu \left(1 - \frac{3}{2} J_1 \right) \right] + \frac{1}{2} \alpha_a \Delta\alpha^* J_1 + \frac{1}{2} |\Delta\alpha|^2 B \right\} e^{i(\gamma+\beta)} + \frac{1}{2} |\Delta\alpha|^2 B e^{i(\gamma-\beta)},$$

$$B = J_1 - J_2 - \sin^2 \nu \left(J_1 - \frac{5}{4} J_2 \right),$$

$$J_1 = \langle \sin^2 \theta \rangle = \frac{2}{\mu} \left[\coth \mu - \frac{1}{\mu} \right], \quad J_2 = \langle \sin^4 \theta \rangle = \frac{4}{\mu^2} (2 - 3J_1). \quad (9)$$

Fig. 5 depicts dependencies of CC and phase δ on the antenna elevation angle at various DPTs and an axis ratio (b/a) of 0.5 and $\langle \theta \rangle = 10^\circ$. The dependencies should be applied to particles at a height of maximum ZDR, i.e., for particles just before they collapse into droplets. It is seen from Fig 5 (right) that δ changes sign: it is positive at DPT from 0° to 180° and is negative in the DPT interval $180^\circ - 360^\circ$ (or from 0° to -180°).

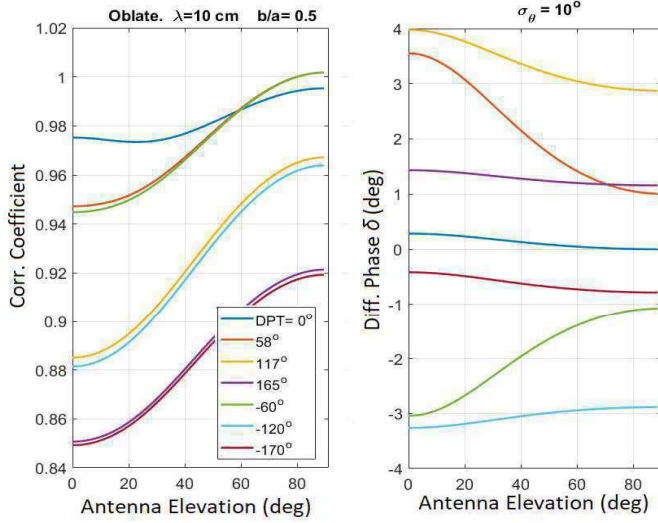


Fig. 5. (left): The correlation coefficient as a function of the antenna elevation angle at indicated DPTs. (right): As in the left, but for the phase δ .

3. Retrieval results

Phase δ depends on the axis ratio, orientation of particles, and DPT. To use δ and CC for microphysical retrievals, the system DPT must be known. The KOUN's DPT has been estimated from observations of insects [8], DPT = 240° (-120°). This DPT results in negative δ (Figs. 2, 3, 5). The radar variables Z, ZDR, DP, CC, and KDP from the range gate of maximal ZDR can be used for estimating the mean size (D), number concentration (N), axis ratio (b/a), and orientation parameter $\langle \theta \rangle$. Table 1 shows dependencies of the radar variables on the microphysical parameters, where 'Yes' indicates a dependence and 'No' means independence.

Our retrieval procedure consists of two steps. On the first step, the mean axis ratio and $\langle \theta \rangle$ are obtained from the measured ZDR, CC, and δ using the best match. These radar variables do not depend on D and N . On the second step, D and N are obtained from measured Z and KDP using obtained b/a and $\langle \theta \rangle$. The radar variables have been taken from a range gate corresponding to maximal ZDR and minimal δ and CC. We assume that in this gate, scattering from ice is insignificant and the backscatter signal can be attributed to water inside wet snowflakes.

Table 1. Dependencies of the radar variables on microphysical parameters.

	Size (D)	Number concentration (N)	Axis ratio (b/a)	Orientation ($\langle \theta \rangle$)	DPT
Reflectivity	Yes	Yes	No	Yes	No
ZDR	No	No	Yes	Yes	No
Diff. Phase	No	No	Yes	Yes	Yes
KDP	Yes	Yes	Yes	Yes	No
Corr. Coefficient	No	No	Yes	Yes	Yes

The retrieval results from a KOUN's case are presented in Fig. 6 where the panels contain 360 data points corresponding to 360 azimuthal degrees, i.e., the retrievals have been performed for each radial. Melting layers are highly nonuniform with quite different radar variables in the radar radials. One can see significant variations in the retrieved D , b/a , and N , but a rather narrow distribution in $\langle \theta \rangle$. The latter shows that the particles had a significant canting. The median retrieved parameters are shown in the angular brackets. These medians have been obtained from the retrieved 360 data points in each panel.

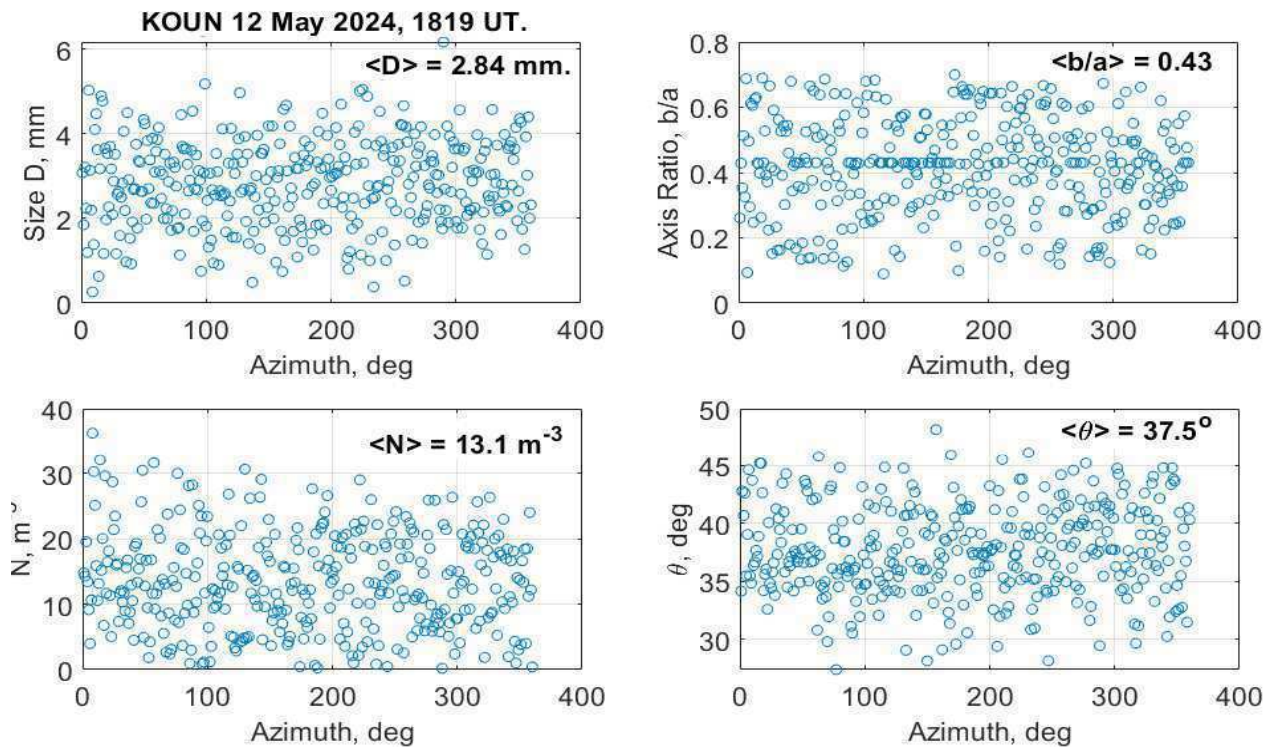


Fig. 6. Retrieval results from KOUN for 12 May 2024 at 1819 UTC,

The median D of 2.8 mm signifies rather large and oblate ($\langle b/a \rangle = 0.44$) scatterers. Most likely, the retrieved data are biased toward large scatterers because of the strong dependence on D as it typically occurs in radar observations. So, we attribute the obtained retrieved results to large particles in the ML. Multiwavelength radar experiments could shed more light on the accuracy of these retrievals.

4. Summary

The following conclusions follow from the presented results for S band polarization radars employing simultaneous transmission and reception of electromagnetic waves.

- Scattering differential phase δ can be positive and negative depending upon the system DPT. To use the differential phase and correlation coefficient in retrieval methods, DPT should be known (measured).
- The differential phase is a powerful variable for retrieval procedures: it is readily measurable and is not biased by noise in contrast to other radar variables.
- Measured Z , ZDR , DP , CC , and KDP (five radar variables) can be used to obtain sizes, axis ratios, orientation, and number concentration (four variables) of hydrometeors. The discussed approach could not be limited to melting layers and could be applied, for instance, to the dendritic growth layer.
- Radar with a digital transmitter can be capable of changing its DPT. This capability can be used to measure CC , DP , and KDP at various DPTs and make microphysical retrievals more precise.

References

- [1] S. Trömel, N. Kumjian, A. Ryzhkov, C. Simmer, M. Diederich, *J. Atmos. Oceanic Technol.*, 30 (11), 2529 – 2548, 2013.
- [2] S. Trömel, A. Ryzhkov, P. Zhang, C. Simmer, *J. Atmos. Oceanic Technol.*, 31 (10), 2344 – 2359, 2014.
- [3] D.S. Zrnić and V. Melnikov, *J. Atmos. Oceanic Technol.*, 40 (10), pp. 1221-1239, 2023.
- [4] F. Fabry and W. Szyrmer, *J. Atmos. Sci.*, **56**, 3593-3600, 1999.
- [5] Y. Fujyoshi, “Melting snowflakes”. *J. Atmos. Sci.*, **43**, 307-311, 1986.
- [6] V. Melnikov, D.S. Zrnić, and D. Mirkovic, *IEEE Trans. Geosci. Remote Sens.*, 2024.
- [7] V.N. Bringi and V. Chandrasekar, *Polarimetric Doppler Weather Radar: Principles and Applications*. Cambridge University Press, 2001, 636 pp.
- [8] V. Melnikov and E. Bridge, *IEEE Geosci. Remote Sens. Lett.*, 21, 2024.

Investigating the Spatiotemporal Characteristics of Motion Fields Using Three-Dimensional Radar Echoes to Construct an Ensemble Nowcasting System.

Kao-Shen Chung¹, Yu-Chiao Hsu¹, Yi-Hao Tsou², Hsin-Hung Lin³

¹*Department of Atmospheric Sciences, National Central University, Taoyuan City, Taiwan*

²*Data Quality Control Section, Remote Sensing Division, Central Weather Administration*

³*National Science and Technology Center for Disaster Reduction, New Taipei City, Taiwan*



Kao-Shen Chung

1 Introduction

Radar echo extrapolation is a more effective method for short-range weather prediction but loses accuracy with longer lead times due to errors in estimating convective system generation, dissipation, and radar echo motion fields (Germann et al. 2006; Tsonis and Austin 2010; Turner et al. 2004). These uncertainties challenge in capturing the full range of temporal and spatial variations in precipitation and motion fields. To address these issues, various methods introduce stochastic perturbations into the rainfall or motion field to develop an ensemble nowcasting, such as Short-term ensemble prediction systems (STEPS), which decomposes precipitation fields into different spatial scales to determine variations in precipitation at smaller scales and generate ensemble nowcasting, and other approaches that use historical meteorological data to inform perturbations (Atencia and Zawadzki 2014, 2015; Pulkkinen et al. 2019; Sokol et al. 2017). Some research in Taiwan also has improved forecasts by integrating MAPLE with wind field data and high-resolution numerical models, enhancing predictions, particularly in complex terrains (Chung and Yao 2020; Lin et al. 2020).

This study builds on these previous research by conducting a spatial and temporal analysis of three-dimensional motion fields derived from radar data for five weather events in Taiwan: autumn precipitation, Meiyu front, squall line, afternoon thunderstorm, and typhoon. The results inform the development of an ensemble nowcasting scheme, where perturbations are introduced into the two-dimensional motion field and adjusted based on the 3D motion field spatiotemporal analysis. The effectiveness of this ensemble nowcasting framework is then compared to deterministic MAPLE using various verification scores, focusing on the accuracy of radar echoes and accumulated rainfall forecast.

2 Methodology

The following section introduce the deterministic MAPLE and the ensemble version of MAPLE that were used in this study.

2.1 Deterministic MAPLE

MAPLE, a nowcasting system developed by the J. S. Marshall Radar Observatory at McGill University, was employed. MAPLE uses the VET technique to compute the motion fields based on past radar echo observations. These motion fields were subsequently applied in extrapolation forecasting through a semi-Lagrangian backward scheme, in combination with the observed radar data at the forecast's initial time. Expanding on the MAPLE nowcasting system, this study incorporated the observed radar echo data at each height. The VET method was employed to estimate motion fields at different altitudes. These two-dimension motion fields at each height, called 3D motion fields, were then analyzed and applied to the ensemble nowcasting scheme developed in this study, which is based on MAPLE.

$$J_{VET}(\mathbf{U}) = J_{\Psi} + J_V \quad (1)$$

$$J_{\Psi} = \iint_{\Omega} \beta(\mathbf{x}) [\Psi(t_0, \mathbf{x}) - \Psi(t_0 - \Delta t, \mathbf{x} - \mathbf{u}\Delta t)]^2 dx dy \quad (2)$$

$$J_V = \Upsilon \iint_{\Omega} \left[\left(\frac{\partial^2 u}{\partial x^2} \right)^2 + \left(\frac{\partial^2 u}{\partial y^2} \right)^2 + 2 \left(\frac{\partial^2 u}{\partial x \partial y} \right)^2 + \left(\frac{\partial^2 v}{\partial x^2} \right)^2 + \left(\frac{\partial^2 v}{\partial y^2} \right)^2 + 2 \left(\frac{\partial^2 v}{\partial x \partial y} \right)^2 \right] dx dy \quad (3)$$

The cost function for the VET technique is represented by Eq. (1). \mathbf{U} is a two-dimensional motion vector, which represents the 2D radar echo motion field information obtained after minimization of this cost function. J_{Ψ} represents the sum of squares of the residuals, serving as a conservation of reflectivity constraint. J_V in Eq. (1) denotes a smoothness penalty function, which aggregates the squares of the second derivatives of the motion field in space. In the above equations, β and Υ is the weight for the constraint of conserved reflectivity and the coefficient for the smoothing penalty weight, respectively

By using the aforementioned VET computation, a set of radar echo motion field information with a vector count of $m \times n$ was obtained. The semi-Lagrangian backward scheme proposed by Germann and Zawadzki (2002) was used for extrapolation forecasting.

2.2 Ensemble version of MAPLE

One of the underlying nowcast uncertainties in radar echo extrapolation comes from the uncertainty of the motion field at different heights. To address this issue, this study employed the VET method to compute the 2D radar echo motion field based on the observed composite radar reflectivity at different heights from previous observations. Perturbations were introduced into the motion field, and the standard deviation values for the added perturbations were adjusted based on the spatiotemporal characteristics of the 3D motion field across different weather events. This approach tries to capture the variation of motion field and forms the foundation of the ensemble nowcasting scheme implemented in this study.

A 2D perturbation field can be generated using a power-law filter, as demonstrated by Schertzer and Lovejoy (2012) and Zhivomirov (2018). The standard deviation and mean of the color noise obtained after the Gaussian white noise undergoes the power-law filter process remain 1 and 0, respectively. To generate perturbation magnitudes suitable for different weather events, it is necessary to readjust the standard deviation values of the perturbations based on the analysis results of the motion fields over time and vertical spatial heights. Eqs (4) and (5) are the formulas for calculating the mean and standard deviation of motion fields at different heights over time and space. Because grid points lacking radar echo information are considered less reliable in the VET method, our analysis of standard deviation and mean values focuses solely on grid points with available radar echo data.

$$\bar{x}_{i,j} = \frac{1}{N} \sum_{k=1}^N x_{i,j,k} \quad (4)$$

$$\sigma_{i,j} = \sqrt{\frac{1}{N} \sum_{k=1}^N (x_{i,j,k} - \bar{x}_{i,j})^2} \quad (5)$$

In the spatial analysis, i and j in Eqs (4) and (5) represent the grid points in the x and y directions of the 2D motion field, N represents the total number of vertical height layers and k is the number of vertical levels. On the other hand, when the Eqs (4) and (5) are used in the temporal analysis, the variable k denotes the number of time steps, and N is the total number of time steps. After that, the standard deviation of perturbations in the u and v directions was adjusted to the suitable values for each weather event based on the spatiotemporal analysis of the 3D motion field across various weather events. By incorporating these adjusted perturbations into the initial motion field derived from the observed 2D composite reflectivity, a revised motion field is obtained after perturbation. Figure 1 presents the process of integrating random perturbations. Because each set of perturbations in the u and v directions is randomly generated from Gaussian white noise fields, the ensemble size can be determined by the number of generated perturbation sets. To derive ensemble nowcasting outcomes, these newly generated motion fields will ultimately be combined with observed radar echo data at the initial time for extrapolation forecasting.

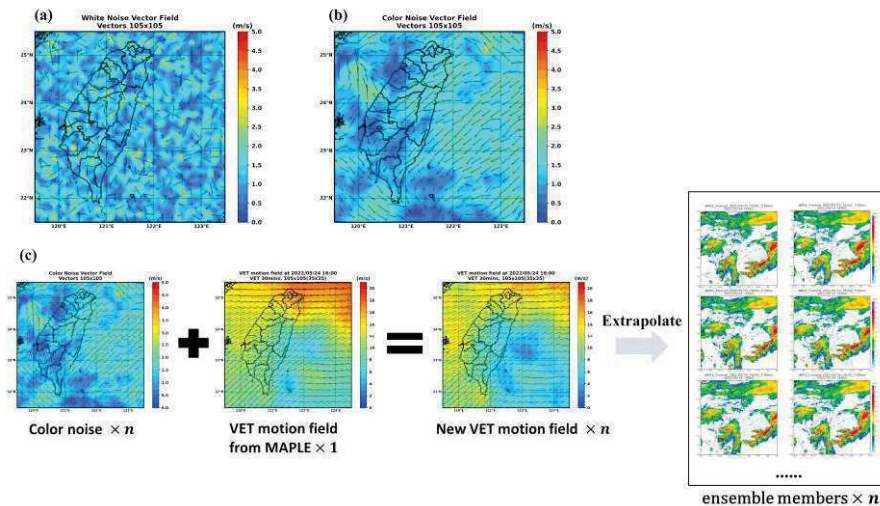


Figure 1: (a) Both the u - and v -velocity are the Gaussian white noise fields, forming the distribution of the motion field. (b) The color noise from (a), which is produced by the power-law filter. (c) The process of adding the perturbation into motion field. Adjust the standard deviation of u - and v -velocity color noise field to the standard deviation with spatial and temporal analysis (left, color noise $\times n$). Add the perturbation to the motion field which calculated by VET methods (middle, VET motion field from MAPLE) and produce the new motion field (right, new VET motion field $\times n$). The new motion field will be used as the motion field of the ensemble nowcasting and produce n ensemble members.

3 Dataset

For this study, 374 3-h rainfall events were selected, including squall lines, Meiyu front, autumn precipitation, afternoon thunderstorms, and typhoon. Since Yilan, in northeastern Taiwan, experiences more autumn precipitation than other regions, the analysis and discussion of motion fields and accumulated rainfall will be focused on the performance in this region. Specific details regarding the selected weather events are presented in Table 1. The precipitation data and high-resolution radar observations utilized in this study were sourced from the quantitative precipitation estimation and segregation using multiple sensor (QPESUMS) severe weather monitoring system, regulated by the Central Weather Administration. The 2D reflectivity mosaic was used in ensemble nowcasting scheme. 3D reflectivity mosaic dataset was constructed by interpolating polar coordinate data from the ten individual radars into a 3D Cartesian coordinate system (Zhang et al. 2009). This dataset facilitates the computation of the 3D motion field. The vertical resolution comprises 21 layers, with a resolution of 1 km for altitudes exceeding 6 km and 0.5 km for altitudes ranging from 1 to 5 km. Both 2D and 3D reflectivity mosaic has a spatial resolution of 0.0125° and a temporal resolution of 10 min. The domain of these dataset can refer to Fig 2.

Table 1. The weather events used in this study.

Event type	Event date	Number of periods for 3-h forecast (hr)
Autumn precipitation	2021/11/26~11/28	52
Meiyu front	2022/05/24~05/26, 2022/06/06~06/08	96
Afternoon thunderstorm	2022/06/24, 2022/06/25, 2022/07/04, 2022/07/05	32
Squall line	2022/06/09, 2022/07/02, 2023/04/19	26
Typhoon	2010/09/18~09/20, 2015/08/07~08/09, 2016/09/26~09/28, 2017/07/28~07/30	168
Total	14 events	374 (total 1122 hours)

The precipitation data used in this study were subject to the quantitative precipitation estimation method corresponding to the radar band specific to each of the ten meteorological radars in Taiwan (see in Figure 2). the estimated quantitative precipitation over land areas was adjusted using data from ground-based rainfall stations (Chang et al. 2021). This precipitation estimate served as the foundation for the observed precipitation in the present study. To translate the predicted reflectivity into a precipitation value, Chang et al. (2017) specified a method of using of the Z–R relationship that is suitable for applications involving Taiwanese rainfall (refer to Eq. (6)). The verification domains for rainfall and reflectivity corresponding to each of the five categories of weather events are presented in Figure 4(b). Specifically, the rainfall verification domain included only the rainfall data over land areas.

$$Z = 223.04 \times R^{1.51} \quad (6)$$

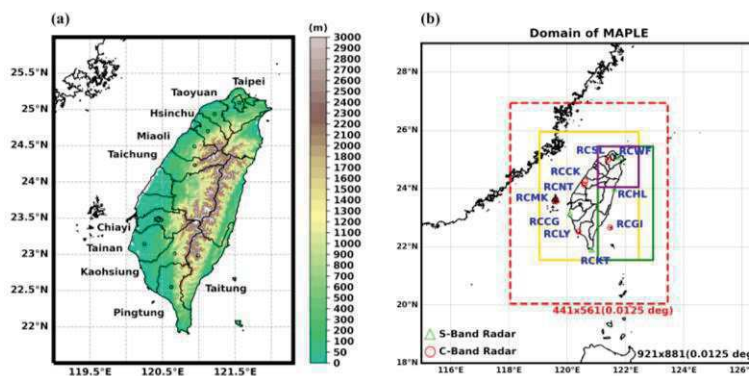


Figure 2: (a) Topographic map of Taiwan. The shaded represents terrain height in meter. The locations and names of cities mentioned in this study are also indicated. (b) The radar data and verification domain in this study. Green triangles and red circles are the location of S-band and C-band radar. Black rectangle is the domain of 2-Dimension composite reflectivity data. Red dash line rectangle is the domain of 3-Dimension radar data. Yellow rectangle is the domain of Meiyu front, afternoon thunderstorm, squall line and typhoon events for reflectivity and rainfall verification. Green and purple rectangle are the domain of autumn precipitation for reflectivity verification and rainfall verification, respectively.

4 Results

To examine the spatiotemporal properties of the motion field in each precipitation event, we computed the mean and standard deviation of the u- and v-component at each grid point in the 3D motion field across different vertical heights and

time intervals (see in Section 2.2). On the basis of the spatial and temporal statistics, Table 2 shows the average means and standard deviations in the u and v directions under various weather events. These results served as the basis for generating motion field perturbations in the ensemble nowcasting scheme. This study utilized 100 ensemble members to conduct a three-hour ensemble forecast.

Table 2. The mean and standard deviation of motion fields from five types of weather events in this study.

Standard deviation		
	u(m/s)	v(m/s)
Autumn precipitation	1.5	1.3
Meiyu front	1.75	0.8
Afternoon thunderstorm	0.6	0.7
Squall line	1.4	0.97
Typhoon	1.13	1.21

For the investigation which employ comparisons between ensemble forecast radar echoes and observed radar echoes in order to verify the ensemble nowcasting, we use the ROC curves, reliability diagram and rank histogram. Figure 3 shows the overall performance of these five weather events in this study. It demonstrates that the ensemble version of MAPLE outperforms the deterministic MAPLE (dash line) over a lead time of three hours in ROC curves, indicating robust discrimination capabilities for events involving anticipated rainfall. The reliability diagram shows the ensemble version of MAPLE demonstrates stable reliability performance within a three-hour forecast period across all weather events. But it also tends to show overestimation at high forecast probability and underestimate at low forecast probabilities. This indicates that the ensemble nowcasting system may produce overconfident forecast results due to its inability to accurately capture the generation and dissipation of precipitation. However, the rank histogram shown in Fig. 3(c) generally exhibits a U-shape and is slightly left-skewed overall, indicating a minor overestimation by the ensemble forecasting system. For the maximum and minimum ranks, the proportion is approximately 10%, while the distribution of other ranks remains consistent over time, demonstrating the forecast stability of this ensemble system.

A comparison of 3-h accumulated rainfall forecasts between deterministic MAPLE and the ensemble version of MAPLE, including QFPF20, PM, and NPM, was conducted across five different weather events: autumn precipitation, the Meiyu front, squall line, afternoon thunderstorm, and typhoon in Taiwan. Figures 4(a) and 4(b) present the average SCC and RMSE scores across the five types of weather events examined in this study. Overall, the ensemble nowcasting system developed in this research more accurately represents the distribution and magnitude of 3-h accumulated rainfall compared to the deterministic MAPLE, aligning more closely with observed accumulated rainfall. This indicates that the ensemble version of MAPLE indeed improves forecast accuracy. Figures 4(c) and 4(d) illustrate the differences in the ETS and BIAS scores between deterministic MAPLE and the ensemble version of MAPLE for 3-h accumulated precipitation across five weather patterns at various precipitation thresholds. The ensemble version of MAPLE performs better at rainfall thresholds exceeding 0.5 mm/hr. Among these methods, QFPF20, which places more emphasis on intense precipitation characteristics, shows a BIAS value closer to 1 at higher thresholds, indicating the smallest deviation from the observed accumulated rainfall.

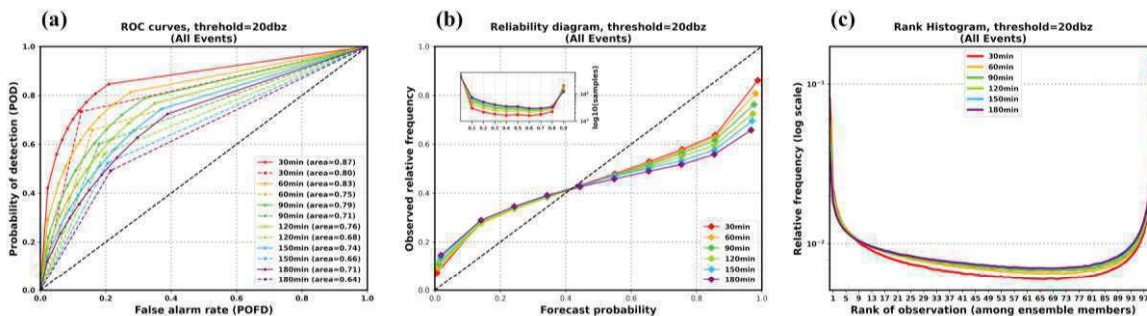


Figure 3: The average (a) ROC curves, (b) reliability diagram and (c) rank histogram of five weather events (autumn precipitation, Meiyu front, afternoon thunderstorm, squall line and typhoon) in Taiwan with 100 ensemble members. The dash lines in ROC curve represent the deterministic MAPLE and the solid lines are ensemble version of MAPLE.

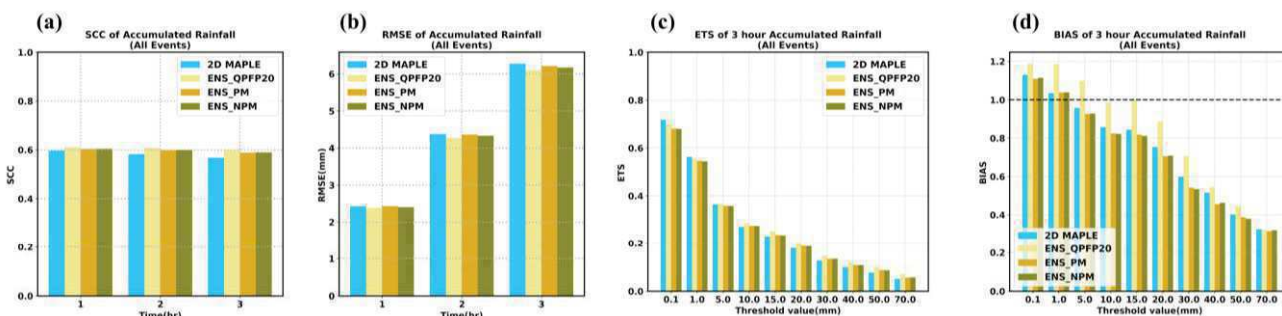


Figure 4: The average (a) SCC, (b) RMSE, (c) ETS and (d) BIAS score of five weather events (autumn precipitation, Meiyu front, afternoon thunderstorm, squall line and typhoon) in Taiwan.

5 Conclusions

The radar echo extrapolation is effective for short-term weather forecasting but encounters significant limitations as forecast lead times increase. These limitations primarily arise from the uncertainty in estimating motion fields and an inadequate representation of convection growth and decay. To address these challenges, this study expands on the concept of radar extrapolation by using 3D radar observation data to compute the comprehensive motion fields of radar echoes. This approach captures movement details across different spatial heights. Through an analysis of temporal and spatial variations, this study developed an ensemble nowcasting system based on radar echo extrapolation. The study examined and analyzed forecast accuracy across five prevalent weather patterns in Taiwan: afternoon thunderstorms, squall lines, Meiyu front, autumn precipitation and typhoon.

When tested with 100 ensemble members, the ensemble nowcasting system displayed robust performance, extending its forecasting capabilities to 180 minutes across various weather scenarios in Taiwan. Notably, it significantly improved the accuracy of rainfall predictions and mitigated overestimation issues commonly observed in the deterministic MAPLE forecast. However, despite these advancements, the ensemble nowcasting system still faces challenges in accurately forecasting convective generation and dissipation, which are critical for predicting weather systems with high variability, such as thunderstorms. Overall, the study highlights the potential of ensemble nowcasting to provide more reliable and precise forecasts, while also recognizing the need for further refinement to address the inherent uncertainties associated with convective processes.

6 Acknowledgements

This work is supported by the Taiwan National Science and Technology Council (NSTC 112-2625-M-008-003).

7 References

- Atencia, A., and I. Zawadzki, 2014: A Comparison of Two Techniques for Generating Nowcasting Ensembles. Part I: Lagrangian Ensemble Technique. *Monthly Weather Review*, **142**, 4036-4052. doi:10.1175/Mwr-D-13-00117.1
- , 2015: A Comparison of Two Techniques for Generating Nowcasting Ensembles. Part II: Analogs Selection and Comparison of Techniques. *Monthly Weather Review*, **143**, 2890-2908. doi:10.1175/Mwr-D-14-00342.1
- Chang, P. L., and Coauthors, 2021: An Operational Multi-Radar Multi-Sensor QPE System in Taiwan. *Bulletin of the American Meteorological Society*, **102**, E555-E577. doi:10.1175/Bams-D-20-0043.1
- Chung, K. S., and I. A. Yao, 2020: Improving Radar Echo Lagrangian Extrapolation Nowcasting by Blending Numerical Model Wind Information: Statistical Performance of 16 Typhoon Cases. *Monthly Weather Review*, **148**, 1099-1120. doi:10.1175/Mwr-D-19-0193.1
- Germann, U., and I. Zawadzki, 2002: Scale-dependence of the predictability of precipitation from continental radar images. Part I: Description of the methodology. *Monthly Weather Review*, **130**, 2859-2873. doi:10.1175/1520-0493(2002)130<2859:Sdotpo>2.0.Co;2
- Germann, U., I. Zawadzki, and B. Turner, 2006: Predictability of precipitation from continental radar images. Part IV: Limits to prediction. *Journal of the Atmospheric Sciences*, **63**, 2092-2108. doi:10.1175/Jas3735.1
- Lin, H. H., C. C. Tsai, J. C. Liou, Y. C. Chen, C. Y. Lin, L. Y. Lin, and K. S. Chung, 2020: Multi-Weather Evaluation of Nowcasting Methods Including a New Empirical Blending Scheme. *Atmosphere*, **11**, 1166. doi:ARTN 116610.3390/atmos1111166
- Pulkkinen, S., D. Nerini, A. A. P. Hortal, C. Velasco-Forero, A. Seed, U. Germann, and L. Foresti, 2019: Pysteps: an open-source Python library for probabilistic precipitation nowcasting (v1.0). *Geoscientific Model Development*, **12**, 4185-4219. doi:10.5194/gmd-12-4185-2019
- Schertzer, D., and S. Lovejoy, 2012: Physical modeling and analysis of rain and clouds by anisotropic scaling multiplicative processes. *Journal of Geophysical Research: Atmospheres*, **92**, 9693-9714. doi:10.1029/JD092iD08p09693
- Sokol, Z., J. Mejsnar, L. Pop, and V. Bliznák, 2017: Probabilistic precipitation nowcasting based on an extrapolation of radar reflectivity and an ensemble approach. *Atmospheric Research*, **194**, 245-257. doi:10.1016/j.atmosres.2017.05.003
- Tsonis, A. A., and G. L. Austin, 2010: An evaluation of extrapolation techniques for the short-term prediction of rain amounts. *Atmosphere-Ocean*, **19**, 54-65. doi:10.1080/07055900.1981.9649100
- Turner, B. J., I. Zawadzki, and U. Germann, 2004: Predictability of precipitation from continental radar images. Part III: Operational nowcasting implementation (MAPLE). *Journal of Applied Meteorology*, **43**, 231-248. doi:10.1175/1520-0450(2004)043<0231:Popfcr>2.0.Co;2
- Zhang, J., and Coauthors, 2009: High-Resolution QPE System for Taiwan. *Data Assimilation for Atmospheric, Oceanic and Hydrologic Applications*, Springer, 147-162.
- Zhivomirov, H., 2018: A method for colored noise generation. *Romanian journal of acoustics and vibration*, **15**, 14-19

Operational aspects

Radar-based studies of terrain-induced windshear and microbursts near the Hong Kong International Airport during the passage of Super Typhoon Saola in September 2023

Chan Ying-wa¹

¹*Hong Kong Observatory, Hong Kong, China*



Ying-wa Chan

1 Introduction

Super Typhoon Saola came very close to Hong Kong on 1 and 2 September 2023 with maximum sustained wind near its centre exceeding 200 km/h. During the passage of Saola, significant terrain-induced windshear and microbursts as well as severe turbulence affected the Hong Kong International Airport (HKIA). As the Hong Kong Observatory (HKO) has installed a C-band Terminal Doppler Weather Radar (TDWR) at Brothers Point (BP) for monitoring windshear and microburst at HKIA, observations from the BP TDWR as well as other X-band and S-band weather radars operated by HKO (Figure 1) were used for studying the characteristics of terrain-induced windshear and microbursts caused by an intense tropical cyclone.



Figure 1: The locations of Phased Array Weather Radar (PAWR) at Sha Lo Wan (SLW), S-band weather radar at Tate's Cairn (TC), X-band weather radar at Siu Ho Wan (SHW) and C-band Terminal Doppler Weather Radar (TDWR) at Brothers Point (BP).

2 Methodology

Spatial density maps showing the frequency occurrence of windshear and microbursts alerts issued by the BP TDWR and SHW X-band radar were compiled for identifying the spatial relationship between the alerts and the mountainous regions near the HKIA. Eddy Dissipation Rate (EDR) maps estimated using spectral width data from the weather radar at TC and SLW PAWR were used for assessing the severity of turbulence. The fields of Doppler velocity and spectral width as well as the associated cross-sections from the radars were analysed for studying the characteristics and structures of high and low wind streaks propagating out from the terrain near the HKIA.

3 Dataset

The dataset used in the study included primarily observations from the HKO's weather radar network including X-band PAWR at SLW, S-band radar at TC, X-band radar at SHW and C-band BP TDWR together with SLW's wind profiler data and wind data recorded by the HKO's automatic weather station (AWS) network during the period of 1-2 September 2023.

4 Results

Observations from HKO's wind profiler at SLW showed that winds over Hong Kong were generally from the north to northwest on the night of 1 September 2023 which then veered to the east to southeast in the morning of 2 September 2023 in line with the westward movement of Saola (Figure 2).

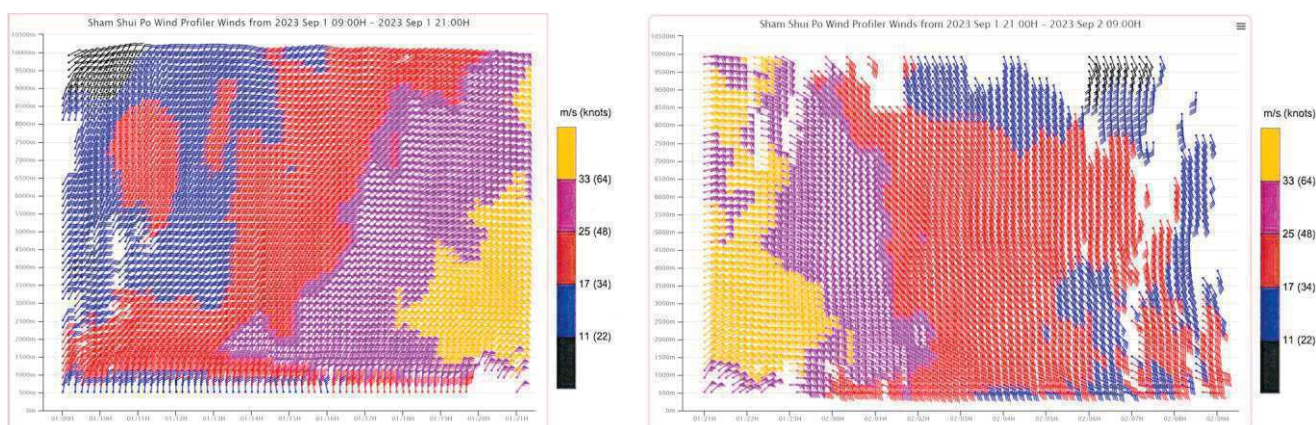


Figure 2: Wind profiler measurements at Sha Lo Wan (SLW), Hong Kong on 1-2 September 2023. One pennant, one long barb, and one short barb indicate each 25.7 ms^{-1} (50 knots), 5.1 ms^{-1} (10 knots), and 2.6 ms^{-1} (5 knots), respectively. The x-axis is the local time (UTC + 8 hours) in the format of DD/HH and the y-axis is the height.

The spatial density maps showing the frequency occurrence of windshear and microbursts alerts issued by the BP TDWR and SHW X-band radar from 16:30 HKT on 1 September 2023 to 07:00 HKT on 2 September 2023 were compiled (Figure 3). The maps suggested the presence of two NNW-SSE orientated high wind streaks propagating southeastwards from two major mountains (Castle Peak and Kau Keng Shan with heights over 500 m amsl and 400 m amsl respectively) to the north of the HKIA when local prevailing winds were from the north to northwest. As Saola moved further west in the early morning of 2 September 2023 and local winds veered to the east and southeast, more windshear and microbursts alerts were triggered which were associated with three separate WNW-ESE orientated high wind streaks emanating from the northwestern side of the mountainous Lantau Island to the south of the HKIA. Those high wind streaks tied in well with the positions of Por Kai Shan (over 400 m amsl), Nei Lak Shan (over 700 m amsl) and Cheung Shan (over 400 m amsl) respectively. Also, high frequency occurrence of windshear and microburst was detected by the SHW X-band radar over the northeastern part of the HKIA (blue ellipse in the right panel of Figure 3) which was thought to be caused by the high-speed gap flow near the Lo Fu Tau mountain similar to the study by Chan et al. [1].

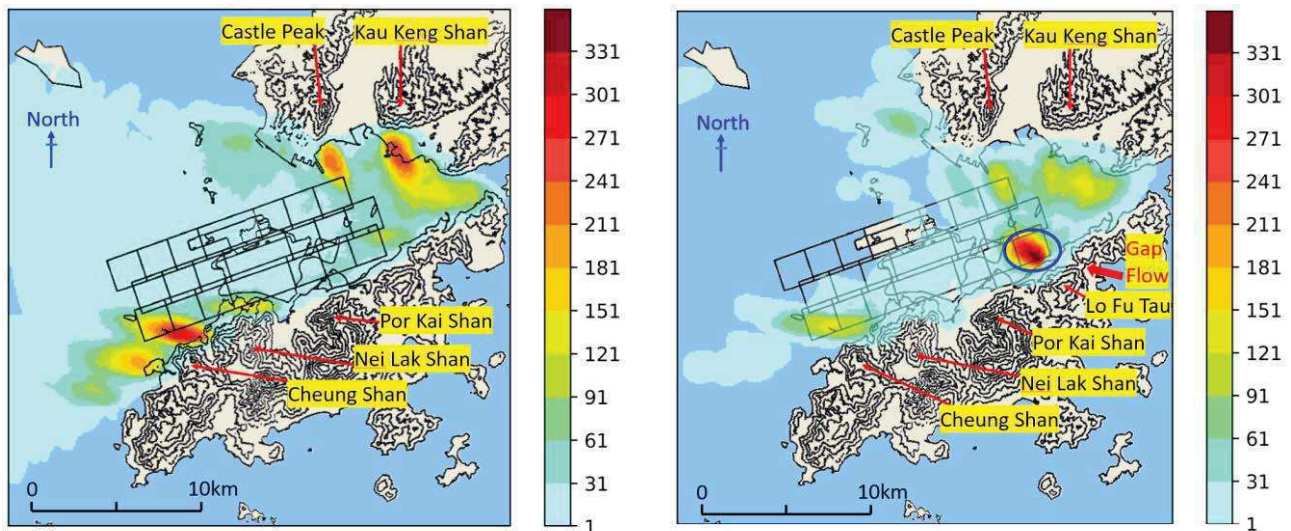


Figure 3: Spatial density maps showing the frequency occurrence of windshear and microbursts alerts issued by the BP TDWR (left) and SHW X-band radar (right) from 16:30 HKT on 1 September 2023 to 07:00 HKT on 2 September 2023. Terrain contours are in 100 m intervals.

Detailed analysis of radial velocity fields from 0.9° scans of SHW X-band radar around 16:30 HKT on 1 September 2023 showed NNW-SSE orientated high and low wind streaks when the prevailing winds were from the north to northwest. Similar observations were found in Shun and Lau [2] and Chan and Hon [3]. The high wind streaks with width of around 1-2 km exhibited meandering wavy characteristics which suggested the possible existence of vortex shedding (Figure 4).

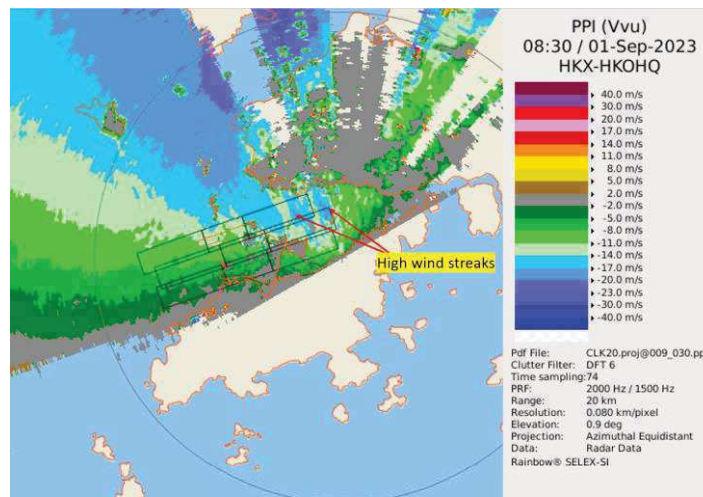


Figure 4: High wind streaks detected by the SHW X-band radar at 16:30 HKT on 1 September 2023 when local prevailing winds were from the north to northwest.

From 16:29 to 16:32 HKT, pockets of high wind (radial velocity more than 20 ms^{-1}) were observed bursting out from the Castle Peak and propagated southeastwards with a speed of around 90-100 km/h. The Eddy Dissipation Rate (EDR) at 1 km height estimated using spectral width data from the weather radar at TC and SLW PAWR showed high EDR (with maximum values reaching the range of 0.45 - 0.50 $\text{m}^{2/3}\text{s}^{-1}$) southeast of the Castle Peak, indicating the occurrence of severe turbulence (Figure 5).

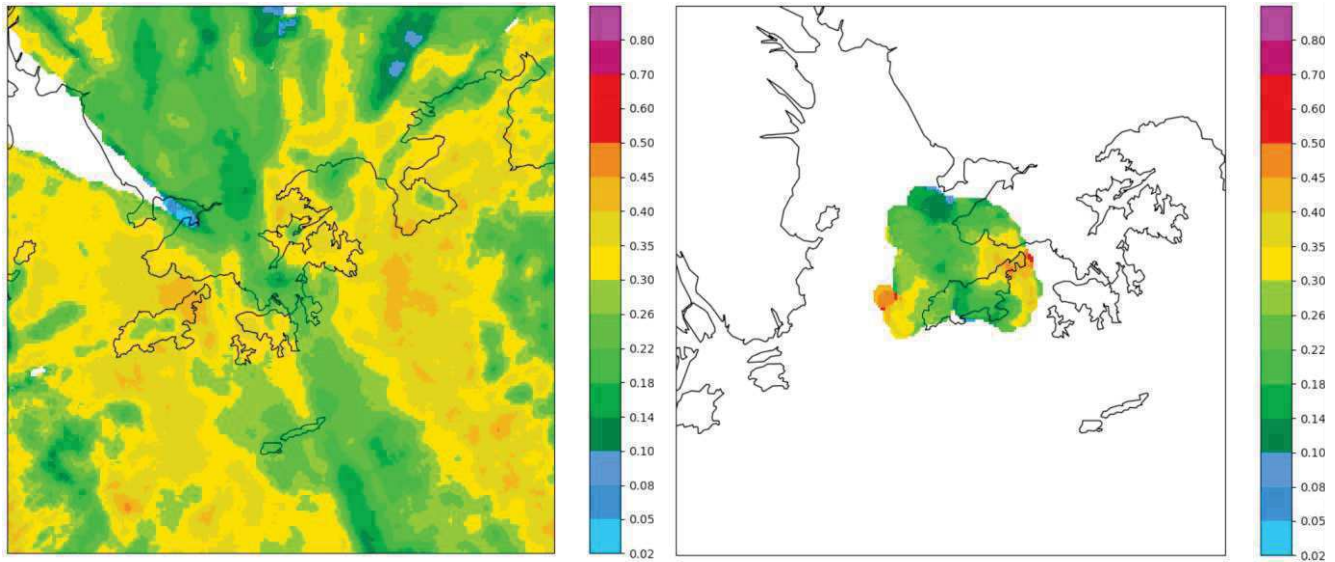


Figure 5: EDR (in units of $m^{2/3}s^{-1}$) maps at height of 1 km based on the spectral width data of the weather radar at TC (left, 16:30 HKT) and the SLW PAWR (right, 16:32 HKT) on 1 September 2023.

When low-level winds changed to east to southeasterlies, bursting of high wind pockets (radial velocity over 17 ms^{-1}) from Nei Lak Shan was observed by BP TDWR at 0.6° scan in 02:51– 02:54 HKT on 2 September 2023. The pockets propagated west-northwestwards with a speed of around 80-90 km/h. The 1-km height EDR values to the west of Nei Lak Shan were in the region of $0.35 - 0.40\text{ m}^{2/3}\text{s}^{-1}$ (moderate turbulence). These high wind pockets lasted for a few minutes before losing the identity for tracking their movements.

The SLW PAWR provided useful observations of the vertical structure of those high wind streaks. When surface winds prevailed from the north to northwest such as 16:30 HKT on 1 September 2023, cross section of radial velocity from SLW PAWR showed that the jet core of the NNW-SSE orientated high wind streaks was around 0.6 to 1 km in height. When surface prevailing winds were from the east to southeast as in the case at 03:06 HKT on 2 September 2023, the jet core of the WNW-ESE orientated high wind streaks was about 1 km in height but the core thickness grew further downwind with a tendency to spread downwards closer to the ground beyond 5 km from the coast of the Lantau Island. Similar heights for the jet cores of the above NNW-SSE and WNW-ESE high wind streaks were also observed through the cross sections of radial velocity from both BP TDWR and SHW X-band radar. In addition, cross section of spectral width from SLW PAWR at 02:55 HKT on 2 September 2023 showed apparent sign of turbulence with spinning eddies below 2 km (Figure 6). The above observations suggested the downward transport of momentum and vorticity aloft.

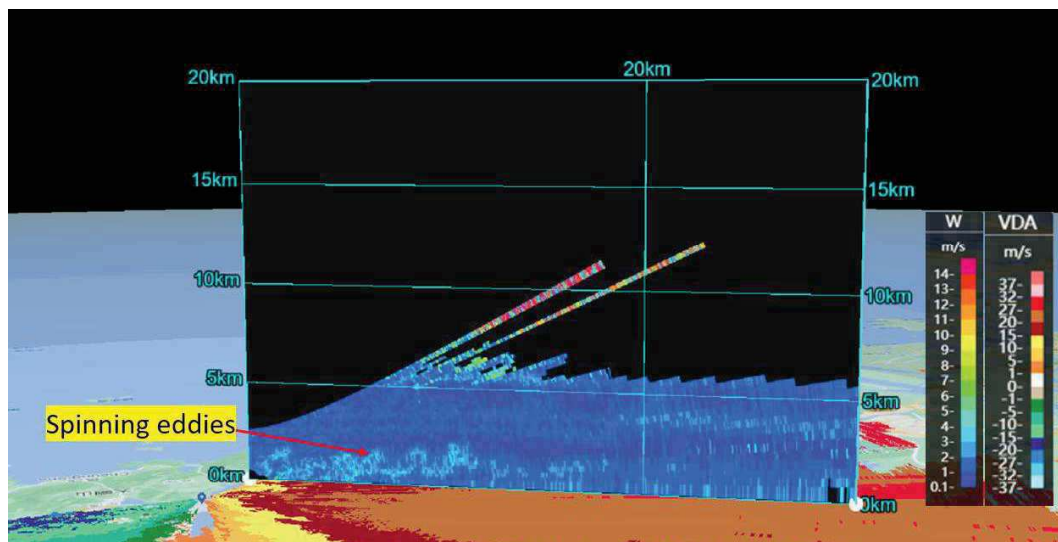


Figure 6: Cross-section of spectral width from SLW PAWR at 02:55 HKT on 2 September 2023 showing apparent sign of turbulence with spinning eddies below 2 km.

5 Conclusions

The passage of Saola on 1-2 September 2023 provided an invaluable opportunity to study the characteristics of terrain-induced windshear and microbursts caused by gale to hurricane force low-level winds first from the north and then the south relative to the HKIA. The complementary use of radar observations from a network of weather radars in Hong Kong helped to characterise those high wind streaks generated as a result of Saola's circulation and their relations to the mountains/peaks to the north and south of the HKIA. The study enhanced understanding of terrain-induced windshear and microbursts during the passages of tropical cyclones which was essential for the operations of landing/departing aircraft at the HKIA.

6 Acknowledgements

Special thanks to Messrs Chung Tsz-hong and Wong Tim-chun in preparing various figures for the paper.

7 References

- [1] P.W. Chan, P. Cheung and K.K. Lai, 2024: Observation and numerical simulation of terrain-induced airflow leading to low level windshear at the Hong Kong International Airport based on Range-Height-Indicator scans of a LIDAR, Meteorol. Z. Vol. 33, 255-262. DOI: [10.1127/metz/2024/1221](https://doi.org/10.1127/metz/2024/1221).
- [2] C.M. Shun and S.S.Y. Lau, "Terminal Doppler Weather Radar (TDWR) observation of atmospheric flow over complex terrain during tropical cyclone passages", in Microwave Remote Sensing of the Atmospheric and Environment II, Vol. 4152 of Proceedings of SPIE, Sendai, Japan, December 2000.
- [3] P.W. Chan, K.K. Hon, "Observation and Numerical Simulation of Terrain-Induced Windshear at the Hong Kong International Airport in a Planetary Boundary Layer without Temperature Inversions", Advances in Meteorology, Vol. 2016, Article ID 1454513, 9 pages, 2016. DOI: [10.1155/2016/1454513](https://doi.org/10.1155/2016/1454513).

An Inter-Radar Interference Suppression Method for Weather Radar Data Without Modifying the Radar's Internal Signal Processing

Shota Ochi¹, Noritsugu Shiokawa¹, Tomomi Aoki¹, Masakazu Wada², Satoshi Kida²

¹ TOSHIBA Corporation, Kawasaki, Japan

² TOSHIBA Digital Solutions Corporation, Kawasaki, Japan



Shota Ochi

1 Introduction

Public distribution of data from the Ministry of Land, Infrastructure, Transport and Tourism's (MLIT's) parabolic dual-polarization radars began in 2022, allowing private commercial use of radar data in Japan. Recently, we found that the MLIT's X-band parabolic dual-polarization radar data still contain signals that appear to be interference from other radars, even though each radar's internal signal processing includes interference suppression. When private parties use MLIT radar data, these interference signals must be properly suppressed, but these parties cannot modify the radar's internal signal processing. The aim of this study was to suppress interference signals from the distributed radar data without modifying the current radar's internal signal processing.

2 Overview of the Signal Processing Flow

The MLIT's parabolic dual-polarization radar data consist of plan position indicator (PPI) data for parameters such as radar reflectivity ZH, differential reflectivity ZDR, and specific differential phase KDP, which are generated by the radar's internal signal processing from signals received by a parabolic antenna. The publicly available radar data are structured as polar coordinates (range, azimuth, and elevation) after averaging for each sector (azimuth grid point) and do not include in-phase and quadrature component (I/Q) data or data for each pulse.

The radar's internal signal processing includes interference suppression processing, which detects interference when the received signal amplitude increases instantaneously [1]. However, this method cannot detect interference that is continuously mixed in the range or azimuth direction, leading to the possibility of residual interference in the distributed radar data. These interference signals must be suppressed before the radar data can be used. We have developed a proprietary method to detect and suppress interference signals only from the distributed radar data to prevent the degradation of the quality of our services using radar data. An overview of the signal processing flow is shown in Figure 1.

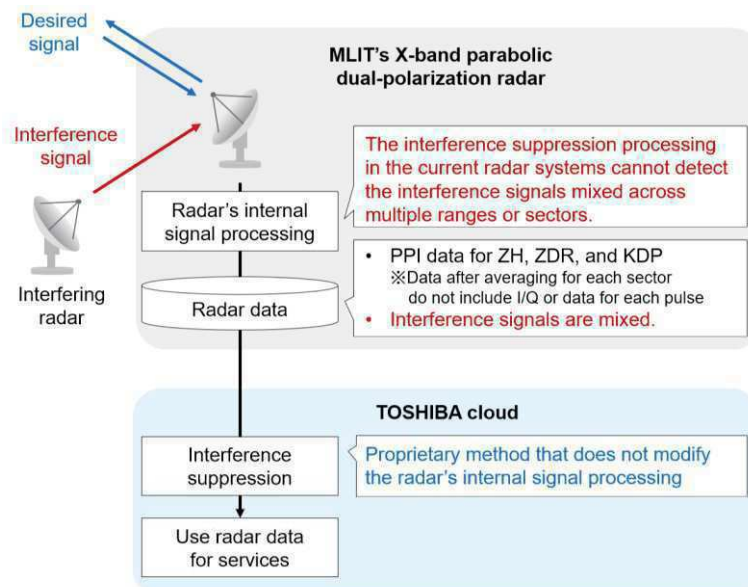


Figure 1: Overview of the signal processing flow

3 Analyzed Cases of Interference

We analyzed the interference signals mixed into the X-band parabolic dual-polarization radar data from the Kantou and Funabashi stations at a date and time when the coverage of each radar station had mostly clear skies. Table 1 shows information on the analyzed interference cases, and Figure 2 shows the locations of the Kantou and Funabashi stations.

Table 1: Analyzed interference cases

	Kantou	Funabashi
Time of day (JST)	2023/6/29 11:59–12:45	2023/6/29 9:23–9:31
Elevation angles	1.38–20.0 deg (all 12 observation angles)	1.6 and 2.6 deg (two low angles)
Number of PPIs	28	3
Direction	Various directions: strong interference signals with ZH >40 dBZ appeared especially in the northeast	Northeast

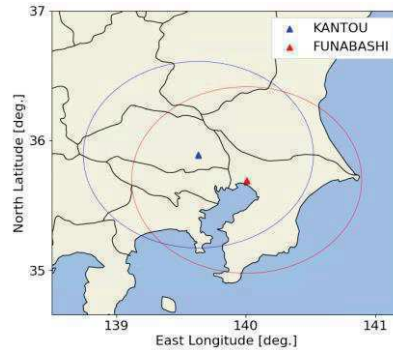


Figure 2: Locations of the Kantou and Funabashi stations

The interference signals were continuously mixed in the range direction at different azimuth angles (sectors) depending on the time and were distributed in a linear or fan shape on the PPIs. The characteristics of the radar reflectivity ZH and the differential reflectivity ZDR showed that these interferences can be roughly classified into three groups: (1) the interferences cover more than five sectors, the maximum ZH value is more than 30 dBZ, and the maximum ZDR value is more than 10 dB; (2) the characteristics of the interference coverage and the maximum ZH value are similar to those of group 1, except that the ZDR is mainly negative and the minimum ZDR value is less than -10 dB; and (3) the interferences cover up to five sectors, ZH is mainly less than 30 dBZ, and ZDR is mainly ± 5 dB or invalid. Table 2 summarizes the characteristics of these three groups, and Figure 3 shows examples of PPIs for ZH and ZDR in each interference group. The areas where the interference signals are mixed are surrounded by red dashed lines.

Table 2: Characteristics of the three interference groups

	Group 1	Group 2	Group 3
ZH	<ul style="list-style-type: none"> Interference signals cover more than 5 sectors Maximum value is >30 dBZ 		<ul style="list-style-type: none"> Interference signals cover 1 to 5 sectors Mainly <30 dBZ
ZDR	<ul style="list-style-type: none"> Mainly positive values Maximum value is >10 dB 	<ul style="list-style-type: none"> Mainly negative values Minimum value is < -10 dB 	<ul style="list-style-type: none"> Mainly ± 5 dB or invalid

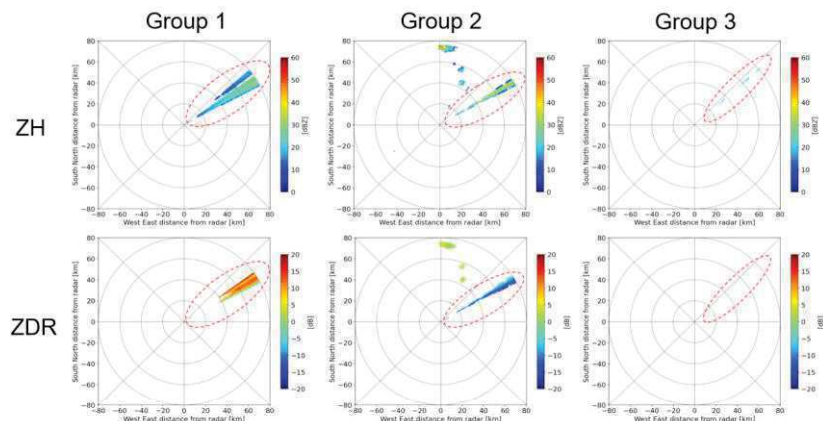


Figure 3: Examples of PPIs for ZH and ZDR in each interference group

4 Results

The actual radar data from the Kantou and Funabashi stations were subjected to interference suppression processing using our proprietary method. The results confirmed that the interference signals were suppressed by the proprietary method in a total of 31 cases that included all 3 groups. Figure 4 shows examples of the PPIs for ZH before and after the interference suppression processing. As shown in Figure 4, the interference signals surrounded by the red dashed line in the ZH PPIs before interference suppression processing (top row) were suppressed in the PPIs after interference suppression processing (bottom row).

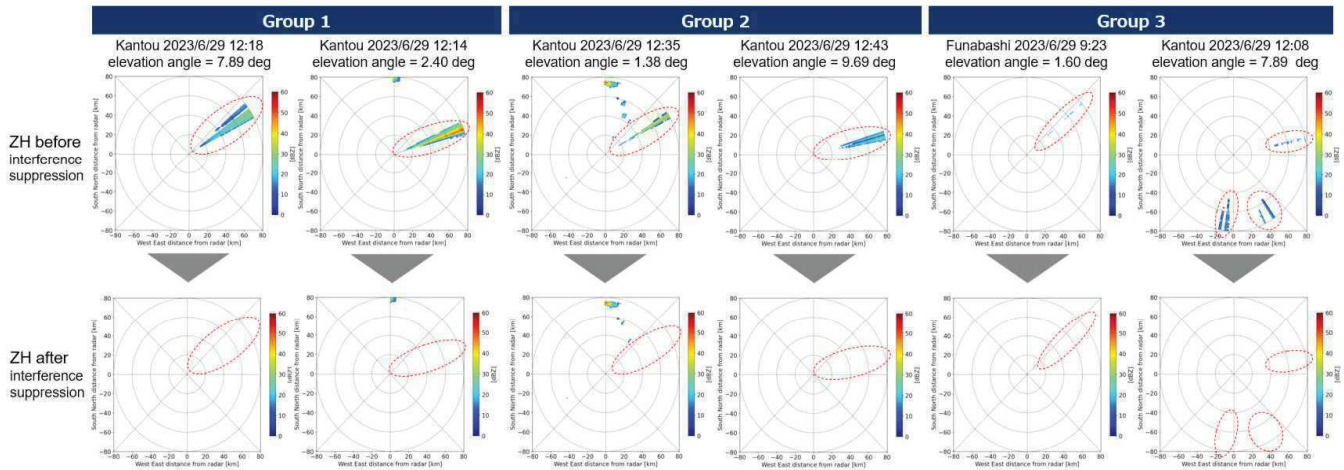


Figure 4: Examples of ZH PPIs before and after interference suppression processing

5 Conclusions

- The MLIT's X-band parabolic dual-polarization radar data contain interference signals from other radars.
- The interference signals were roughly classified into three groups based on the characteristics of the radar reflectivity ZH and the differential reflectivity ZDR.
- We confirmed that the interference signals were suppressed by our proprietary method in a total of 31 cases that included all 3 groups.

6 References

- [1] Tomomi Aoki, et al., "Demonstration experiment of advanced inter-radar interference suppression method for X band weather radar network in Japan," AMS 40th Conference on Radar Meteorology, 2023.

An Innovative Approach for Real-Time Hail Size Estimation

Valentina Gregori¹, Antonio Frigioni², Nicola Carlon², Andrea Chini², Massimo Crespi^{1,2}, Gianluca Ferrari¹

¹*Hypermeteo S.r.l.*

²*Radarmeteo S.r.l.*



Valentina Gregori

1 Introduction

Hail events pose significant threats to sectors such as agriculture, infrastructure, and insurance due to the potential for severe damage. Accurate real-time detection of hail-affected areas and hail size estimation remains challenging. Observational data collected by witnesses are often error-prone and limited, particularly in rural regions, while ground-based stations suffer from sparse distribution, leading to under reporting of localized hail events. Various methods have been developed over the years to estimate hailstone size, often using remote sensing data supplemented with numerical model variables. Weather radars are the most used remote sensing tools, offering a good balance of geographic coverage, temporal resolution, and signal intensity during hail events. However, radar characteristics like frequency band and polarization significantly affect the applicability and accuracy of these methods. This study focuses on the use of single-polarization radars, which, although more challenging to use than dual-polarization radars, are more widely available in countries like Italy, where this research was conducted.

A prominent method in operational meteorology for estimating hail size is the Vertically Integrated Liquid (VIL) density, introduced by Amburn et al. (1997). This method calculates the ratio between the equivalent liquid water content and the echo top—the highest altitude at which radar echoes are observed. Generally, a VIL greater than 3.5g/m³ correlates with hail events of 2cm or larger. Forecasting centers often adjust these thresholds to match their specific instrument characteristics, as seen in the practices of the National Weather Service. Another widely used metric is the Severe Hail Index (SHI), which combines the vertical radar reflectivity profile with a simplified vertical temperature profile. SHI can be further refined into the Maximum Estimated Size of Hail (MESH) using a power curve, originally proposed by Witt et al. (1998) and later refined by Murillo and Homeyer (2019). MESH remains a critical tool in both research and operational forecasting. For example, Schmid et al. (2023) utilized MESH to estimate hail damage to infrastructure, and the Bureau of Meteorology in Australia employs it for thunderstorm warnings (Richter et al., 2007). However, these methods, typically applied to radar's Plan Position Indicator (PPI) data, face limitations when used with Constant Altitude Plan Position Indicator (CAPPI) data, particularly with poor vertical coverage. Further research has integrated these indices with numerical model variables. For instance, Billet et al. (1997) proposed a regression model that combines VIL with parameters like freezing level and mean storm-relative inflow. However, the effectiveness of this approach in estimating hail diameter is limited, likely due to the simplifications inherent in linear modeling. Other studies, such as those by Marcos et al. (2021) and Papavasileiou et al. (2023), have relied solely on numerical model variables for hail size estimation. While these models provide useful indications of atmospheric conditions conducive to hail, they often lack alignment with observed conditions, partly due to inherent errors in the geographical and temporal positioning of storms. Recently, traditional methods have been increasingly compared with artificial intelligence (AI) techniques. For example, Ackermann et al. (2023) employed a neural network to estimate hail damage using insurance claim data. Wu et al. (2021) trained a neural network with satellite and reanalysis data (ERA5), though the results showed limited performance. Similarly, Laviola et al. (2020) used brightness temperature data from Microwave Humidity Sounder (MHS) sensors on polar-orbiting satellites. Despite promising results, this approach is limited by the constraints of polar-orbiting satellite sensor availability.

This study advances the field by developing and validating a real-time hailstorm detection system that combines radar data and numerical weather products with a Machine Learning (ML) algorithm. The results demonstrate the effectiveness of this approach in accurately detecting hail-affected areas and estimating hail diameters up to 5cm, offering significant potential for improving damage assessment and mitigation efforts.

2 Methodology

The proposed system integrates radar data with numerical weather model outputs into a machine learning algorithm to estimate hail size, expressed in centimeters, over a grid with approximately 1km² geographic resolution. The following sections describe the adopted model, and the strategies used for training and validation.

2.1 Mathematical Formulation

The ML model used is the kernel version of Support Vector Regression (SVR) with a Radial Basis Function (RBF) kernel. SVR aims to find a function $f(\vec{x}) = \langle \vec{w}, \phi(\vec{x}) \rangle + b$, where \vec{w} is the weight vector, and b is a bias term, that approximates the

input data \vec{x} within a specified tolerance of error ε . Here, $\phi(\vec{x})$ represents a non-linear transformation of the input data, designed to linearize a non-linear problem. While this transformation function is typically unknown, the kernel function $K(\vec{x}, \vec{x}') = \langle \phi(\vec{x}), \phi(\vec{x}') \rangle$ is used instead, measuring the similarity between two points \vec{x} and \vec{x}' . The RBF kernel is defined as:

$$K(\vec{x}, \vec{x}') = e^{-\gamma \|\vec{x} - \vec{x}'\|^2}.$$

The objective of SVR is to minimize the following loss function:

$$\min_{\vec{w}, b} \left\{ \frac{1}{2} \|\vec{w}\|^2 + \frac{C}{2} \sum_{i=1}^N \zeta_i \right\}, \text{ subject to the constraint: } y_i = \langle \vec{w}, \phi(\vec{x}_i) \rangle + b + \zeta_i, \forall i \in \{1, \dots, N\},$$

where C is a regularization parameter, ζ denotes the errors in the predictions, and y_i is the label associated with the feature vector \vec{x}_i .

The SVR model was selected for its robustness in handling high-dimensional data and its efficacy in regression tasks. The RBF kernel was chosen for its ability to capture complex, non-linear interactions among input features, which are critical for accurate hail size estimation.

2.2 Hyperparameters and Optimization

Hyperparameters are critical in determining the performance of the machine learning model. For the SVR model, key hyperparameters include the regularization parameter C , which controls the trade-off between minimizing training error and model complexity, and the γ parameter for the RBF kernel, which determines the influence of individual training points. To optimize these hyperparameters, a grid search combined with Cross-Validation (CV) was employed. The training dataset was divided into three groups based on the occurrence dates of hail events. For each combination of hyperparameters, three iterations were performed, using two groups for training and one group for validation. The grid search explored the following ranges:

- ☒ C : from 0.1 to 1000, on a logarithmic scale,
- ☒ γ : from 10^{-4} to 10^{-1} , also on a logarithmic scale.

The optimal hyperparameters identified during the CV process were: $C = 100$ and $\gamma = 0.01$.

2.3 Model Training

The feature-label pairs were split into two groups for model training and testing based on the occurrence dates of hail events. Events from the first 20 days of each considered month were used for training, while the remaining events from the 21st day onward, was reserved for testing. Before model training, the features in the training set were standardized by removing the mean and scaling them to unit variance. This standardization was then applied to the test dataset using the transformation derived from the training data. After finalizing the model with the optimal hyperparameters, it was retrained on the entire training set and subsequently evaluated on the test dataset to assess its performance.

3 Dataset

The ground truth dataset used for training the SVR model is a subset of the PRETEMP dataset (<https://pretemp.it/>) holding hail reports across Italy from August 2022 to August 2023. Each report includes the geographic and temporal coordinates of the event, along with the corresponding hailstone size. Additionally, non-hail areas were identified by extracting points with low radar reflectivity near reported hail events. The dataset holds approximately 3000 hail events and 15000 non-hail events.

The SVR model was trained using both observational and model-derived features. Observational features include CAPPI data, which provide vertical profiles of precipitation intensity from weather radars, and the day of the year to capture seasonal variations. CAPPI data, derived from interpolations at fixed altitude levels from radar volumetric data, were provided as open data by the Department of Civil Protection (DPC). These data cover altitudes ranging from 1000 to 8000m, in 1000m increments, with a spatial resolution of 1km² across Italy.

Model-derived features were extracted from the Hypermeteo Forecasting System (HFS), a proprietary numerical weather prediction model based on the WRF-ARW framework, coupled with the WRFDA data assimilation system in a 3DVar configuration. These features include:

- ☒ Freezing level height: indicates the altitude at which freezing occurs.
- ☒ Height of -20°C isotherm: marks the upper boundary where hail formation is likely.
- ☒ Significant Hail Parameter (SHP): combines Convective Available Potential Energy (CAPE) and wind shear to evaluate the atmosphere's potential to sustain hailstone growth.
- ☒ Equilibrium Level: Represents the maximum growth altitude of a thunderstorm cell.

Several preprocessing steps were undertaken to refine the dataset. Temporal and geographic coordinates of the PRETEMP reports were adjusted by aligning them with the time and location of the maximum Vertical Maximum Intensity (VMI) data recorded by the radar within a ± 1 h window and a 5km radius. Observational features were then extracted based on these adjusted coordinates. For model-derived features, extreme values (minimum for the freezing level and maximum for other variables) were considered within a ± 6 h window and a 20km radius around the revised event coordinates, accounting for potential spatial and temporal errors inherent in numerical models. CAPPI radar data were also vertically interpolated to fill any gaps. The processed features were then coupled with the refined PRETEMP reports to train the SVR model.

4 Results

In the following sections, we present the results obtained during the model validation process, highlighting the strengths and limitations of the proposed algorithm. Finally, we demonstrate the method's performance through various case studies.

4.1 Model Performance Evaluation and Statistical Validation

The test dataset, consisting of approximately 6000 events excluded from the CV process, was used to assess the performance of the re-trained model with optimized hyperparameters. The evaluated metrics are presented in Table 1, while Figure 1 compares the observed and predicted hail diameters during this test phase. The results indicate that the proposed index effectively identifies hail with diameters ranging from 0 to 5cm. However, detecting larger hail sizes remains challenging. This difficulty is likely due to the technical limitations of C-band radars, which are not designed to detect targets larger than a few centimeters, and the specific numerical weather features selected, which lack strong signals for recognizing larger hail diameters.

Table 1: Evaluation metrics obtained from the CV process across approximately 6000 events.

Mean Absolute Error	0.20 cm
Mean square error	0.52 cm ²
R ²	0.76

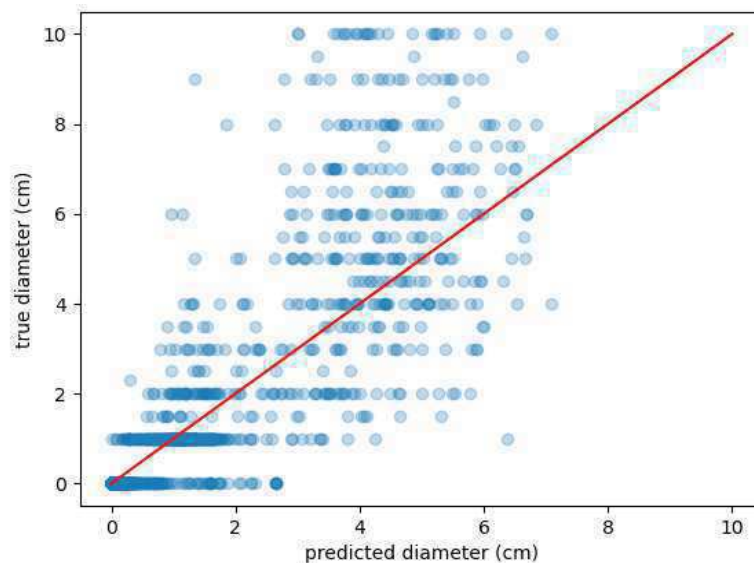


Figure 1: Trend of predicted hail diameter (x-axis) compared to actual diameter (y-axis) across approximately 6000 events.

The percentage of samples correctly or incorrectly classified during the prediction phase was analyzed using confusion matrices calculated for thresholds of 2cm, 3cm, 4cm, and 4.5cm. The results, shown in Figure 2, demonstrate that the model's recognition performance is good for small-diameter hail, but decreases as the hail diameter increases. This trend may be attributed to the imbalance in the training dataset, which is heavily skewed towards cases of small-diameter hail, leading the model to prioritize minimizing error for those cases.

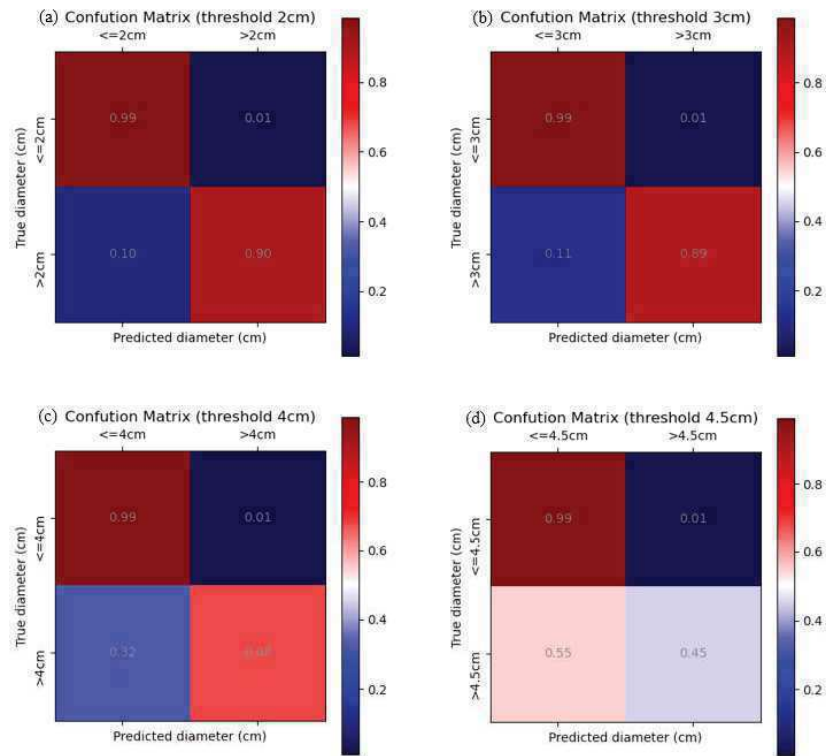


Figure 2: Confusion matrices calculated for thresholds of 2cm (a), 3cm (b), 4cm (c), and 4.5cm (d).

To assess the statistical significance of the CV phase results, a permutation test was conducted. The null hypothesis posited that the model could not exploit the statistical dependencies between features and ground truth, leading to random performance. A significance level of 0.05 was used. In total, 300 random permutations of the data were generated, with the ground truth values shuffled to break any feature dependencies. The p-value obtained from the test was 0.003, indicating that the model's performance is unlikely due to chance and that the null hypothesis cannot be accepted.

The model was subsequently re-trained on the full dataset. The residuals of this final model, assessed by the coefficient of determination, yielded a value of 0.74. This value, being significantly greater than 0, confirms that the model performs substantially better than a constant model predicting the average hail diameter.

4.2 Case Studies

To demonstrate the model's functionality, we selected a series of case studies to illustrate the algorithm's behavior during documented hail events that were excluded from the ML model's training data. Figure 3a shows hail reported in the Po River delta on July 21, 2023, around 23:00 UTC, while Figure 3b displays hail reported in the Abruzzo and Molise regions on July 4, 2024, around 13:30 UTC. In the latter case, the model accurately identified hail with a diameter of 1-2cm, but in the former case, it underestimated the hail size, predicting a maximum diameter of 5cm instead of the observed 8cm. Nevertheless, in both cases, the hail events were correctly located geographically.

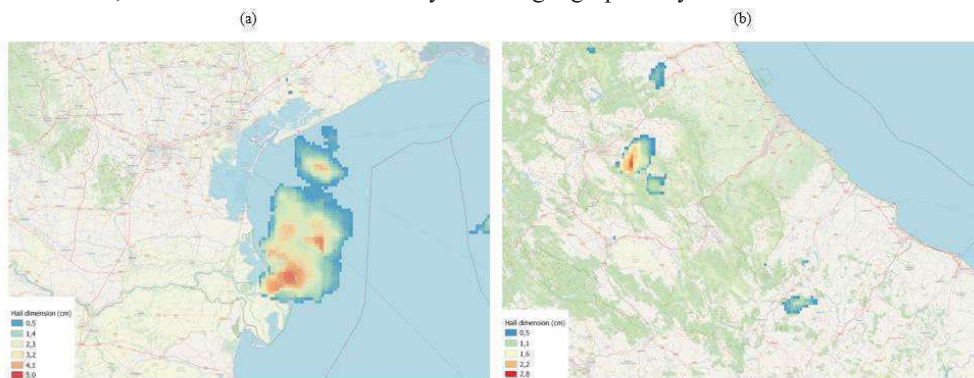


Figure 3: Estimation of hail dimensions on July 21, 2023, at 23:10UTC (a) and on July 4, 2023, at 13:30 UTC (b). PRETEMP documented hail diameters of 8cm in Porto Tolle (Veneto), on July 21, at 23:10UTC and 23:20UTC, and 2cm in L'Aquila (Abruzzo) and 1cm in Capracotta (Molise) on July 4, 2023, at 13:20 UTC and 13:25 UTC.

Figure 4 compares the maximum hail size estimated on July 12, 2024, with the reports from witnesses in the European Severe Weather Database (ESWD). Again, the areas impacted by hail were accurately identified, although some discrepancies were observed in the affected regions. Specifically, the model suggested a broader area of impact than what was reported, possibly indicating false alarms. This overestimation could be attributed to the training process, where non-hail samples were manually assigned based on regions with low reflectivity. Consequently, areas with higher reflectivity but no actual hail were not included in the model, leading to potential overestimation of hail presence in those areas.

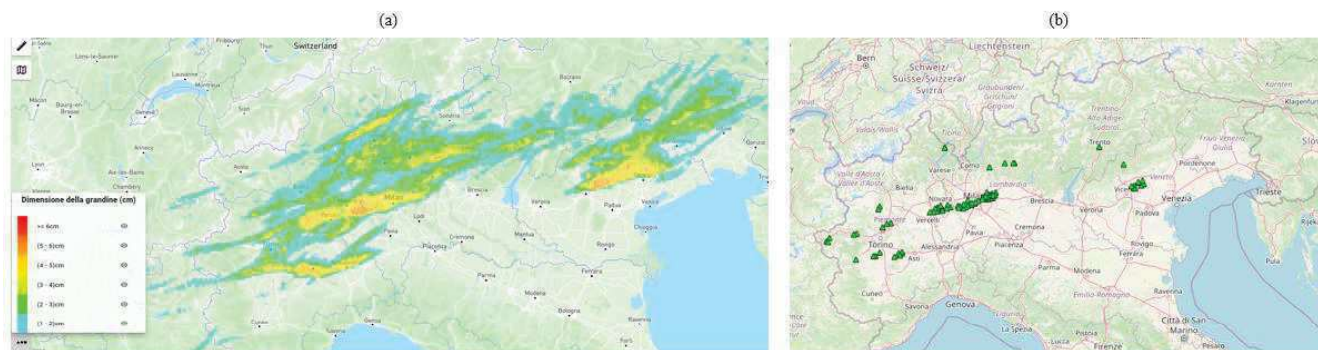


Figure 4: Maximum estimated hail size on July 12, 2024, compared to the reports in ESWD.

5 Conclusions

This study introduces an innovative approach for real-time hail detection and size estimation across Italy by integrating radar data, model-derived atmospheric variables, and advanced machine learning techniques. Utilizing an SVR model, trained on the aforementioned data and a set of validated hail events and non-hail observations, we have demonstrated the system's efficacy in accurately estimating hail-affected areas and hailstone sizes. However, challenges persist, particularly in detecting larger hailstones, due to the inherent limitations of radar systems and the imbalance in the training data.

Future research will focus on addressing these challenges by refining the feature selection process to better capture the dynamics of larger hailstone formation. Additionally, expanding the dataset to include a more balanced representation of hail events across various sizes and geographic regions will be essential for improving the model's capabilities.

6 References

- [1] Amburn, S. A., & Wolf, P. L. (1997). VIL density as a hail indicator. *Weather and forecasting*, 12(3), 473-478.
- [2] https://www.weather.gov/lmk/vil_density
- [3] Witt, A., Eilts, M. D., Stumpf, G. J., Johnson, J. T., Mitchell, E. D. W., & Thomas, K. W. (1998). An enhanced hail detection algorithm for the WSR-88D. *Weather and Forecasting*, 13(2), 286-303.
- [4] Murillo, E. M., & Homeyer, C. R. (2019). Severe hail fall and hailstorm detection using remote sensing observations. *Journal of applied meteorology and climatology*, 58(5), 947-970.
- [5] Billet, J., DeLisi, M., Smith, B. G., & Gates, C. (1997). Use of regression techniques to predict hail size and the probability of large hail. *Weather and Forecasting*, 12(1), 154-164.
- [6] Marcos, J. L., Sánchez, J. L., Merino, A., Melcón, P., Mérida, G., & García-Ortega, E. (2021). Spatial and temporal variability of hail falls and estimation of maximum diameter from meteorological variables. *Atmospheric Research*, 247, 105142.
- [7] Papavasileiou, G., Kotroni, V., Lagouvardos, K., & Giannaros, T. M. (2023). Operational hail forecasting in Greece (No. ECSS2023-102). *Copernicus Meetings*.
- [8] Schmid, T., Portmann, R., Villiger, L., Schröer, K., & Bresch, D. N. (2023). An open-source radar-based hail damage model for buildings and cars. *Natural Hazards and Earth System Sciences Discussions*, 2023, 1-38.
- [9] Harald Richter, B. M. R. C., & Melbourne, V. (2007, August). The four large hail assessment techniques in severe thunderstorm warning operations in Australia. In *33rd Conference on Radar Meteorology*.
- [10] Ackermann, L., Soderholm, J., Protat, A., Whitley, R., Ye, L., & Ridder, N. (2023). Radar and environment-based hail damage estimates using machine learning. *Atmospheric Measurement Techniques Discussions*, 2023, 1-24.
- [11] Wu, Q., Shou, Y. X., Ma, L. M., Lu, Q., & Wang, R. (2021). Estimation of maximum hail diameters from fy-4a satellite data with a machine learning method. *Remote Sensing*, 14(1), 73.
- [12] Laviola, S., Levizzani, V., Ferraro, R. R., & Beauchamp, J. (2020). Hailstorm detection by satellite microwave radiometers. *Remote Sensing*, 12(4), 621.

Real-Time Tornado Vortex Detection System Using Deep Learning - Towards Mitigation of Localized and Sudden Meteorological Disasters.



Kenichi Kusunoki

Kenichi Kusunoki¹, Naoki Ishitsu¹, Toru Adachi¹, Osamu Suzuki¹, Ken-Ichiro Arai¹,
Hiroto Suzuki², Chusei Fujiwara³, Takuo Shinomiya³,
Kengo Ashikawa⁴, Takeru Suda⁵, And Ichitaro Ogawa⁵

¹ Meteorological Research Institute

² National Graduate Institute for Policy Studies

³ East Japan Railway Company

⁴ MTI Ltd.

⁵ Laboro.AI Inc.

Notes: This manuscript includes content from a paper that has been accepted for publication in the journal *Artificial Intelligence and Data Science* (Kusunoki et al. 2024).

1 Background and purpose of the study

The BRIDGE project, launched in 2023 in Japan, is a research initiative within the broader BRIDGE program (BRIDGE 2023). Led by the Meteorological Research Institute, this project focuses on localized severe weather countermeasures, building upon the successes of the previous "Public/Private R&D Investment Strategic Expansion Program (PRISM)" (PRISM 2021). Specifically, the project aims to significantly advance both the deep learning-based tornado vortex detection technology and the railway safety operations enhanced by this technology, both of which were developed during the PRISM period, and to expand their applications to benefit society at large.

The BRIDGE project has three primary objectives (Figure 1):

1. Enhanced Accuracy: Improve the accuracy of deep learning models for tornado vortex detection using data from the Japan Meteorological Agency's airport weather radar system, building on previous research by the Meteorological Research Institute.
2. Expanding Applications for Societal Benefit: Expand the technology's application beyond railway operations to benefit various sectors by integrating GPS location data for real-time disaster prevention information delivery.
3. Collaborative Innovation: Promote industry-academia-government collaboration, including partnerships with startups, to accelerate the practical application of the developed technologies and address societal challenges.

Promoting collaborative innovation, the BRIDGE project utilizes the strengths of research institutions, established corporations, and agile startups. This collaborative approach ensures rapid development, deployment, and societal impact of the enhanced tornado vortex detection technology. This initiative aims to create a real-time disaster prevention system that enhances societal resilience by providing accurate warnings and targeted information. The project also contributes to academic understanding of large-scale weather patterns and promotes collaboration for practical application of research findings.

2 Deep learning technique for detecting tornado vortex patterns using Doppler radar

A deep learning method for identifying tornado vortices using Doppler radar data (Figure 2) is introduced. By leveraging Doppler radar's ability to analyze the radial component of wind speed, this technique effectively detects the unique velocity patterns within a tornado. A convolutional neural network was trained on a vast dataset of Doppler radar images, learning to differentiate between tornado and non-tornado patterns (Ishitsu et al. 2019, Kusunoki et al. 2022). The system rapidly analyzes Doppler radar data to identify potential tornado signatures, calculate maximum wind speed and trajectory, and enable the timely implementation of safety measures. This collaboratively developed technology underpins a real-time wind gust detection system that enhances train safety along Japan's Sea of Japan coast (Figure 3) (Fujiwara and Suzuki 2021, East Japan Railway Company 2020). Future research will focus on enhancing the deep learning models and expanding the application of this technology to other sectors impacted by severe weather events.

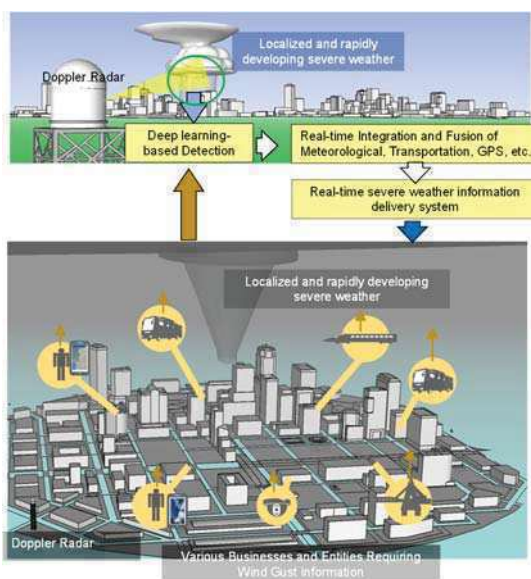


Figure 1: Conceptual overview of the real-time severe weather information delivery system leveraging deep learning-based detection and multi-source data integration. (Adapted from Kusunoki et al. 2024, Figure 10, in press.)

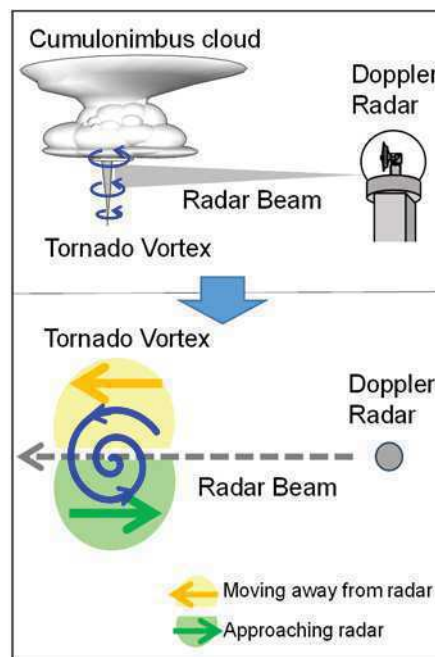


Figure 2: Conceptual illustration of a vortex pattern observed by Doppler radar (Adapted from Kusunoki et al. 2024, Figure 2, in press; originally published in Kusunoki et al. 2022, Figure 2). A radar beam intersecting a tornado vortex (top panel) measures the radial velocity of precipitation, revealing the vortex's rotation as approaching (green) and receding (orange) motions (bottom panel). This distinct Doppler velocity pattern identifies a tornado vortex.

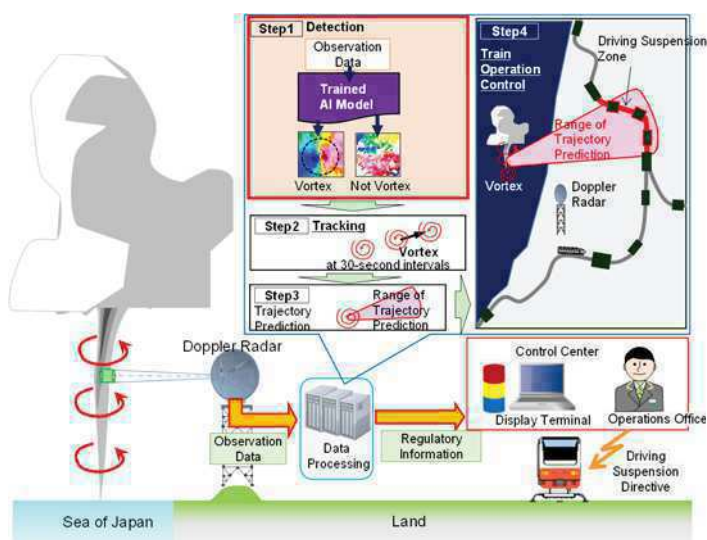


Figure 3: Flowchart illustrating the process of detecting and monitoring tornadoes using radar data and AI. This process begins with "Doppler radar observation" (not shown), which observes the lower atmosphere within a 60 km radius at 30-second intervals. This figure is a modified version of Figure 5 from Kusunoki et al. (2024, in press), rendered in English, and is based on the flowchart presented in the JR East press release "Implementation of Train Operation Control Using AI-based Wind gust detection Method" (East Japan Railway Company 2020).

3 Initial results

Advancements in deep learning models for tornado vortex detection and efforts towards real-time disaster prevention information dissemination are presented as part of the BRIDGE project. The research developed and evaluated three types of deep learning models: Convolutional Neural Network (MobileNetV3) (Howard et al. 2019), Neural Architecture Search (EfficientNetV2) (Tan and Le 2021), and Vision Transformer (SwinTransformerV2) (Liu et al. 2022). These models were trained using a dataset of Doppler radar data obtained from the Japan Meteorological Agency's airport weather radar system. The newly developed deep learning models demonstrated superior performance compared to the previously employed VGG model (Simonyan and Zisserman 2015). Notably, EfficientNetV2 and SwinTransformerV2 surpassed VGG in terms of the area under the precision-recall curve (Figure 4). Importantly, the MobileNetV3 model demonstrated efficient inference on CPUs, enabling potential deployment on a wide range of devices, including edge devices and mobile platforms (Figure 5). This efficiency on CPUs makes MobileNetV3 particularly suitable for deployment on edge devices and mobile platforms, thereby facilitating wider accessibility to the tornado detection system and enabling rapid dissemination of critical information to vulnerable populations.

Alongside the deep learning model development, the project focused on disseminating real-time disaster prevention information to enhance the safety of mobile entities. The project implemented a system that combines meteorological radar data with the location information of mobile entities, providing customized alerts and guidance - for example, tailored for display on tablets used in public transportation systems - directly to these entities via dedicated communication channels (Figure 6). Expanding the focus beyond the railway domain represents a novel approach aimed at serving various mobile entities and the general public. By utilizing GPS functionality, the system can deliver targeted and timely severe weather information over a secure internet connection, thereby contributing to enhanced disaster prevention capabilities across different sectors of society. The collaborative nature of the BRIDGE project, involving industry, academia, and startups, has enabled the development and practical implementation of these advanced deep learning models and the real-time disaster prevention information dissemination system.

4 Conclusion - future developments and expected effects

This chapter presents the expected benefits and future developments of the advanced deep learning models for tornado vortex detection and the real-time disaster prevention information dissemination system developed as part of the BRIDGE project. The project's key outcomes include the development of deep learning models that outperform traditional approaches in accurately detecting tornado vortices from radar data, as well as the implementation of a system that integrates the detection technology with GPS location data and applications for use on devices such as tablets.

4.1 *Expanding Applications: From Railway Safety to Global Tornado Disaster Mitigation*

In addition to the railway sector, the deep learning-based tornado detection technology developed in the BRIDGE project has the potential to significantly contribute to improving the safety and business continuity of other critical infrastructure domains in Japan, such as expressways, ports, as well as vital service providers like power and telecommunications companies. By expanding the application of this technology beyond the initial railway focus, it can enhance the overall resilience of Japan's important transportation and lifeline infrastructure. While initially focused on railway safety in Japan, the BRIDGE project's deep learning-based tornado detection technology holds significant promise for mitigating tornado risks worldwide. This is especially relevant for regions frequently facing tornado threats, such as the United States. There have also been numerous reports of tornado occurrences in Europe in recent years, highlighting the relevance of this technology for the European context (Antonescu et al. 2017, Miglietta et al. 2019). Additionally, Europe has well-developed high-speed rail networks, making this technology potentially applicable for enhancing the safety of train operations in Europe.

By integrating location data from public transportation systems and critical infrastructure operators, the technology can deliver targeted, real-time severe weather information directly to entities responsible for public safety and service continuity. This capability stands to significantly enhance public safety and disaster preparedness, ultimately improving societal resilience and recovery capacity against tornadoes on a global scale. It is important to note that the effectiveness of this technology is inherently dependent on the capabilities of the underlying radar systems, including their performance and scanning frequency, as well as the regional characteristics of tornadoes. Tornadoes exhibit diverse characteristics across different regions, such as frequency, scale, structure, and conducive meteorological conditions. Adapting this technology to different radar systems, particularly those utilized in Europe and the United States, will require careful consideration of these regional variations, including disparities in radar capabilities and the unique tornado climatology of each region. Fine-tuning the deep learning models to align with these factors, alongside potential further research and development, will be crucial to ensure optimal performance and maximize its effectiveness in diverse geographical contexts.

4.2 *Expected Academic Contributions*

The expected academic insights from the deep learning-based tornado vortex detection technology developed as part of the BRIDGE project are discussed. While the primary purpose of this technology is to provide real-time disaster prevention information, it also has the potential to significantly contribute to the academic understanding of tornado phenomena. Previously, understanding the occurrence and development mechanisms of tornadoes required detailed analysis of individual tornado cases. However, conducting such analysis on large-scale data has been challenging due to time and resource constraints. The deep learning-based detection technology can automatically and rapidly extract tornado vortex patterns from massive amounts of radar data with high precision. This capability is expected to enable efficient investigation of tornado occurrence characteristics, including frequency, geographical distribution, seasonality, development processes, and relationships with environmental conditions. Applying this technology to radar data globally is anticipated to yield significant advances in academic tornado research, including a more comprehensive understanding of global tornado climatology, improved monitoring of tornado occurrence and development, and the development of more accurate forecast models. The introduction of a machine learning approach also raises expectations for new discoveries and awareness beyond existing knowledge. Data-driven analytical techniques may reveal overlooked features and relationships, paving the way for a more comprehensive understanding of the climatological reality of tornado phenomena globally. This approach is expected to have a major scientific

impact by enabling detailed understanding of tornado occurrence mechanisms, contributing to advancements in meteorological science.

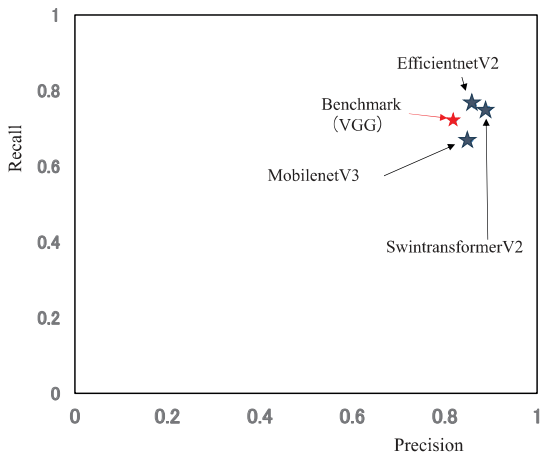


Figure 4: Precision-Recall scatter plot for tornado detection performance comparison of EfficientNetV2, SwinTransformerV2, MobileNetV3, and the benchmark VGG model from the previous PRISM program. (Adapted from Kusunoki et al. 2024, Figure 10, in press.)

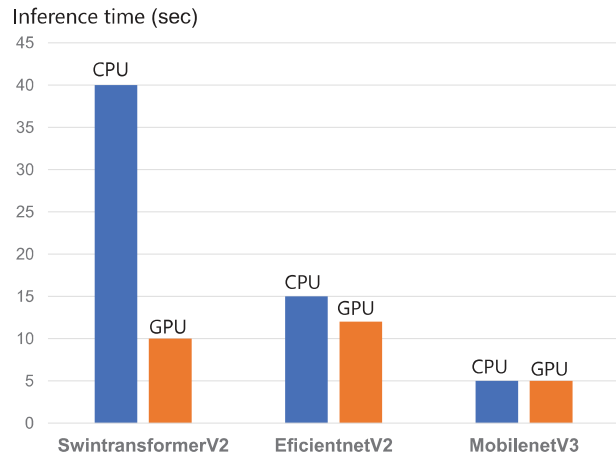


Figure 5: Inference time comparison of EfficientNetV2, SwinTransformerV2, and MobileNetV3 on CPU and GPU for 89 system's delivery of real-time severe weather alerts. (Adapted from Kusunoki et al. 2024, Figure 10, in press.)

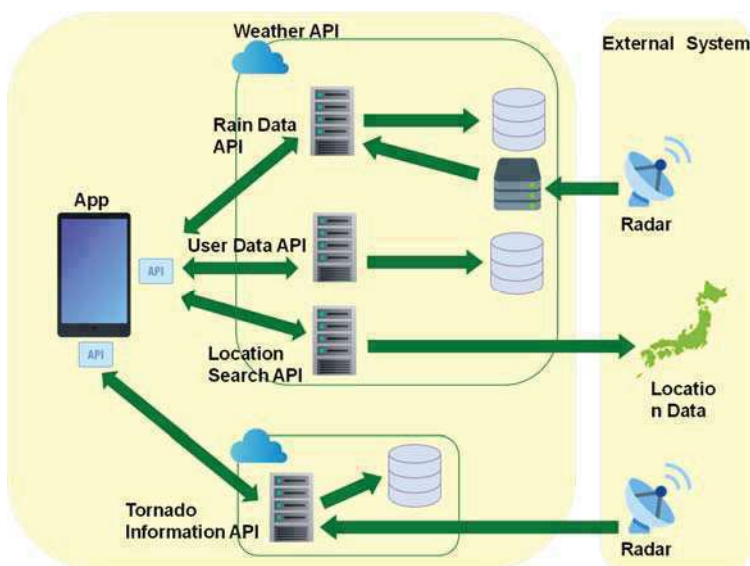


Figure 6: This diagram illustrates the system's delivery of real-time severe weather alerts. By integrating meteorological radar data with the location of mobile entities, such as tablets used in public transportation, the system generates personalized alerts for imminent wind gusts and tornadoes and disseminates them through dedicated channels. (Adapted from Kusunoki et al. 2024, Figure 10, in press.)

5 Acknowledgements

This research project was conducted with the support of the 'Basic Research Promotion System in the Transport Field,' the 'Public/Private R&D Investment Strategic Expansion Program (PRISM),' and the 'BRIDGE: Programs for Bridging the Gap Between R&D and the Ideal Society (Society 5.0) and Generating Economic and Social Value.'

6 References

Kusunoki, K., Ishitsu, N., Adachi, T., Suzuki, O., Arai, K., Suzuki, H., Fujiwara, C., Shinomiya, T., Ashikawa, K., Suda, T., Ogawa, I., Deep learning-based tornado vortex detection through the BRIDGE program: Advancing technology and multidisciplinary applications. *Artificial Intelligence and Data Science*. (In press).

Programs for Bridging the gap between R&D and the IDEal society (society 5.0) and Generating Economic and social value (BRIDGE), https://www8.cao.go.jp/cstp/english/society5_0/index.html, 2023.

Public/Private R&D Investment Strategic Expansion Program (PRISM), https://www8.cao.go.jp/cstp/panhu/prism2021_e/2021.html, 2021.

- Ishitsu, N., Kusunoki, K., Adachi, T., Arai, K., Inoue, H.Y., Fujiwara, C., Suzuki, H.: Detection of tornadic vortex from Doppler velocity field using convolutional neural networks, *Proc. 10th European Conf. on Severe Storms*, 4–8 November 2019, Kraków, Poland.
- Kusunoki, K., Ishitsu, N., Adachi, T., Suzuki, O., Arai, K., Fujiwara, C., and Suzuki, H., Development of tornado detection technique with Doppler radar using deep learning. *Wind Engineers, JAWE*, 47(3), 218–223, 2022. <https://doi.org/10.5359/jawe.47.218> [in Japanese].
- Fujiwara, C. and Suzuki H., Development of train operation control method against wind gusts using Doppler radar, *JR EAST Tech. Rev.*, Vol. 66, pp.40-43, 2021 [in Japanese].
- East Japan Railway Company, implementation of Train operation control using AI-based wind gust detection method, https://www.jreast.co.jp/press/2020/20201006_ho03.pdf, 2020. [in Japanese].
- Howard, A., Sandler, M., Chu, G., Chen, L., Chen, B., Tan, M., Wang, W., Zhu, Y., Pang, R., Vasudevan, V. and Le, Q.V., Searching for MobileNetV3, *Proc. IEEE/CVF Inter. Conf. on Computer Vision (ICCV)*, 2019.
- Tan, M. and Le, Q., EfficientNetV2: Smaller Models and Faster Training, *Proc. 38th Inter. Conf. on Machine Learning (ICML)*, 2021.
- Liu, Z., Lin, Y., Cao, Y., Hu, H. et al., Swin Transformer V2: Scaling Up Capacity and Resolution, *Proc. IEEE/CVF Conf. on Computer Vision and Pattern Recognition (CVPR)*, 2022.
- Simonyan, K. and Zisserman, A., Very deep convolutional networks for large-scale image recognition. *Inter. Conf. on Learning Representations (ICLR)*, 2015.
- Antonescu, B., Schultz, D., & Groenemeijer, P. (2017). Tornadoes in Europe: An underestimated threat. *Bulletin of the American Meteorological Society*, 98(5), 953-968_ <https://doi.org/10.1175/BAMS-D-16-0171.1>
- Miglietta, M. M., K. Arai, K. Kusunoki, H. Inoue, T. Adachi, H. Niino, 2019: Observational analysis of two waterspouts in northwestern Italy using an OPERA Doppler radar. *Atmospheric Research*, 234. <https://doi.org/10.1016/j.atmosres.2019.104692>

Implementation of open-source software in an operational radar processing chain using Rainbow

Tiemo Mathijssen¹, Aart Overeem¹, Mando de Jong¹, Sebastian Knist², Ronald Hannesen²

¹Royal Netherlands Meteorological Institute. PO Box 201, 3730 AE De Bilt, The Netherlands.

²LEONARDO Germany GmbH, Raiffeisenstraße 10, 41470, Neuss, Germany.

Poster ID: 341



Tiemo Mathijssen

Abstract

The Royal Netherlands Meteorological Institute (KNMI) operates two identical METEOR 735CDP10 Magnetron based C-band Dual polarization weather radars from Leonardo together with software Rainbow for processing of operational data. Research and development on radar data processing on the other hand is often conducted using open-source software, such as BALTRAD, Py-ART, LROSE, and wradlib for its flexibility and possibility to add new functions. A link between Rainbow and open-source radar software is created, that allows for quick implementation of new algorithms in such software. The work presented here describes the implementation of a dual-pol clutter correction algorithm, available in wradlib, into the operational cloud-based data processing chain of KNMI.

1 Introduction

The Royal Netherlands Meteorological Institute (KNMI) operates two identical METEOR 735CDP10 Magnetron based C-band Dual polarization weather radars from Leonardo, located in Herwijnen (5.1379E 51.8370N, WSG-84) and at a naval base in Den Helder (4.78997E 52.9533N, WSG-84). After elementary signal processing and data reduction on-site at the radar locations [1], data is aggregated in a central Linux-based server at Amazon Web Services (AWS) at which proprietary software Rainbow is running for further processing and compositing into data products. A clutter algorithm using single- and dual-pol moments [2] is available in Python-based open-source software wradlib [3]. Implementation of this algorithm into the operational data processing would need to be done before pseudo-CAPPI generation, and thus require adaptation of Rainbow by the manufacturer, despite the algorithm being available in wradlib. Instead, a future-proof solution has been devised by creating a connection between Rainbow and open-source software. In this way, intermediate steps in the processing using open-source software can be achieved, allowing for quick implementation of new developments into the operational processing chain.

2 Measurement chain

A visual representation of the data chain at KNMI is displayed in figure 1. The digitalized signals are sent to a signal processor at the radar location, where data reduction and moment generation takes place [Beekhuis2018]. Subsequently this moment data is sent to an Amazon Elastic Compute Cloud (EC2) in Amazon Web Services (AWS), where an instance of Rainbow for each radar receives and stores the data on an Elastic File System (EFS). These servers are called the Data Receivers.

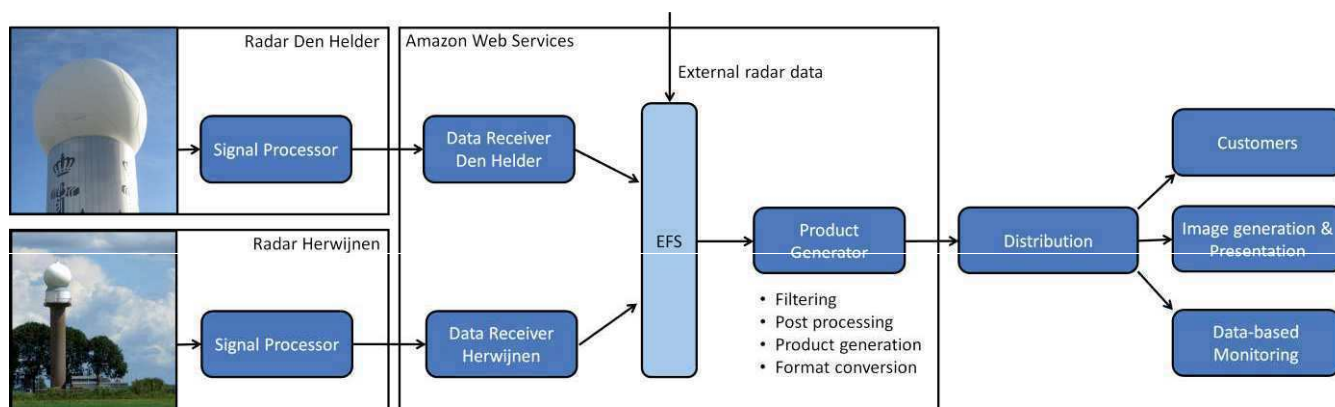


Figure 1: Schematic representation of the measurement data chain at KNMI. Moments are generated in the signal processor. Data is sent to the specific Data Receiver EC2 instance at AWS, which stores the data in Rainbow format on the EFS. Rainbow running on the Product Generator EC2 instance picks up the radar data and creates products and composites. The open-source software is implemented within the Rainbow Product Generator.

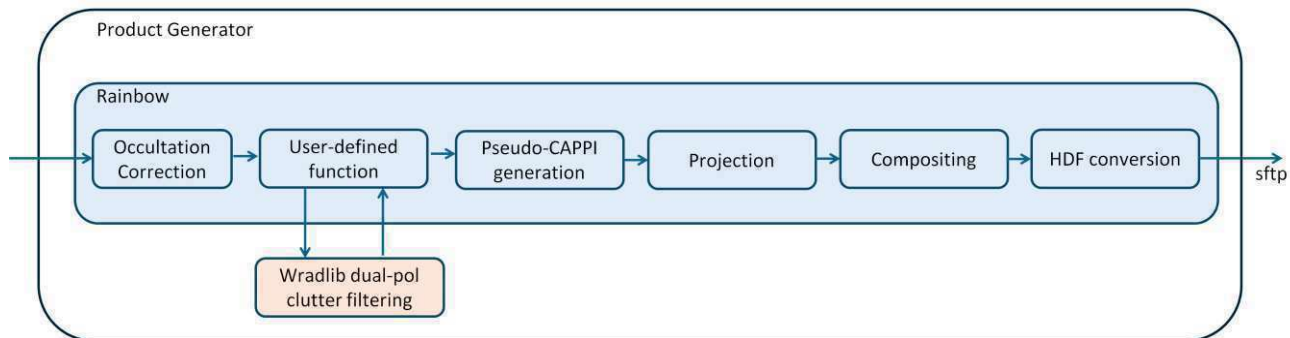


Figure 2: Implementation of a user-defined function that converts Rainbow data into ODIM-HDF format, applies the wradlib open-source dual-pol clutter correction algorithm and returns the filtered data to Rainbow.

Data from neighbouring countries is also sent to the same EFS. The Product Generator Rainbow instance aggregates data of all these radars from the EFS, and processes them into products and composites, after which they are converted into HDF-format and distributed, see figure \ref{Fig:ProductGenerator}. The setup of these EC2 servers together with Rainbow configuration is entirely scripted, which facilitates easy deployment of a new server. The configuration is stored in a Git repository ensuring strict version control. Changes to these servers are implemented in a controlled manner by creating a branch of this repository, after which an identical version of these servers is generated for testing purposes.

An infinite number of test branches can be generated concurrently. Before integration in the production environment, all changes are first tested in an acceptance environment, which is identical. To ensure continuity of radar production, a strict separation is made between the production servers and the test and acceptance servers. A Continuous Integration / Continuous Development (CI/CD) pipeline in Gitlab aids in this process by having a visual representation of the standardized procedure of the roll-out of new servers. New production servers are deployed one by one, in which old servers are only stopped after the new ones are rolled out in order to minimize loss of data availability. A new Product Generator is deployed without any interruption, and deployment of a Data Receiver server leads to the interruption of one 5-minute cycle of each respective radar only.

3 Connection of Rainbow with open-source software

A user-defined function is created in Rainbow that calls an external Python script. This script converts Rainbow data into ODIM-HDF format and loads the open-source software. After modification using the open-source software, the data is converted back into Rainbow format and reloaded into Rainbow, and further processing on the modified data takes place. This enables implementation of any open-source software while keeping Rainbow for radar configuration, product generation, data process control and logging.

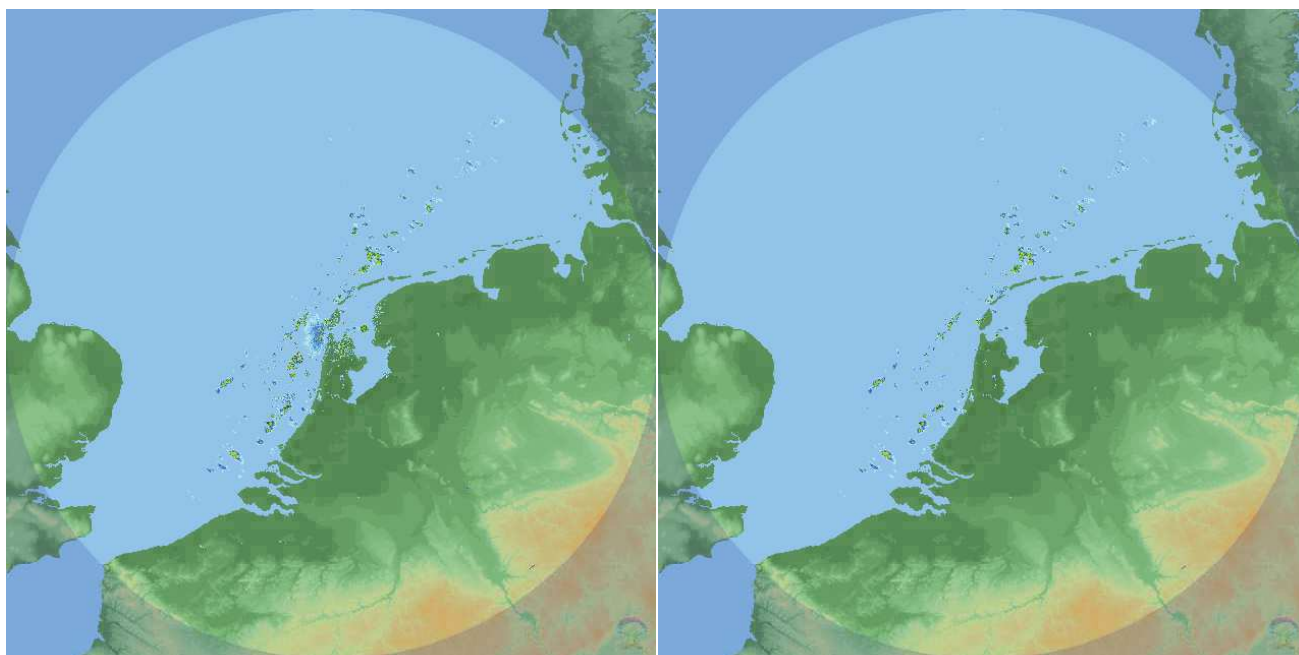


Figure 3: PPI of the lowest elevation (0.3°) of radar Den Helder without (left) and with (right) the dual-pol clutter filter applied. The sea clutter and reflections from a wind park in front of the coast is filtered, while the showers are kept in the image.

As an example, we use a filtering algorithm [2] available in wradlib. Figure 3 shows an example of the application of the wradlib dual-pol clutter filter. The left image shows a Plan Position Indicator (PPI) of the lowest elevation (0.3° above the horizon) of radar Den Helder, after Rainbow DFT filtering and occultation correction. The right image shows the same PPI after subsequent application of the wradlib open-source dual-pol clutter filter, reloaded into the Rainbow processing chain. The wradlib clutter filter is able to eliminate residual sea clutter and reflections from a wind park on the North Sea, while leaving the showers in the data unaffected. The additional time spent on the conversion to ODIM-HDF, filtering, and converting back of all elevations is 20 seconds.

4 References

[1] Beekhuis, H., and T. Mathijssen, 2018: From pulse to product, highlights of the upgrade project of the Dutch national weather radar network. 10th European Conf. on Radar in Meteorology and Hydrology, Wageningen, Netherlands, Wageningen University and Research, 960–965, <https://doi.org/10.18174/454537>.

[2] Overeem, A., R. Uijlenhoet, and H. Leijnse, 2020: Full-Year Evaluation of Nonmeteorological Echo Removal with Dual-Polarization Fuzzy Logic for Two C-Band Radars in a Temperate Climate. *J. Atmos. Oceanic Technol.*, 37, 1643–1660, <https://doi.org/10.1175/JTECH-D-19-0149.1>

[3] Heistermann, M., Jacobi, S., and Pfaff, T.: Technical Note: An open source library for processing weather radar data (wradlib), *Hydrol. Earth Syst. Sci.*, 17, 863–871, <https://doi.org/10.5194/hess-17-863-2013>, 2013.

Computing Echo Top Products with Fast Quality-Weighted Sliding Windows

Markus Peura

Finnish Meteorological Institute



1 Introduction

In theory, defining echo top height is straightforward: it is the highest altitude where radar reflectivity exceeds a given threshold, say 10 or 20 dBZ. Echo top height provides information on the dynamics of precipitation phenomena, for example in distinguishing strong convection. Real-time echo top products are valuable in aviation weather service, for example.

As to practical computation, the geometry of radar measurements brings in a challenge. Typical operational scanning routines consist of azimuthal sweeps at a relatively small number of elevation angles. As illustrated in Fig. 1, by traversing a single radar beam it is basically easy to track the bin(s) where the reflectivity decreases and passes the reflectivity threshold - but for practical horizontal image products those bins are too sparsely distributed. This means that heuristics like interpolation and extrapolation are needed for approximating echo tops in radar image area. Lakshmanan et al. (2013) proposed interpolation between radar beams, using nominal value -14 dBZ for replacing missing echoes on higher beams. In the applied Next Generation Weather Radar (NEXRAD) environment the echo top threshold was 18 dBZ. Motivations for choosing Z or dBZ for linear interpolation were also discussed.

In radar range, there are also vertical columns of bins where the threshold is exceeded in the highest bin or echo remains under the threshold in all the bins. In these cases, approximating echo top height involves more uncertainty. To each computed echo top height we propose assessing a certainty value – a heuristic measure between zero and one – that can also be identified as a *quality index* (Holleman et al., 2006). Then, the values of higher quality can be used for improving values of lower quality. As illustrated in the paper, this can be done with single-radar data and also in the compositing stage.

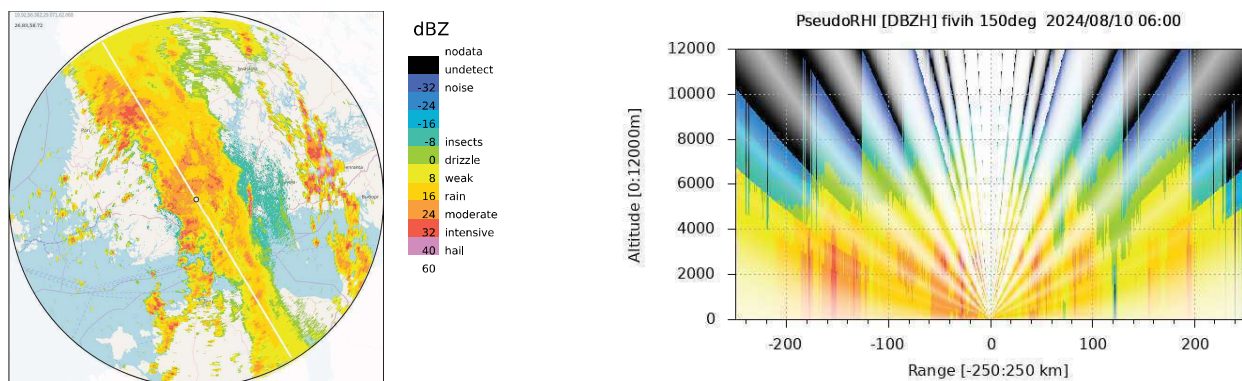


Figure 1: Perceiving echo top height – visually or computationally – is difficult due to the limited number of elevation angles. At right, pseudo RHI product computed from volume data on a line shown at left (dBZ product).

2 Proposed method

2.1 Definitions

The proposed algorithm detects highest bins where the threshold is exceeded and interpolates up or down, towards the threshold value. The algorithm, implemented in the latest versions of Rack software (Peura, 2012), consists of the following nesting loops. Let us denote measured reflectivity with Z . The main parameter for echo top is threshold reflectivity Z_{thr} . The outermost loop traverses the volume radially; the applied coordinate r is the distance from the radar along the ground. The next loop is azimuthal, with coordinate $\alpha \in [0, 360^\circ[$. The innermost loop inspects reflectivities Z_i in the vertical column of bins $i = 1, \dots, N$ above each ground point (r, α) . The following measurement cases are distinguished. WELL-DEFINED: the highest bin with $Z_i \geq Z_{thr}$ has a weak echo in the above bin: $Z_{i+1} < Z_{thr}$. SPAN-LIMITED: the highest bin with $Z_i \geq Z_{thr}$ has only “dry bins” above, that is, bins without echoes exceeding the detection threshold. MIN-HEIGHT-LIMITED: the highest bin with $Z_i \geq Z_{thr}$ is on the highest beam measured. MAX-HEIGHT-LIMITED: the column contains only weak precipitation, $Z_i < Z_{thr} \forall i$. CLEAR: no echo. The names refer to conditions under which echo top height can be approximated, illustrated in Fig. 2.

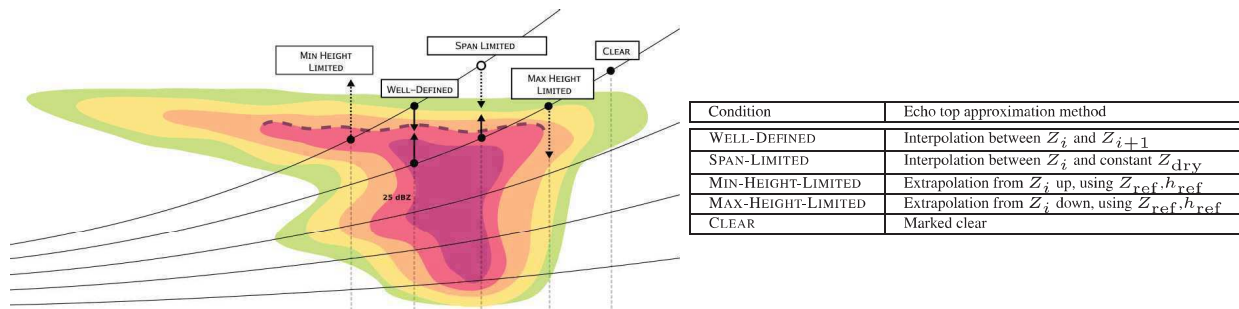


Figure 2: Approximating echo top in different geometrical cases.

At this point, let us define reflectivity gradient in a vertical column of bins as

$$Z_d = \frac{\Delta Z}{\Delta h} = \frac{Z_j - Z_i}{h_j - h_i}, \quad (1)$$

where Z_i and Z_j are reflectivities (dB) in bins i and j at heights h_i and h_j , respectively. Each gradient Z_d defines a line in (h, Z) space:

$$h = h_i + (Z - Z_i)/Z_d \quad (2)$$

2.2 Approximating echo top height

Among the cases listed above, WELL-DEFINED is the most straightforward one: h for given threshold Z_{thr} is obtained directly with interpolation between (h_i, Z_i) and (h_j, Z_j) . Obviously, it is also gives the most accurate (certain) approximation. Almost as reliable is SPAN-LIMITED case, substituting undetected echo with $Z_j = Z_{dry}$. This fixed value should be compatible with the applied radar system¹.

In MIN-HEIGHT-LIMITED and MAX-HEIGHT-LIMITED cases, there is only one measurement (h_i, Z_i) . Basically, given any measurement, echo top height h can be approximated from (2) using $Z = Z_{thr}$. For obtaining a virtual gradient for such interpolation, we define reference ‘‘point’’ (h_{ref}, Z_{ref}) substituting (h_j, Z_j) in (1). We propose using relatively large height, say $h_{ref} = 30$ km, and relatively small reflectivity, say $Z_{ref} = -50$ dBZ. So, like Z_{dry} above, the reference point imitates reflectivity, toward which observed reflectivities are assumed to approach with height. Hence, observations in MIN-HEIGHT-LIMITED and MAX-HEIGHT-LIMITED cases are interpolated (extrapolated) upwards or downwards, respectively, using the reference point. It must be noted that this is only a heuristic providing an initial approximation. Default dBZ gradients with (2) could be used just as well.

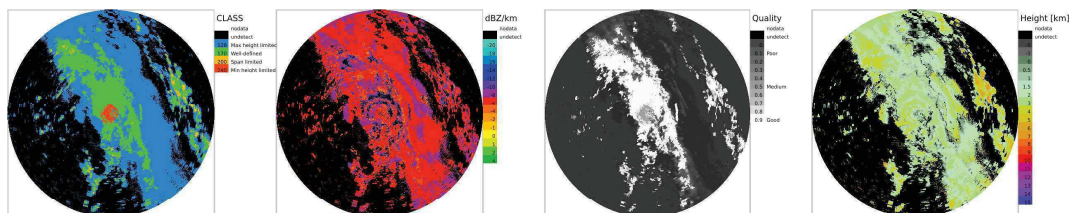


Figure 3: Computing echo top (20dBZ) product for the same input volume as in Fig. 1. From left to right: measurement cases (CLASS) as defined in Fig. 2, reflectivity gradient (dBZ/km), quality index (QIND) based on CLASS, and the actual product: approximated echo top height.

2.3 Using sliding windows for spreading gradient information

Practically, areas of high gradient quality – where WELL-DEFINED and SPAN-LIMITED interpolation can be done – co-exist with areas of lower quality. This problem is illustrated also in Fig. 3, where higher-quality areas (appearing green and orange in CLASS panel) populate less than half of the precipitation area.

As a partial solution, we propose propagating high-quality gradient measurements to (nearby) areas of lower quality. More specifically, we propose applying *averaging window operator* that applies *quality information in weighting the averages*. First, the quality information is generated by using ‘‘a priori’’ quality indices for each class, preferably as a descending series like WELL-DEFINED: 1.0, SPAN-LIMITED: 0.8, MIN-HEIGHT-LIMITED: 0.6, and MAX-HEIGHT-LIMITED: 0.4. In addition, for MIN-HEIGHT-LIMITED

¹Lakshmanan et al. (2013) proposed using $Z_{dry} = -14$ dBZ while in these experiments we have used $Z_{dry} = -32$ dBZ.

and MAX-HEIGHT-LIMITED, which are based on a single measurement Z_i , a (fuzzy) function decreasing with distance $|Z_i - Z_{thr}|$ is applied as additional decay.

Window operations imply nesting loop in programming, easily increasing computation time which may be an issue in operational environments. Fortunately, window averaging is one of the operations that can be carried out in a pipeline fashion using *sliding windows* that update sums continuously (Peura, 2016). That is, at each step the applied sums are updated by adding values on the leading side of the window and subtracting values on the trailing side as illustrated in Fig. 4. When using a window of $M \times N$ pixels, this technique speeds up computation by a factor of $\max(M, N)$ which is of practical value. An example of weighted smoothing of dBZ gradients is shown in Fig. 5.

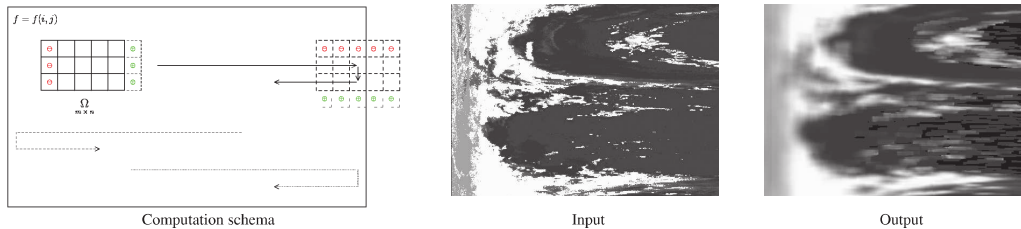


Figure 4: Illustration of the path of a sliding window Ω in image $f(i, j)$. Applied statistics – like average in our case – are updated continuously by adding and removing values on leading \oplus and trailing \ominus side, respectively.

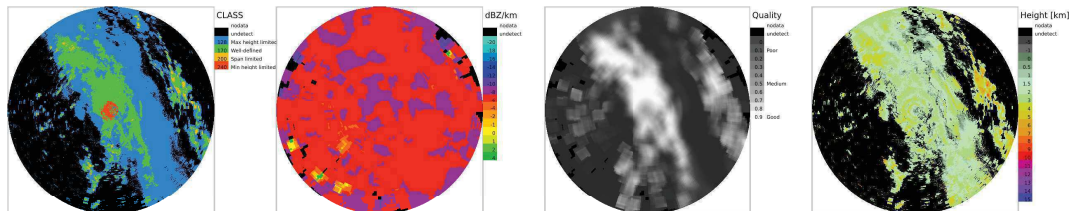


Figure 5: Gradient (dBZ/km) and quality fields (two center panels) of Fig. 3 after $25.5 \text{ km} \times 51^\circ$ window smoothing.

3 Experiments

3.1 Radar pair comparison

A natural method of assessing performance of an echo top algorithm is visual inspection. Especially, one should look for abrupt steps and rings in the product. We tested different sizes for the averaging window. Some results are shown in Fig. 6. For this test, to highlight the effect of averaging, we chose reference point (50 km, -40 dBZ) with poor performance, appearing as rings in the raw image. Within this set, the largest window provided the best result.

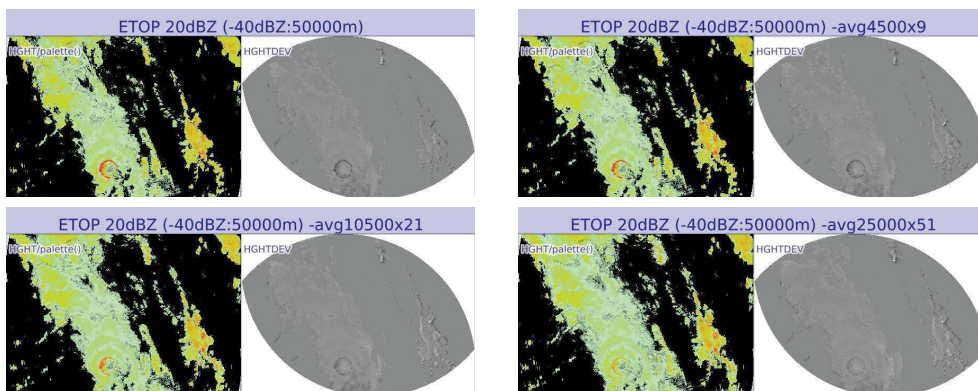


Figure 6: Testing different window sizes in weighted averaging of dBZ gradients: no averaging, $4500\text{m} \times 9^\circ$, $10500\text{m} \times 21^\circ$, and $25000\text{m} \times 51^\circ$.

3.2 Compositing

Radar geometry – sparsity of elevation angles and Earth curvature – is a problem also for echo top products. Creating radar image composites (mosaics) improves spatial accuracy. We tested compositing of echo top products using four composition methods: average, maximum, weighted average and maximum-quality (Peura et al. (2006)). Inputs are shown in Fig. 7 and results in Fig. 8.

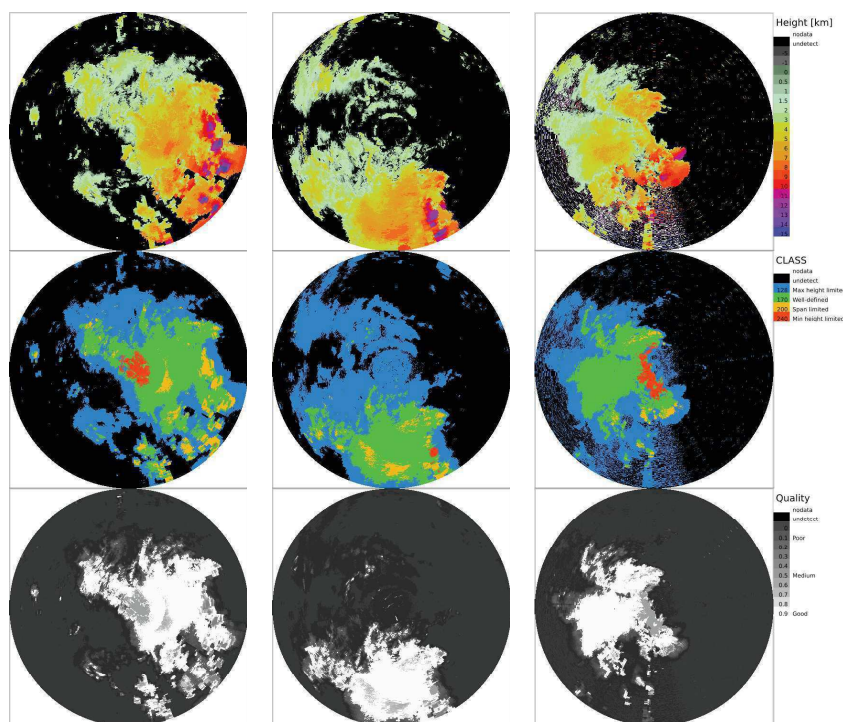


Figure 7: Echo top (20 dBZ) inputs for a composite. FMI radars *fiika*, *fikor*, *fivan* on 2017/08/12 16:00 UTC.

4 Discussion

We introduced methods for extending echo top computation from well-defined (two-beam) interpolation areas towards more uncertain areas. The problems originating from radar geometry – beams too low near the radar and too high far from the radar as well as the sparsity of beams – were admitted and handled using quality indices, allowing further processing to make decisions on contribution of each bin (pixel). In locations where a single-beam measurement of reflectivity could be used only, initial echo top approximation was obtained by extrapolation towards a “dry” reference point aloft. As a further heuristic, the quality was set to decrease with extrapolated distance. Second, high-quality gradients were propagated to areas of lower quality. Third, the quality was used in compositing methods (Quality-weighted average and Maximum quality), again allowing measurements of high quality override those of low quality.

In this study, we did not consider winter conditions. In northern climate, winter time precipitation initiates low, often around 2 km height. Due to radar geometry, most of the precipitation is detected then by the lowest sweep only, hence (well-defined) gradients (1) cannot be applied. On the other hand, as precipitation remains low, the echo top products have less overall importance.

More research is needed in assessing optimal values for applied parameters, for example in dynamically determining reflectivity gradients (or reference points) as well as parameters for weighted smoothing (initial quality indices and window dimensions).

References

- Holleman, I., Michelson, D., Galli, G., Germann, U., and Peura, M. (2006). Quality information for radars and radar data. Technical report, EUMETNET/OPERA. OPERA_2005_19_DataQuality.
- Lakshmanan, V., Hondl, K., Potvin, C. K., and Preignitz, D. (2013). An improved method for estimating radar echo-top height. *Weather and Forecasting*, 28(2):481 – 488.
- Peura, M. (2012). Rack - a program for anomaly detection, product generation, and compositing. In *7th European Conference on Radar in Meteorology and Hydrology (ERAD2012)*. Météo France. Software can be downloaded from <https://github.com/fmidev/rack>.
- Peura, M. (2016). Fast sliding window techniques for computing motion vectors. In *Proceedings of the 9th European Conference on Radar in Meteorology and Hydrology (ERAD2016)*.
- Peura, M., Koistinen, J., and Hohti, H. (2006). Quality information in processing weather radar data for varying user needs. In *Proceedings of the Fourth European Conference on Radar in Meteorology (ERAD2006)*, pages 563–566. Copernicus.

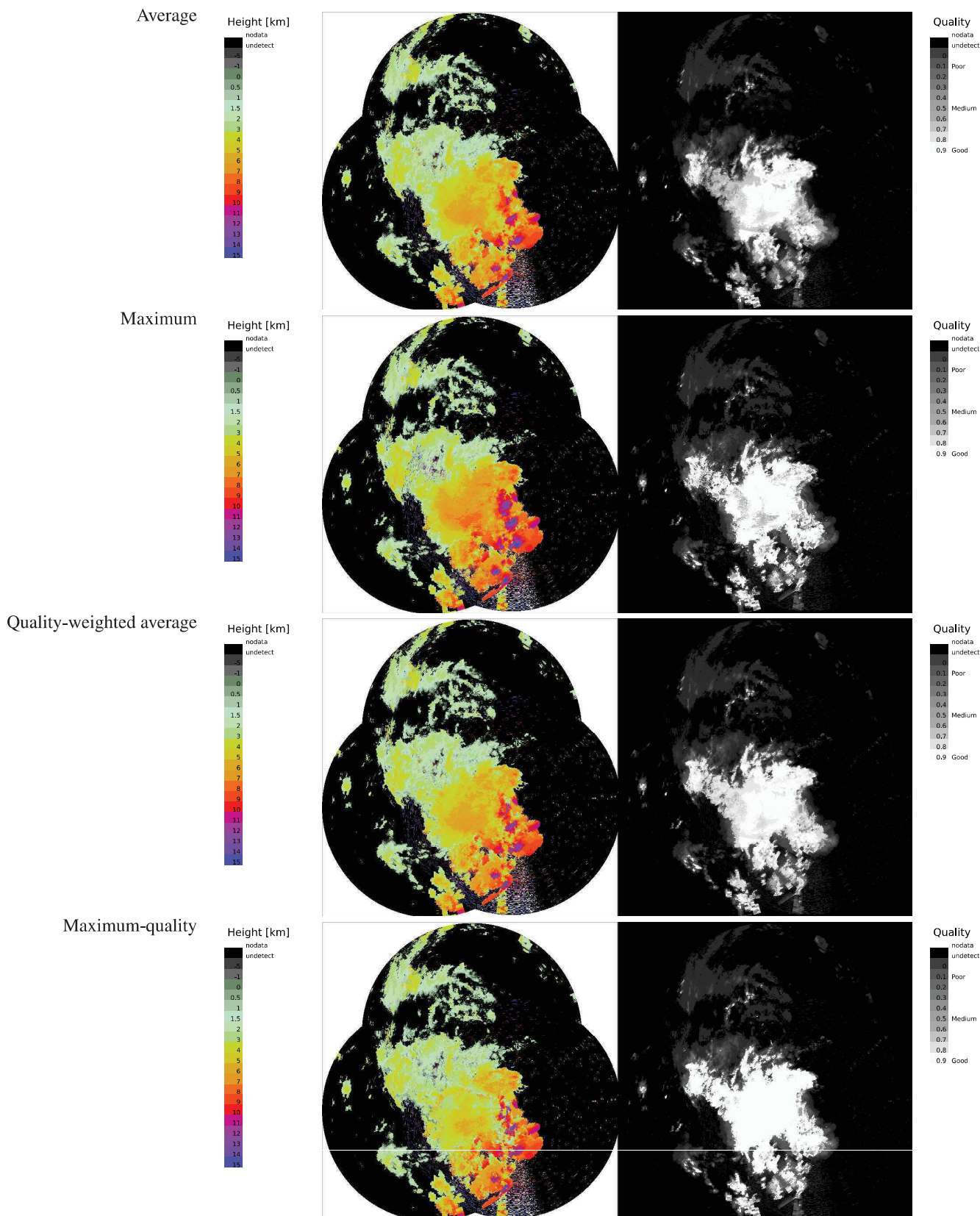


Figure 8: Echo top composite images (left panels) and resulting quality fields (right) when using conventional and quality-supported compositing methods. Conventional Average blurs information. A cautious client probably prefers Maximum echo top, for example in flight routing. Climatological applications might appreciate Quality-weighted average or Maximum-quality product, as they should be statistically more accurate than Average and Maximum.

Weather radar and climate

Classification of convective systems yielding tornadoes in Japan

Taisei Shibayama¹, Koji Sassa²

¹Kochi University, Graduate School of Integrated Arts and Sciences

²Kochi University, Natural Science Cluster



Taisei, Shibayama

1 Introduction

Tornadoes frequently occur in Japan. Japan Meteorological Agency (JMA) lists them in the database with environmental situation or synoptic disturbances. The kinds of convective system yielding tornadoes, however, have not been classified in detail. Niino et al. (1997) said that most of tornadoes in Japan are non-supercell type. Hazardous wind watch is issued from JMA based on the indices for supercell. We expect to make the watch more accurate if we introduce the indices for the other non-supercell systems. We have not understood which systems are major source of tornado at this time. Therefore, we need to investigate the tornado climatology in Japan, especially the viewpoint of the types of convective systems as classified by Agee (2014) in United States. We found 6 types of parent convective system even only in Kochi Prefecture (Fujii and Sassa 2022). The present study aims to classify the parent convective systems of tornadoes in Japan based on the shape of radar reflectivity. After we establish the tornado climatology in Japan, we can investigate the detailed environmental situations for each convective system and then we can propose indices suitable for each convective system. Moreover, the risk of tornado damage will be evaluated easily based on the types of convective systems.

2 Radar analysis

The tornado events those located within the observation range of JMA radars are picked up from the tornado database. Analysis periods are 12 years from 2013 to 2024. We draw reflective intensity and Doppler velocity images by using Draft, drawing tool developed by Meteorological Research Institute of JMA. The kinds of convective system are classified based on the shape and size of strong echo region more than 40dBZ in reflectivity as shown in Fig. 1. The vortices in the convective system are also detected as a caplet of maximum and minimum Doppler velocities. Then we evaluate the characteristics of the vortices, e.g., diameter, velocity difference, vorticity and moving velocity.

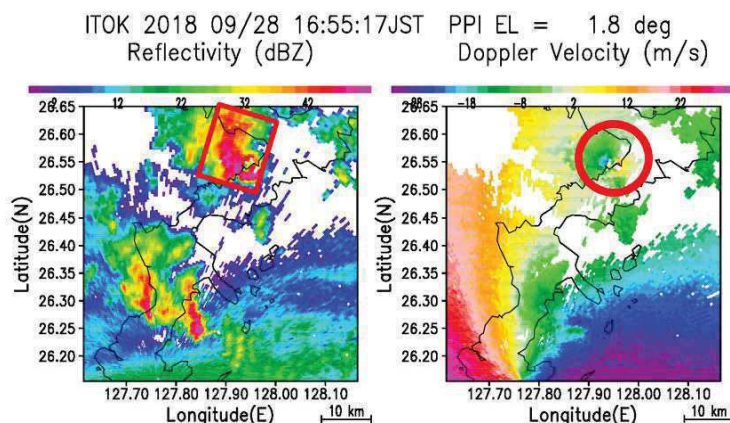


Figure 1: Examples of reflective intensity (left) and Doppler velocity (right) images. The red square indicates a convection system, and the red circle indicates a vortex.

3 Dataset

The analyzed events are 116. There are 464 events associated with tornado in the tornado database for 12 years. Unfortunately, the other events occur outside of the observation range of JMA radars. Some events are also removed from the analysis because of complicated change in strong echo region.

4 Results

We are classified to 6 kinds of convective system as shown in Fig.2 from 116 events. Isolated cumulonimbus has a relatively small scale and strong echo regions in surrounding area are clearly apart from it as shown in Fig 2a. We found 44 isolated

cumulonimbi. 13 supercells are identified. They are also isolated from surrounding area, but their size is quite larger than that of the isolated cumulonimbus as shown in Fig 2b. Horizontal scale of Fig.2b is twice of that of Fig.2a. Supercell also has a large-scale vortex called as mesocyclone. A mesocyclone is defined as a vortex of more than 2 km in diameter and a vorticity of 0.01/s or more. Cloud cluster is composed of many convective cells but their cells cannot be distinguished with each other as shown in Fig. 2c. Then, Strong echo region of it is extended to relatively large area. 53 cloud clusters are found. It is major convective system yielding tornadoes in Japan. Squall line is a kind of linear rain band which moves fast at a large angle for its trend direction. The squall line in Fig. 2d moves southeast. There are 4 events as squall line. Figure 2e shows local front that is also a kind of linear rain band composed of small-scale cells and it moves very slowly. Figure 2f shows inner rainband of typhoon is the case the vortex locates in the eye wall of typhoon. Typhoon sometimes causes tornadoes. The most of such tornadoes occur in the supercell in the outer rainband. Therefore, inner rainband case is very rare.

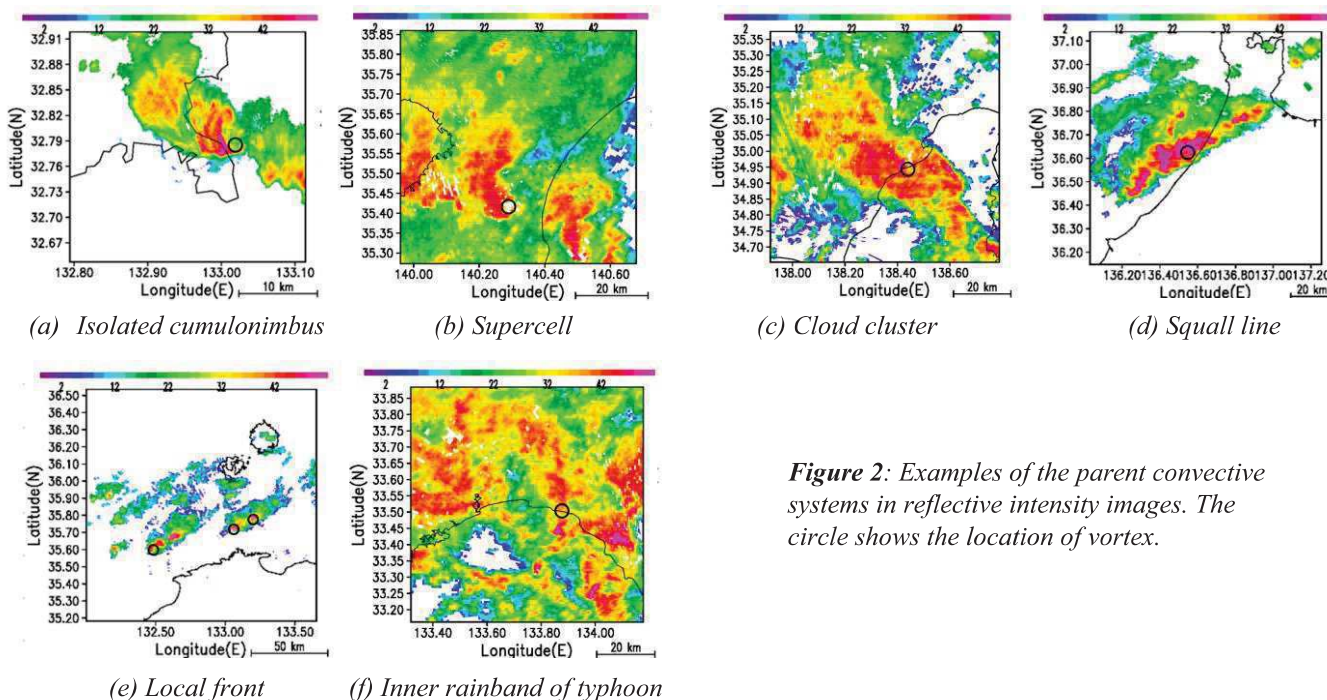


Figure 2: Examples of the parent convective systems in reflective intensity images. The circle shows the location of vortex.

Figure 3 shows the distribution of parent convective systems. The isolated cumulonimbus occurs on the sea and coastal area. The cloud cluster occurs south coast of Japan faced on the Pacific Ocean, Tohoku district faced on the Sea of Japan and inland area. Figure 4 shows the occurrence number of convective systems per month. The isolated cumulonimbus occurs from summer to autumn, and cloud clusters occur throughout the year except January and February. They frequently occur especially from early summer to autumn. Figure 5 shows the distribution of the occurrence season of convective systems. Events tended to occur on the Pacific Ocean side or inland area during the warm season. In the Sea of Japan side area, some events occur during the cold season but also do even in warm season. Figure 6 shows the occurrence time of convection systems. The isolated cumulonimbii tend to occur in the late afternoon and cloud clusters occur in the morning and early afternoon, especially.

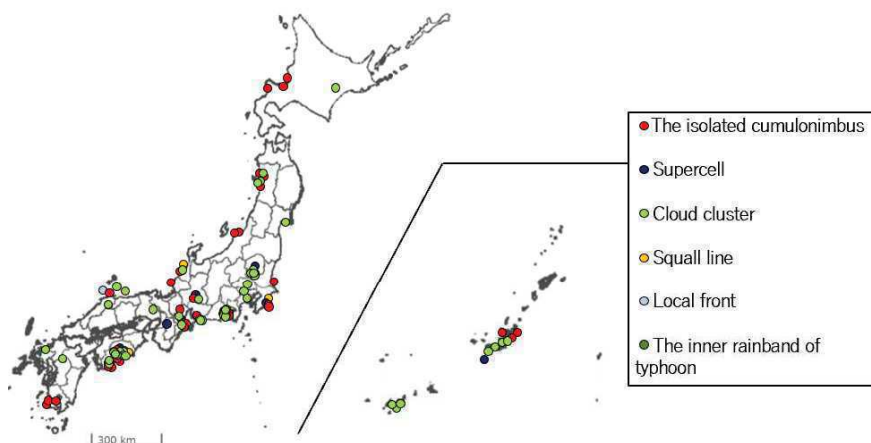


Figure 3: The distribution of convective systems.

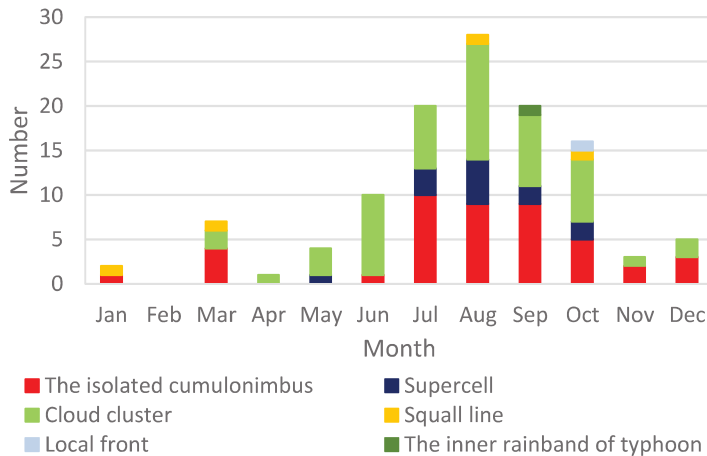


Figure 4: The occurrence number of convective systems per month.

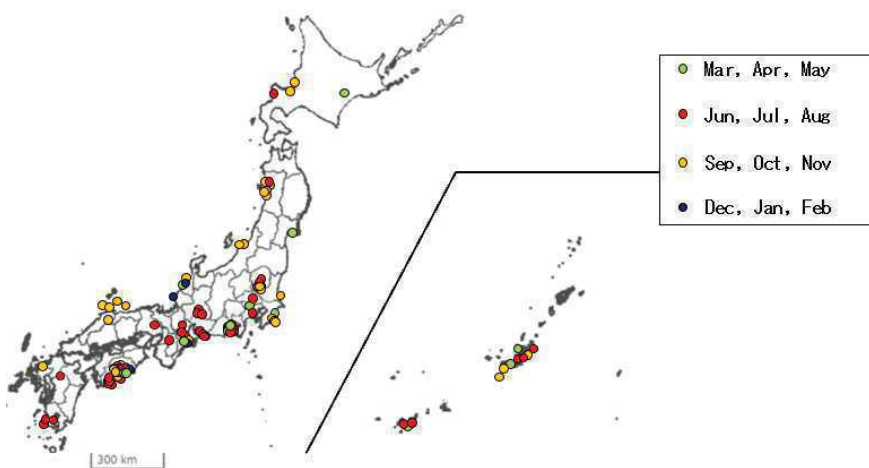


Figure 5: The distribution of the occurrence season of convective systems.

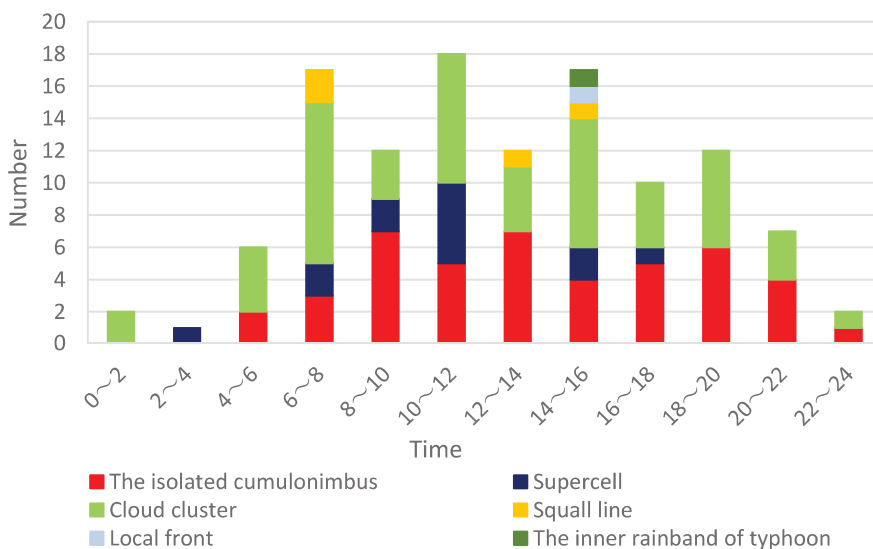


Figure 6: The time of occurrence of convection systems.

Figure 7 shows the moving direction of parent convective systems. Some systems change their echo patterns, then we decided the moving direction by tracking the vortices. Most of systems move east or landfall from the sea. The major moving direction is affected by westerly wind but landfall cases may show that the source of parent convective system is moist warm

air on the sea. As the vortex landfall, its velocity difference tends to decrease, and the vortex diameter tends to shrink as shown in Fig.8. Such facts may be caused by the friction of lands. Figure 9 shows the scatter plots between the maximum wind velocity of vortices and vortex diameter. The maximum wind speed is obtained by the sum of the tangential velocity of vortex and its moving velocity. Blue colored symbols show the vortices in supercell. Most of them are mesocyclone. Because of the spatial resolution of JMA operational radar, some mesocyclones cause damage in this figure. But actual damages are caused by tornadoes buried in mesocyclones. The scatter plots do not show any trends. But, we can see that the vortices of less than 22 m/s do not cause any damages. It may show the limit of marginal tornado (Wurman and Koshiha 2013).

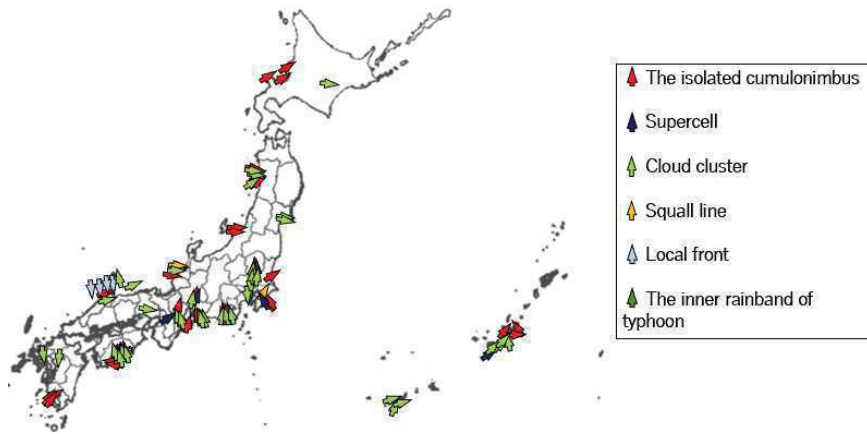


Figure 7: The moving direction of parent convective system.

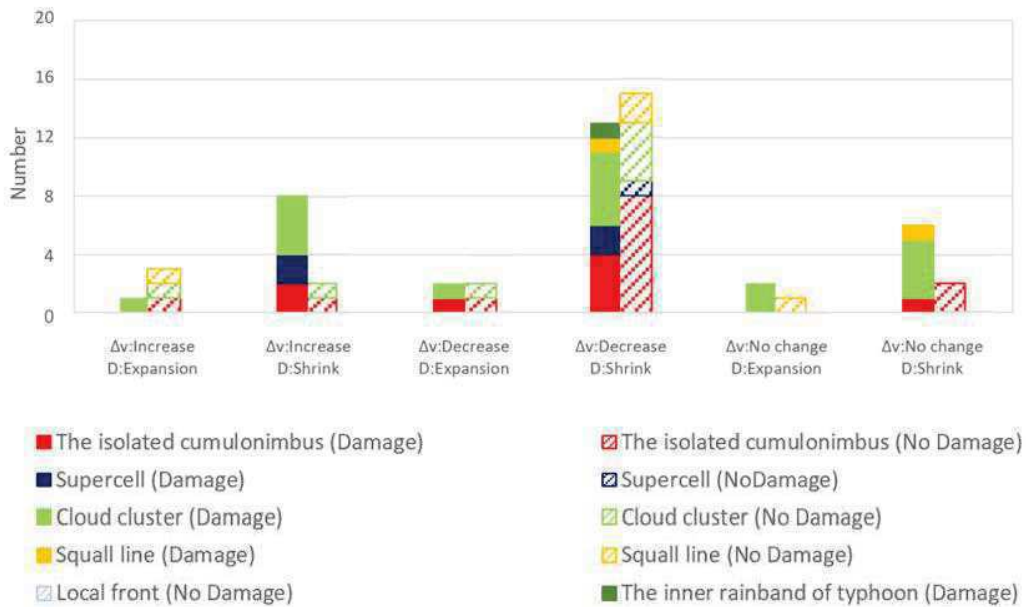


Figure 8: The vortex velocity difference and vortex diameter after landfall. Events with damage are colored and Events without damage are shaded.

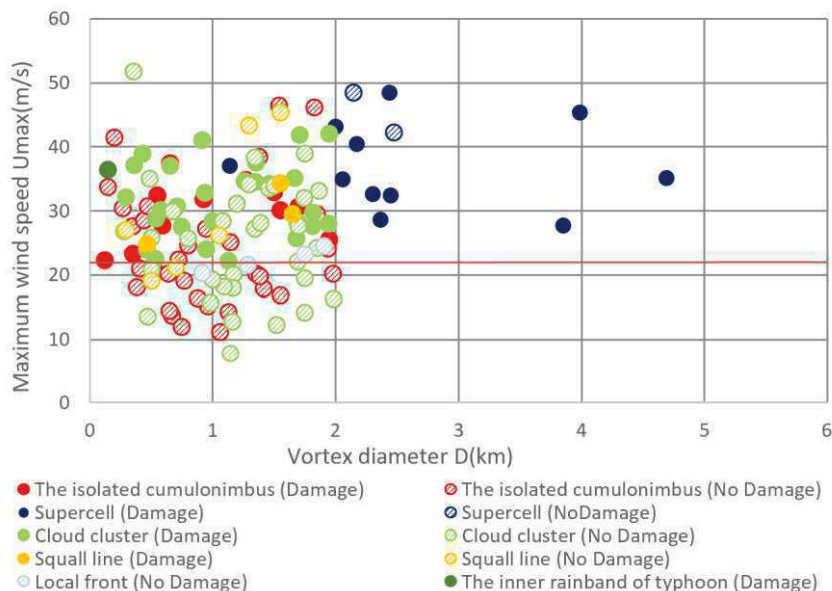


Figure 9: The scatter plots between maximum wind speed and vortex diameter. Vortices caused damage are shown by filled colored symbols and events without damage are shown by shaded symbols. The red line shows 22m/s which mean the lower limit of the velocity yielding damage.

5 Conclusions

Convective systems yielding tornadoes in Japan could be classified into six types. Major events are cloud clusters and the isolated cumulonimbus. Cloud clusters tend to occur on south coast of Japan faced on the Pacific Ocean, Tohoku district faced on the Sea of Japan and inland area, throughout the year, and in the morning and early afternoon. The isolated cumulonimbi occur on the sea and coastal area in late afternoon from summer to autumn. Most of convective systems tend to move east or landfall from the sea. When the vortices landfall, the velocity difference of them tends to decrease, and their diameter tends to shrink. The vortices of less than 22 m/s in maximum wind velocity are found not to cause any damage.

Further detailed classification and characterization through analysis using high-resolution radar networks (e.g., XRAIN) and environmental field analysis of each event will be the subject of future work.

6 Acknowledgements

The present study is supported by a Grant-in-Aid for Core Research Project from Kochi University and JSPS KAKENHI 24K01134.

7 References

- Agee, E.M.: A Revised Tornado Definition and Changes in Tornado Taxonomy, *Wea Forecasting*, 29, 1256–1258, 2014.
- Fujii, K. and Sassa K., 2022: Classification of parent convective systems of tornadoes by using radar reflectivity, *Ext. abstract of ERAD 2022*.
- Niino, H., Fujitani, T. and Watanabe, N., 1997: A Statistical Study of Tornadoes and Waterspouts in Japan from 1961 to 1993, *J. Climate*, 10, 1730-1752.
- Wurman, J. and Kosiba, K. 2013: Finescale Radar Observations of Tornado and Mesocyclone Structures, *Wea. Forecasting*, 28, 1157-1174.

Weather Radar technologies

A study on missing data correction technique for weather radar data using machine learning

Tomomi Aoki¹, Noritsugu Shiokawa¹, Shota Ochi¹, and Yasunori Nakagawa²

¹Toshiba Corporation, Tokyo, Japan

²Toshiba Digital Solutions Corporation, Kanagawa, Japan



Tomomi Aoki

1 Introduction

Due to recent climate change, water disasters caused by localized torrential rains and tornadoes have become a societal problem, and there is high anticipation of more accurate weather radar data for predicting these events. However, weather radar observations are sometimes missing data due to obstructions such as surrounding mountains and interference, which are problematic because they can cause the signs of dangerous weather phenomena such as heavy rainfall to be missed.

Currently, missing data are interpolated using observation data from weather radars installed at different locations or using data from another elevation angle that are not obstructed [1],[2]. However, when interpolating far from the interpolating weather radar, the quality of the interpolated data deteriorates due to the deterioration of resolution caused by beam width expansion and misalignment of the interpolated data. In Japan, the maximum observational range of C-band weather radar is 300 km. At this maximum range, the beamwidth expands to 3.1 km, and because the interpolation radius is set to this beamwidth, the spatial representativeness at the edge of the observation range is reduced.

Another approach is to utilize machine learning technologies such as generative adversarial networks (GANs) and convolutional neural networks (CNNs) to fill in the missing data [3],[4]. In [4], interpolation of missing data by a CNN and conditional GAN (CGAN) were quantitatively tested, and it was shown that while the CGAN could produce realistic output, the accuracy of interpolation was inferior to that of the CNN. Whether a CNN or CGAN is more suitable depends on the task. For example, when applied to scenarios such as predicting localized and extreme weather conditions, like guerrilla rainstorms, the realistic fake data generated by a CGAN may degrade the accuracy of the prediction. In this report, we examine a method of interpolating missing data using a U-net based model that uses precipitation data from the previous period and other elevation data as input for learning precipitation motion and upper airspace information for regions of missing data, with the goal of improving prediction accuracy for local weather phenomena.

2 Dataset

Missing weather radar data has a variety of causes. For example, radio waves may be blocked by obstructions such as mountains or tall buildings, or from undesired signals caused by interference with other systems, clutter, or anomalous propagation. The former type of missing data tends to occur regularly depending on the terrain, while the latter occurs irregularly depending on the weather and surrounding conditions. We propose a method for interpolating the former type of regularly occurring missing data using machine learning. Japanese weather radar systems deliver quality control (QC) information consisting of 8 bits along with the observed weather data. In the QC information, 3 bits are allocated for indicating missing data, consisting of the masked region, the invalid value region such as due to shielding, clutter, and interference, and the radio dissipation region. By utilizing the QC information, it is possible to determine the location and size of regularly missing data caused by masked regions and shielding.

2.1 Radar data information

The plan position indicator (PPI) data used in this report are from two C-band parabolic weather radars installed by the Ministry of Land, Infrastructure, Transport and Tourism in Japan, which are located at Mt. Akagi and Mt. Takasuzu. Figure 1 shows the locations of these weather radars. The interpolation models are trained using PPI data from the Mt. Akagi radar, and PPI data from the Mt. Takasuzu radar is used as a comparison target for evaluating interpolation performance. As shown in Figure 1, the Mt. Akagi radar is installed almost directly west of the Mt. Takasuzu radar, and the distance between the radars is about 120 km. The radars can observe up to 300 km with a range resolution of 250 m and switch between two observation elevation angles every minute. The data size is 1200 (range) × 512 (azimuth).

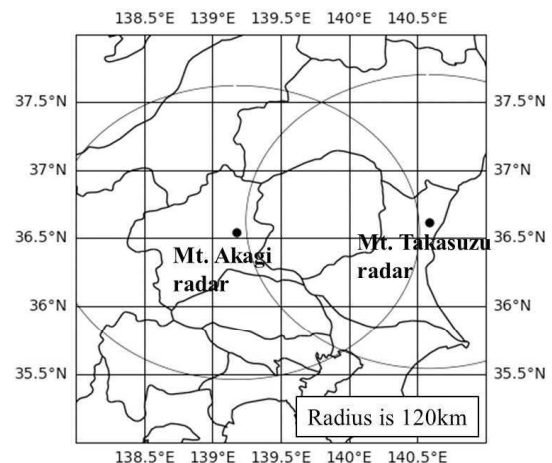


Figure 1: Radar locations.

2.2 Method for generating datasets

Although training datasets with and without missing data are needed in order to generate the interpolation model, it is impossible to obtain data without missing data in regions where the data are actually missed. To address this, we developed a method for creating a training dataset by selectively extracting segments from other azimuthal PPI data that were intact and intentionally removing a portion of the extracted segments based on the size of the missing QC information (Figure 2). Figure 3 shows an example of a basic training dataset. As shown in Figure 3, we constructed the training dataset by trimming the original data to a new size of approximately 120 km (range: M_{range}) by 90° (azimuth: $M_{azimuth}$).

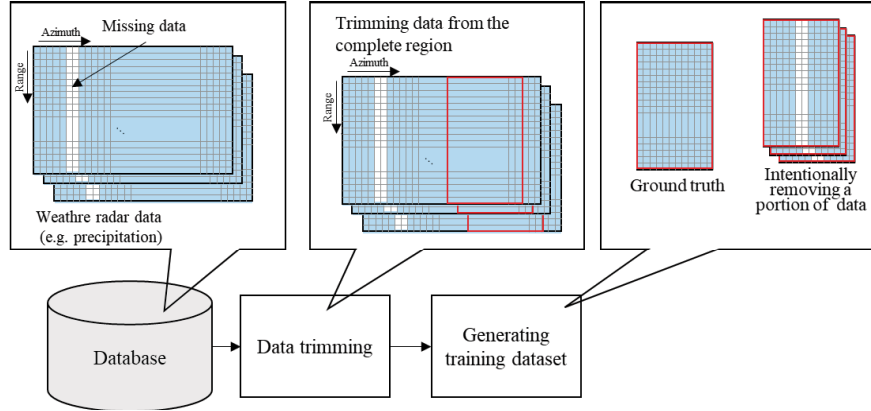


Figure 2: Example of basic training dataset.

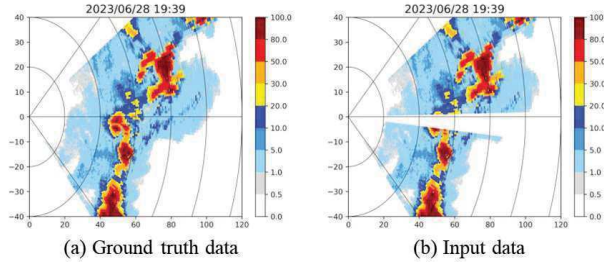


Figure 3: Example of basic training dataset.

In this study, we test two other types of datasets as shown in Figures 4 and 5. The dataset shown in Figure 4 is an extension of that shown in Figure 3, incorporating observational data from times preceding performing the interpolation processing. In the example shown in Figure 4, data observed 8 min and 16 min before the ground truth data collection time are added as additional inputs. This dataset aims to improve interpolation accuracy by learning the movement of precipitation. The dataset presented in Figure 5 is an extension of that in Figure 3, with the addition of upper elevation angle data. Observations at upper elevation angle through volume scanning are less affected by shielding, making it easier to obtain complete observation data. Although there are differences in observation altitude and timing, using this as supplementary information from the upper atmosphere is expected to improve interpolation accuracy.

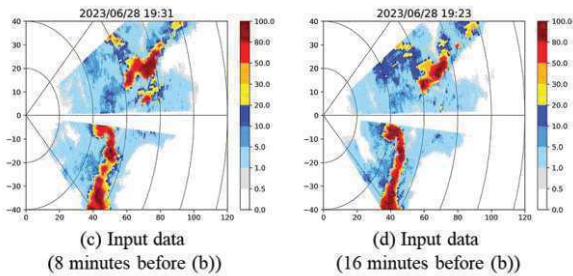


Figure 4: Example of training dataset with previous period

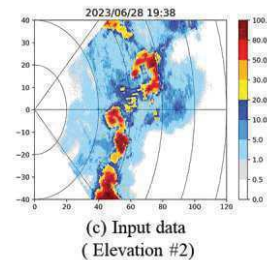


Figure 5: Example of training dataset with other elevation.

3 Methodology

In this report, U-net is employed to train the interpolation model. U-net is a CNN architecture originally designed for biomedical image segmentation. Its effectiveness in precise localization and use of context makes it well-suited for tasks such as interpolating missing data in weather radar data. The U-net architecture comprises two main parts: an encoder path for capturing context and a decoder path that enables precise localization. The encoder consists of repeated application of convolutions, each followed by a rectified linear unit and a max pooling operation for downsampling. Conversely, the decoder path consists of upsampling of the feature map followed by a transpose convolution. A key feature of U-net is skip connections

that provide the decoder with context information from the encoder. These connections help in recovering full spatial resolution at the network output, which is vital for detailed interpolation.

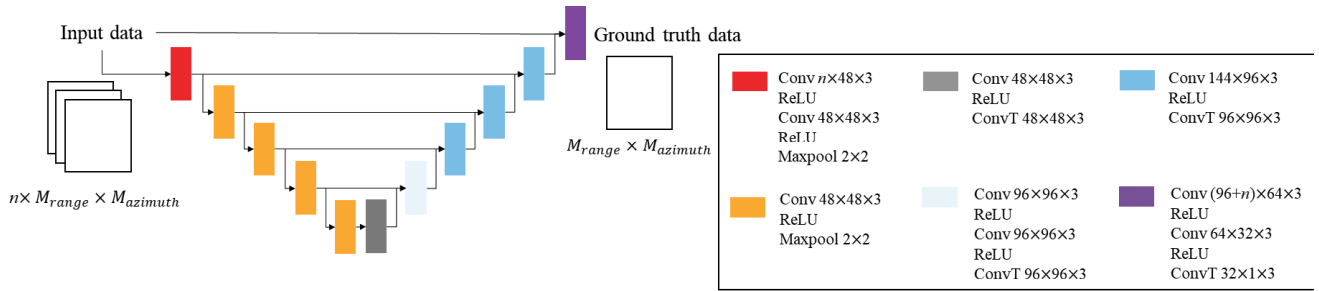


Figure 6: U-net training structure for interpolating weather radar data.

Figure 6 shows the U-net training structure of this report, where n indicates the number of input channels. The interpolation model is pre-trained using the mean absolute error (MAE) loss as follows,

$$\mathcal{L} = \mathbb{E}_{x,y} [|y - G(x)|] \quad (1)$$

where y is the true value and $G(x)$ is the U-net output value. This training is applied to a subset of PPI data that has been trimmed using the method shown in Section 2.2. We utilized the PPI data from Mt. Akagi radar on 2023/6/28 and 2023/7/3, when localized heavy rainfall occurred due to unstable atmospheric conditions.

During operation, the trained U-net model is used to interpolate the data missing by the following steps.

1. Trimming data

Trim off some of the PPI data according to the QC information including the missing regions so that the size and missing positions after trimming match the state during training.

2. Interpolation

Input the trimmed data of Step 1 into the pre-trained U-net model to generate data with the missing regions filled.

3. Replacing interpolated data

Interpolate the missing regions by replacing the data in the missing regions with the output from Step 2, based on the QC information.

4 PERFORMANCE EVALUATION

4.1 Case of 7° width of missing data

Figure 7 shows an example of interpolation results assuming a 7° width of missing data occurring from an azimuth of approximately 90° to 97°. Figure 7(a), (b), and (c) respectively represent the missing data, the ground truth, and an example of interpolation using the nearest neighbor method with PPI data from the Mt. Takasuzu radar installed at a different site than the trained data. Figure 7(d) to (f) show the results of interpolation using the U-net model, with (d) to (f) using the inputs shown in Figures 3 to 5, respectively.

The localized rainfall cells enclosed by the black circles in Figure 7(b) have disappeared due to missing data, as shown in Figure 7(a). It is suspected that linear interpolation using data around the missing regions may be insufficient for recovering these. However, Figure 7(c) to (f) demonstrate an almost successful reconstruction of the localized rainfall cells. More specifically, although Figure 7(c) shows high reproducibility for the middle and right cells, the left cell appears to have collapsed. This issue is likely due to the left cell being the farthest from the Mt. Takasuzu radar, resulting in degraded spatial representativeness and an inability to accurately reproduce local phenomena. Figure 7(d) reasonably reproduces the shape of the cells but tends to underestimate their overall intensity. Figure 7(e) fails to reproduce the right cell, indicating that the advantages of using time-series input have not been confirmed. This failure may be attributed to differences in the movement of the rainfall cells between training and validation stages. To address this, it is necessary to either increase the size of the dataset to cover a wider range of motions or incorporate additional features such as advection vectors to represent cell movement. The highest reproducibility in both the shape and intensity of the three cells is observed in Figure 7 (f), confirming that using upper elevation angles is effective for defect recovery.

To quantitatively evaluate the performance of the interpolation methods, Figure 8 shows the root mean squared error (RMSE) versus the ground truth of the interpolation region. We evaluated three cases of localized heavy rainfall on 2023/8/9, 2023/7/4, and 2023/9/5. By using interpolation with the U-net model on the results of the nearest neighbor method for PPI data from a different site, we confirmed an improvement in RMSE for all cases. Notably, the model using

upper elevation angles achieved the lowest RMSE. In the model using upper elevation angles, RMSE improved by up to 41% compared with the nearest neighbor method results for different site data, and by up to 21% compared with the nearest neighbor method results using upper angle data itself.

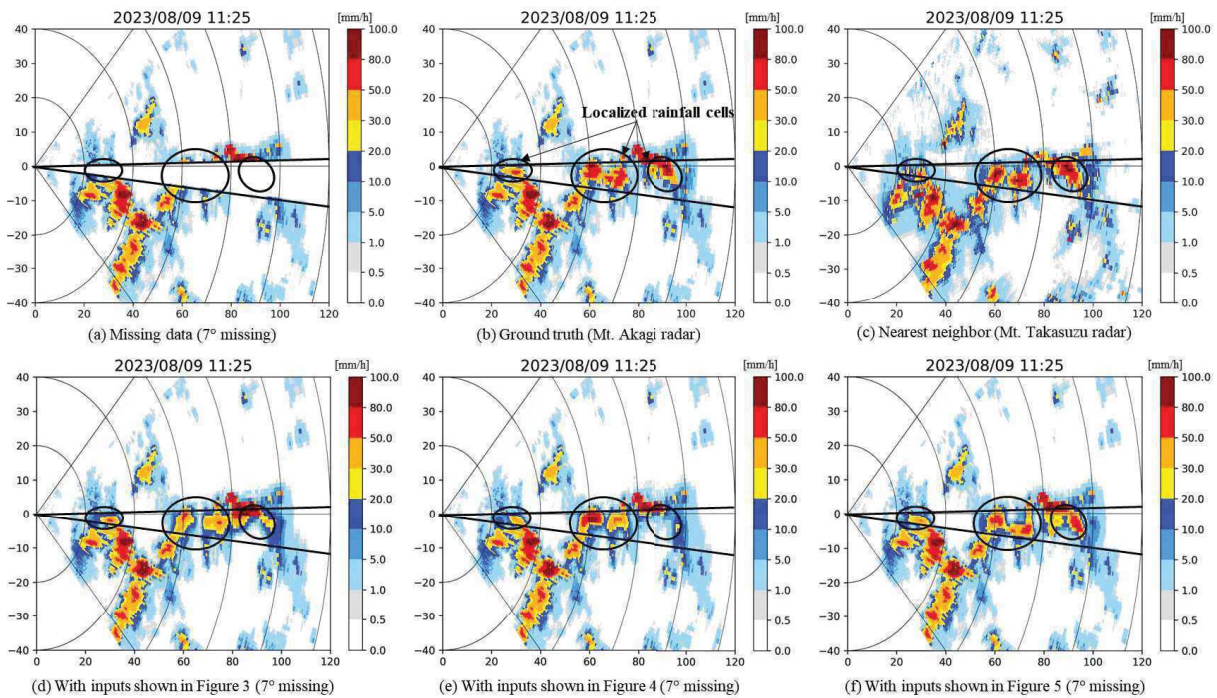


Figure 7: Interpolation results assuming a 7° width of missing data.

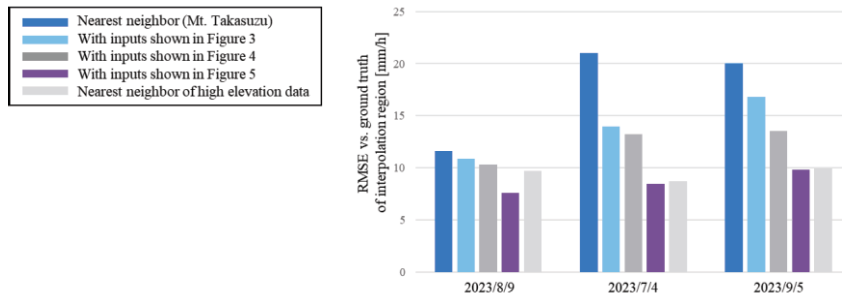


Figure 8: RMSE vs. ground truth of the interpolation region [mm/h].

4.2 Case of 14° width of missing data

Figures 9 and 10 show an example of interpolation results assuming a 14° width of missing data occurring from an azimuth of approximately 90° to 104° and the RMSE versus the ground truth in the interpolation region, respectively.

First, focusing on Figure 9(c) and (f), the localized rainfall cells are appropriately reconstructed as well as in Figure 7. Additionally, in the RMSE of Figure 10, the results of the U-net model with upper elevation angle data as input showed up to a 56% reduction in RMSE compared with the nearest neighbor method results for different site data. Furthermore, even compared with the results of using upper elevation angle data itself with the nearest neighbor method, the U-net model with upper elevation angle data as input achieved up to a 9% reduction in RMSE, demonstrating the effectiveness of the U-net model using upper elevation angle data.

However, it was confirmed that the interpolation results using the U-net model with other inputs can sometimes result in worse accuracy compared with interpolation using the nearest neighbor method with different site data. Compared with the results in Figure 7, the interpolated regions in Figure 9(d) and (e) are clearly overly smoothed, causing the rainfall cells in Figure 9(b) to merge and lose variation in precipitation. This degradation occurs because larger missing regions provide less contextual information for the network to infer the missing details accurately. Although the U-net utilizes skip connections between the encoder and decoder to supplement local information, when the missing regions become larger, the surrounding information becomes insufficient, resulting in overly smoothed outputs. It is preferable to interpolate the missing data using only the own observation data of a site, as there may be cases where data from upper elevation angles are also missing or in regions not covered by other site radar data. To overcome this, it is thought to be effective to employ data augmentation to learn various missing patterns and to introduce attention mechanisms to emphasize important local features. These approaches will be needed in future work.

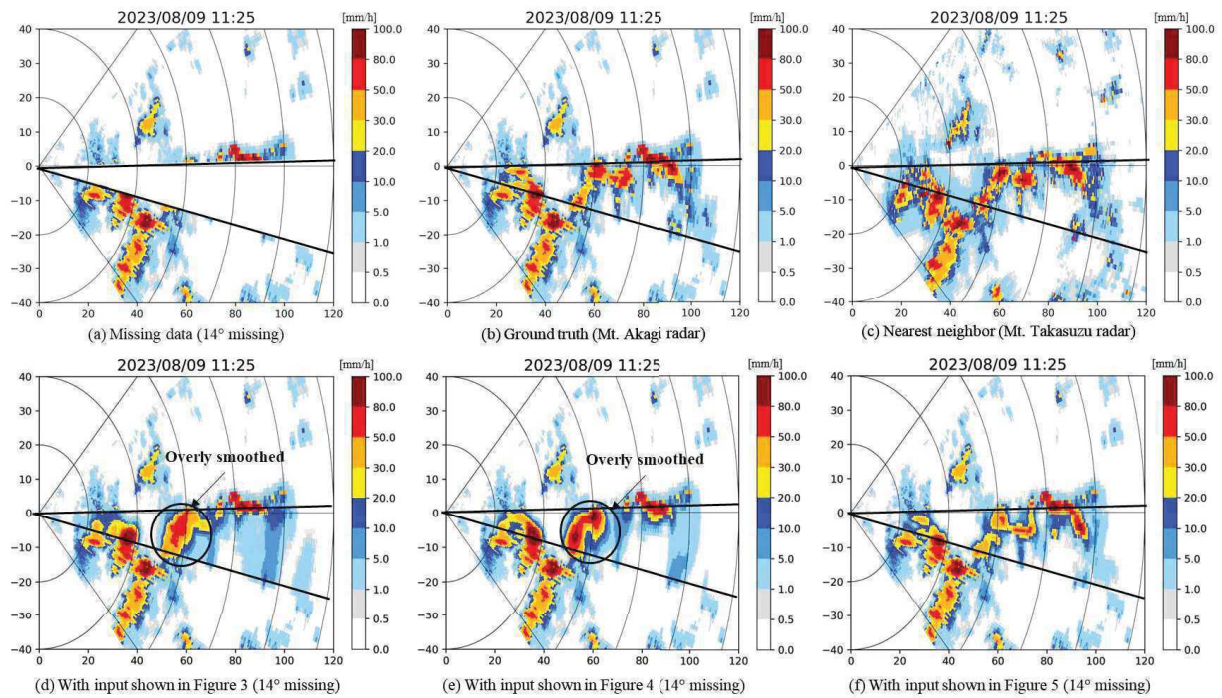


Figure 9: Interpolation results assuming a 14° width of missing data.

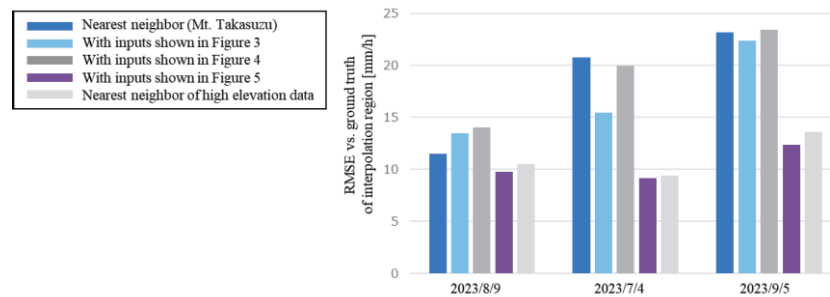


Figure 10: RMSE vs. ground truth of the interpolation region [mm/h].

5 Conclusions

This report explored the interpolation of missing weather radar data using machine learning, specifically employing the U-net model. We constructed models with three different inputs: missing data only, data from the time before the interpolation timing, and data from another elevation angle without missing values. Our findings indicated that for small missing areas, the U-net model outperformed the nearest neighbor method using data from a different site, with the highest accuracy achieved by the U-net model utilizing data from another elevation angle without missing values. However, for larger missing areas, while the U-net model with another elevation angle data showed improved accuracy compared with the nearest neighbor method using other site data, models with other inputs exhibited decreased accuracy, highlighting regions for further improvement.

6 References

- [1] J. Zhang, K. Howard, C. Langston, S. Vasiloff, B. Kaney, A. Arthur, V. Cooten, K. Kelleher, D. Kitzmiller, F. Ding, D. Seo, E. Wells, and C. Dempsey, “National Mosaic and Multi-Sensor QPE (NMQ) System: Description, Results, and Future Plans,” *BAMS*, vol. 92, no. 10, pp. 1321–1338, Oct. 2011.
- [2] J. Brook, A. Protat, J. Soderholm, R. Warren, and H. McGowan, “A Variational Interpolation Method for Gridding Weather Radar Data,” *J. Atmos. Oceanic Technol.*, vol. 39, no. 11, pp. 1633–1654, Nov. 2022.
- [3] S. Tan and H. Chen, “Conditional GAN for weather radar beam blockage correction,” *IEEE Trans. On Geos.*, vol. 61, June 2023.
- [4] J. A. Geiss and J. Hardin, “Inpainting radar missing data regions with deep learning,” *Atmos. Meas. Tech.*, vol. 14, no. 12, pp. 7729–7747, <https://doi.org/10.5194/amt-14-7729-2021>, 2021.

Postprocessing methods to characterize multimodal precipitation in Doppler spectra from DWD's C-band radar birdbath scan

M. Gergely¹, P. Ockenfuß², S. Kneifel², M. Frech¹

¹Deutscher Wetterdienst (DWD), Observatorium Hohenpeißenberg, Germany

²Meteorological Institute, Ludwig-Maximilians University, Munich, Germany



Mathias Gergely

1 Introduction

Since modifying DWD's operational C-band radar (vertically pointing) birdbath scan in spring 2021, profiles of radar moments and full Doppler spectra are routinely recorded at all 17 operational weather radars across Germany every 5 minutes. These data complement polarimetric measurements from the radar volume scans at low elevation angles to investigate precipitation processes in detail (Trömel et al., 2021). Furthermore, they can be exploited for atmospheric profiling of precipitation, similar to how higher-frequency Doppler radars have been used to study cloud processes (Gergely et al., 2022).

A particularly valuable feature of these weather radar birdbath scans is that the data are only weakly affected by atmospheric attenuation over the depth of the troposphere. Therefore, these radar measurements provide a unique view into extreme precipitation events like hailstorms, which can enhance the information inferred from radar polarimetry (Ryzhkov and Zrnica, 2019). However, due to the pronounced clutter signal and hard- and software constraints, a detailed analysis of the C-band radar Doppler spectra recorded in various types of precipitation, ranging from light snow to heavy rain and large hail, requires flexible postprocessing methods that are adapted to each use case.

This article presents the main spectral postprocessing routines for identifying and quantifying different precipitation modes in the recorded profiles of C-band radar Doppler spectra.

2 Methodology

The postprocessing chain for the dual-polarization C-band radar Doppler spectra consists of three main steps: isolating the weather signal from non-meteorological contributions like static clutter, identifying the individual precipitation modes contained in every Doppler spectrum within the weather signal, and calculating the corresponding modal and multimodal properties, e.g. mode power, mean Doppler velocity, spectral width, and bimodal separation. Depending on the type of precipitation event, the desired degree of detail of the multimodal analysis, and the required robustness of the analysis, different options can be selected for postprocessing.

2.1 Adaptive postprocessing for Doppler spectra of snow

For narrow Doppler spectra of relatively low reflectivities, non-meteorological contributions such as static clutter near Doppler velocities of 0 m s⁻¹ can form a significant part of the overall signal (s. Fig. 1). Therefore, an effective filtering procedure is essential for a detailed multimodal analysis of the Doppler spectra of snow.

As outlined by Gergely et al. (2022), a spectral filter based on the polarimetric characteristics of spectral differential reflectivity and its texture together with signal power (illustrated in Fig. 1b) can often mitigate the contamination from clutter and background signal sufficiently to isolate the weather signal (s. Fig. 3a). Appropriate filter thresholds are determined

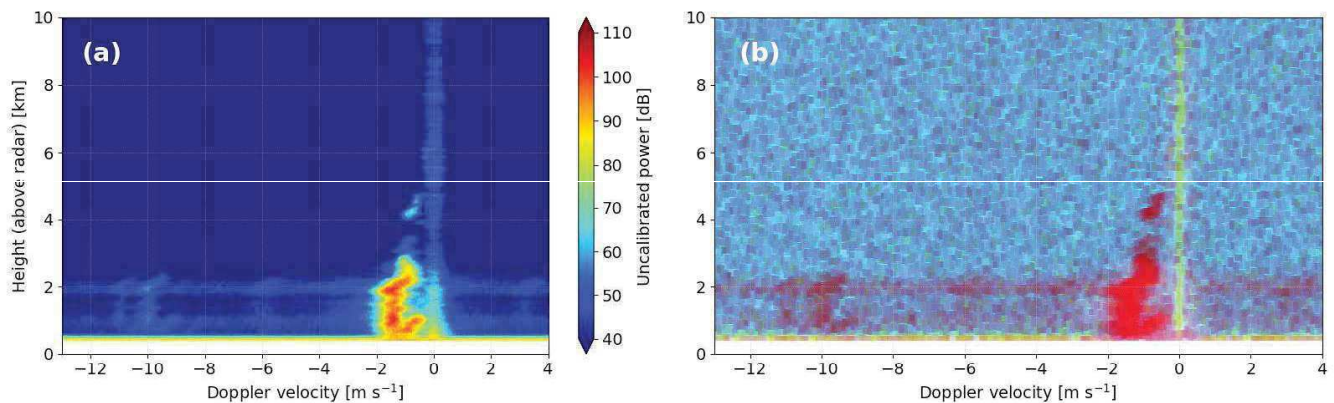


Figure 1: Summary of radar output for a birdbath scan of the Memmingen radar in southern Germany during snowfall on 27 March 2023; (a) profile of Doppler (power) spectra in (H)orizontal polarization channel $\sim sZ_H$, where negative velocities indicate particles falling downward toward the radar, (b) pseudo-color RGB image of sZ_H (Red), absolute value of spectral differential reflectivity sZ_{DR} (Green), and texture parameter $SD(sZ_{DR})$ (Blue).

automatically and objectively by HDBSCAN clustering (McInnes et al., 2017) or by trial and error when emphasizing simplicity and robustness of the algorithm.

After isolating the weather signal, individual precipitation modes at each height bin can be identified automatically by UniDip clustering (Maurus and Plant, 2016) or by manually prescribing a fixed peak prominence. Then, the Doppler moments can be calculated for each precipitation mode, e.g., mean Doppler velocity and spectral width (given as standard deviation SD), as well as multimodal properties that describe the relationship between multiple simultaneously occurring precipitation modes and uncertainty estimates of all Doppler moments and multimodal properties based on the differences between executing the analysis for smoothed and unsmoothed Doppler spectra (Gergely et al., 2022).

2.2 Efficient postprocessing for Doppler spectra of convective storms

For broad Doppler spectra of convective precipitation, e.g. in hailstorms, the adaptive postprocessing routine requires much more computational resources or computation time (due to the cluster analysis). Additionally, due to the similarity between the polarimetric characteristics of intense precipitation and clutter in the recorded Doppler spectra, a separation of those different contributions to the spectra is often not possible. Therefore, no clutter filter is applied, and the threshold value of the peak prominence for identifying all relevant precipitation modes is set to (an uncalibrated spectral power of) 8 dB, based on evaluating Doppler spectra for 15 hailstorms from 2021 through 2023. As the weather signal is much stronger and wider in convective storms, the lack of a clutter filter usually has only a minor effect on the key analysis results (s. Fig. 5).

To resolve hailstones falling faster than the birdbath-scan Nyquist frequency of 13.3 m s^{-1} , the Doppler velocity range has to be extended. As outlined in Fig. 2, the recorded (folded) Doppler spectra are cyclically expanded at the slow- and fast-falling edges and then cut to only retain the dealiased contiguous center profile of Doppler spectra, using an approach similar to Garcia-Benadi et al. (2020). Doppler moments of each precipitation mode and multimodal properties are then calculated analogously to the adaptive postprocessing routine.

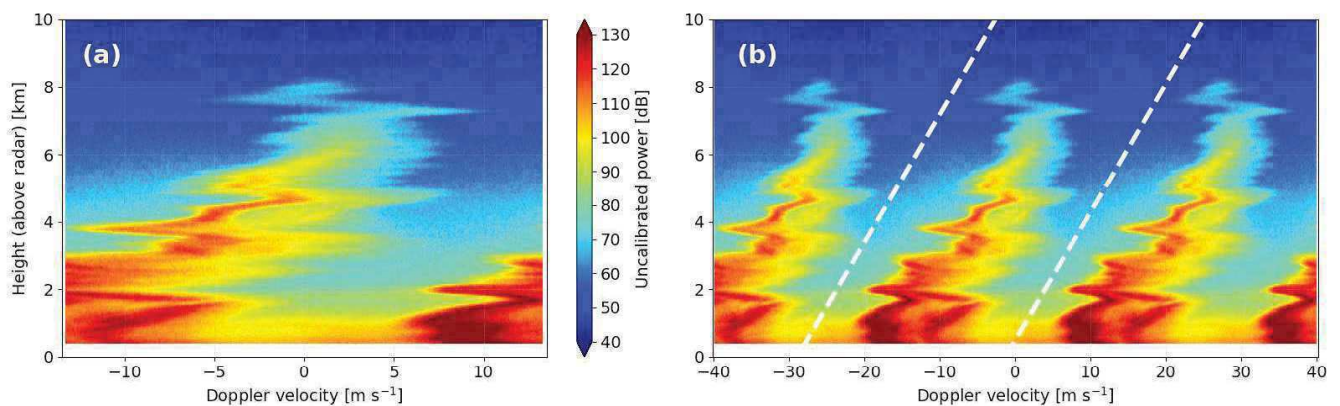


Figure 2: Summary of radar output for a birdbath scan at the Hohenpeißenberg radar in pre-alpine Bavaria during a hailstorm on 30 April 2021; (a) profile of (still folded) Doppler spectra, (b) expanded Doppler spectra with white dashed lines indicating cuts for isolating the dealiased center profile of Doppler spectra.

3 Dataset

Doppler spectra are recorded routinely for the (vertically pointing) birdbath scans at all 17 German C-band radars with a radar pulse width of $0.4 \mu\text{s}$. For each birdbath scan, 15 Doppler spectra are recorded at every range bin between 0.4 and 13.2 km above the radar site with a 25 m sampling interval and at a spectral (velocity) resolution of about 2.6 cm s^{-1} for 1024 velocity bins. Further details on the German C-band radar network and the operational DWD birdbath scan are listed by Frech et al. (2017) and Gergely et al. (2022).

Currently, HDF5 birdbath data can be requested for individual test cases at kundenservice@dwd.de. The postprocessing methods presented in Chapter 2 and several examples are available at <https://github.com/birdbathDWD/PyBathSpectra>

4 Results

Figure 3 illustrates the results of using adaptive postprocessing for the snowfall data shown in Fig. 1. Clutter and background signal are filtered out effectively in Fig. 3a. Below about 1.3 km above the radar, 2 precipitation modes are found in the Doppler spectra in Fig. 3b. These bimodal spectra may indicate slow-falling pristine crystals coexisting with faster falling lightly to moderately rimed crystals or aggregates, for example. Skewness and kurtosis values are generally unremarkable, but show a sharp spike at a height of 1.2 km, where the postprocessing routine fails to identify the second precipitation mode. Extreme values of these very sensitive higher-order moments indicate a hidden multimodality that cannot be resolved (here, missed by the multimodal postprocessing routine or, generally, in unimodal signal processing methods that do not account for multimodality a priori). Multimodal properties are discussed by Gergely et al. (2022).

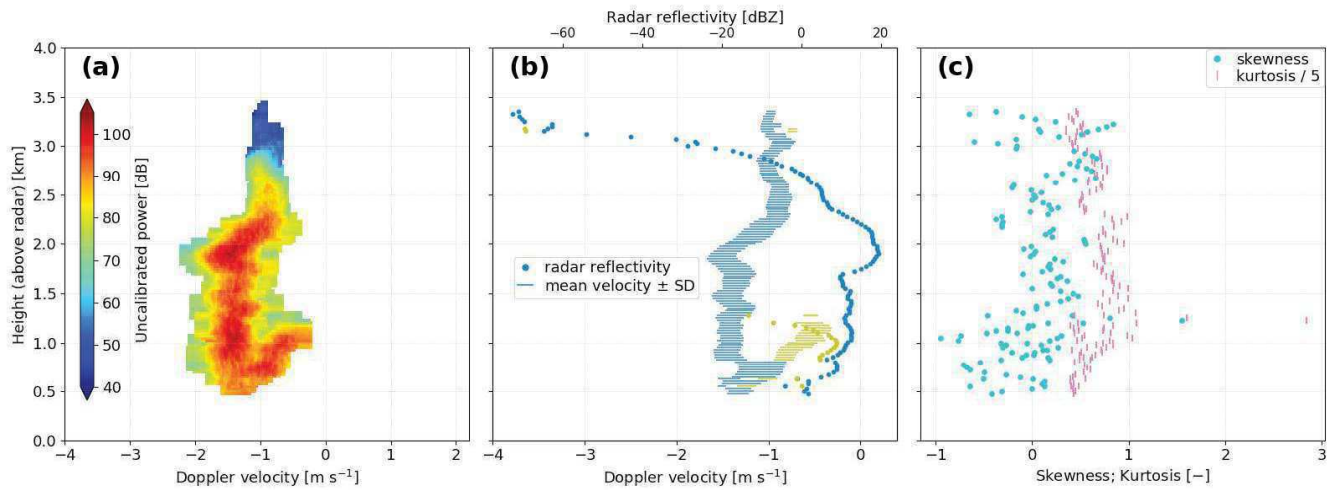


Figure 3: Results of multimodal postprocessing for radar data shown in Fig. 1; (a) isolated weather signal, (b) radar reflectivity, mean Doppler velocity, and spectral width for all identified precipitation modes (1st mode in blue, 2nd mode in green), (c) higher-order Doppler moments of skewness and kurtosis.

Figure 4 indicates that the relative uncertainties in the calculated Doppler moments are mostly below 10%. Only the higher-order moments of kurtosis and, particularly, skewness are characterized by much larger uncertainties, because they are strongly affected by the low-power left and right tails of the Doppler spectra, where the presented postprocessing routine can sometimes produce spurious artifacts.

Figure 5 illustrates the postprocessing results for a supercell convective storm. At the time of the birdbath scan, intense rain and hail with maximum hailstone diameters of about 2.5 cm were observed at the ground. While no clutter filter is applied here (s. Chapter 2.2), no disturbing clutter signal or spurious clutter peaks are observed in Figs. 5a and b, in contrast to the snowfall analysis in Fig. 1. The relative uncertainties of calculated mean Doppler velocity, spectral width, and radar reflectivity are generally below 10% while the uncertainties for the higher-order moments of skewness and kurtosis can be much higher (not shown), similar to the results summarized in Fig. 4 for the snowfall example.

The postprocessing results in Fig. 5 show the bimodal Doppler spectra of slower falling rain (orange in Figs. 5b, c) and fast-falling hail (dark blue in Figs. 5b, c) below the 0 °C level at a height of ~ 1.8 km above the radar. The third precipitation mode (green in Figs. 5b, c) around the 0 °C level could indicate shedding of meltwater from hailstones. However, a detailed interpretation of the evolution of the precipitation column is difficult due to the very limited (in space and time) 15 s snapshot each birdbath scan can provide of the highly dynamic convective storm.

Nonetheless, Figs. 5b to e demonstrate that these birdbath Doppler data can also be used to separate hail and rain modes for a multimodal analysis, analogous to how different snow modes were identified in Fig. 3. In Fig. 5c, for example, hail at heights below the 0 °C level is characterized by a reflectivity of more than 50 dBZ, while the rain mode contributes only a lower reflectivity of about 30 to 47 dBZ to the overall radar signal. Similarly, the typical Doppler velocity (i.e., particle terminal fall velocity + vertical air movements) can be derived separately for hail (15 to 20 m s⁻¹) and rain (5 to 12 m s⁻¹), instead of relying only on a single (average) value for both precipitation modes combined that is provided by common unimodal radar signal processing.

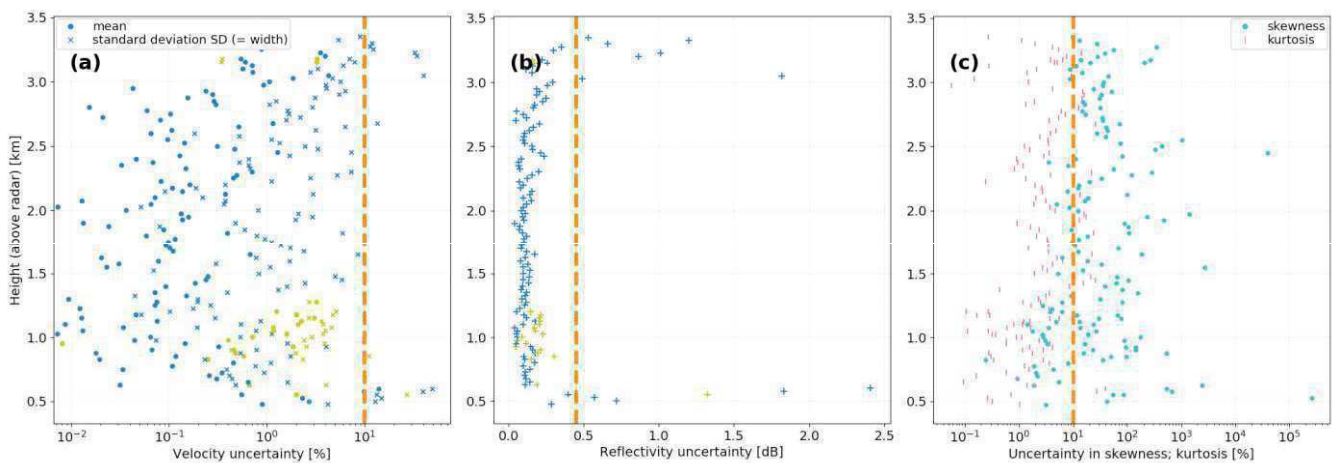


Figure 4: Uncertainty estimates for the Doppler moments illustrated in Fig. 3. Vertical dashed lines indicate relative uncertainties of 10%.

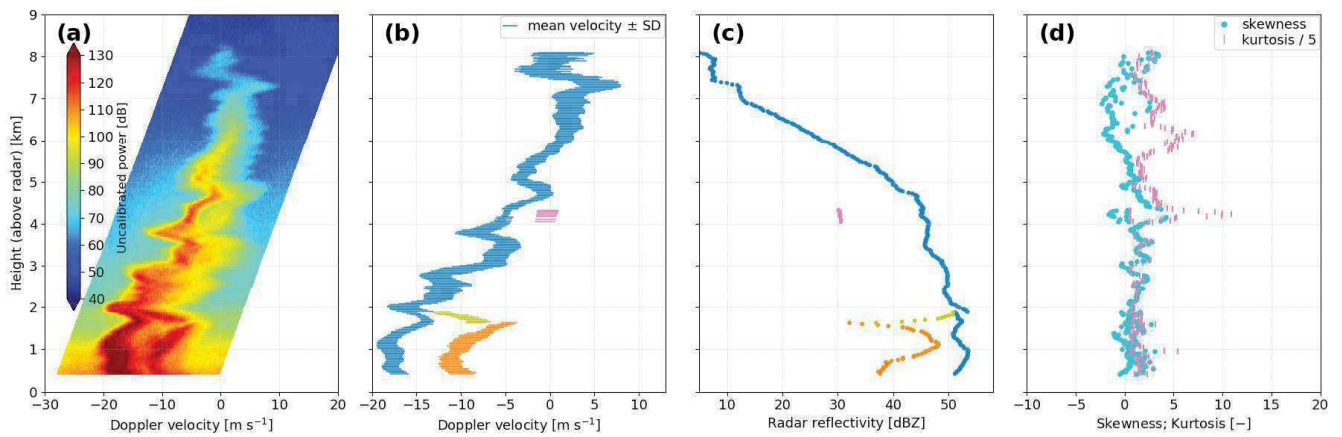


Figure 5: Results of multimodal postprocessing for radar data shown in Fig. 2; (a) profile of expanded and dealiased Doppler spectra, (b) mean Doppler velocity and spectral width for all identified precipitation modes with (c) corresponding radar reflectivity for each mode, (d) higher-order Doppler moments.

Not every hailstorm features such a clear vertical structure as the birdbath scan of a well-isolated supercell shown in Fig. 5. A hail cell that generated hailstones of more than 4 cm diameter at the ground, for example, produced more convoluted Doppler spectra that proved more difficult to dealias and analyze. But, the bimodality consisting of a slower (rain or small-ice) and a faster falling (hail) mode can generally be observed as a common feature, either close to the ground or higher up in the precipitation column, for all 15 hailstorms that have been analyzed by the presented multimodal postprocessing methods for DWD's C-band radar birdbath scan, so far.

Figure 6 shows another example of applying the spectral postprocessing methods to a birdbath scan that was recorded while a supercell moved over the radar. This supercell again produced hailstones with sizes of up to about 2.5 cm in the vicinity of the radar site, but during the birdbath scan, the bimodal Doppler spectra indicating the occurrence of hail can only be observed at heights above 2 km. Between 2 and 3.5 km above the radar, the (orange) hail mode does not show much higher reflectivities than the (dark blue) rain mode. Compared to the reflectivities of over 50 dBZ for the hail mode in Fig. 5, the reflectivities of mostly less than 40 dBZ in Fig. 6 indicate a much lower hail concentration, or hail amount, at the radar location for the latter hailstorm (assuming a similar general shape of the hail size distribution). Furthermore, Fig. 6 reveals multiple regions along the precipitation column where the characteristic bimodal structure that indicates the occurrence of hail can be found (also around 4 and 6 km above the radar), suggesting that multiple pulses of hail were produced by this supercell.

Compared to Fig. 3, the Doppler spectra of hail in Figs. 5 and 6 are much more affected by turbulence, leading to significant spectral broadening, and by vertical air motion, evident from the pronounced zig-zag shape and the sometimes strong deviation of the slow spectral edge by several m s⁻¹ from a Doppler velocity of 0 m s⁻¹. Nevertheless, modifying the detailed adaptive postprocessing methods to emphasize resource efficiency and algorithm robustness as described in Chapter 2.2 allows for an illuminating multimodal analysis of the birdbath scans recorded even in hailstorms, which has not been possible up to now.

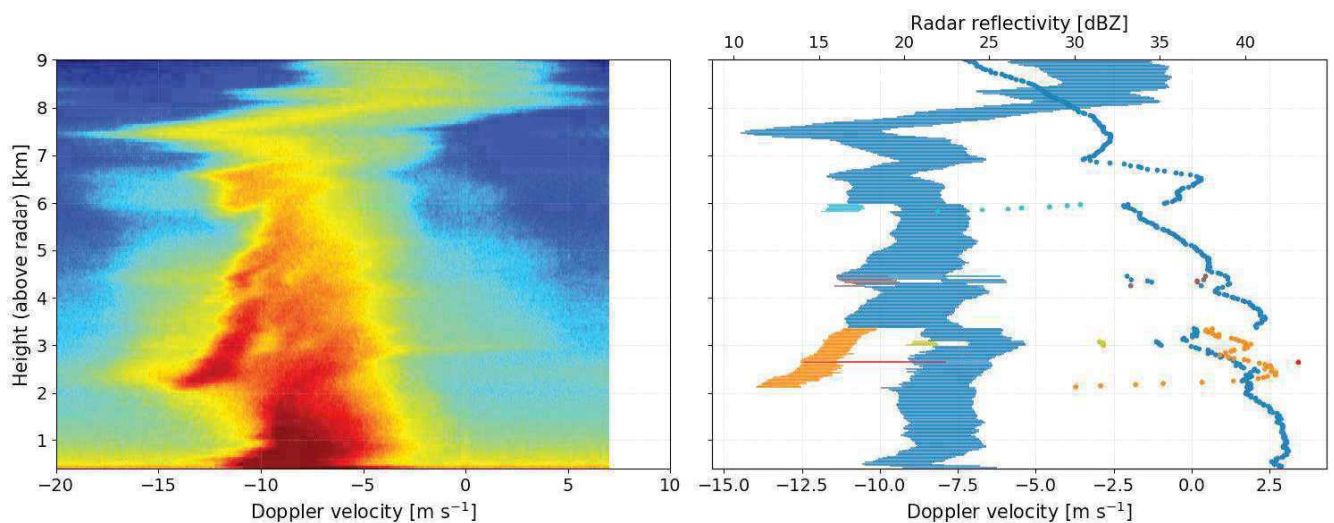


Figure 6: Results of multimodal postprocessing for a birdbath scan recorded at the Flechtdorf radar in central Germany during a hailstorm on 22 June 2023; (left) profile of expanded and dealiased Doppler spectra, (right) mean Doppler velocity and spectral width for all identified precipitation modes with corresponding radar reflectivity, similar to Fig. 5 with clear(est) hail mode colored in orange.

5 Conclusions

Doppler spectra from operational C-band radar birdbath scans can provide a unique view into precipitation processes from snowfall to strong convective hailstorms. Together with Gergely et al. (2022), this presentation introduces spectral postprocessing methods for the analysis of multimodal precipitation (i.e. multiple simultaneously occurring precipitation regimes) in these birdbath scans. The radar signal-processing routine is implemented in the *PyBathSpectra* toolkit (available for download and testing at <https://github.com/birdbathDWD/PyBathSpectra>) and can be adapted to the desired degree of detail of the analysis results or the required robustness of the postprocessing methods.

One particularly intriguing application of the presented weather-radar Doppler spectra and postprocessing routine is the analysis of the Doppler characteristics of hail. Hail reflectivity, mean Doppler velocity and spectral width can be separated from the simultaneous contributions of other precipitation modes, e.g., rain near the ground, and then investigated in detail for all hailstorms that pass over a radar site. If it is possible to estimate and filter out the vertical air motion from the Doppler spectra, these spectra can then be used to retrieve the full hail size distributions similar to Ulbrich (1974), after converting the corrected Doppler velocities to hail sizes based on previously determined hail fall velocity–size relationships (e.g., given by Heymsfield et al., 2020). Such an approach can open a new avenue toward deriving the hail characteristics that determine the damage potential of hailstorms more comprehensively than merely estimating a single maximum hail size (Grieser and Hill, 2019), which we will explore in our future work.

6 Acknowledgements

The authors acknowledge support from the German Research Foundation (DFG) 'PROM' priority program SPP-2115 and from DWD; <https://www2.meteo.uni-bonn.de/spp2115>

7 References

- Frech, M., Hagen, M., and Mammen, T., 2017, *J. Atmos. Oceanic Technol.*, 34, 599–615, <https://doi.org/10.1175/JTECH-D-16-0076.1>
- Garcia-Benadi, A., Bech, J., Gonzalez, S., Udina, M., Codina, B., and Georgis, J.-F., 2020, *Remote Sensing*, 12, 4113, <https://doi.org/10.3390/rs12244113>
- Gergely, M., Schaper, M., Toussaint, M., and Frech, M., 2022, *Atmos. Meas. Tech.*, 15, 7315–7335, <https://doi.org/10.5194/amt-15-7315-2022>
- Grieser, J., and Hill, M., 2019, *J. Appl. Meteor. Climatol.*, 58, 2329–2345, <https://doi.org/10.1175/JAMC-D-18-0334.1>
- Heymsfield, A., Szakall, M., Jost, A., Giammanco, I., Wright, R., and Brimelow, J., 2020, *J. Atmos. Sci.*, 77, 405–412, <https://doi.org/10.1175/JAS-D-19-0185.1>
- Maurus, S., and Plant, C., 2016, *Proc. 22nd ACM SIGKDD International Conference on Knowledge Discovery and Data Mining*, <https://doi.org/10.1145/2939672.2939740>
- McInnes, L., Healy, J., and Astels, S., 2017, *Journal of Open Source Software*, 2, 205, <https://doi.org/10.21105/joss.00205>
- Ryzhkov, A. V., and Zrnic, D. S., 2019, <https://doi.org/10.1007/978-3-030-05093-1>
- Trömel, S., and others, 2021, *Atmos. Chem. Phys.*, 21, 17291–17314, <https://doi.org/10.5194/acp-21-17291-2021>
- Ulbrich, C. W., 1974, *J. Appl. Meteor.*, 13, 387–396, [https://doi.org/10.1175/1520-0450\(1974\)013<0387:AODRSO>2.0.CO;2](https://doi.org/10.1175/1520-0450(1974)013<0387:AODRSO>2.0.CO;2)

Verifying the clutter suppression capability of X- and C-band weather radars equipped with solid state power amplifier transmitters

Pekka Puhakka, Jere Mäkinen, Marjan Marbouti

Vaisala Oyj, Finland



Marjan Marbouti

1 Introduction

Clutter means unwanted echoes in the received radar signal caused by, for example, ground, buildings, or birds. Ground clutter suppression is critically important for improving the radar data quality of any weather radar system. If not removed, the ground clutter may produce strongly biased estimates of the fundamental spectral moments such as mean power, mean Doppler velocity, and spectrum width. It is desirable to have a ground clutter filter providing good clutter suppression while minimizing the radar parameter estimation errors, namely, standard deviation and bias (Nguyen and Chandrasekar, 2013).

There are different approaches that apply clutter filtering in weather radar signal processing. In the simplest transmission scheme where radar pulses are transmitted and received with uniform spacing, ground clutter can be filtered in time domain by using infinite impulse response (IIR) or finite impulse response (FIR) filters. These are high-pass filters having sharp narrow notches characterized by their type, rejection depth, and the notch width. In many applications, these filters are sufficient. However, when the signal and clutter overlap in the frequency domain as in the case of weather radar, the use of these filters removes clutter but also notches out a part of the weather signal and causes bias in the estimates.

To mitigate this problem, advanced filtering methods have been developed. High-speed signal processors such as Vaisala RVP series offer sufficient storage and computational power to implement frequency domain filters that, in some cases, are adaptive. The frequency domain filters available in the RVP signal processor are:

- Fixed width filters with interpolation
- Variable width single slope adaptive processing
- Gaussian model adaptive processing (GMAP)

Fixed width clutter filter removes a specified number of Doppler spectrum components in the vicinity of the zero velocity and then interpolate across the gap using a minimum of a specified number of the edge points at each end of the gap. This simple approach attempts to preserve the noise level and possible overlapping weather targets. However, there can be still some attenuation of the weather targets present especially if the weather spectrum is very narrow.

Variable width clutter filter is like the fixed width filter with an exception that the algorithm adapts automatically to the width of the clutter. Thus, narrower nominal filter can be used, and the interpolation preserves the overlapped weather better compared to the fixed width filter.

GMAP is a frequency domain approach that uses a Gaussian clutter model to remove ground clutter over a variable number of spectral components that is dependent on the assumed clutter width, signal power, Nyquist interval and number of samples. A Gaussian weather model is then used to iteratively interpolate over the components that have been removed, if any, thus restoring any overlapped weather spectrum with minimal bias caused by the clutter filter. GMAP uses a discrete Fourier transform (DFT) rather than an FFT approach to achieve the highest possible spectrum resolution. The algorithm is first performed with a Hamming window and then, based on the outcome, the Hamming results are kept, or the algorithm is repeated with either the rectangular or Blackman window. This allows the least aggressive spectrum window to be used, depending on the strength of the ground clutter, to minimize the negative impact of more aggressive windows on the variance of the moment estimates. Due to the high level of adaptivity, minimal operator intervention is required to setup the filter.

The GMAP technique is fully implemented and operational in Vaisala RVP signal processor and has been evaluated in comprehensive tests to meet all requirements of the Next Generation Weather Radar network (NEXRAD) in the United States (Siggia and Passarelli, 2004). Detailed info about GMAP algorithm can be found in (Siggia and Passarelli, 2004). GMAP filtering is also the standard method used in Vaisala weather radars operationally.

In this study, ground clutter filtering performance of Vaisala X- and C-band weather radars with solid state power amplifier (SSPA) transmitter and Vaisala RVP signal processing technology is verified. Considering the limitations of measurements with real clutter targets, results show that expected performance can be well achieved. Clutter suppression ratios of over 50dB were measured during this study for both radar types.

2 Measurements

Vaisala WRS series polarimetric weather radars are based on antenna mounted transceiver architecture using separate SSPA transmitters for each polarization and Vaisala RVP signal processing technology. Measurements of this study were performed using WRS400 X-band and WRS300 C-band weather radars, both providing data with high resolution and excellent precision for short and long range meteorological, hydrological and aviation purposes, typically up to 50...150km for WRS400 and up to 150...300km for WRS300, depending on application.

WRS400 X-band radar used under this study is located at the Vaisala headquarters, 12km north of Helsinki and WRS300 C-band at the University of Helsinki campus, 4km north of Helsinki, Finland. Both radars are equipped with Vaisala RVP900 signal processor. High duty cycle and low peak power of the SSPA transmitter encourages to use long transmit pulses to benefit from high sensitivity. These long pulses are compressed for high range resolution using non-linear frequency modulation (NLFM). Blind range caused by the long pulse in the vicinity of the radar is covered by hybrid pulsing technique, where a conventional short pulse with slightly different frequency is transmitted right after the long one and data streams of these separated pulses are combined in the signal processor to form a single measurement file.

Main specifications of both radars are listed in Table 1. Most relevant specification related to this study is the phase stability and the table shows the corresponding theoretical clutter suppression CS [dB], computed directly from the phase stability, or phase noise PN [°] as

$$CS = -20 \log_{10} \left(\frac{PN}{180^\circ} \pi \right). \quad (1)$$

Table 1: Main specifications of the Vaisala WRS weather radars. WRS400 used in this study was equipped with 2.4m antenna and 400W transmitter, whereas WRS300 was equipped with 4000W transmitter option.

Parameter	Unit	WRS400	WRS300
Frequency	MHz	9300...9700	5500...5700
Transmit peak power	W	> 400	> 4000
Phase noise PN	°	< 0.5	< 0.1
Clutter suppression CS	dB	> 41	> 55
Antenna			
Diameter	m	2.4	4.5
Gain	dBi	> 45	> 45
Beamwidth	°	< 1	< 1
Typical calibration reflectivity at 1km			
Pulse width 90μs (compressed to 1μs)	dBZ	-42.0	-47.8
Pulse width 44μs (compressed to 0.5μs)		-35.9	-41.7

Clutter suppression capability was studied using two types of measurements. First, the actual phase noise of the radar system was verified by pointing the antenna towards a distinguishable fixed ground target and checking the obtained phase noise computed by the RVP signal processor. Doppler spectrum was measured using 256 radar pulses and 8 consecutive spectrums were averaged for the result.

Hybrid pulsing of 44μs + 1μs was used, but as the targets were selected around 10km range from the radars, only the data stream from the 1μs conventional pulse was used. Short range and short pulse ensured that the echo signal was strong enough and that width and length of the contributing volume was as small as practicable to minimize possible interfering targets in the same volume. Measurements were performed on 5th February 2021 for the WRS400 and on 14th December 2023 for the WRS300.

Second measurement was to verify the actual clutter suppression and performance of the GMAP Doppler filter by using radar scans introduced in Table 2. For WRS400, the data was collected on 11th April 2021 by measuring a clutter target embedded in mild to moderate precipitation. For WRS300, measurements were performed on 28th August 2023 from clutter target embedded in moderate precipitation. Totally 120 volume measurement files were collected for the WRS400 and 97 files for the WRS300.

WRS400 used 44μs NLFM pulse only, compressed to 0.5μs, whereas WRS300 used 90μs + 4μs hybrid pulsing with long pulse compressed to 1μs. However, in this study, the clutter target was located far enough from the radar so that only data from the long pulse region was used for analysis. Data from the lowest available elevation angle of 0.5° of the volume scans were used for both radars.

Table 2: Scan configurations used in this study for WRS400 and WRS300 weather radars.

Parameter	Unit	WRS400	WRS300
Scan name		VOL-GMAP	VOL-02
Pulse width	μs	44	90 + 4 (hybrid)
Range resolution	m	75	150
Pulse repetition frequency	Hz	1000	
Number of samples		32	
Elevation angle	°	0.5	

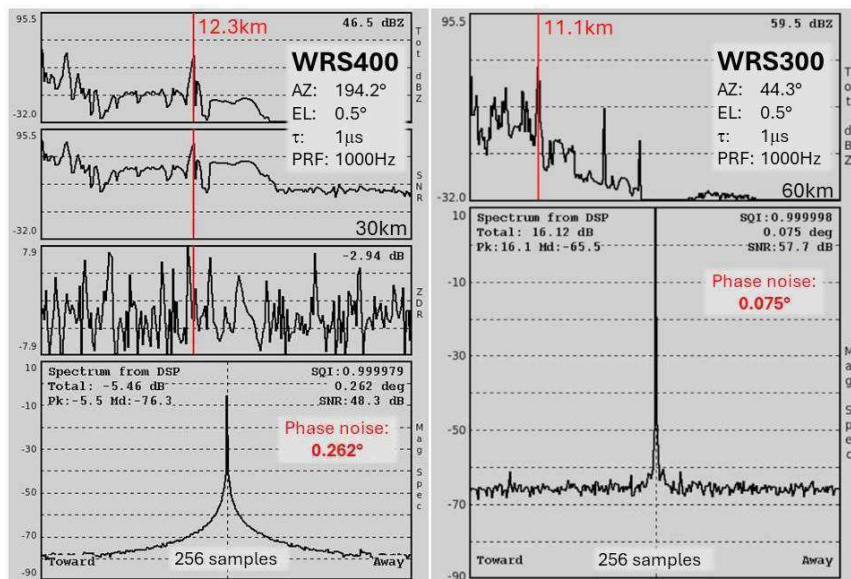
3 Methods and Results

3.1 Verifying phase noise with fixed ground targets

Ascope utility of the Vaisala weather radar software was used to display the data measured from the fixed ground targets, which were high concrete buildings for both radars. RVP signal processor computes the phase noise PN from signal quality index SQI as

$$PN = \frac{180}{\pi} \sqrt{-\ln(SQI)}, \quad (2)$$

where SQI is the normalized magnitude of the autocorrelation at lag 1 and varies between 0 for an uncorrelated signal (white noise) to 1 for a noise free signal with spectral width of zero (pure tone). Ascope utility plots the Doppler spectrum and displays the computed phase noise PN and other related parameters directly in real time. Figure 1 shows results of the measurements from both WRS400 and WRS300 radars.


Figure 1: Screenshots of the phase noise measurements from fixed ground targets using the Ascope utility software. WRS400 radar (5th February 2021) on the left and WRS300 (14th December 2023) on the right.

As can be seen, both radars clearly fulfill the phase noise specification listed in Table 1. Using equation (1), the corresponding clutter suppression is 46.8dB for WRS400 and 57.7dB for WRS300.

3.2 Identifying clutter points from radar images

Vaisala IRIS Focus software provides a large set of tools for viewing and analyzing the weather radar data and it was used to identify clutter targets for this study. Potential clutter targets can be identified by looking at total reflectivity data moment T , which is reflectivity before any clutter filtering is applied. Clutter points appear as considerably high individual T values on the IRIS Focus map view. In this study, we concentrated on immobile ground clutter targets. Therefore, the high total reflectivity value should always appear in the same location and at approximately constant magnitude. When the GMAP clutter

filter works as intended, filtered reflectivity Z from the clutter target location should have same magnitude with the surrounding part of the measurement volume.

By this simple method, two ground clutter target locations were chosen for further analysis. For the WRS400 radar, a chimney of Myllypuro heating plant constructed from concrete at 13km range south-east of the radar site was selected, whereas for the WRS300, a radio mast with steel lattice structure in Porkkala region, 38km south-west from the radar was used.

Figures 2 and 3 show these clutter targets displayed by IRIS Focus software. Myllypuro heating plant shows up as 55.5dB clutter echo in T data moment measured by WRS400. The corresponding filtered reflectivity Z is 6.1dB in this individual measurement, which is well in line with surrounding weak weather echoes from light rain. The radio mast in Porkkala shows up as 53.8dB clutter echo in T data moment measured by the WRS300. The corresponding filtered reflectivity Z is 33.2dB, which is also in line with the surrounding weather echoes from moderate rain.

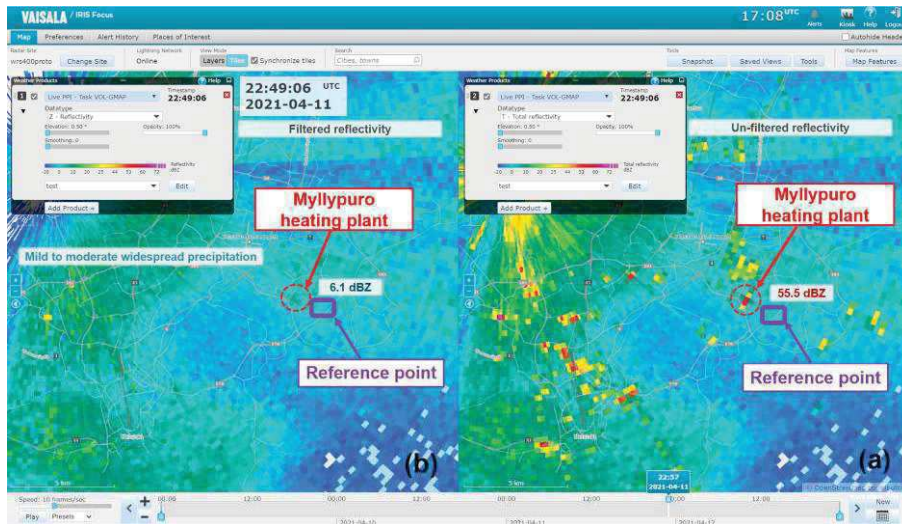


Figure 2: PPI plots of the WRS400 radar from April 11th 2021 showing the unfiltered reflectivity T on the right (a) and the filtered reflectivity Z after GMAP processing on the left (b).

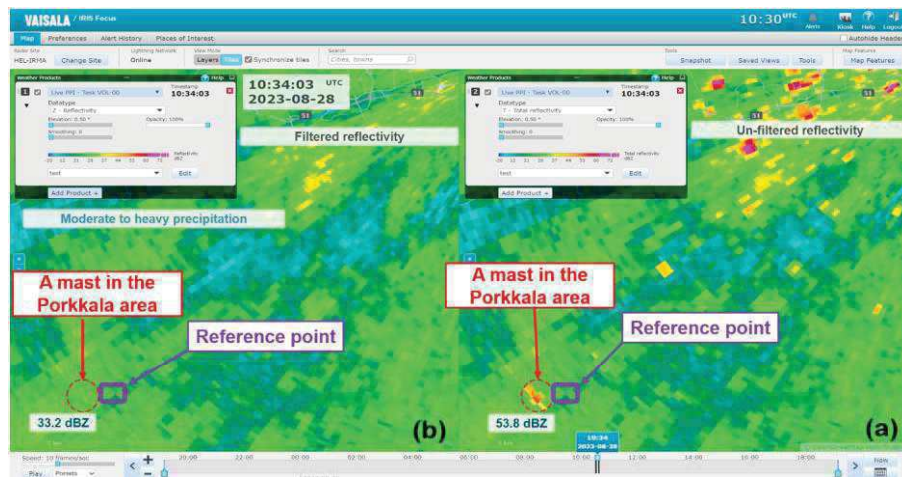


Figure 3: PPI plots of the WRS300 radar from August 28th 2023 showing the unfiltered reflectivity T on the right (a) and the filtered reflectivity Z after GMAP processing on the left (b).

3.3 Time series analysis of clutter points

The performance of the GMAP clutter filter was analyzed quantitatively using time series of the reflectivity data from the identified ground clutter targets. The time series data was composed by collecting the values of the unfiltered reflectivity T and the filtered reflectivity Z from the clutter target location from multiple consecutive radar measurements using the scan configurations specified in Table 2. Same data was also collected from a location that does not have clutter source but is located near the ground clutter target, see reference points in Figures 2 and 3. This enables analyzing if the weather echoes are preserved by the clutter filter.

The unfiltered total reflectivity of the clutter targets was high, approximately 50dB, depending on the target. The filtered reflectivity should follow the surrounding weather conditions implied by the nearby reference point with no clutter. Subtracting the filtered reflectivity Z from the unfiltered reflectivity T gives the clutter suppression. The time series are shown in Figures 4 and 5.

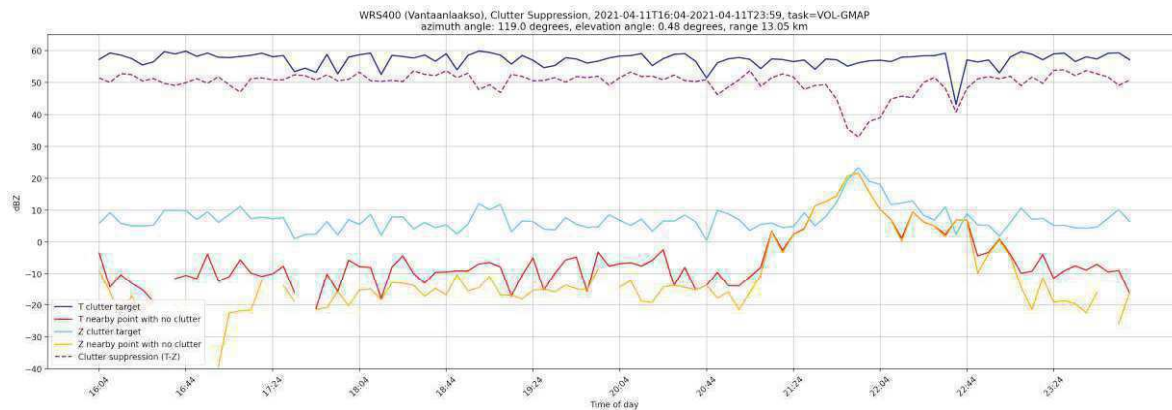


Figure 4: Time series data of the unfiltered (T) and filtered (Z) reflectivity data measured with WRS400 radar on 11th April 2021 from Myllypuro heating plant and from the reference location with no clutter present. Clutter suppression is plotted with dashed line and has maximum value of 54.0dB.

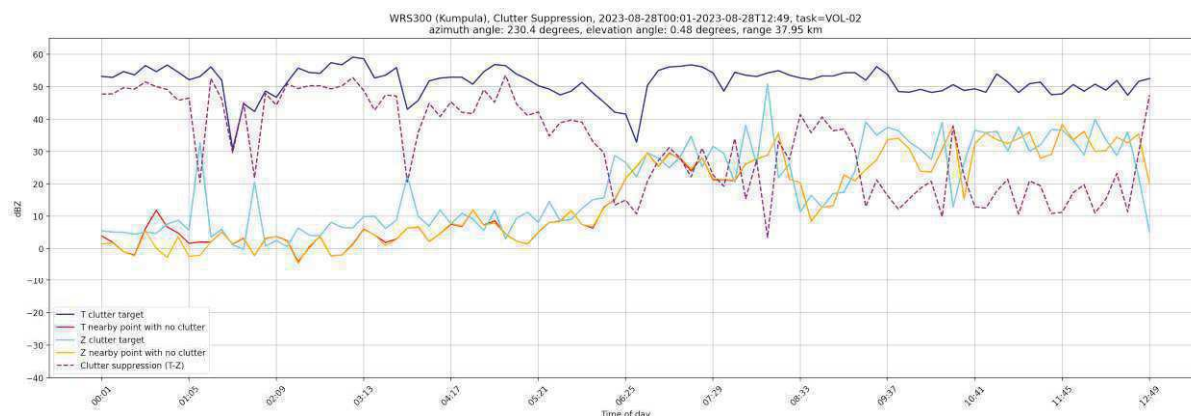


Figure 5: Time series data of the unfiltered (T) and filtered (Z) reflectivity data measured with WRS300 radar on 28th August 2023 from the radio mast in Porkkala and from the reference location with no clutter present. Clutter suppression is plotted with dashed line and has maximum value of 53.5dB.

Figures 4 and 5 show that both WRS400 and WRS300 radars consistently reaches clutter suppression values of better than 50dB with the GMAP clutter filter. The maximum suppression values obtained from these time series are 54.0dB for the WRS400 and 53.5dB for the WRS300. Looking at the last half of both time series with some weather present, as indicated by the increased reflectivity, the curve of the filtered reflectivity Z follows the reflectivity measured from the reference location. This implies that the GMAP processing is not filtering out overlapping weather from the clutter location too aggressively.

The obtained clutter suppression value for the WRS400 radar fulfills the specification of Table 1 very well, being occasionally even better. However, the corresponding value for the WRS300 is slightly less than specified. This is likely caused by the measured clutter target being a mast, rather than a concrete chimney. Furthermore, the distance to the WRS300 target was significantly longer, making the echo signal weaker, contributing volume wider for possible interfering targets and finally, allowing slightly longer time for the radar's local oscillator to drift while waiting for the echo signal.

4 Summary

Results of this study show that both WRS400 X-band and WRS300 C-band SSPA weather radars achieve their phase noise specifications very well when measuring a fixed ground target around 10km range. Measured phase noise values correspond to clutter suppression of 46.8dB and 57.7dB for WRS400 and WRS300 respectively. Time series analysis show that both systems can consistently reach clutter suppression of better than 50dB with the GMAP algorithm. With WRS400, this is even better than what is expected with respect to the phase noise measurements. For WRS300, the result is still good, considering the longer range and lower quality of the available target. It was also verified that the GMAP clutter filter algorithm can preserve the meteorological echoes without suppressing them significantly.

5 References

- Nguyen, C. M., and V. Chandrasekar, 2013. "Gaussian Model Adaptive Processing in Time Domain (GMAP-TD) for Weather Radars." *J. Atmos. Oceanic Technol.*, 30, 2571–2584, <https://doi.org/10.1175/JTECH-D-12-00215.1>.
- Siggia, A.D., and R.E. Passarelli, 2004. "Gaussian model adaptive processing (GMAP) for improved ground clutter cancellation and moment calculation." In proceedings of the Third European Conference on Radar Meteorology (ERAD) together with the COST 717 Final Seminar. Visby, Island of Gotland, Sweden, 6-10 September 2004; p.67-73

Comparing the sensitivity of weather radars with conventional magnetron and modern solid state power amplifier transmitter technologies

Pekka Puhakka, Jere Mäkinen, Marjan Marbouti

Vaisala Oyj, Finland



Marjan Marbouti

1 Introduction

Minimum detectable weather signal, or sensitivity, is one of the key parameters when estimating the basic performance of any weather radar system. It describes how weak target can be detected by the radar at a certain range, or it can be used to solve the maximum range of detection for weather target having certain intensity.

Detected signal at the radar receiver is a combination of echo signal and thermal noise, both varying significantly from sample to sample. For this reason, threshold value for the signal to noise ratio (*SNR*) required for weather detection must be used. This value depends on the expected fluctuations of the echo signal, signal processing techniques used as well as false alarm rate (*FAR*) and probability of detection (*POD*) accepted. In the literature, there are theoretically computed values available for *SNR* required for different kind of fluctuations, *FAR*, *POD* and number of radar pulses averaged.

In this study, the sensitivity of X- and C-band compact weather radars with antenna mounted transceiver and solid-state power amplifier (SSPA) transmitters are compared with a conventional C-band system using a magnetron transmitter. Radars under study are Vaisala WRM200 (C-band magnetron), WRS300 (C-band SSPA) and WRS400 (X-band SSPA).

Sensitivities are first estimated using the conventional weather radar equation with typical parameter values of each radar type, and the theoretical value of the *SNR* required from the literature. Finally, the actual performance of the installed radar systems is verified by analysis with real weather data.

2 Theoretical background

Several factors affect the minimum detectable weather signal of a weather radar. This includes factors that are independent of the radar system design, such as propagational effects of the atmosphere. However, when comparing the performance of different radar types, the most relevant factors are those defined by the technical properties of the radar itself, such as system attenuations, signal processing methods used and characteristics of the transmitter, receiver, and the antenna.

With the conventional weather radar equation, these factors can be used to calculate the power of the received echo signal from a target of known intensity. However, as weather target consists of distribution of moving scatterers, the echo intensity varies significantly from pulse to pulse. At the same time the receiver also detects thermal noise with varying amplitude. For this reason, detected signal must be threshold so that data points with weak echo signals are mostly kept, while most of the data points with noise will be removed.

Amount of remaining noise after threshold is quantified with *FAR*, which describes how often in average the noise power is high enough to pass the threshold. Number of weak echoes passing the threshold is quantified with *POD*. The threshold value is called *SNR* required for detection (also known as detectability factor). Fluctuations of both echo and noise signals can be reduced by averaging many radar pulses for a single data point. This consequently reduces the *SNR* required for detection but increases the time for the radar scan to complete.

In the literature, there are theoretically computed graphs available for the dependence between the *FAR*, number of samples and the *SNR* required. Separate graphs are typically available for targets with different kind of expected fluctuations and different *POD*. For example, if assuming fluctuation according to Swerling case 1, averaging 40 pulses and allowing *FAR* = 10^{-4} and *POD* = 50%, the resulting *SNR* required according to Skolnik (1990) is 0dB. This can be considered a typical value for a modern polarimetric weather radar system considering constraints, such as time available for an operational scan.

When the *SNR* required is known, then corresponding minimum radar reflectivity factor z_{min} for a target with range r can be solved from the conventional weather radar equation as

$$z_{min} = \frac{1024 \ln(2)}{c \pi^3 |K|^2} \left(\frac{s}{n} \right)_{min} \frac{\lambda^2 r^2 n' b}{p_t \tau g_f g_t g_e^2 \theta^2 g_r} a r, \quad (1)$$

where c is the speed of light, K is the dielectric constant of liquid water ($|K|^2 = 0.93$) and a is the 2-way specific attenuation of air, value defined according to International Organization for Standardization, ISO (2019). The ratio inside the parenthesis is the SNR required for detection, s being the echo signal and n the noise power.

Other parameters of equation (1) are related to the radar system. λ is the wavelength used, n' is the spectral noise and b the noise equivalent bandwidth of the receiver signal processor. p_t is the transmit peak power and when multiplied by the pulse length τ , it yields to transmit pulse energy. Attenuation g_f considers the pulse energy that is lost in digital filtering of the signal processor, whereas attenuations g_t and g_r accounts for waveguide losses in transmit and receive respectively. g_e and θ are the antenna gain and beamwidth values respectively. Relation of these parameters with respect to the block diagrams of the radar systems under study are illustrated in Figure 1.

SNR required for detection can be further reduced by using advanced signal processing methods, such as Vaisala enhanced reflectivity algorithm, which utilizes coherent averages of the echo signals from both the horizontal and vertical channels of the weather radar. In case of 40 averaged pulses, the SNR required reduces approximately by 3 dB according to Keränen (2014). Furthermore, the actual FAR can be reduced up to two orders of magnitude by utilizing speckle filtering, where isolated pixels of detected signals are removed from the data.

3 Weather radars under study

This study verifies the sensitivity of three different weather radar types, which are Vaisala WRM200 with conventional C-band magnetron transmitter, WRS300 with C-band SSPA transmitter and WRS400 with X-band SSPA transmitter. Latter two utilizes compact antenna mounted transceiver architecture, whereas the WRM200 has the transceiver cabinet located in a separate equipment room. WRM200 and WRS300 operate in frequency range of 5.5...5.7GHz, whereas WRS400 operates in range of 9.3...9.7GHz. All radars are polarimetric and uses parabolic center fed antenna reflector.

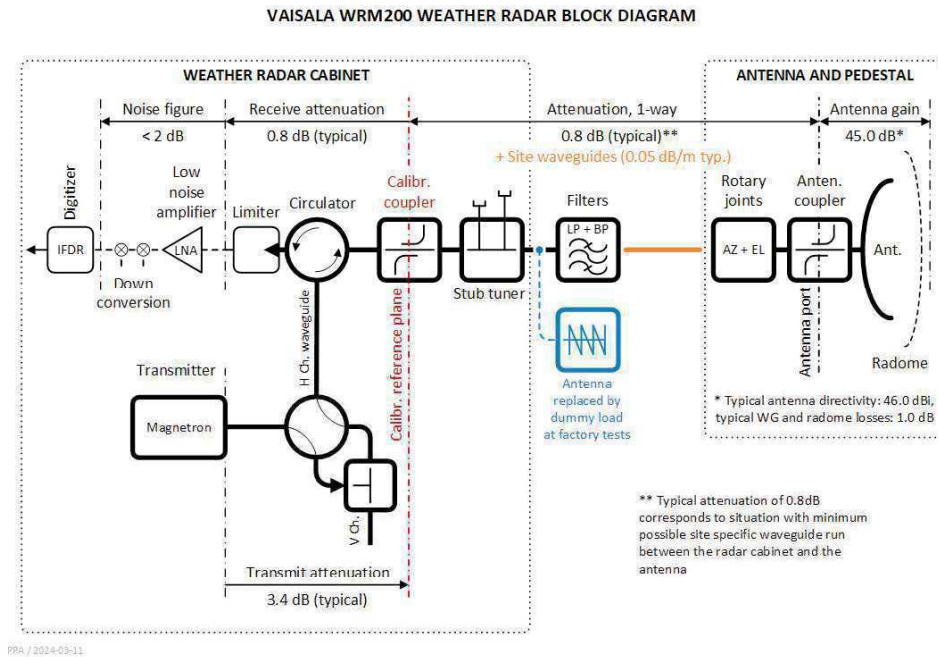
WRM200 system used in this study is equipped with Vaisala RVP10 signal processor and a magnetron transmitter with maximum duty cycle of 0.12% and pulse width range of 0.5...3.0 μ s. Transmit output is divided between horizontal and vertical polarizations in simultaneous transmission and receive mode (STAR) for polarimetric measurements. WRS300 and WRS400 systems are equipped with RVP900 processor, and each polarization has a dedicated SSPA transmitter with maximum duty cycle of 10% and pulse width range of 0.5...90.0 μ s. Typical values of all relevant parameters with respect to the sensitivity of each radar type are listed in Table 1 and block diagrams in Figure 1 illustrates the main components.

High duty cycle and low peak power of the SSPA transmitter encourages to use long transmit pulses to benefit from high sensitivity. These long pulses are compressed for high range resolution using non-linear frequency modulation (NLFM). Blind range caused by the long pulse in the vicinity of the radar is covered by hybrid pulsing technique, where a conventional short pulse with slightly different carrier frequency is transmitted right after the long one and data streams of these separated pulses are combined in the signal processor to a single measurement file. To make the sensitivity gap between the long and short pulse regions less pronounced, the signal processor can be configured to blend the data streams of short and long pulses by a configurable linear transition within a transition range.

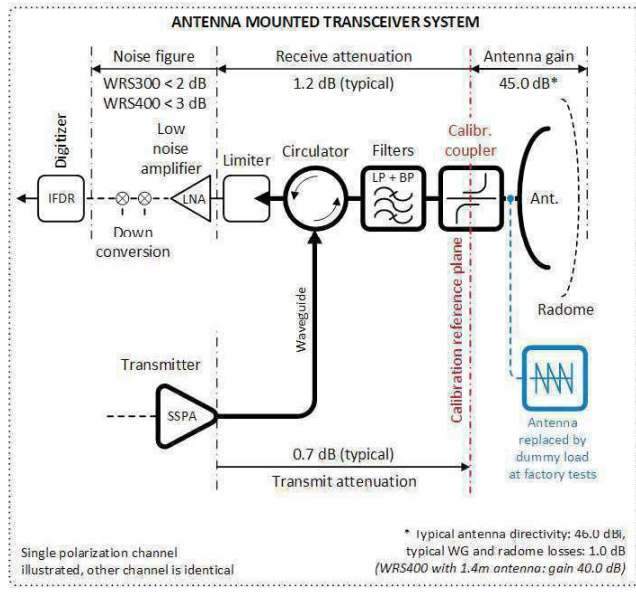
Table 1: Typical values of the radar equation parameters and resulting sensitivity for each radar type under study.

Parameter	WRM200	WRS300 ¹⁾	WRS400 ²⁾
Wavelength λ	5.33cm		3.10cm
Antenna gain g_e	45.0dBi ³⁾	45.0dBi ⁴⁾	
Antenna beamwidth θ	0.95°		
Transmit power p_t	250.0kW ⁵⁾	4.0kW ⁴⁾	400W ⁴⁾
Pulse width τ	2.0 μ s	90.0 μ s	
Digital filter loss g_f	1.2dB	4.5dB	
Transmit loss g_t	4.2dB	-- ⁶⁾	
Receive loss g_r	0.8dB	-- ⁶⁾	
Noise equivalent bandwidth b	0.6MHz	0.4MHz	
Spectral noise ⁷⁾ n'	-111.5dBm/MHz	-112.0dBm/MHz	-111.5dBm/MHz
Typical sensitivity at 100km ⁸⁾	-3.8dBZ	-6.4dBZ	-0.2dBZ

¹⁾ WRS300 with 4kW transmitter option. ²⁾ WRS400 with 400W transmitter and 2.4m antenna options. ³⁾ At antenna port. ⁴⁾ At calibration reference plane. ⁵⁾ At TX output. ⁶⁾ Attenuation of fixed waveguides incl. in antenna gain and transmit power values. ⁷⁾ At calibr. ref. plane, antenna pointing at clear sky. ⁸⁾ Equation (1), SNR required = 0dB, 2-way specific attenuation of air $a = 0.014$ dB/km (C-band), $a = 0.018$ dB/km (X-band).



PPA / 2024-03-11



PPA / 2024-03-22

Figure 1: Calibration block diagrams of WRM200 (top) and WRS300/WRS400 (bottom).

4 Measurements and results

To validate the actual sensitivity, three datasets were collected, one for each radar type. PPI scans were used with low elevation angle and a typical pulse width for a long-range surveillance scan, providing optimal combination of sensitivity and range resolution. WRS300 and WRS400 SSPA radars used hybrid pulsing with blending algorithm, while WRM200 used a conventional pulse. Doppler filtering was used to reduce the ground clutter returns, but other quality thresholding was done only in post processing. Details of the scan configurations are listed in Table 2.

Collected data was visualized by plotting cumulated distributions of measured radar reflectivity as a function of range, see Figures 2...4. Data was post-processed with signal quality index (*SQI*) threshold of 0.4 and *RhoHV* threshold of 0.85. *SQI* describes the coherency between transmit and receive pulse with value range of 0...1 (from non-coherent to fully coherent). It was used to remove most of the noise and possible 2nd trip echoes. *RhoHV* is the correlation coefficient between horizontal and vertical echo signals and was used to filter out noise and non-meteorological targets.

Results show that for each radar system, the distribution clearly goes below the typical sensitivity of the radar type in question, plotted with a black dark curve in the figures. This confirms that the actual sensitivity is as expected according to

equation (1) with *SNR* required of 0dB. This is the case for WRS300 and WRS400 also, even though the data was measured with 32 pulses only, which according to Skolnik (1990) would correspond to 0.5...1.0dB higher *SNR* required for detection.

The actual *FAR* with the used scan settings was studied for WRM200 and WRS300 by a separate set of measurements with the transmitter turned off to measure noise only. Scan configurations were as in Table 2 with the exception that 40 samples were averaged for both radars and elevation of 10° and suitable azimuth sector was selected to avoid interfering signals and excess noise from ground and obstacles. Data set for each radar contained of order of 10⁶ or more range gates in total. These noise data files were then filtered with *SNR* threshold of 0dB and corresponding *FAR* was calculated as a ratio of number of noise data points left divided by the number of original range gates in total and the resulting *FAR* was 10^{-3.5}, which is close to but slightly more than the assumed 10⁻⁴ according to Skolnik (1990).

The improvement of the sensitivity by the Vaisala enhanced reflectivity algorithm has been verified earlier for the WRM200 in Keränen (2014) and recently for the WRS400, showing an improvement of 2.8dB with 32 averaged pulses according to Puhakka (2023).

Table 2: Information about the scan configurations, radar sites and the datasets used.

Parameter	WRM200 ¹⁾	WRS300 ²⁾	WRS400 ³⁾
Pulse width	2.0µs	90.0µs (compressed to 1.0µs) + 4.0µs hybrid	
Range gate length	300m	150m	
Range gate width	1°		
Pulse repetition frequency	500Hz	1000Hz	
Number of samples	40	32	
Scanning speed	12.5°/s	15.6°/s	31.3°/s
Elevation angle	0.5°	1.0°	
System calibration date	2023-11-13	2023-04-26	2023-10-19
Actual sensitivity at 100km	-4.4dBZ	-6.3dBZ	-0.4dBZ
Measurement date	2024-02-13	2023-11-06	2023-11-04
Number of scans measured	97	75	112

¹⁾ WRM200 site 26km north-northeast of Helsinki, Finland. ²⁾ WRS300 site 4km north-northeast of Helsinki and equipped with 4kW transmitter option.
³⁾ WRS400 site 12km north-northwest of Helsinki, Finland and equipped with 400W transmitter and 2.4m antenna options.

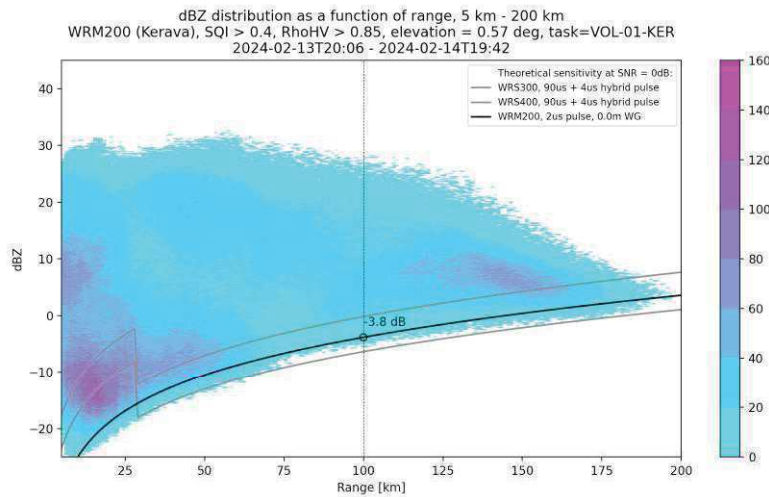


Figure 2: Cumulated distributions of the measured radar reflectivity as a function of range for WRM200.

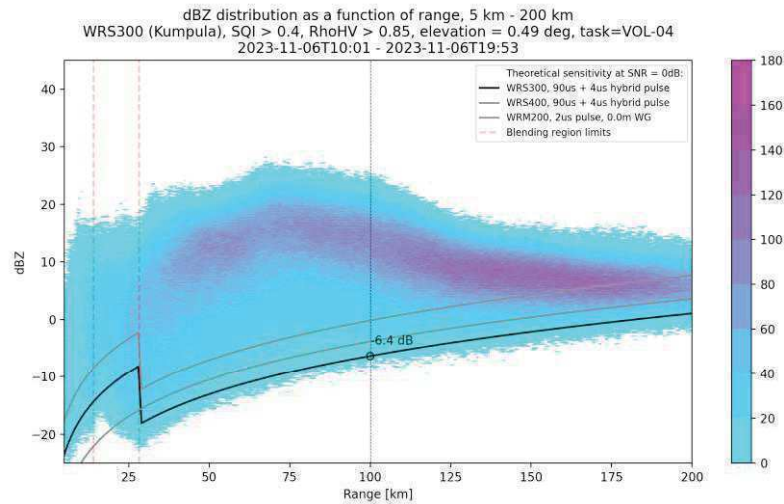


Figure 3: Cumulated distributions of the measured radar reflectivity as a function of range for WRS300.

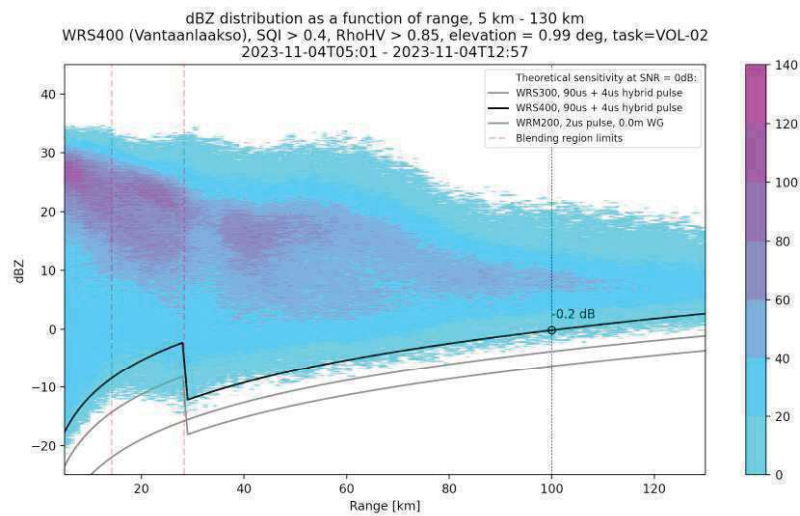


Figure 4: Cumulated distribution of the measured radar reflectivity as a function of range for WRS400.

5 Conclusions and discussion

This study verifies that the installed WRM200, WRS300 and WRS400 weather radar systems achieve well the theoretically estimated sensitivity, even though the observed *FAR* due to noise was slightly more than what was expected in the literature. Considering the C-band radars, the minimum detectable weather signal of -6.4dBZ at 100km range for the WRS300 SSPA system is 2...3dB better compared to the conventional WRM200 magnetron system. This is due to the compact antenna mounted architecture with significantly reduced waveguide runs and successfully utilized high duty cycle of the SSPA transmitter to improve the transmit pulse energy. With NLFM pulse compression techniques, this improvement of the sensitivity is achieved with spatial resolution of 150m, being only half of the 300m used with the conventional magnetron transmitter. The sensitivity of the WRS400 X-band SSPA radar is approximately 6 dB less compared to the WRS300 C-band alternative, which is expected as the X-band system has been designed for short range measurements and thus, with significantly lower transmit power and furthermore, with slightly higher noise figure of the receiver.

6 References

- ISO, International Organization for Standardization, 2019: Meteorology – Weather radar – Part 1: System performance and operation (ISO standard 19926-1:2019), Ch. 6., table 5.
- Keränen, R., Chandrasekar, V., 2014: Detection and Estimation of Radar Reflectivity from Weak Echo of Precipitation in Dual-Polarized Weather Radars, *J. Atmos. Oceanic Technol.*, 31, 1677 – 1693, figure 3.
- Skolnik, M., 1990: Radar Handbook, 2nd edition, Mc Graw-Hill, 2.1 – 2.68., figure 2.6.
- Puhakka, P., Marbouti, M. and Mäkinen, J., 2023: Defining and validating the minimum detectable weather signal for an X-band weather radar system, 40th AMS Radar Meteorology conference.

A Physics-Informed Machine-Learning Algorithm to Recover corrupted or blanked Data in Weather Radar Velocity Measurements

C. Schiefer ¹, S. Kauczok ¹, A. Töws ¹, F. Gekat ¹, A. Weipert ¹, P. Wilhelm ², M. Eggert ²

¹Leonardo Germany GmbH Raiffeisenstrasse 10, 41470 Neuss, Germany

²Physikalisch-Technische Bundesanstalt (PTB), Bundesallee 100, 38116 Braunschweig, Germany



Christian Schiefer

1 Introduction

Weather radars are valuable tools for meteorological and hydrological applications due to their ability to measure precipitation and wind. However, blockages in the measurements often occur at low elevation angles caused by high buildings, vegetation or mountains. In addition to these blockages, WiFi signals or wind turbines can also disturb the measurements and affected range gates or even whole sectors might be lost. Furthermore, due to the local nature of rain, plan position indicator (PPI) measurements are generally not homogeneously filled along the entire range, which naturally causes a fragmented data distribution. It is desirable to close all these types of data gaps in order to maximize data availability and to increase the overall situational awareness. For example, these data gaps can have a negative impact on meteorological data products like wind shear at airports or for data assimilation into NWP models.

Physics-Informed Neural Networks (PINN) is a research field in which neural networks are trained to solve partial differential equations (PDE) that describe physical phenomena. The PINN method presented in this paper applies the Navier-Stokes equations (NSE) as the underlying PDE to reconstruct 3D wind fields by taking the radar radial velocity measurement data as boundary conditions into account. This approach offers the possibility to fill data gaps in radial velocity PPI (V-PPI) measurements.

In this contribution, examples of the reconstruction of disturbed or incomplete weather radar PPI's of radial velocity measurements are demonstrated. Statistical results on more than 900 radar measurements showed that 10 degrees azimuthal sectors could be reconstructed with an absolute error of 2 m/s in 97% of all cases. This result is in good agreement with a Doppler lidar measurement campaign in which almost one year of data was analyzed. Doppler lidars as the "clear air" counterpart of weather radars with regard to remote wind measurement were used, because they provide data much more often than radars. Lidar measurement data were also used to evaluate the three velocity components for a 30° reconstructed sectors which showed an absolute error of ~1m/s.

The advantage of PINN in contrast to data-driven ML models is twofold; firstly, the ML decision-making process offers more transparency to the user (white box approach) and secondly, the collection of a theoretically all-encompassing training dataset is not required. With PINN, a neural network is trained from scratch for each new set of measurement data. By using a pre-trained network (Transfer Learning (TL)) or Meta Learning techniques, the training time of PINN can be accelerated to ensure a real-time capability while avoiding demanding hardware requirements. By applying these methods, an acceleration of the PINN algorithm resulted in runtime reduction by a factor of 5 and 107 for TL and Meta Learning, respectively.

2 Methodology

Neural Networks (NN) are usually trained with very large amounts of data. These so-called Deep Learning models have two drawbacks: 1) the decision-making process is incomprehensible for the user (black box), 2) they require a very comprehensive, carefully prepared and labelled training dataset that represents the underlying pattern and contains minimal spurious correlations. Contrary to this, Physics-Informed Machine Learning is a Deep Learning approach for solving differential equations describing physical phenomena using boundary conditions from data. The subject area develops rapidly since the work of Raissi [1] who introduced the PINN data driven approach in 2017.

In contrast to the black box models, PINN presents a transparent (white box) algorithm due to the integrated physical equations. Many acronyms like physics-informed, physics-guided in combination with neural networks (NN), deep learning (DL) or machine learning (ML) exist [2], but all of them relate to a machine learning approach using neural networks to approximate a solution to a differential equation describing a physical phenomenon. In this regard, they present an alternative to the classical methods of integrating these equations in a straightforward manner for specific initial and boundary conditions and can be likened to function fitting rather than numerical integration.

The goal of this contribution is to describe the coupling between the PINN algorithm with weather radar velocity data to reconstruct missing or disturbed sections. In the literature, according to the authors' knowledge, there is no publication dealing with PINN and weather radar velocity data. For wind lidars, Zhang (Zhang & Zhao, 2021), is known for having reported the application of a Physics-informed neural networks with short range wind lidar data [3], [4].

For wind monitoring at an airport, a dedicated weather radar usually performs multiple plan PPI scans under different elevation angles and reports radial velocity within a certain range in a number of range gates per line of sight (LOS). To reconstruct a PPI-sector, only the left and right adjacent radar LOS measurements serve as an input to the PINN algorithm. The architecture of the PINN coupled with weather radar data is shown in Fig. 1. The neural network applied here consists of five hidden layers, each of which features fifteen neurons (in Fig.1 only 3 layers, each accommodates five neurons, are depicted for simplicity). The spatial and temporal domain data in Cartesian coordinates (x, y, z) and time (t) of the blanked sector serve as inputs for the neural network. The output data set consists of the three velocity components U, V and W suggested as a best-fit solution of the NSE, for the given input data. Please note that we use the 3D NSE in Cartesian coordinates for the wind component evaluation shown in section 4.2. However, it is straightforward to transform them or to use the NSE directly in spherical coordinates as we used in section 4.1. An implementation can be found in [5].

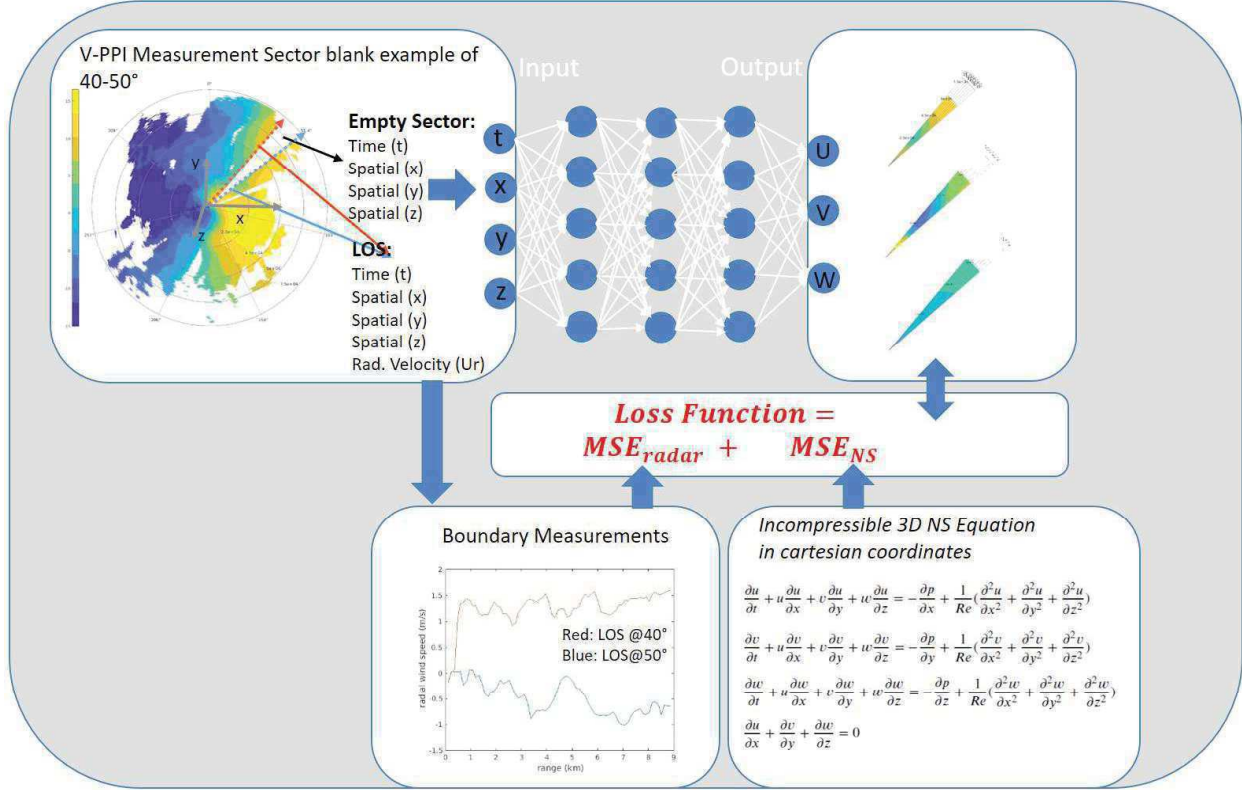


Figure 1: Method of PINN applied to weather radar data (or Doppler lidar data)

The NSE is integrated into the loss function together with the adjacent left and right LOS radar measurements. The non-dimensionalized incompressible Cartesian 3D NSE is depicted in Fig.1.

Here, R_c is the Reynolds number, U, V, W denote the three velocity components. For the calculation, all variables will be non-dimensionalized through selection of appropriate scales for the characteristic length L_c (200 m) and velocity U_c (10 m/s) to $r_i = r/L_c, U_i = U/U_c, t_i = t/(L_c/U_c)$ and $R_c = U_i r_i/\nu$, where ν is the kinematic viscosity of air ($1.5 \cdot 10^{-5} \text{ m}^2/\text{s}$). The characteristic length L_c and velocity U_c were chosen according to the assumptions of meteorological scale analysis [6]. The Rossby number $R_o \sim U/(L_c \cdot f)$ (with $f = 10^{-4} \text{ s}^{-1}$, Coriolis parameter,) needs to be significantly larger than one for non-geostrophic wind (boundary layer phenomena) for which the Coriolis forces can be neglected. To minimize the loss function, the mean squared error (MSE) composed of the lidar data and the residual of the NS equation are calculated in (5).

$$\text{Loss Function} = \text{MSE}_{NS} + \text{MSE}_{Lidar} \quad (1)$$

$$\text{MSE}_{NS} = \frac{1}{N_S} \sum_{i=1}^{N_S} |f_{NS}(x_i^S, y_i^S, z_i^S, t_i^S)|^2 \quad (2)$$

$$\text{MSE}_{Lidar} = \frac{1}{N_{LL}} \sum_{i=1}^{N_{LL}} |(U_i^{LL}(x_i^{LL}, y_i^{LL}, z_i^{LL}, t_i^{LL}) - V_i)|^2 + \frac{1}{N_{LR}} \sum_{i=1}^{N_{LR}} |(U_i^{LR}(x_i^{LR}, y_i^{LR}, z_i^{LR}, t_i^{LR}) - V_i)|^2 \quad (3)$$

This form of loss function follows the approach of Zhang & Zhao [4], where $x_i^S, y_i^S, z_i^S, t_i^S$ are the spatial and temporal data characterizing the PPI sector to be reconstructed by the PINN-algorithm. $x_i^{LL}, y_i^{LL}, z_i^{LL}, t_i^{LL}$ are the spatial and temporal data corresponding to the left and $x_i^{LR}, y_i^{LR}, z_i^{LR}, t_i^{LR}$ for the right lidar beam. U_i^{LR}, U_i^{LL} are the radial velocities corresponding to

the left and right lidar beams where V_i correspond to the radial velocities of the reconstructed domain, i.e. the proposed solution of the NS equation. N_{NS} is the number of range gates inside the reconstructed domain, while N_{LL} , N_{LR} are the respective numbers of range gates in the left and right boundary LOSs. f_{NS} is the residual function modelling the adequacy of the NN output to the NS equation and thereby contributing to the total mean square error assigned (MSE_{NS}). The learnable parameters (weights and biases) within the NN need to be trained by enforcing that for the inputs (x_i^S , y_i^S , z_i^S , t_i^S), the output of the network U_i approximates a solution of the NS equation, while at the same time reproducing the boundary conditions as good as possible. In contrast to NN not constrained by physics, PINN has to be re-trained for every new set of input radar data. Therefore, in order to minimize the loss function recurrently, the training process must be carried out very quickly for real-time applications. To control the training run-time process, two parameters are specified as truncation criteria: The optimization algorithm minimizing the loss function stops, if either a tolerance of 10^{-6} , or a number of 1500 iterations is reached. This leads to a compromise between computation time and accuracy. For the wind field reconstruction algorithm for a weather radar in real-time operation, the PINN algorithm has to work very fast in order to not significantly decrease the radar data update rate.

3 Dataset

Data from two measurement campaigns were used in this contribution. Firstly, high resolution wind measurement data provided by a SKIRON^{3D} 3D scanning Doppler lidar recorded during an almost one-year test bed campaign at Frankfurt airport in 2020 have been used to evaluate the performance of PINN. We focused our investigation on 360° PPIs taken with an azimuthal resolution of 2.5 degrees. The elevation angle was 1.5 degrees and the range resolution was 120 m. For the development of the wind field reconstruction, a sector of 35°, ranging from 70° to 105°, has been cut out. The result of the reconstruction is compared to the measurement.

Secondly, we used selected (with a certain amount of values) V-PPI data from a mobile X-Band (Meteor 50Dx) weather radar, located at Braunschweig in 2015 were chosen to reconstruct a 10 degree sector applying the PINN algorithm. The azimuthal resolution of the radar was 1°, the elevation angle was 0.5°, the range resolution 150 m and the maximum range was 75 km.

Thirdly, a comparative measurement campaign was carried out to characterize the wind measurement capabilities of the Doppler lidar SKIRON^{3D}. The Physikalisch-Technische Bundesanstalt (PTB) in Braunschweig has built a bistatic coherent Doppler lidar capable of measuring all three wind components. For highly accurate optical remote wind measurements traceable to SI units, the PTB developed a wind tunnel with an open volume to calibrate the wind lidar [7]. Due to its high spatial and temporal resolution and low measurement uncertainty, the PTB lidar serves as the reference instrument in these comparative measurements. Both wind measurement systems had been separated by a distance of 1100 m between a site on the PTB campus and the premises of the Deutscher Wetterdienst (DWD). In order to compare the reconstructed velocity components with the PTB lidar, a 30° azimuthal sector was reconstructed by PINN in which the middle LOS coincides with the measured volume of the PTB device. In this LOS the range gate was analyzed which corresponded to the measurement volume of the PTB lidar profiler [8].

4 Performance results

4.1 Reconstruction of radial velocity

In Fig. 2 a V-PPI with data gaps is shown as an example for a fragmented measurement. To analyze the performance of PINN, we divided each V-PPI in 36 sectors, deleted the measured data, reconstructed these sectors and compare the results with the measurements (if any present). Therefore, PINN uses 36 LOS (red dashed lines) as boundary conditions to reconstruct the complete V-PPI. In case of small data gaps inside the boundary LOS, we applied standard interpolation and extrapolation methods. Note, the measurements contained no disturbances but only incomplete PPIs (as can be seen in Fig.2 (left)). However, if disturbances are detected, it is easy to choose an adjacent undisturbed LOS in order to reconstruct the sectors containing corrupted data, because most disturbances (e.g. from wind turbines) occur always at the same positions. Therefore, the localization and reconstruction of the corresponding sectors is manageable.

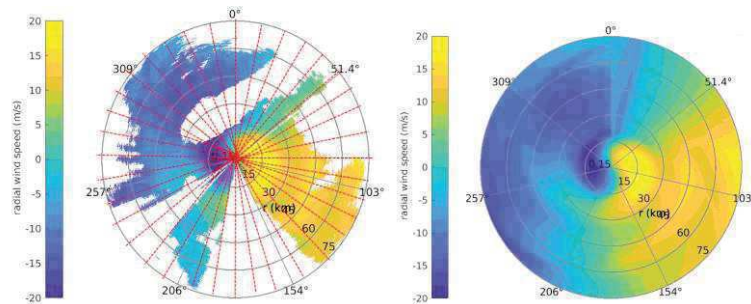


Figure 2: X-Band Radar Example 3°V-PPI, 30/03/2015, 214:20hrs @ Braunschweig; Left: Measurement with boundary LOS (red), right: Reconstructed PPI using PINN

In Fig. 2 (right) the corresponding V-PPI reconstructed using PINN is depicted. To assess the performance of the PINN algorithm, samples of more than 900 cases were selected where a V-PPI contained at least 60% of data. The reconstructed radial velocities V_r have been evaluated by the absolute errors (ABE) of their differences to the actual measurements on a range gate basis:

$$ABE = V_r(\text{reconstructed}) - V_r(\text{measured}) \quad (4)$$

As described in the introduction, PINN must be retrained with every new set of boundary LOS. To accelerate PINN, two techniques, Transfer Learning (TL) and Meta Learning [9], were investigated. TL is a machine learning technique that uses a previously trained model for a specific purpose as the starting point for a new, yet related model. This approach means that what has already been learnt from a trained network can be re-used for a new project. Meta Learning is a class of machine learning methods aiming to quickly adapt a learning model to new tasks. To this end, machine learning typically extracts important meta-information, such as the initial values of model parameters and other hyperparameters, from a set of training tasks that are correlated with new, unseen tasks. Both techniques eliminate computationally intensive and time-consuming activities required for training a new neural network from scratch. Fig. 3 shows the fitting curves of the histogram distributions for the ABE (left) and the run-time (right). The results show that PINN has an error of approx. 2 m/s in 97% of cases. By using Meta and TL methods, this error increases, whereas the Meta method performs better than the TL method. However, the run-time accelerations are enormous; if PINN still requires approx. 15 min on average, the use of TL and Meta reduced it to 2.94 min and 0.14 min respectively.

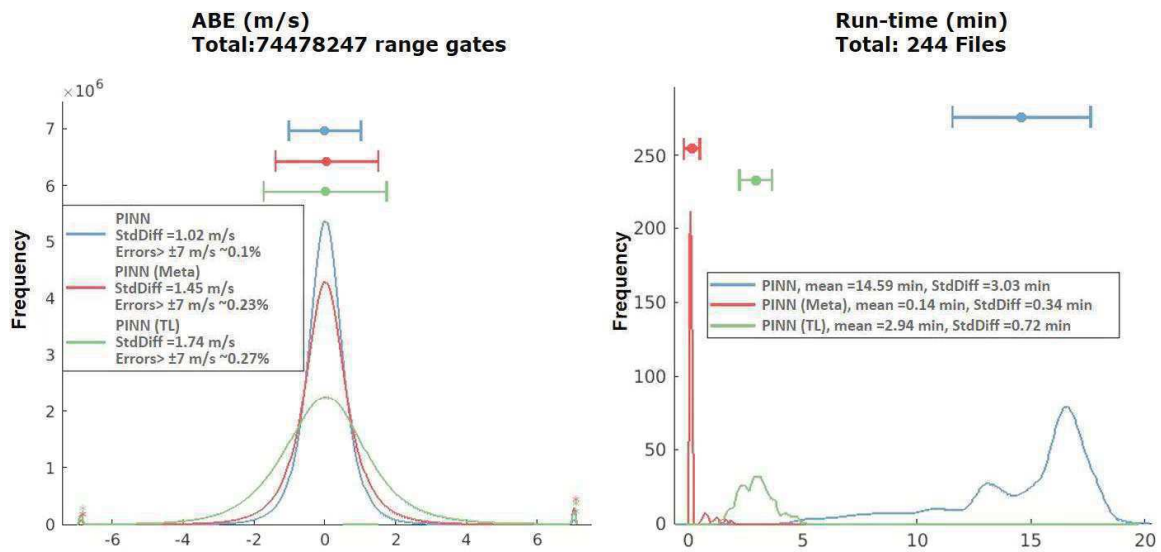


Figure 3: Fitting curve of the histogram distribution of the ABE calculated for almost 7.5 Mio range gate (left) and the calculation time (right) for PINN algorithm (blue curves), for PINN algorithm with Meta Learning (red curves) and Transfer Learning (green curves) techniques.

4.2 Comparison with Doppler lidar data and evaluation of 3D wind components

4.2.1 Comparison with Doppler lidar data

The PINN algorithm was originally tested on Doppler lidar (DL) data, because of the high data availability. Fig. 4 (left) shows the ABE between measurement and reconstruction for almost one year of measurement data for a 35° azimuthal single sector. In contrast to the radar use case in section 4.1, the azimuth angle is larger because of the smaller operational range.

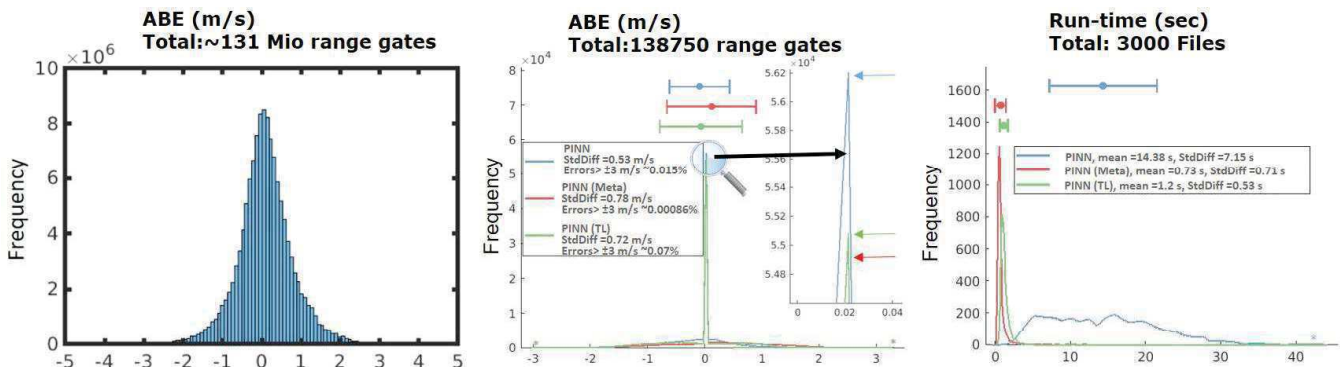


Figure 4: Histogram of the ABE (left). Fitting curve of the histogram distribution of the absolute error (middle) and the calculation time (right). Using PINN (blue curve), PINN with Meta Learning (red curve) and PINN with TL (green curve) calculated for subset of cases.

4.2.2 Evaluation of the 3D wind components

In 2024, comparative measurements were carried out between PTB's bistatic wind lidar as a reference instrument and LEONARDO's SKIRON^{3D} scanning wind lidar. Both systems were located 1100 m apart and aligned to capture the same measurement volume. For the time-averaged comparison of vectors, the NS equations in Cartesian coordinates were used to determine time-averaged velocity vector fields. For the analysis, PINN reconstructs an empty sector of 30° where the LOS in the middle corresponds exactly to the overlapping measurement volumes of the PTB lidar. Fig. 5 shows the time series comparison between the V-component (left), the U-component (middle) and the W-component (right) between the PTB measurements and the reconstruction PINN algorithm for the overlapping range gate for almost one week. The result shows that the U and the V component are reconstructed with an acceptable absolute error of ~1 m/s whereas the W-component shows a larger discrepancy of 1.38 m/s.

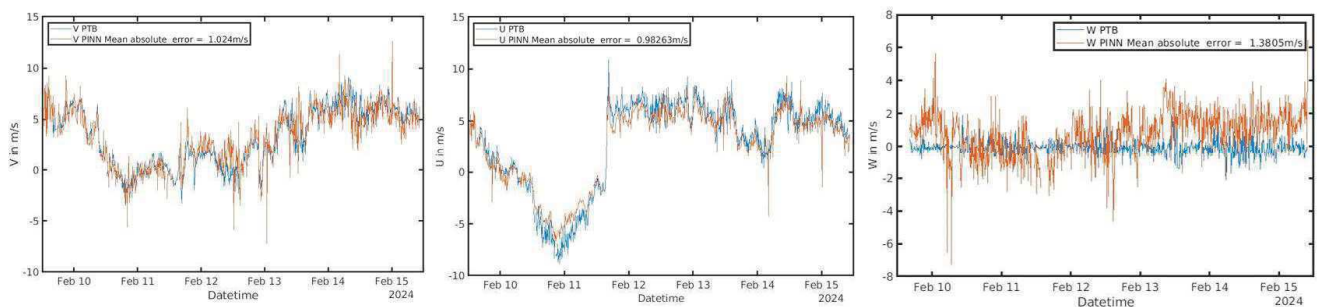


Figure 5: Time series plot of the U, V and W wind components. Blue curve PTB lidar, red reconstructed by PINN.

5 Conclusions & Future research

In this publication, a physics-informed machine learning algorithm has been used to reconstruct data gaps of wind fields measured by an X-Band weather radar and a 3D scanning Doppler lidar. The results show that the reconstruction of 10° azimuth sectors for the radar with an operational range of 75 km and of 35° azimuth sectors for the lidar with a range up to 15 km features absolute errors of less than ± 2 m/s in 97% and 98%, respectively, of all cases. There are differences in absolute error and runtime between lidar and radar data when applying Meta and Transfer Learning techniques to achieve real-time performance. For radar, the error increases significantly when using TL, whereas TL has only a marginal impact on the accuracy of the reconstruction results for the lidar. The acceleration factor for the run-time showed a significantly higher value (factor 107) for radar than for lidar (factor 20) when applying the Meta learning method, whereas the TL method showed an equal acceleration of a factor of five for both. This needs to be investigated in the future. However, applying the Meta learning method on radar data could achieve real time processing (by using ordinary hardware like an Intel Xeon 3,8 GHz processor with a single CPU).

PINN offers the possibility to reconstruct the full wind vector by taking only the radial velocity as boundary conditions into account. For reconstructing the velocity components, PINN showed an absolute error of 1 m/s for the U and V components compared to the reference device, which seems to be acceptable for most applications, especially by considering that no data is available in these sectors. However, the W component showed a larger absolute error and highly fluctuates over time. This behavior and the higher absolute error caused by applying Transfer Learning on radar data will be investigated in the future. Another future task is the analysis of the reconstruction performance of larger azimuthal sectors.

6 References

- [1] Reference I M. Raissi, P. Perdikaris, and G.E. Karniadakis, "Physics Informed Deep Learning (Part I): Data-Driven Solutions of Nonlinear Partial Differential Equations", 2017. arXiv: 1711.10566." 28 11 2017.E. P. Wigner, "Theory of traveling-wave optical laser," *Phys. Rev.*, vol. 134, pp. A635–A646, Dec. 1965.
- [2] P. Ni, L. Sun, J. Yang, Y. Li, "Multi_End Physic-Informed Deep Learning for Seismic Response Estimation." *Sensor* 12 05 2022: 3697.
- [3] J. Zhang, X. Zhao, "Spatiotemporal wind field prediction based on physic-informed deep learning and lidar measurements." *Applied Energy* 288, 116641 02 2021.
- [4] J. Zhang, X. Zhao, "Three-dimensional spatiotemporal wind field reconstruction based on physic-informed deep learning." *Applied Energy*, Elsevier, vol. 300, 117390 2021.
- [5] Bringi, V. N., Mishra, K. V., & Thurai, M. (2024). Advances in weather radar. In *Emerging applications* (Vol. 3, pp. 1-378) <https://doi.org/10.1049/SBRA557H>
- [6] R. K. Smith, "Lectures on Dynamical Meteorology." Ludwig-Maximilians-University of Munich 16 June 2014.
- [7] Oertel, S., Eggert, M., Gutsmuths, C., Wilhelm, P., Müller, H., and Többen, H., "Validation of threecomponent wind lidar sensor for traceable highly resolved wind vector measurements", *J. Sens. Sens. Syst.*, 8, 9–17, 2019.
- [8] S. Kauczok et al.: Accuracy of a Scanning Pulsed Coherent Wind Lidar Determined by Comparing With a Bistatic CW Lidar Traceable to SI Units, 2024. 22nd Coherent Laser Radar Conference, CLRC 2024, June 23 – June 28.
- [9] A. A. P. M. A. S. Timothy Hospedales, "Meta-Learning in Neural Networks: A Survey," arXiv:2004.05439 [cs, stat] (2020), 2020.

Observations using an X-Band Phased-Array Bistatic Radar Network

Steven Beninati¹, Stephen Frasier¹, Pavlos Kollias^{2,3}, Edward Luke³, Jorge Salazar Cerreno⁴

¹*Microwave Remote Sensing Lab, University of Massachusetts Amherst*

²*Stony Brook University*

³*Brookhaven National Laboratory*

⁴*University of Oklahoma*



Steven Beninati

1 Introduction

The availability of low-cost electronic components for microwave signal processing has created new interest in the use of multistatic radar for weather observation [e.g. 1,2]. Multistatic radar networks consist of a single transmitting radar and multiple receivers positioned some distance away from the transmitter and each other. The remote receivers observe the forward scattering of the transmitted pulse by weather phenomena. By combining observations from multiple receivers, it is possible to obtain additional information on the scatterers. For example, multiple components of velocity can be obtained from Doppler measurements [e.g. 3, 4]. The use of a single transmitter and multiple passive receivers offers benefits over multiple independent radars both in terms of cost savings and in temporal synchronization of the measurements [3].

The Microwave Remote Sensing Laboratory at the University of Massachusetts Amherst, in collaboration with teams from Stony Brook University/Brookhaven National Laboratory (SBU/BNL) and the University of Oklahoma, are leveraging the SBU/BNL Skyler-2 X-Band mobile phased-array radar to construct a multistatic radar network using the phased-array as the transmitter. Skyler-2 is a low-power, dual-polarized, phased-array developed by Raytheon Technologies, now Collins Aerospace [5]. The multistatic network is to be used to study deep convection in storm cells. The rest of this publication will discuss the expected and experimental performance of the Skyler-2 radar used in conjunction with a single low-gain passive receiver. Section 2 discusses the theory behind bistatic scattering and wind retrieval from bistatic networks and the design parameters of the proposed bistatic network. Section 3 presents experimental results using a single receiver and the Skyler 2 transmitter. Section 4 discusses the conclusions of this paper and further work.

2 Methodology

2.1 Bistatic Weather Observation Theory

While the principles for weather observation using a bistatic radar network are similar to the traditional monostatic (single radar receiver and transmitter) case, the bistatic geometry introduces changes to the observation volume, scattering characteristics, and observed Doppler velocity depending on the observation angle of the target. Particularly of interest in this study is the interaction of the retrieved Doppler velocity and the observation angle, as additional velocity components can be extracted from the forward scattered signal [1-4]. In order to analyze these effects, it is necessary to understand the nature of the signal being measured by the receiver.

The received power P_r from a bistatic network can be described by an extension of the standard radar equation for monostatic radar (1) [6].

$$P_r = P_t * \frac{G_t A_{er} \eta_{bi} V}{(4\pi)^2 R_t^2 R_r^2} \quad (1)$$

Where P_t is the transmitted power, G_t is the transmitter gain, A_{er} is the effective area of the receiver, η_{bi} is the bistatic volume reflectivity, V is the observation volume, and R_t and R_r are the distances from the target to the transmitter and to the receiver, respectively. In addition to separate path lengths from the transmitter and receiver and the separate gains of the two antennas, this bistatic formulation also results in changes to η_{bi} and V .

In the traditional monostatic radar case, the volume observed by the radar consists of the intersection of a sphere formed by the range resolution of the transmitted pulse and the beam pattern of the radar [7]. In the bistatic network configuration, the transmitter and receiver are the two foci of a constant delay ellipsoid formed by the sum of the range from the observation volume to the transmitter R_t and the range from the observation volume to the receiver R_r [3]. The observation volume is then further constrained by the intersection of the transmitter and receiver antenna beam patterns [8]. Thus, the size and shape of the observation volume varies with the observation direction relative to the baseline, as both the intersection of the beam patterns and the range resolution vary with the observation direction [3]. Figure 1 shows an example of how the constant delay ellipsoids and the receiver and antenna beam patterns combine to create a resolution volume. According to Willis [9], the range resolution as a function of the bistatic angle α and pulse duration τ can be approximated as (2), which reduces to the typical

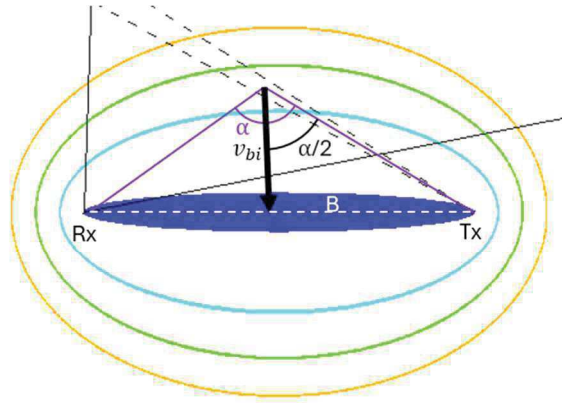


Figure 1: Cross-section of bistatic radar geometry. Resolution volumes are formed by the intersection of the receiver beam (solid black lines), transmitter beam (dashed black lines), and constant delay ellipsoids (colored ellipses). The bistatic velocity v_{bi} is normal to the ellipses.

monostatic range resolution equation for $\alpha = 0^\circ$.

$$\Delta R \approx \frac{c\tau}{2 \cos\left(\frac{\alpha}{2}\right)} \quad (2)$$

The bistatic configuration also results in changes to the Doppler velocity measured by the bistatic network. In the monostatic configuration, the measured velocity is the projection of the target's velocity along the range direction of the radar [7]. The velocity measured by the bistatic network reflects the projection of the target's velocity along the bisector of α (Figure 1) [4], which is a vector normal to the surface of the constant delay ellipsoid [3]. As the location of the observation volume changes, the distance between the inner and outer delay ellipsoids varies with the bistatic angle (see Figure 1) [9]. The apparent velocity v_a seen by the bistatic receiver is related to the true velocity of the target along the bistatic angle bisector v_{bi} by (3) [4].

$$v_a = v_{bi} \cos\left(\frac{\alpha}{2}\right) \quad (3)$$

While the receiver sees the projection of velocity along the bisector of the network, the traditional monostatic velocity can still be obtained from the transmitting radar. It is here that the benefits of the bistatic network for velocity measurement become apparent, as the additional bistatic velocity measurement can be used to derive wind fields [1-4].

The volume reflectivity η_{bi} of a target also varies with the angle between the electric field and the scattering direction χ [6]. For Rayleigh scattering targets such as most rain at X-Band, Tulu provides a modification to the standard equation for volume reflectivity which incorporates χ , the operating wavelength λ , the dielectric factor K, and the reflectivity factor Z (4) [6].

$$\eta_{bi} = \frac{\pi^5}{\lambda^4} |K|^2 Z \sin^2(\chi) \quad (4)$$

Based on this relation, Wurman, Heckman, and Boccippio [3] concluded vertical polarization was more effective in minimizing nulls as a result of χ for measuring horizontal velocities with bistatic networks.

2.2 Implemented Bistatic Network

The bistatic network used for this experiment is shown in Figure 2. It consists of the Skyler-2 X-Band mobile phased-array radar operating as the transmitter, and a single passive receiver constructed by the University of Massachusetts Amherst. The receiver uses a low-gain patch antenna developed by the University of Oklahoma. The technical parameters of the network are presented in Table 1.

Table 1: Bistatic Network Characteristics

Transmitter Antenna Gain	~35 dB
Receiver Antenna Gain	16.6 dB
Center Frequency	9.43 GHz
Transmit Power	< 250 (W)
Polarization	Vertical
Pulse Width	1.0 μ s
Pulse Repetition Frequency	2.404 kHz

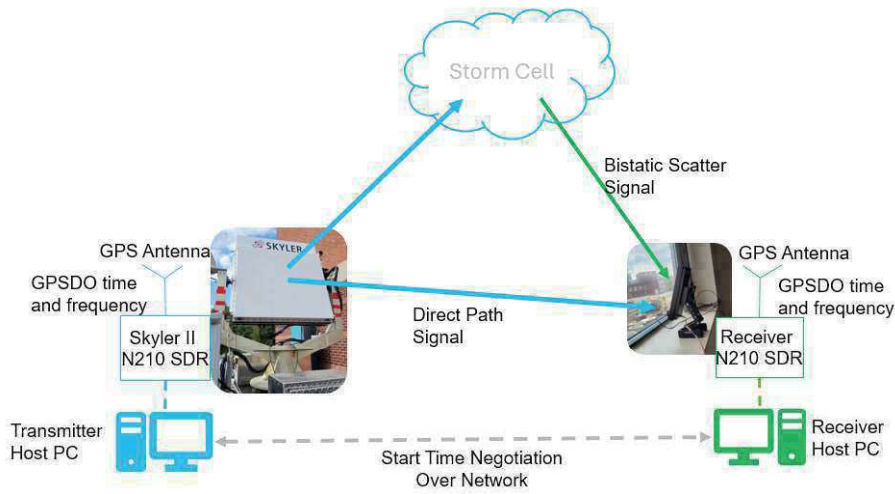


Figure 2: Implemented Bistatic Network Configuration. Adapted from [11].

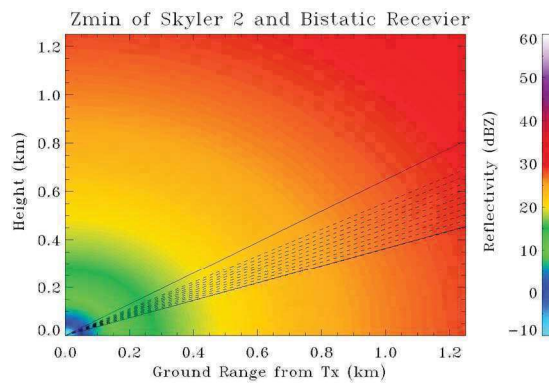


Figure 3: Theoretical minimum reflectivity factor (Z_{min}) for the bistatic network in a pseudo-monostatic configuration with a $1.0\mu s$ CW pulse for 3 dB SNR. Solid lines indicate the receiver beam, and dashed lines indicate transmitter beams

Synchronization of the receiver and the transmitter is accomplished using a pair of Ettus Research USRP N210 Software Defined Radios (SDR) and GPS disciplined oscillators (GPSDOs), similar to the system implemented by Wurman, Heckman, and Boccippio [3]. The GPSDOs provide synchronized timing data and fix the reference oscillators of both systems to the GPS Pulse-Per-Second (PPS) signal. A local copy of the scan parameters is stored on both the transmitter and the receiver, and a start time is automatically coordinated using a network link between the systems. Once the start time is established, both systems issue timed commands to the N210 SDRs to ensure simultaneous transmission and reception times.

For this experiment, the transmitter and receiver are separated by a baseline of 30 m and observe a target region located approximately 90° off the baseline. In this configuration, the bistatic angle α for targets as close as 100m (less than the range resolution of the radar) is 17° , resulting in a deviation from the monostatic case of 1.1%. Therefore, this configuration can be modeled as a monostatic configuration for this test with an expected error of $< 1.1\%$ for any targets beyond the first range resolution. Figure 3 shows the expected minimum reflectivity factor, Z_{min} , required to achieve a signal to noise ratio (SNR) of 3 dB as a function of the target position in the vertical plane along the viewing direction in vertical polarization in this pseudo-monostatic case using a continuous wave (CW) pulse with a width of $1.0 \mu s$.

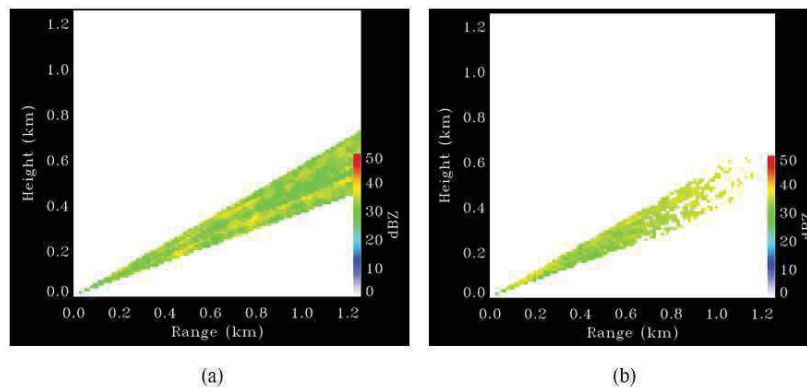


Figure 4: Reflectivity factor values during the moderate rainfall event for Skyler-2 (a) and for the bistatic receiver (b), filtered to exclude points with SNR < 3 dB.

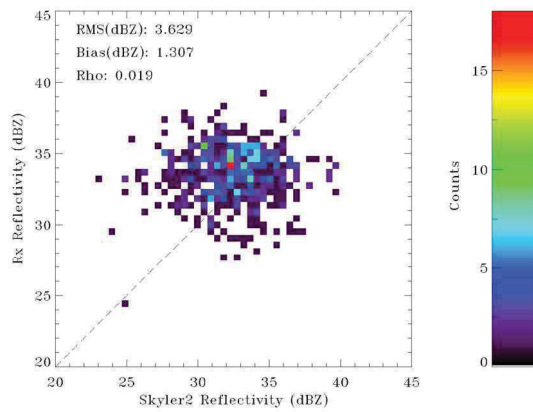


Figure 5: Reflectivity factor values obtained using the bistatic receiver versus values obtained using Skyler-2.

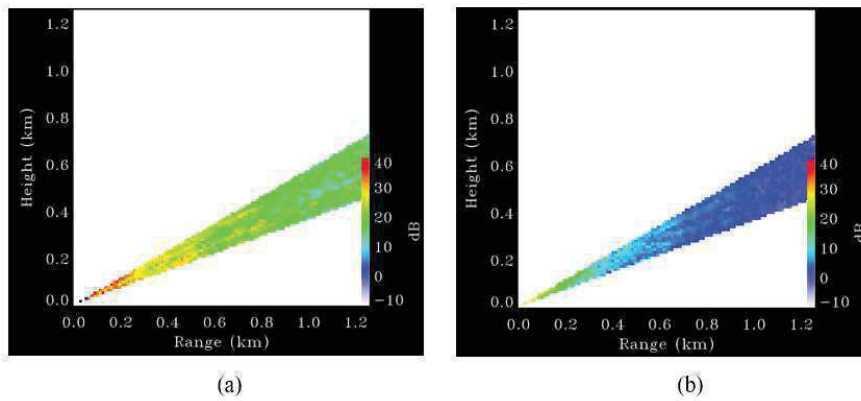


Figure 6: SNR of observations during the moderate rainfall event for Skyler-2 (a) and for the bistatic receiver (b).

3 Experimental Results

The bistatic network was tested by observing a moderate rainfall event in Amherst, MA, USA using the configuration discussed in Section 2. A Range-Height Indicator (RHI) plot was obtained at elevation angles from 20° to 30°. The scan was performed using a 1 μs continuous wave (CW) pulse pattern at a Pulse Repetition Frequency (PRF) of 2.404 kHz. Figure 4 shows the measured reflectivity values from both Skyler-2 and the bistatic receiver. As seen in Figure 5, the values obtained from the receiver agree with the values from Skyler-2 within an RMS error of 3.6 dBZ.

Figure 6 shows the SNR of the received echoes in the RHIs from Skyler-2 and the bistatic receiver. The SNR observed by the bistatic receiver is approximately 15.6 dB lower than the corresponding SNR for Skyler-2. The theoretical difference in the SNR between the two systems should be approximately equal to the difference between the Skyler-2 antenna gain and the bistatic receiver antenna gain, 18.4 dB, assuming that the noise figures of both systems are equal.

For reflectivity factor values from 30-40 dBZ as seen here, the maximum observation range for the bistatic receiver should be on the order of 1km (Figure 3). Figure 4 and Figure 6 show that the SNR of the receiver remains above the 3dB threshold until about 1km, indicating that the experimental performance of the system is similar to the theoretical performance.

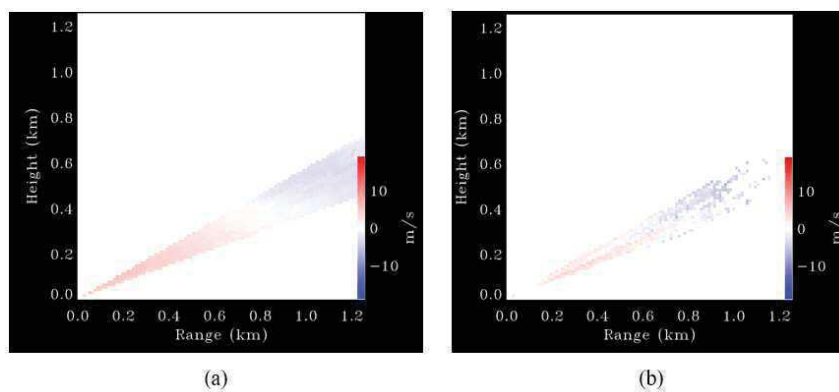


Figure 7: Doppler velocity RHI from (a) Skyler-2 and (b) the bistatic receiver, filtered to exclude points with SNR < 3 dB.

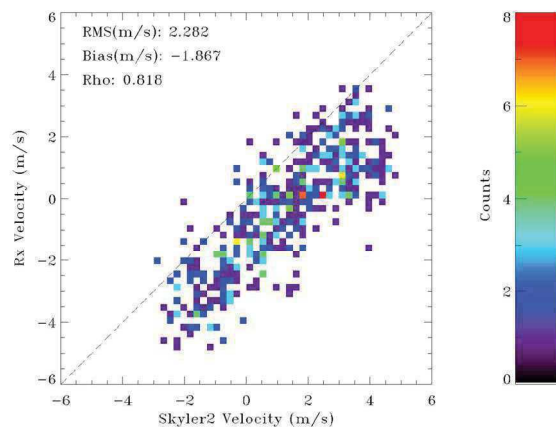


Figure 8: Scatter plot of precipitation velocities measured using the bistatic receiver and Skyler-2.

Doppler velocity measurements were acquired using the pulse-pair method. To correct phase offsets between the transmitter and the receiver, the center of the transmit pulse as observed by the receiver was used to set the zero-phase point of the receiver. The RHI plots for Doppler velocity obtained using this method are shown in Figure 7.

Figure 8 shows a scatterplot of the velocities measured using the bistatic receiver and Skyler-2 from the RHIs shown in Figure 7. The velocities measured using the bistatic receiver have a bias of -1.867 m/s relative to those measured using Skyler-2, with an RMS error of 2.28 m/s.

4 Conclusions

The bistatic network consisting of the Skyler-2 X-Band mobile phased-array radar and a low gain bistatic receiver was tested in a pseudo-monostatic configuration during a moderate precipitation event. The system achieved the expected SNR performance in this configuration. Reflectivity values observed by Skyler-2 and the receiver were in a similar range.

Doppler velocity measurements obtained by the receiver and Skyler-2 likewise were similar, with the receiver underestimating the velocity relative to Skyler-2 by 1.86 m/s. This value is larger than the bias observed by Byrd, Palmer, and Fulton [1] and by Friedrich and Hagen [12]. The overall RMS error of 2.28 m/s is within the ranges reported by [1] and [12]. It should be noted that the sample size of velocities measured was small, and additional observations may result in a lower overall error.

Further work on this topic includes improving the timing and frequency synchronization of the Skyler-2 and the bistatic receiver, as well as achieving sufficient synchronization such that the receiver does not need to observe the transmitter pulse.

5 References

- [1] A. Byrd, R. D. Palmer, and C. Fulton, 2019. "Development of a low-cost multistatic passive weather radar network," *IEEE Trans. Geosci. Remote Sensing*, vol 58(4), 2796–2808.
- [2] S. Emmerson, R. D. Palmer, D. J. Bodine, D. Schwartzman, P. Kirstetter, and P. S. Skinner, 2023. "Validation of multistatic wind retrievals using a vertically pointing mobile radar," 40th AMS Conference on Radar Meteorology, Minneapolis, MN.
- [3] J. Wurman, S. Heckman, and D. Boccippio, 1993. "A bistatic multiple-Doppler radar network," *Journal of Applied Meteorology*, 32(12), 1802–1814.
- [4] A. Protat, and I. Zawadzki, 1999. "A Variational Method for Real-Time Retrieval of Three-Dimensional Wind Field from Multiple-Doppler Bistatic Radar Network Data," *Journal of Atmospheric and Oceanic Technology*, vol. 16(4), 432-449.
- [5] Skyler, Collins Aerospace, <https://www.collinsaerospace.com/what-we-do/industries/air-traffic-management/surveillance/skyler>, accessed 10 April 2024.
- [6] Z. C. Tulu, S. J. Frasier, R. Janaswamy, and D. J. McLaughlin, "Considerations for bistatic probing of clear-air winds in the atmospheric boundary layer," *Radio Science*, vol. 41, no. 3, 2006.
- [7] R. J. Doviak, and D. S. Zrnicek, *Doppler Radar and Weather Observations*, 2nd ed. Mineola, New York, USA: Dover Publications, Inc, 2006
- [8] D. Atlas, K. Naito, and R. E. Carbone, "Bistatic microwave probing of a refractively perturbed clear atmosphere," *Journal of the Atmospheric Sciences*, vol. 25, no. 2, pp. 257–268, Mar 1968.
- [9] N. J. Willis, *Bistatic Radar*, 2nd ed. Raleigh, North Carolina, USA: SciTech Publishing Inc, 2004
- [10] P. Kollias, E. P. Luke, K. Tuftedal, M. Dubois and E. J. Knapp, "Agile Weather Observations using a Dual-Polarization X-band Phased Array Radar," 2022 IEEE Radar Conference (RadarConf22), New York City, NY, USA, 2022, pp. 1-6, doi: 10.1109/RadarConf2248738.2022.9764308
- [11] S. Beninati, S. J. Frasier, P. Kollias, E. Luke, and J. L. Salazar-Cerreno. "A Phased-Array Bistatic Radar Network for Measuring Atmospheric Convection," 40th AMS Conference on Radar Meteorology, Minneapolis, MN, 2023
- [12] K. Friedrich and M. Hagen, "Evaluation of Wind Vectors Measured by a Bistatic Doppler Radar Network," *Journal of Atmospheric and Oceanic Technology*, vol. 21, 1840-1854, 2004, doi: 10.1175/JTECH-1679.1.

Radar hydrometeorological applications

HYDROLOGICAL MODELING OF PROBABILISTIC RAINFALL FORECASTS FOR IMPACT-BASED FLOOD WARNING SYSTEM

D. E. Villarreal-Jaime^{1,2}, P. Willems¹, L. De Cruz^{2,3}, R. Reinoso-Rondinel^{1,2}

¹Hydraulics and Geotechnics Section, KU Leuven, Belgium

²Royal Meteorological Institute of Belgium, Belgium

³Electronics and Informatics Department, Vrije Universiteit Brussel, Belgium



D. E. Villarreal-Jaime

1 Introduction

Extreme precipitation events are significant natural hazards that impact economies and populations globally (Calvin et al., 2023). These events are challenging to predict due to their high spatial and temporal variability, leading to increased uncertainties in flood forecasts, especially in urban catchments (Bruni et al., 2015; Willems et al., 2012). As climate change intensifies extreme weather events, accurate flood forecasting and early warning systems become crucial. Precisely estimating severity and associated uncertainties is essential for mitigating damages and enhancing preparedness, especially in urban areas characterized by high population density and critical infrastructure.

Traditional flood forecasting relies on deterministic rainfall estimates, which often fail to capture the inherent uncertainty associated with spatial and temporal precipitation patterns. In contrast, probabilistic rainfall forecasts offer a deeper understanding by accounting for occurrence variability and confidence intervals (Cloke & Pappenberger, 2009). However, translating these probabilistic forecasts into actionable information for flood risk management and impact-based flood warnings is a challenge (Dale et al., 2014).

The main objective of this research is the integration of operational and forecasting radar products, provided by the Royal Meteorological Institute of Belgium (RMIB), into a distributed urban-hydrological model towards the implementation of an impact-based flood warning system (Reinoso-Rondinel et al., 2024). Our research couples state-of-the-art hydro-meteorological radar measurements (Goudenhoofdt & Delobbe, 2016) and nowcasts adapted from pySTEPS (Pulkkinen et al., 2019) with hydrologic and hydraulic model using Delft-FEWS (Werner et al., 2013) and Python. A distributed urban-hydrological model is designed with EPA SWMM (Rossman, 2017; Rossman & Huber, 2016) and TELEMAC-2D (Hervouet, 2007) and by integrating probabilistic rainfall forecasts into these models, we aim to improve flood predictions in urban areas.

The next sections will describe in more detail the models and datasets used, as well as preliminary results and conclusions for the flood event occurred on July 4th, 2021, in Antwerp, Belgium.

2 Data and methods

In this study, we present a comprehensive methodology for the integration of radar observations and probabilistic rainfall forecasts (6 h lead time) to a distributed urban-hydrological model to assess urban flood risks. Our approach combines different hydrologic and hydraulic software using Python and Delft-FEWS. We detail the steps taken to achieve the flood predictions, emphasizing the importance of replicability using free and/or open-source software.

2.1 Integration platform

Delft-FEWS, which was developed by Deltares, serves as a powerful platform for visualization, analysis, and integration of diverse datasets and models. Its flexibility, compatibility, and modularity allow seamless collaboration with Python, which is used for downloading, pre-processing, and post-processing data required in the hydrological and hydraulic models. Together, both create our integration platform to download and process radar rainfall data and radar nowcasts from RMIB, pre-process input data, post-process, and visualize results for SWMM and TELEMAC-2D, as shown in Figure 1.



Figure 1: Integration platform of datasets and models.

2.2 RMIB radar products

RMIB delivers a set of Quantitative Precipitation Estimation (QPE), forecasting and nowcasting operational products. The RADCLIM product is obtained after merging the real-time RADQPE product, observed by the operational C-band weather radar network in and near Belgium, with an extended network of rain gauge measurements. This product provides QPE fields at 1 km resolution for 5 min and 1 h accumulation periods.

The seamless precipitation forecast product (pySTEPS-BE) is achieved by blending the radar-based nowcast using the STEPS-BE approach (Bowler et al., 2006), which is a probabilistic rainfall nowcast of 48 members every 5 min up to 2 h lead time, with precipitation fields from the deterministic numerical weather prediction (NWP) ALARO/AROME models. The blending is performed by each cascade level with skill-dependent weights in the nowcast, NWP, and stochastic noise (Imhoff et al., 2023). This is a pre-operational RMIB product developed based on the open-source Python library pySTEPS, spanning up to 12 h lead time and 48 ensemble members (De Cruz et al., 2024).

2.3 Hydrologic and hydraulic models

Our distributed urban-hydrological model combines a 1D pluvial network model using EPA SWMM with a 2D mesh for streets and inundation areas built in TELEMAC-2D. This coupling captures the urban hydrological processes and the hydrodynamic interactions between the drainage network and surface water to improve the flood risk analysis in urban areas. Figure 2 shows the interactions between the data and models.

SWMM is a hydrologic-hydraulic model, mostly used in urban areas, for single-event or continuous simulations. The model operates on a collection of sub-catchment areas that receive precipitation and route runoff through the pluvial network. Here, only the nodes discharge is used as input for the TELEMAC-2D model.

TELEMAC-2D is an open-source two-dimensional hydrodynamic model used to simulate free-surface flows in horizontal space using a triangular mesh. It solves the shallow water equations, also known as the Saint-Venant equations, using either the finite-element or finite-volume method and it computes water depth and velocity at each point of the mesh. In this case, the model was modified to compute the backflow to the drainage system according to the orifice or weir equation, depending on the water depth at each timestep. This is only to simulate the backflow effect and loss volume from the surface when there is no inflow from each node, but no further simulation or adjustment is made in the SWMM model.



Figure 2: Models and data flow diagram.

2.4 Case study

The study area is the city of Antwerp, Belgium, located in the banks of the river Scheldt. It is highly prone to urban and fluvial floods, which could cause large socio-economic impacts. The total area of the urban catchment is around 6.5 km² with a mean slope of 0.028. The pluvial network of the city is divided in 5 zones with a total length of 1012 km with 393 control structures, and pipes or channels dimensions up to 12 m. About 60,000 subcatchments and 21,000 nodes are considered. Figure 3 shows the model extent and the drainage networks used for the analysis.

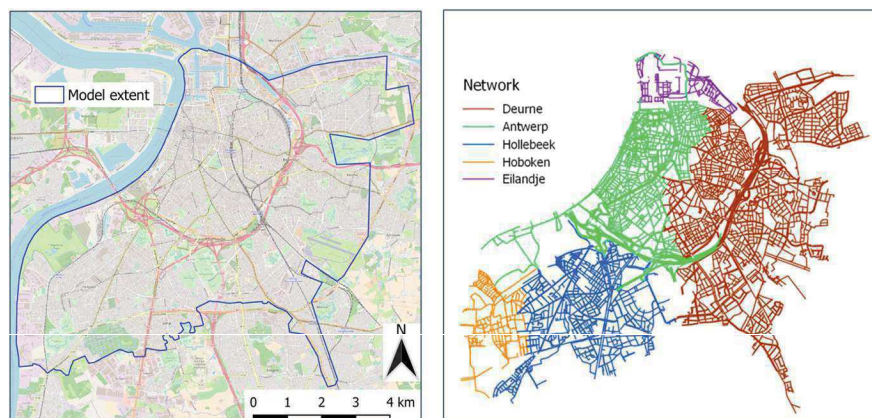


Figure 3: Antwerp model extent and drainage networks.

Due to scarce hydrological data in the urban area, the model is validated using a collection of reports of flood interventions by the Fire Brigade of the city of Antwerp. The model uses various precipitation events from RADCLIM to generate a flood map and compares it with the map of reported Fire Brigade interventions. After model validation, the probabilistic rainfall forecast is used to generate an ensemble hydrological forecast and estimate flood uncertainties for the impact-based flood warning system. Figure 4 shows the flood reports collected (around 180 in Antwerp) during the flood event on July 4th, 2021.

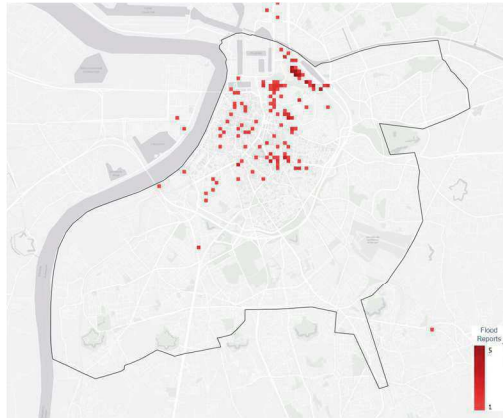


Figure 4: Flood interventions from Fire Brigade collected in Antwerp during the flood event on July 4th, 2021.

3 Results

3.1 Rainfall forecast

Probabilistic rainfall forecasts with different starting times (T_0) were compared with observed precipitation for the event occurred on July 4th, 2021, as shown in Figure 5. Even at 1 h nowcast, it is possible to notice differences in the development of the spatial and temporal precipitation patterns and its intensities.

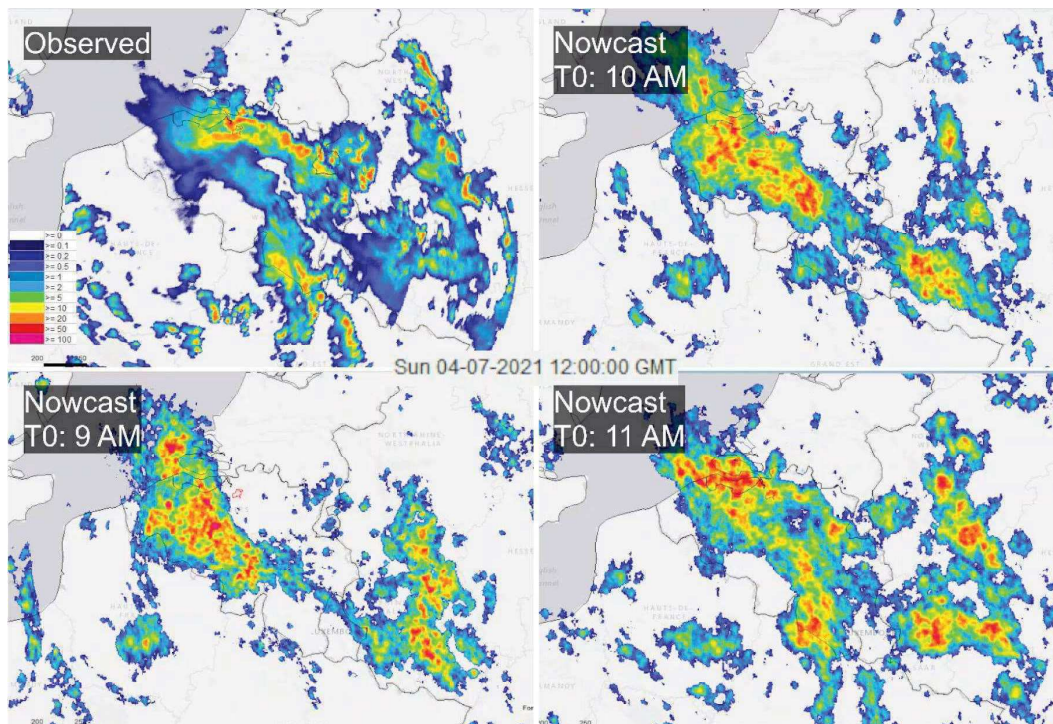


Figure 5: Comparison of RADCLIM and pySTEPS-BE at 12 pm starting at different T_0 over Belgium during the flood event on July 4th, 2021.

Figure 6 shows the time series comparison in one pixel over Antwerp. In the nowcasts started at 8 am, 9 am and 10 am, there is a lag of around 2 or 3 h between the observed precipitation peak and the ensemble forecast, but some members can predict the intensity, which could be used to issue a first preliminary warning. It is until the nowcast at 11 am, which is around 30 to 40 min before the observed peak, that the time and peak intensities are better predicted, but they still overestimate the duration of the event. These differences, combined with the hydrologic-hydraulic model uncertainties, create higher uncertainties in the ensemble hydrological forecast to be used in an impact-based flood warning system.

3.2 Flood forecast

After simulation of the observed precipitation with RADCLIM and the blended nowcasts in the hydrologic-hydraulic model, it was possible to obtain conventional and probabilistic flood hazard maps with a resolution of 100 m. If these results are compared with the flood reports map, as shown in Figure 7, it is possible to identify certain similarities on the flood prone areas in the city of Antwerp. Many of these flood prone areas coincide with the flood hazard maps provided by the authorities in the Flanders region (not shown).

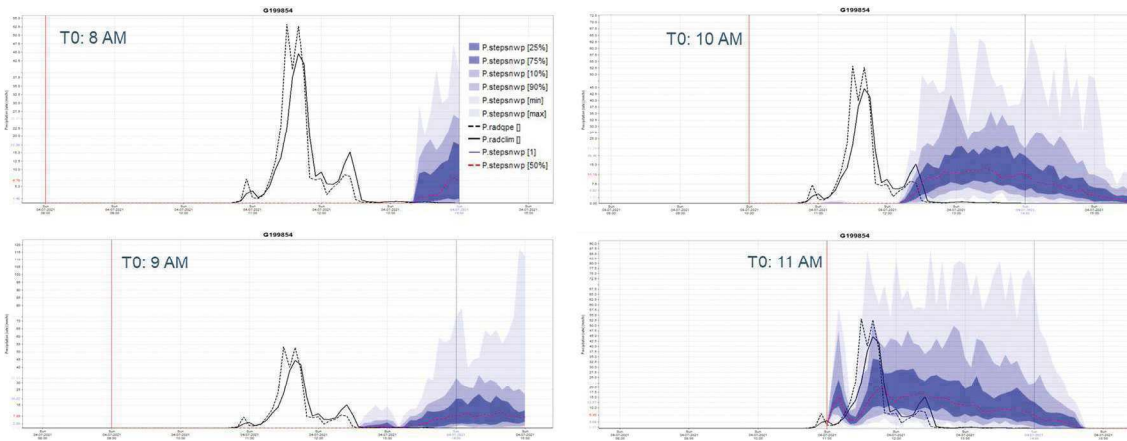


Figure 6: Time series comparison of radar observations (P_{radqpe} and $P_{radclim}$) and blended nowcasts ($P_{stepsnwp}$) with uncertainty bands started at different T_0 over Antwerp during the flood event on July 4th, 2021.

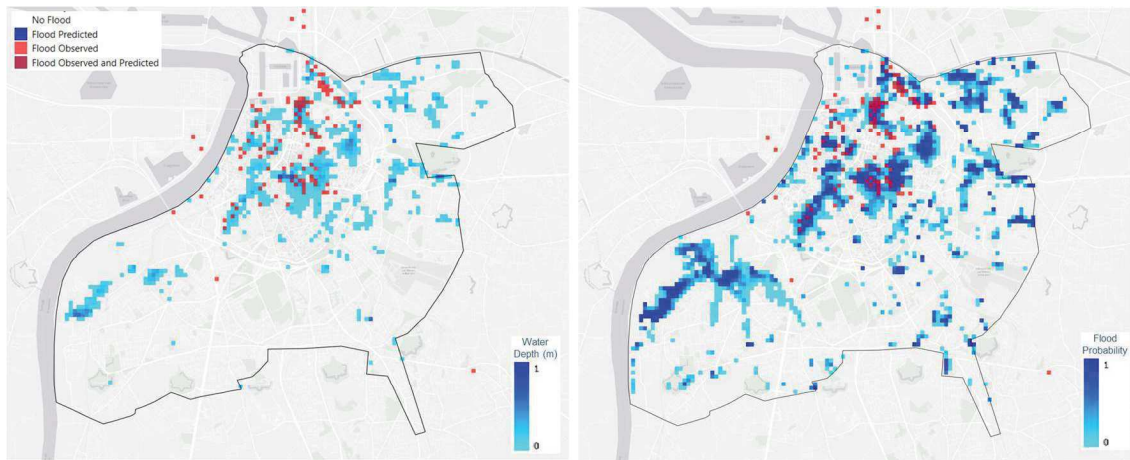


Figure 7: Comparison of flood reports map (red) with flood extent obtained with hydrologic-hydraulic model (blue) for observed precipitation (left) and blended nowcasts started at 11 am (right).

These similarities in the flood extent maps obtained with observed precipitation and blended nowcasts are good preliminary results, but the latter have bigger extent and last longer due to the overestimation of the event duration from the precipitation nowcasts and the variability between the ensemble members. Figure 8 shows the water discharge in one node of the SWMM model obtained with observed precipitation and uncertainty bands from the blended nowcasts started at 11 am.

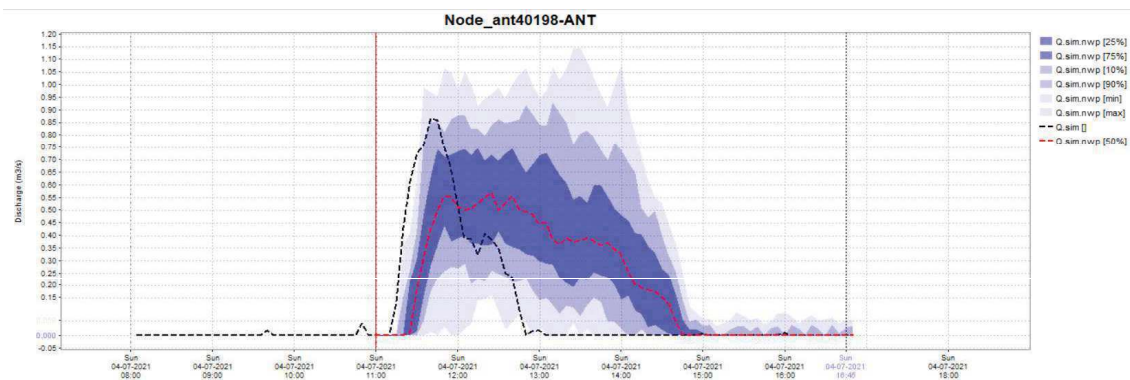


Figure 8: Comparison of discharge in one node of SWMM model obtained with observed precipitation (Q_{sim}) and uncertainty bands from the blended nowcasts started at 11 am ($Q_{sim.nwp}$).

4 Conclusions and perspectives

Although this research is in its early stages and further investigation is needed to implement the best forecasting scheme, modelling, and operational practices, preliminary results for the city of Antwerp are shown. It is important to note that uncertainty levels are high and it is required to validate the blended nowcasts and hydrological-hydraulic models with different statistical metrics for several precipitation events to assess their accuracy and reliability.

It is worth to mention that the coupling between SWMM and TELEMAC-2D models using Delft-FEWS and Python is a good manner to assess urban flood hazards with free and/or open-source software. The main limitation for its operational use would be the required computational power, which results in long simulation times. However, this will serve as the foundation for developing a Physically Informed Data-Driven Model for a rapid real-time impact-based flood warning system, spanning both urban and larger scales.

In summary, our study tries to fill the gap between rainfall forecasting and hydrological-hydraulic modelling for its future implementation in a warning system. Rather than focusing solely on water levels, we aim for an impact-based flood warning system, which will consider the potential consequences of flooding on buildings, infrastructure, and communities. By using probabilistic approaches, it is possible to assess uncertainties associated to every step of the process. Probabilistic flood hazard maps could later be combined with depth-damage curves to estimate the probable damage costs of a flood event. This would give decision-makers better information about the possible outcomes and allow them to make informed decisions regarding evacuation, resource allocation, and emergency response to mitigate flood risks effectively.

5 Acknowledgements

We extend our heartfelt thanks to KU Leuven and the Belgian Science Policy Office for funding this PhD. Special appreciation goes to RMIB for providing radar data and their expertise. Additionally, we are grateful to the open-source community for their invaluable contributions.

6 References

- Bowler, N. E., Pierce, C. E., & Seed, A. W. (2006). STEPS: A probabilistic precipitation forecasting scheme which merges an extrapolation nowcast with downscaled NWP. *Quarterly Journal of the Royal Meteorological Society*, 132(620), 2127–2155. <https://doi.org/10.1256/qj.04.100>
- Bruni, G., Reinoso, R., van de Giesen, N. C., Clemens, F. H. L. R., & ten Veldhuis, J. A. E. (2015). On the sensitivity of urban hydrodynamic modelling to rainfall spatial and temporal resolution. *Hydrology and Earth System Sciences*, 19(2), 691–709. <https://doi.org/10.5194/hess-19-691-2015>
- Calvin, K., Dasgupta, D., Krinner, G., Mukherji, A., Thorne, P. W., Trisos, C., Romero, J., Aldunce, P., Barrett, K., Blanco, G., Cheung, W. W. L., Connors, S., Denton, F., Diongue-Niang, A., Dodman, D., Garschagen, M., Geden, O., Hayward, B., Jones, C., ... Ha, M. (2023). *IPCC, 2023: Climate Change 2023: Synthesis Report. Contribution of Working Groups I, II and III to the Sixth Assessment Report of the Intergovernmental Panel on Climate Change [Core Writing Team, H. Lee and J. Romero (eds.)]. IPCC, Geneva, Switzerland.* <https://doi.org/10.59327/IPCC/AR6-9789291691647>
- Cloke, H. L., & Pappenberger, F. (2009). Ensemble flood forecasting: A review. *Journal of Hydrology*, 375(3–4), 613–626. <https://doi.org/10.1016/j.jhydrol.2009.06.005>
- Dale, M., Wicks, J., Mylne, K., Pappenberger, F., Laeger, S., & Taylor, S. (2014). Probabilistic flood forecasting and decision-making: an innovative risk-based approach. *Natural Hazards*, 70(1), 159–172. <https://doi.org/10.1007/s11069-012-0483-z>
- De Cruz, L., Van Genderachter, M., Reyniers, M., Deckmyn, A., Dehmous, I., De Kock, S., Dewettinck, W., Imhoff, R., Montandon, E., & Reinoso-Rondinel, R. (2024). Project IMA: Lessons Learned from Building the Belgian Operational Seamless Ensemble Prediction System. *EGU General Assembly 2024*. <https://doi.org/https://doi.org/10.5194/egusphere-egu24-12855>
- Goudenhoofd, E., & Delobbe, L. (2016). Generation and Verification of Rainfall Estimates from 10-Yr Volumetric Weather Radar Measurements. *Journal of Hydrometeorology*, 17(4), 1223–1242. <https://doi.org/10.1175/JHM-D-15-0166.1>
- Hervouet, J. (2007). *Hydrodynamics of Free Surface Flows*. Wiley. <https://doi.org/10.1002/9780470319628>
- Imhoff, R. O., De Cruz, L., Dewettinck, W., Brauer, C. C., Uijlenhoet, R., van Heeringen, K., Velasco-Forero, C., Nerini, D., Van Genderachter, M., & Weerts, A. H. (2023). Scale-dependent blending of ensemble rainfall nowcasts and numerical weather prediction in the open-source pysteps library. *Quarterly Journal of the Royal Meteorological Society*, 149(753), 1335–1364. <https://doi.org/10.1002/qj.4461>
- Pulkkinen, S., Nerini, D., Pérez Hortal, A. A., Velasco-Forero, C., Seed, A., Germann, U., & Foresti, L. (2019). Pysteps: an open-source Python library for probabilistic precipitation nowcasting (v1.0). *Geoscientific Model Development*, 12(10), 4185–4219. <https://doi.org/10.5194/gmd-12-4185-2019>
- Reinoso-Rondinel, R., Buekenhout, D., van Genderachter, M., Imhoff, R., De Cruz, L., & Willems, P. (2024). A flood prediction framework: integrating seamless predictions into urban hydrological modeling. *EGU General Assembly 2024*. <https://doi.org/https://doi.org/10.5194/egusphere-egu24-10727>
- Rossman, L. A. (2017). Storm Water Management Model Reference Manual. In *EPA/600/R-17/111: Vols. II – Hydraulics*. National Risk Management Research Laboratory, United States Environmental Protection Agency.
- Rossman, L. A., & Huber, W. C. (2016). Storm Water Management Model Reference Manual. In *EPA/600/R-15/162A: Vols. I – Hydrology*. National Risk Management Research Laboratory, United States Environmental Protection Agency.
- Werner, M., Schellekens, J., Gijsbers, P., van Dijk, M., van den Akker, O., & Heynert, K. (2013). The Delft-FEWS flow forecasting system. *Environmental Modelling & Software*, 40, 65–77. <https://doi.org/10.1016/j.envsoft.2012.07.010>
- Willems, P., Arnbjerg-Nielsen, K., Olsson, J., & Nguyen, V. T. V. (2012). Climate change impact assessment on urban rainfall extremes and urban drainage: Methods and shortcomings. *Atmospheric Research*, 103, 106–118. <https://doi.org/10.1016/j.atmosres.2011.04.003>

A Hydrometeor Classification Method for Dual Polarization Weather Radar Based on Gaussian Mixture Model using Bayesian Inference

Takahisa Wada¹, Yuta Ozawa¹, Satoshi Kida², Masakazu Wada²,
Yasunori Nakagawa², Osamu Yamanaka¹

¹ *Infrastructure Systems Research and Development Center, Toshiba Infrastructure Systems & Solutions Corporation*

² *Toshiba Digital Solutions Corporation*



Takahisa Wada

1 Introduction

In recent years, hail-related damage has rapidly increased worldwide due to climate change, making the development of hail forecast technology urgent. In the development of hail forecasting technology based on conventional meteorological radar data, there has been a lack of a sufficient number of fixed observation points capable of detecting hail, which is a short-term and localized weather phenomenon. This limitation has made it difficult to evaluate and improve the accuracy of hail forecasts. Therefore, we propose a new method (T-SHIBA: Two-Stage, Hydrometer classification and forecasting Induced By SNS, Algorithm), which utilizes the rapidly expanding use of social media platforms (SNS) in recent years. Through SNS posts by the general public about hail events, we identified approximate hail locations and times, enabling the evaluation and improvement of hail forecasting technology. This method consists of two stages: the first stage involves hydrometeor classification in three dimensions based on observations from meteorological radar, and the second stage forecasts hail locations in two dimensions (latitude and longitude) based on the results of the first stage.

This report presents the method for hydrometeor classification in the first stage. The forecast method for the second stage will be reported separately. To encourage user actions to reduce hail damage based on forecast results, it is essential to increase the reliability of these forecasts. Therefore, reducing false alarm rates is crucial, even if it means decreasing the accuracy of hail forecasts.

In traditional particle classification methods, torrential rain events without hail and hail events are grouped into the same category. This results in forecasting hail even in cases of torrential rain without hail, leading to a high false alarm rate. To address this issue, we created training data exclusively for torrential rain events without hail from SNS posts where no hail was reported. We applied a Gaussian mixture model using Bayesian inference to separate the hail and torrential rain categories. This approach allows us to build a classification model in a data-driven manner, eliminating the need to determine thresholds for each category based on an in-depth understanding of meteorological radar technology. As a result, we have introduced a hydrometeor classification method with distinct classifications for hail and torrential rain.

2 Methodology

In the last few decades, a number of researches on hydrometeor classification using polarimetric radar have been conducted. In the early years, decision-tree method was used in order to classify hydrometeor types. Subsequently, fuzzy-based method has been the dominant method for hydrometeor classification. In these methods, dual-polarization information such as Z_h (radar reflectivity of horizontal wave), Z_{dr} (differential reflectivity), phv (correlation coefficient), and K_{dp} (specific differential phase), along with variables such as temperature and humidity, are considered. To classify hydrometeor types from polarimetric radar data, fuzzy-logic hydrometeor classification algorithm is adopted, classifying hydrometeor types into 10 categories; 1)drizzle, 2)rain, 3)wet snow, 4)dry snow, 5)ice crystal, 6)dry graupel, 7)wet graupel, 8)small hail, 9)large hail and 10)rain and hail. These techniques include studies conducted using S-band and C-band polarimetric radars[1], and studies conducted using X-band polarimetric radars[2]. Although, X-band radars are significantly affected by attenuation behind heavy precipitation, they have the advantage of being able to detect weak precipitation (lower reflectivity), such as drizzle, snow and ice crystal, than S-band or C-band polarimetric radars.

In addition to methods using fuzzy logic, approaches employing Bayesian inference are also commonly applied[3]. Although methods using Bayesian inference demonstrate better discrimination accuracy compared to methods using fuzzy-logic, they present a challenge in that the workload for creating multidimensional probability density distribution models is considerably greater than that for developing membership functions in fuzzy logic. Furthermore, Bayesian inference constitutes ‘supervised learning’ in machine learning, necessitating a substantial amount of labeled training data for classification purposes. However, the creation of labeled training data for particle discrimination using dual-polarization information has been challenging due to the limited number of samples available for creating detailed training data, as it was created by comparing ground observations such as optical disdrometers and high-altitude observations such as video sondes. In response to this, preliminary studies have been conducted to create labeled training data from observation data through cluster analysis of observation data. However, these methods have been limited by poor particle discrimination accuracy and the fact that the work is done manually, resulting in a significantly small number of labeled training data samples.

In our study, we focus particularly on hail within hydrometeor classification and propose a new method for hydrometeor classification with the goal of forecasting hail. This hydrometeor classification method is used in the first stage of our proposed new hail forecasting method (T-SHIBA: Two-Stage, Hydrometer classification and forecasting Induced By SNS, Algorithm), which takes three-dimensional observation data from an X-band polarimetric radar as input and outputs the results of hydrometeor classification in three dimensions (Fig. 1). In the second stage, the method predicts the two-dimensional locations of hail in terms of latitude and longitude based on these three-dimensional hydrometeor classification results. In this hail forecasting technology, we utilize social networking services (SNS), which have rapidly expanded in recent years, and evaluate and improve the hail forecasting technology by identifying the approximate hail locations and the rough times of hail through SNS posts about hail made by the general public.

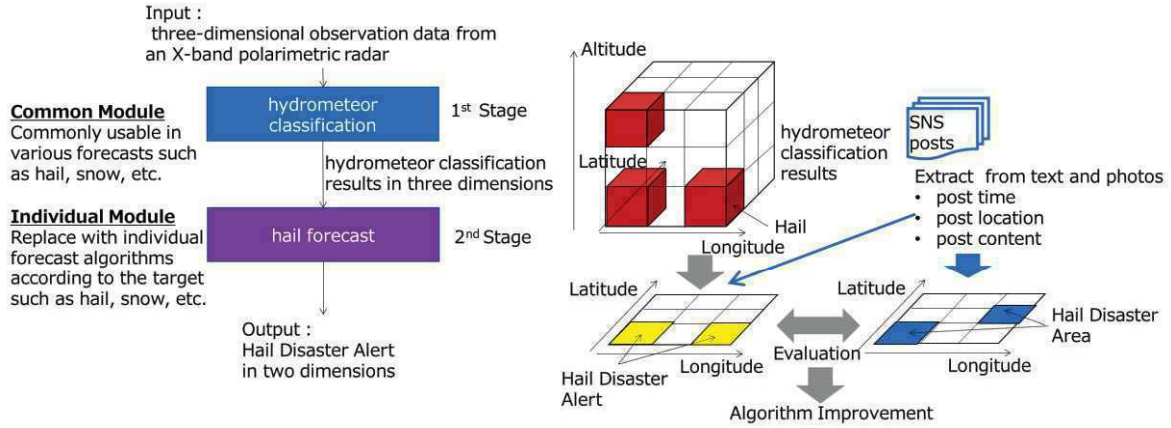


Figure 1: our proposed new hail forecasting method (T-SHIBA)

2.1 Our hydrometeor classification method

In our proposed new method for hydrometeor classification, we improve upon the conventional method with an X-band polarimetric radar using fuzzy logic to classify hydrometeor types into 10 categories; 1)drizzle, 2)rain, 3)wet snow, 4)dry snow, 5)ice crystal, 6)dry graupel, 7)wet graupel, 8)small hail, 9)large hail, 10)rain and hail. Our aim is to establish a method of hydrometeor classification that can reduce the false alarm rate in hail forecasting. In the conventional method, torrential rain without hail is classified as the rain and hail, so even in the case of weather with only torrential rain and no hail, hail is classified, resulting in a high false rate in hail forecasting. Therefore, in our method, we aim to reduce the false rate by adding a category of only torrential rain to the conventional classification, classifying hydrometeor types into 11 categories; 1)drizzle, 2)rain, 3)wet snow, 4)dry snow, 5)ice crystal, 6)dry graupel, 7)wet graupel, 8)small hail, 9)large hail, 10)rain and hail, and 11)torrential rain.

2.2 Dataset

To classify hydrometeor types, we used the data observed by conventional radars in Japan include the X- and C-band parabolic dual-polarization radars that comprise the Ministry of Land, Infrastructure, Transport and Tourism’s eXtended RADar Information Network (XRAIN) (Fig. 2(a)). In this study, we used observational data from five X-band parabolic dual-polarization radars deployed in the Kanto region of Japan (Kanto, Shinyokohama, Funabashi, Ujiie, Yattajima) (Fig. 2(b)). We performed a three-dimensional synthesis of each radar data (Zh, Zdr, Kdp and ρ_{hv}) using Cressman interpolation and converted it into orthogonal coordinates with a resolution of 250m. Furthermore, for temperature and relative humidity, we used values extracted from MSM data that are numerical weather forecasting data using the Japan Meteorological Agency (JMA) meso-scale model.

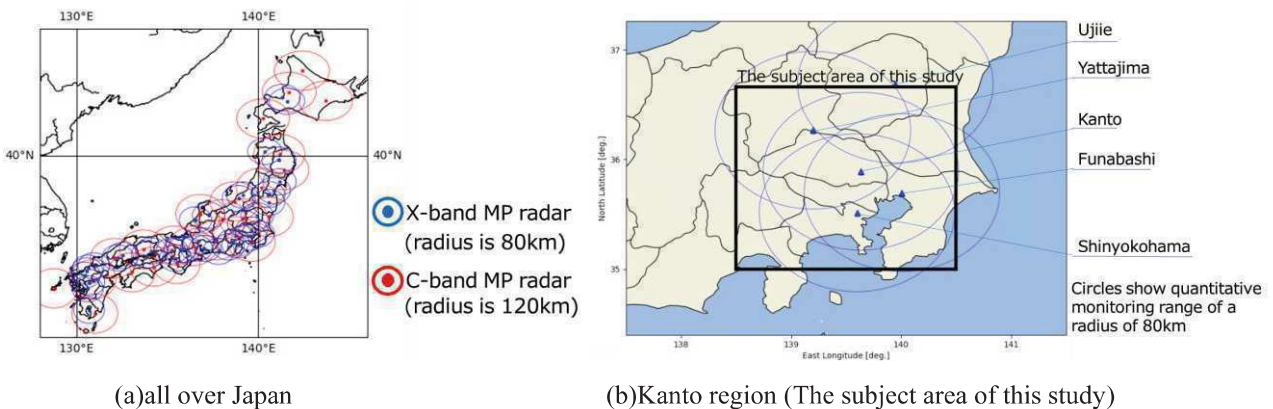


Figure 2: Locations of XRAIN MP radars

3 Gaussian Mixture Model using Bayesian Inference

3.1 Theory and Implementation

The hydrometeor classification algorithm in this study takes four polarization parameters (Zh, Zdr, Kdp, and ρ_{hv}), temperature, and relative humidity as inputs, and outputs classification results for 11 categories; 1)drizzle, 2)rain, 3)wet snow, 4)dry snow, 5)ice crystal, 6)dry graupel, 7)wet graupel, 8)small hail, 9)large hail, 10)rain and hail and 11)torrential rain. To perform this classification, we adopted a mixed Gaussian model using Bayesian inference. In a conventional mixed Gaussian model, once a model is created, it is necessary to relearn from all the accumulated data again if additional learning data is obtained, which requires always saving all data. However, in this study, we used a sequential update type of mixed Gaussian model using Bayesian inference, eliminating the need to save past data. The use of Bayesian inference does have the disadvantage of requiring mathematical knowledge. However, it has many advantages such as being able to handle the uncertainty of the target, naturally incorporating available knowledge, and being less prone to overfitting. Therefore, we judged that it is suitable for adding new categories in a data-driven manner this time, and adopted this method. A mixed Gaussian model is a clustering method that analyzes data under the assumption that it is generated from multiple normal distributions. It estimates which normal distribution each data point belongs to by varying the mean and variance of each normal distribution. In this study, we apply this mixed Gaussian model to supervised learning classification problems.

The graphical model of the assumed Gaussian mixture model is shown in Fig. 3. We assume that there are N independent samples of D-dimensional data, each accompanied by corresponding labeled data S. In our case, D=6, which corresponds to input data consisting of four polarization parameters, temperature, and relative humidity, while S corresponds to output data, which are labels for 11 categories. Here, s is a K-dimensional vector where K is the number of categories; it contains a 1 for the category to which it belongs and 0s for all other elements. For our hydrometeor classification model, since there are 11 categories, K equals 11, resulting in an 11-dimensional vector. To sample this s , we consider a categorical distribution with parameter π , and a model that is a mixture of K Gaussian distributions. We denote the mean of each Gaussian distribution as μ_1, \dots, μ_K , and the precision matrix (the inverse of the covariance matrix) as $\Lambda_1, \dots, \Lambda_K$. In situations where we do not deal with each parameter individually, for simplicity of notation, we denote all parameters of these Gaussian mixture distributions collectively as Θ . Furthermore, in the framework of Bayesian inference, parameters such as the parameter π of the categorical distribution and the μ, Λ of each Gaussian distribution are considered to follow a probability distribution. Here, we assume that each follows a conjugate prior distribution. Parameters such as the parameter π of the categorical distribution and the μ, Λ of each Gaussian distribution follow the distributions shown in equations (1) and (2), respectively. Here, $\text{dir}(\cdot)$ indicates a Dirichlet distribution, and $\text{NW}(\cdot)$ indicates a Gaussian-Wishart distribution. α, m, β, ν, W are hyperparameters, and m is set to a value obtained from insights in the fuzzy logic model. Therefore, considering the joint distribution of the random variables X, S, π, Θ , we get equation (3). Here, $N(\cdot)$ indicates a Gaussian distribution, and $\text{Cat}(\cdot)$ indicates a categorical distribution.

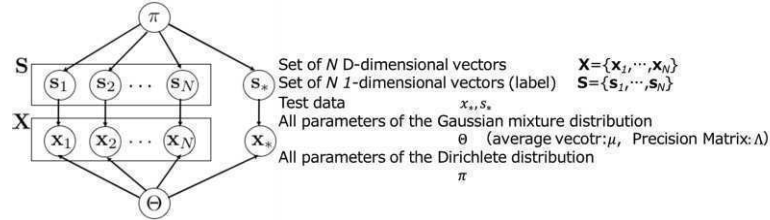


Figure 3: The graphical model of the assumed Gaussian mixture model

$$p(\pi) = \text{dir}(\pi|\alpha) \quad (1)$$

$$p(\mu_k, \Lambda_k) = \text{NW}(\mu_k, \Lambda_k, \mathbf{m}, \beta, \nu, \mathbf{W}) \quad (2)$$

$$p(\mathbf{X}, \mathbf{S}, \pi, \Theta) = p(\mathbf{X}|\mathbf{S}, \Theta)p(\mathbf{S}|\pi)p(\Theta)p(\pi) = \left\{ \prod_{i=1}^N \prod_{k=1}^K N(\mathbf{x}_i|\mu_k, \Lambda_k^{-1})^{s_{i,k}} \text{Cat}(\mathbf{s}_k|\pi) \right\} \left\{ \prod_{k=1}^K p(\mu_k, \Lambda_k) \right\} p(\pi) \quad (3)$$

From equation (3), we derive the posterior distribution of the parameters and the predictive distribution, which is the probability distribution of (s_*) given new data (x_*) . In this case, since we have adopted a conjugate prior distribution as the prior distribution, both the posterior distribution and the predictive distribution can be analytically obtained, and ultimately, equation (4) is derived. When we modify equation (4) so that each hyperparameter can be updated sequentially, we obtain equation (5).

$$p(\mu_k, \Lambda_k | X, S) = \text{NW}(\mu_k, \Lambda_k | \hat{\mathbf{m}}_k, \hat{\beta}_k, \hat{\nu}_k, \hat{\mathbf{W}}_k)$$

$$\hat{\beta}_k = \sum_{i=1}^N s_{i,k} + \beta$$

$$\hat{\nu}_k = \sum_{i=1}^N s_{i,k} + \nu$$

$$\hat{\mathbf{m}}_k = \frac{\sum_{i=1}^N s_{i,k} \mathbf{x}_i + \beta \mathbf{m}}{\hat{\beta}_k}$$

$$\begin{aligned}
 \widehat{\mathbf{W}}_k^{-1} &= \sum_{i=1}^N s_{i,k} \mathbf{x}_i \mathbf{x}_i^T + \beta \mathbf{m} \mathbf{m}^T - \hat{\beta}_k \widehat{\mathbf{m}}_k \widehat{\mathbf{m}}_k^T + \mathbf{W}^{-1} \\
 p(\pi|S) &= \text{dir}(\pi|\hat{\alpha}) \\
 \hat{\alpha}_k &= \sum_{i=1}^N s_{i,k} + \alpha \\
 \hat{\beta}_{n,k} &= \hat{\beta}_{n-1,k} + s_{n,k} \\
 \hat{\nu}_k &= \hat{\nu}_{n-1,k} + s_{n,k} \\
 \widehat{\mathbf{m}}_{n,k} &= \frac{s_{n,k} \mathbf{x}_n + \hat{\beta}_{n-1,k} \widehat{\mathbf{m}}_{n-1,k}}{\hat{\beta}_{n,k}} \\
 \widehat{\mathbf{W}}_{n,k}^{-1} &= \widehat{\mathbf{W}}_{n-1,k}^{-1} + s_{i,k} \mathbf{x}_n \mathbf{x}_n^T + \hat{\beta}_{n-1,k} \widehat{\mathbf{m}}_{n-1,k} \widehat{\mathbf{m}}_{n-1,k}^T - \hat{\beta}_{n,k} \widehat{\mathbf{m}}_{n,k} \widehat{\mathbf{m}}_{n,k}^T \\
 \hat{\alpha}_{n,k} &= \hat{\alpha}_{n-1,k} + s_{n,k}
 \end{aligned} \tag{4}$$

$$\begin{aligned}
 P(s_* | \mathbf{x}_*, \mathbf{X}, \mathbf{S}) &= \frac{P(s_*, \mathbf{x}_*, \mathbf{X}, \mathbf{S})}{P(\mathbf{x}_*, \mathbf{X}, \mathbf{S})} = \frac{P(\mathbf{x}_* | s_*, \mathbf{X}, \mathbf{S}) P(s_*) P(\mathbf{S})}{P(\mathbf{x}_*, \mathbf{X}, \mathbf{S})} \\
 P(s_* = 1 | \mathbf{x}_*, \mathbf{X}, \mathbf{S}) &\propto \hat{\eta}_{n,k} \text{St} \left(\mathbf{x}_* | \widehat{\mathbf{m}}_{n,k}, \frac{(1-D+\hat{\nu}_{n,k})\hat{\beta}_{n,k}}{1+\hat{\beta}_{n,k}} \widehat{\mathbf{W}}_{n,k}, 1-D+\hat{\nu}_{n,k} \right)
 \end{aligned} \tag{6}$$

$$\tag{7}$$

The predictive distribution is used for hydrometeor classification, so it is necessary to find the predictive distribution of (s_*) given new data (\mathbf{x}_*). This predictive distribution is given by equation (7). If we transform equation (6), the update formula for the predictive distribution when the n th data is obtained is given by equation (7). Here, ($\text{St}(\cdot)$) represents a multidimensional Student's t-distribution, and D represents the dimension of \mathbf{x} . Using equation (7), we calculate the probability of each classification and output the classification with the highest probability.

3.2 Training data

To use the hydrometeor classification model shown in equation (7), training data is required. Therefore, first, in order to utilize the knowledge of the conventional fuzzy logic model, we sampled data from each category from the fuzzy logic model and created training data. For this sampling, we used the MCMC method (in this case, we applied the Metropolis-Hastings method, which is one of the MCMC methods) to sample the training data for the conventional 10 categories (Fig. 4).

To create training data for learning a new category of torrential rain without hail, we attempt to extract input data that is strongly presumed to be only torrential rain without hail from the input data classified as rain + hail in the conventional fuzzy theory model. First, we input data from days of torrential rain observed in Kanto region in August 2021, when there were no social media posts about hail, into the conventional fuzzy theory model and extracted the input data classified as rain + hail. Next, we assumed that these input data were generated from a single category of torrential rain and created a single unsupervised Gaussian mixture model. Finally, we sampled training data for the classification of torrential rain without hail using the MCMC method from this unsupervised Gaussian mixture model (Fig. 5). The reason for not using the extracted input data classified as torrential rain + hail directly as training data and instead going through an unsupervised Gaussian mixture model is to allow for an arbitrary number of training data. We conducted the training of the Gaussian mixture model using Bayesian inference, using data for total 11 categories.

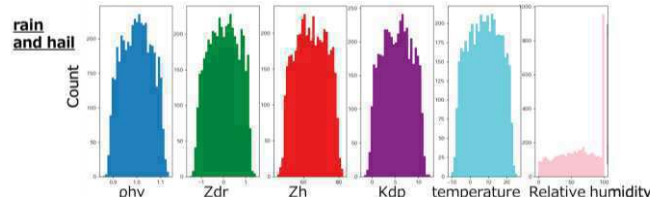


Figure 4: Example of training data sampled from the fuzzy logic model using the MCMC method (rain and hail category)

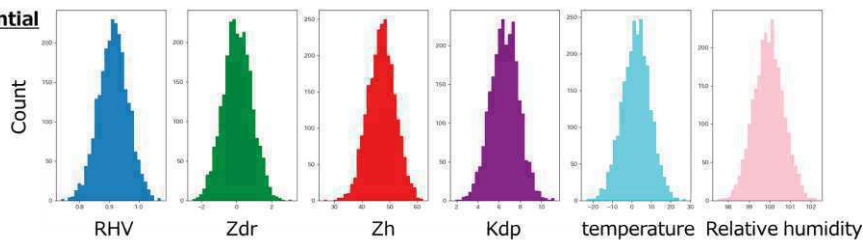


Figure 5: Example of training data sampled from the unsupervised Gaussian mixture model using the MCMC method (torrential rain category)

4 Results

As an example of the classification results by the proposed mixed Gaussian model for the case of a significant hail disaster in the Kanto region of Japan from 14:00 to 18:00 on June 3, 2022, Figure 6 shows a cross-sectional diagram of the hydrometeor classification results at 35.9 degrees north latitude at 15:35 on June 3, 2022. Figure (a) shows the hydrometeor classification results by the Gaussian mixture model before adding the torrential rain category, and Figure (b) shows the hydrometeor classification results by the Gaussian mixture model after adding the torrential rain category.

Figure 6(a) shows the presence of a hail and rain category (indicating the presence of hail) at a latitude of 139.2 degrees and an altitude of 2000-3000 meters, whereas in Figure 6(b), the same area has completely changed to a torrential rain category (indicating no hail). In Figure 6(a), the hail category is present over a wide area, leading to the expectation of social media posts about hail occurrences; however, upon reviewing social media posts for the day and the following day, it was found that there were no posts related to hail in this area during the time frame in question. While it is natural for there to be no social media posts about hail in uninhabited mountainous regions or during the late hours of the night, even if hail actually fell, the area in question is heavily populated and the observations were made during the daytime. Therefore, the absence of social media posts about hail despite the widespread presence of the hail category is unexpected, and it is more reasonable to conclude that no hail occurred.

Figure 7 shows the distribution of Kdp at that time. From the figure, it can be confirmed that the Kdp in the area where the previously mentioned hail and rain category existed is about 5 to 10, indicated by the red color. It is known that Kdp theoretically shows near zero for solids, and if it is about 5 to 10 as in this case, it is strongly presumed to be liquid. Therefore, it can be judged that this part was more likely a torrential rain that contained less solid matter than hail. In this mixed Gaussian model, it can be considered that a model has been constructed that classifies into the torrential rain category unless there is a situation where solids that cause significant hail damage occupy a large proportion in the phenomena of hail and torrential rain, which are meteorologically difficult to separate. As a result, it can be considered that a model that can theoretically reduce the false alarm rate has been obtained.

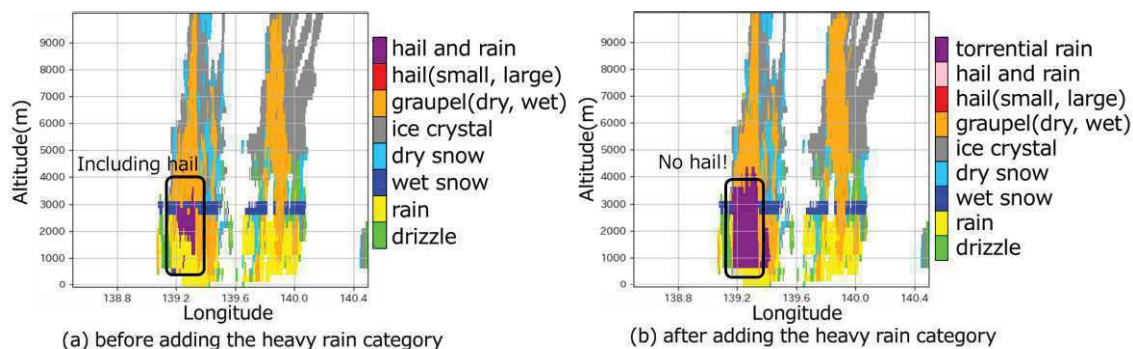


Figure 6: cross-sectional diagram of the hydrometeor classification results at 35.9 degrees north latitude at 15:35 on June 3, 2022

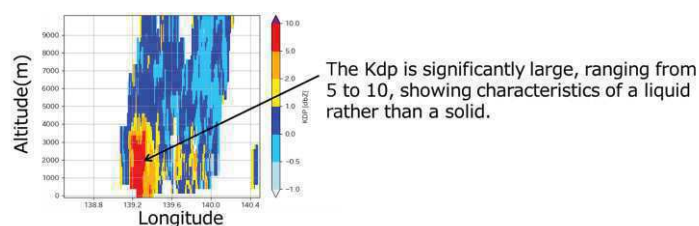


Figure 7: cross-sectional diagram of the Kdp at 35.9 degrees north latitude at 15:35 on June 3, 2022

5 Conclusions

It can be considered that the additional learning of the torrential rain category in the mixed Gaussian model using Bayesian inference has captured the characteristics of Kdp well, and as a result, it has become a model that may reduce the rate of false alarms. A detailed numerical evaluation of the hail forecasting technology using this model will be reported separately.

6 References

- [1]. T.D.Keenan, "Hydrometeor classification with a C-band polarimetric radar", Aust. Met. Mag., 52, 23-31(2003).
- [2]. T.Kouketsu, and H. Uyeda, "Validation of Hydrometeor Classification Method for X-band Polarimetric Radar Comparison with Ground Observation of Solid Hydrometeor", Proc. Sixth European Conference on Radar in Meteorology and Hydrology (ERAD2010), Advances in Radar Technology, Sibiu, Romania, 195-201(2010).
- [3]. Marzano, F. S., D. Scaranari, M. Montopoli, and G. Vulpiani, "Supervised classification and estimation of hydrometeors from C-band dual-polarized radars: A Bayesian approach", IEEE Trans. Geosci. Remote Sens., 46, 85-98(2008).

Rainfall Runoff Analysis Using Rainfall Product with Temporal and Spatial Interpolation of Publicly Accessible Weather Radar Data in Thailand

Kota Tsuzuki ¹, Taichi Tebakari ²

¹*Civil, Human and Environmental Science and Engineering Course, Graduate School of Science and Engineering, Chuo University, Japan*

²*Department of Civil and Environmental Engineering, Chuo University, Japan*



Kota Tsuzuki

1 Introduction

Weather observation systems, including ground rain gauges, radar, and satellites, are essential tools for preventing and mitigating weather-related disasters. Among these, weather radar is particularly valuable for its ability to continuously and quantitatively observe rainfall over large areas with high spatiotemporal resolution. By emitting microwaves and analyzing the reflected signals from raindrops, radar can estimate rainfall intensity, making it a critical resource for applications such as forecasting.

However, the accurate quantitative estimation of precipitation using radar remains a challenge. The widely used Z–R relationship, which estimates rainfall intensity (R) from radar reflectivity (Z), can produce varying results due to differences in raindrop size distribution, measurement heights, and reflectance errors. Research has aimed to refine the Z–R relationship by adjusting it for specific regions, weather conditions, and equipment to improve estimation accuracy. Additionally, issues such as radar beam blockage by topography have prompted studies to develop correction methods that enhance radar accuracy, particularly in complex terrain.

Global advancements in radar technology and data processing have led to significant improvements in precipitation estimation. For instance, Japan's deployment of X-band multiparameter radar and subsequent calibration techniques have markedly increased rainfall measurement accuracy.

The Thai Meteorological Department (TMD) has installed 189 telemetric weather stations throughout Thailand to monitor rainfall. The average area covered by each station is approximately 2,734 km²; however, the resulting data are both spatially and temporally insufficient. Most current studies on weather radar data in Thailand has focused on estimating rainfall intensity based on parameters that can be obtained from radar observations, such as radar reflection factors and interpolation phase differences, as well as composite processing. However, because the data distributed by the TMD are limited to hourly rainfall intensity data after composite processing, it remains difficult to estimate precipitation by performing composite processing on data with known quality issues.

Given these limitations, this study aims to enhance the accuracy and usefulness of weather radar data in Thailand by proposing a new spatiotemporal interpolation method. This approach seeks to generate high-density rainfall data in both space and time, addressing the shortcomings of current methods and contributing to more reliable hydrological data for disaster prevention and mitigation.

2 Target Area / Usage Data

The target area for this study is the entire country of Thailand, using radar rainfall data distributed by the Thai Meteorological Department (TMD). Thailand is equipped with 23 C-band radars. These radars provide data with a temporal resolution of 1 hour and a spatial resolution of 0.01°. The authors have been collecting weather radar data from the TMD since 2018, although some data are missing due to gaps in collection. This study focuses on the period from April 2019 to March 2020, when data availability was relatively better, though still imperfect with a temporal error rate of 39.8%.

Figure 1 illustrates an example of the spatial distribution of rainfall intensity observed by TMD radar, where beam-shaped radar echoes indicate interference from radio waves at the same frequency. These echoes, attributed to insufficient non-precipitation echo elimination, are categorized as error values in this study. Additionally, the radar data show significant spatial gaps, likely due to the shutdown of specific radar sites. Ground rainfall data, used for comparison and validation, were also provided by the TMD and are based on hourly measurements from ground rain gauge.

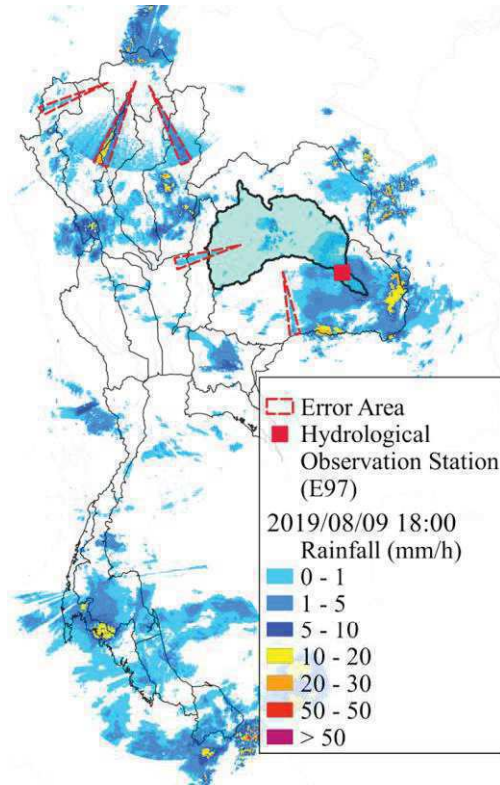


Figure 1: Example of the spatial distribution of rainfall intensity observed by radar of the Thai Meteorological Department (TMD)

3 Methods

3.1 Proposed method for constructing rainfall products

To estimate the spatial distribution of rainfall using weather radar, Foehn *et al.* (2018) proposed a method for spatial correction of radar-estimated rainfall intensity using ground rain gauge data. While most previous research has focused on spatial correction, few studies have addressed temporal gaps in radar data. Therefore, this research introduces a new method for spatiotemporal interpolation of radar data, aiming to create a hybrid rainfall product, as illustrated in Figure 2.

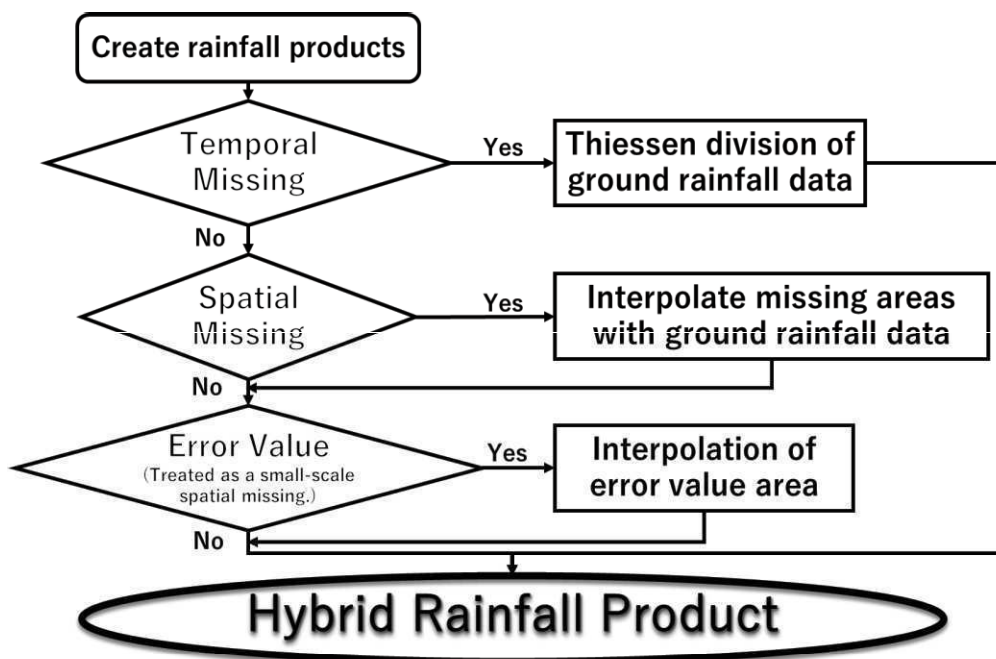


Figure 2: Flow chart of the construction of the proposed rainfall product

To address missing radar precipitation data, we first performed temporal interpolation using Thiessen-divided ground precipitation data, followed by spatial interpolation. For large spatial gaps, ground rainfall data were divided into Thiessen segments and subjected to areal interpolation. Figure 3 shows the seasonal spatial distribution of accumulated rainfall, highlighting regions with error values forming a fan shape around the radar site. These error-prone regions, identified from the accumulated rainfall distribution, were treated as missing observations. These missing values were corrected and interpolated using inverse distance weighting, where the remaining data points were weighted by the inverse of their distances.

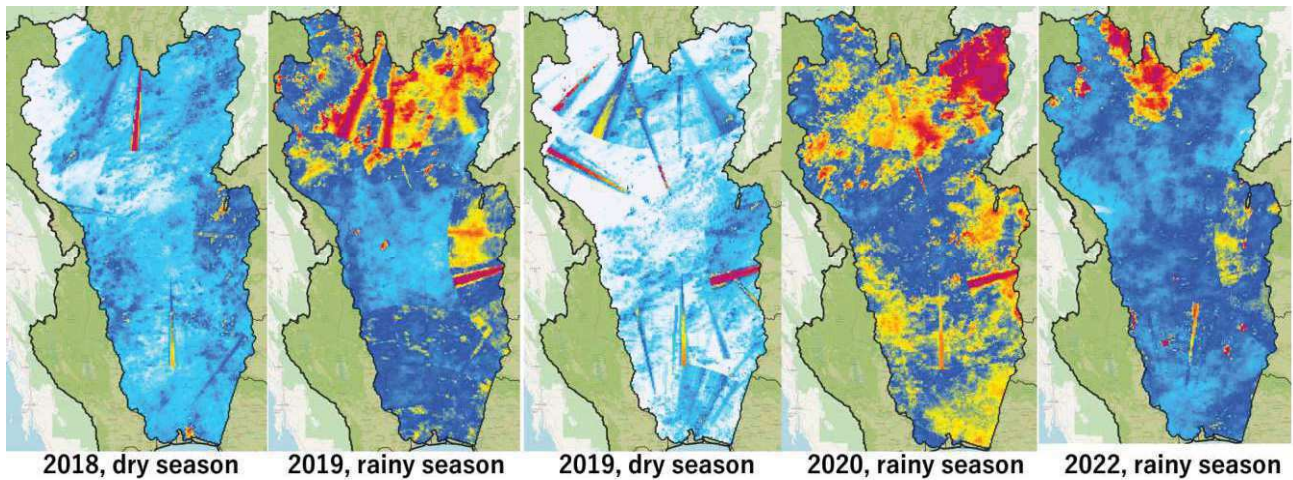


Figure 3: Spatial distribution of seasonal accumulated rainfall according to radar rainfall data in Chao Phraya River basin

Three approaches to error value interpolation were considered, as shown in Figure 4. Error regions are outlined in purple, with error value meshes in black. The red mesh indicates the area targeted for interpolation, while the yellow areas represent the data used for interpolation. In Approach 1, interpolation was performed using observed values in four directions outside the error region. Approach 2 used observed values in eight directions, including diagonals, thus incorporating more data points. Approach 3 interpolated based on values in two directions, reflecting the circular nature of radar observations. The interpolation process started at the edges of the error regions and proceeded inward.

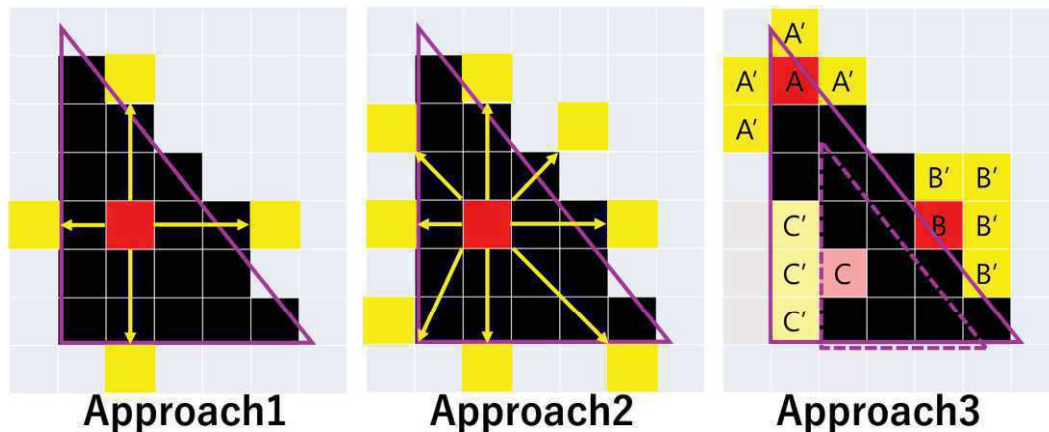


Figure 4: Overview of the three interpolation methods

The differences among the three interpolation methods were evaluated to identify the most accurate approach. This was done by comparing the rainfall data before and after interpolation in areas observed by the radar without errors, determining the most reliable complementation approach.

3.2 Application of the proposed hybrid rainfall product for runoff analysis

The applicability of the rainfall product generated using the proposed method was evaluated through a comparison between observed discharge and rainfall–runoff analysis results. The analysis used the proposed hybrid rainfall product as input into

the Rainfall-Runoff-Inundation (RRI) model (Sayama *et al.*, 2011). The study focused on the Mun and Chi River basins in northeastern Thailand (Figure 1). Ground elevation data were sourced from the MERIT Hydro hydrography dataset, evapotranspiration data were obtained from the Japanese 55-year Reanalysis product (Kobayashi *et al.*, 2015), and land use data were provided by the Land Development Department of Thailand.

4 Results

4.1 Comparison of interpolation results for different approaches

Figure 5 presents scatter plots of observed data for each grid point, alongside the spatial distribution of rainfall before and after interpolation using the three approaches examined in this study. Virtual error value regions (indicated by pink lines) were arbitrarily set in the original data, and comparisons were made by applying each interpolation approach. All approaches tended to underestimate precipitation over time after interpolation, likely due to difficulties in reproducing localized heavy rainfall within the error regions. Among the methods, interpolation approach 2 produced a rainfall distribution that most closely matched the pre-interpolation data, showing greater continuity compared to the other approaches.

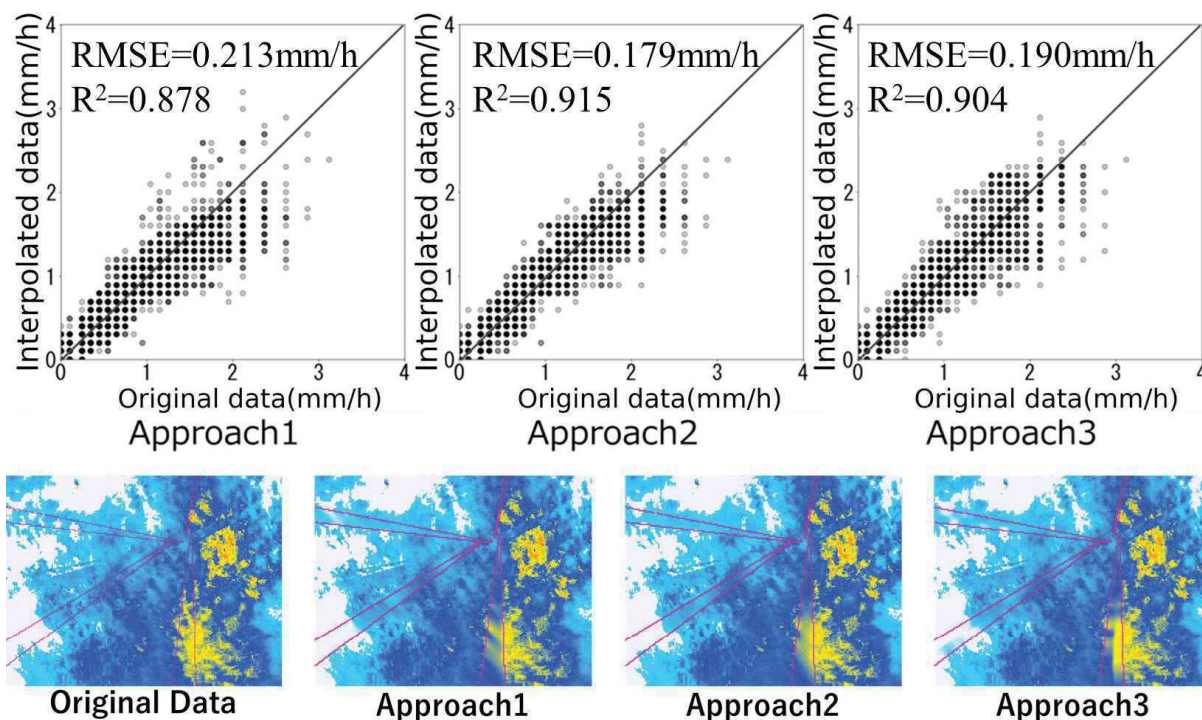


Figure 5: (Upper) Observation data before and after interpolation for each grid point and (lower) spatial distribution of rainfall before and after interpolation using each approach

Approach 3, which interpolates from two directions based on a circular pattern around the radar site, led to abrupt changes in rainfall values at the center of the fan-shaped regions. This resulted in less accurate precipitation estimates. The comparison of the three interpolation approaches revealed that approach 2 demonstrated the highest accuracy, based on both the coefficient of determination and root mean square error (RMSE) values. This makes it the most effective method among the approaches tested. While a larger data set could improve reproducibility, approach 2 was selected for its balance between accuracy and the effective use of available data, making it the basis for the subsequent runoff analyses.

4.2 Runoff analysis results

Figure 6(a) presents the accumulated precipitation time series for ground gauge precipitation (red lines) and the hybrid rainfall product (green lines). While the two products are similar, differences in total annual precipitation were noted: 1,097 mm for the ground gauge and 987 mm for the hybrid product. This discrepancy is attributed to the insufficient number of ground rain gauges and the lack of topographical considerations. Both products show more rainfall on the eastern side of the basin, but the hybrid product differs from the ground gauge data, which is limited by the sparse distribution of rain gauges. This suggests that inadequate gauge coverage hinders accurate precipitation estimates across the entire basin.

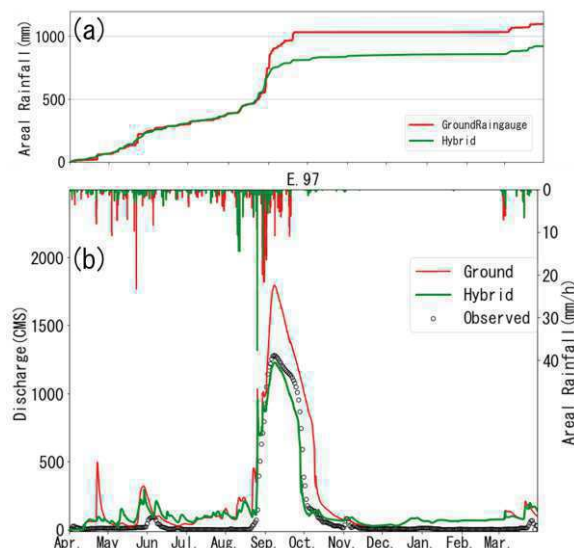


Figure 6: Time series of accumulated precipitation and discharge for each rainfall product

Runoff calculation results using each rainfall product are shown in Figure 6(b), focusing on discharge at station E.97 (Figure 1). The runoff analysis using ground rainfall (red line) and hybrid rainfall (green line) produced different results, with the hybrid product yielding higher accuracy. The Nash-Sutcliffe (N-S) coefficient and peak flow error were 0.90 and $-61.0 \text{ m}^3/\text{s}$ for the hybrid rainfall, and 0.70 and $504 \text{ m}^3/\text{s}$ for the ground rainfall, respectively. These results demonstrate that the hybrid rainfall product, despite some spatiotemporal errors, is effective for runoff analysis.

In summary, the proposed hybrid rainfall product, developed through the interpolation and modification of radar data, proves useful for runoff analysis and is effective for disaster prevention and water resource management, though further refinement may be necessary to address remaining data quality issues.

5 Conclusions

This study developed a hybrid rainfall product by interpolating publicly available weather radar data from the Thai Meteorological Department (TMD) and evaluated its suitability for runoff analysis. Temporal and large-scale spatial data gaps were addressed using ground rainfall data, and radar data errors were corrected through spatial interpolation. Various interpolation approaches were compared, with the hybrid product achieving a Nash–Sutcliffe coefficient of 0.90, demonstrating accurate discharge reproduction.

The proposed hybrid rainfall product is expected to be valuable for flood and water resource management, especially in areas with sparse ground rain gauges. It offers an additional option for rainfall datasets in Thailand, contributing to more accurate rainfall estimation. Future research should focus on enhancing rainfall intensity estimation and refining composite methods to further improve the accuracy of TMD radar-based rainfall estimates.

6 References

- Foehn A, Hernandez JG, Schaeffli B, Cesare GD. 2018. Spatial interpolation of precipitation from multiple rain gauge networks and weather radar data for operational applications in Alpine catchments. *J. Hydrology*. 563: 1092–1110. DOI: 10.1016/j.jhydrol.2018.05.027.
- Kobayashi S, Ota Y, Harada Y, Ebata A, Moriya M, Onoda H, Onogi K, Kamahori H, Kobayashi C, Endo H, Miyaoka K, Takahashi K. 2015. The JRA-55 reanalysis: general specifications and basic characteristics. *Journal of the Meteorological Society of Japan*. Ser. II 93: 5–48. DOI: 10.2151/jmsj.2015-001.
- Sayama T, Tatebe Y, Iwami Y, Tanaka S. 2011. Hydrologic sensitivity of flood runoff and inundation: 2011 Thailand floods in the Chao Phraya River basin. *Natural Hazards Earth System Science* 15:1617–1630. DOI: 10.5194/nhess-15-1617-2015.

Raincell project: Commercial Microwave Links to estimate rainfall at Météo-France

Dominique Faure¹, Pauline Mialhe¹, Pierre Lepetit¹, Laurent Brunier¹, Marielle Gosset², Olivier Laurantin¹, Ludovic Bouilloud¹

¹METEO-FRANCE, Toulouse, France

²IRD/GET, OMP, Toulouse, France



Dominique Faure
Pauline Mialhe
presenting Authors

1 Introduction: Origin of the project

Météo-France has been supporting for many years research works on the integration of new opportunistic sources of data in its operational systems. In 2017, Météo-France started a project named Raincell with two partners, in order to use commercial microwave links (CML) data to improve quantitative precipitation estimation (QPE) in complementarity with standard sensors as rain gauges and weather radars. The scientific partner is IRD (Institut de Recherche pour le Développement) which has a long experience on CML data use, particularly in Africa [1]. The CML data provider is the telecommunication operator Orange. The main feature of this project is to operationally retrieve in real time CML data over the whole country, to produce early after measurement a new fusion QPE product merging CML, radar and rain gauges data.

From December 2022 to June 2024, Orange collected and transmitted in real time to Météo-France high resolution CML data (15 seconds, 0.1 dB of digitalisation, 2 channels by link), covering mainland France and some overseas territories. The network of CML varied a little in time, but more than 4500 links was available each minute.

2 Methodology: Classic method for CML estimation of rainfall

The estimation is based on the attenuation by liquid precipitation of the signal between a pair of CML antennas which constitute a link [2],[3],[4]. Different steps allow to estimate rainfall from the measurement of the raw attenuation (figure 1):

- Definition of wet and dry periods.
- Estimation of a baseline representing the maximal path integrated attenuation (PIA) during the last dry period.
- Estimation of the total PIA_L (in dB) only due to liquid precipitation.
- Estimation of the mean specific attenuation k (in dB/km) by dividing by the length L of the link.
- Then the rain intensity R (in mm/h) can be directly estimated by a k - R relationship:

$$PIA_L = (\text{raw attenuation} - \text{baseline}) = L k = L a R^b \quad (1)$$

with (a,b) depending on the signal frequency [5].

An interest of the k - R relationship is that the b value is close to 1.0 for a large range of frequencies used by CML. Between 18 to 23 GHz the k - R relationship is quite linear.

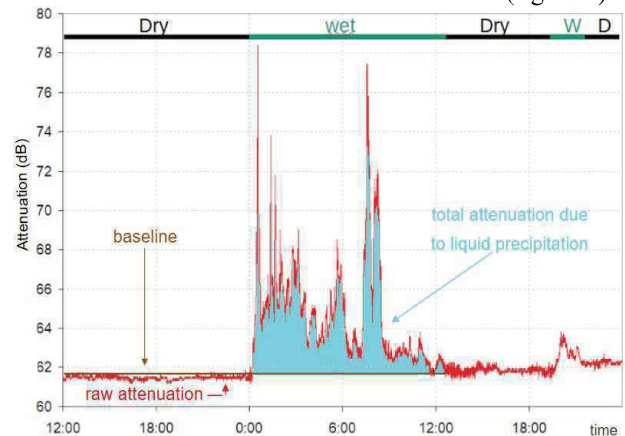


Figure 1: Principle of the CML estimation of rainfall.

3 Incertitude, limits and sources of errors

The sensibility to liquid precipitation increases with frequency, and decreases with length as the attenuation is integrated on all the path. As a result, in general the CML lengths diminish with frequency. Figure 2 shows that each link provided by Orange in 18 months has its own minimal and maximal rainfall detection limits, depending on its couple of frequency and length characteristics. Consequently, some links cannot be used to estimate rainfall on account of their low sensibility, and heavy rainfall can completely attenuate the signal of other links (in this case CML data is missing but not wrong).

But liquid precipitation is not the only source contributing to raw attenuation between two antennas, and the data processing is not perfect. We can notice several sources of error in the CML estimation of rainfall [6],[7],[8],[9]:

- Wrong identification of wet/dry periods, and wrong estimation of the baseline.
- Wet antenna attenuation (WAA) during and after the end of a rain event, or due to dew, drizzle or fog.
- Diurnal variation of the dry attenuation, related for example to the sensibility of each antenna to temperature.
- Atmospheric conditions causing abnormal propagation of the signal between antennas.
- Environment of the link, as tree(s) between two antennas, causing high frequency variations of attenuation when the wind is blowing, or slow drift in spring when the leaves are growing.
- Abrupt or gradual variation of the alignment of the two antennas, which has to be filtered.
- Fog, drizzle, ocean spray which seems to cause great over-estimations for links between islands and continent.
- In winter, ice over the antennas may be the cause of a strong attenuation, reducing the limit of detection (figure 3).
- In winter, and in mountain, we observed great CML over-estimation of precipitations when wet snow occurred (figure 4). The utilisation of HYDRE, a fusion product of Météo-France, to invalidate CML data during short periods of time has been validated, and showed good improvement of the precipitation estimation performance in winter: better correlation (figure 5), suppression of extreme over-estimations.

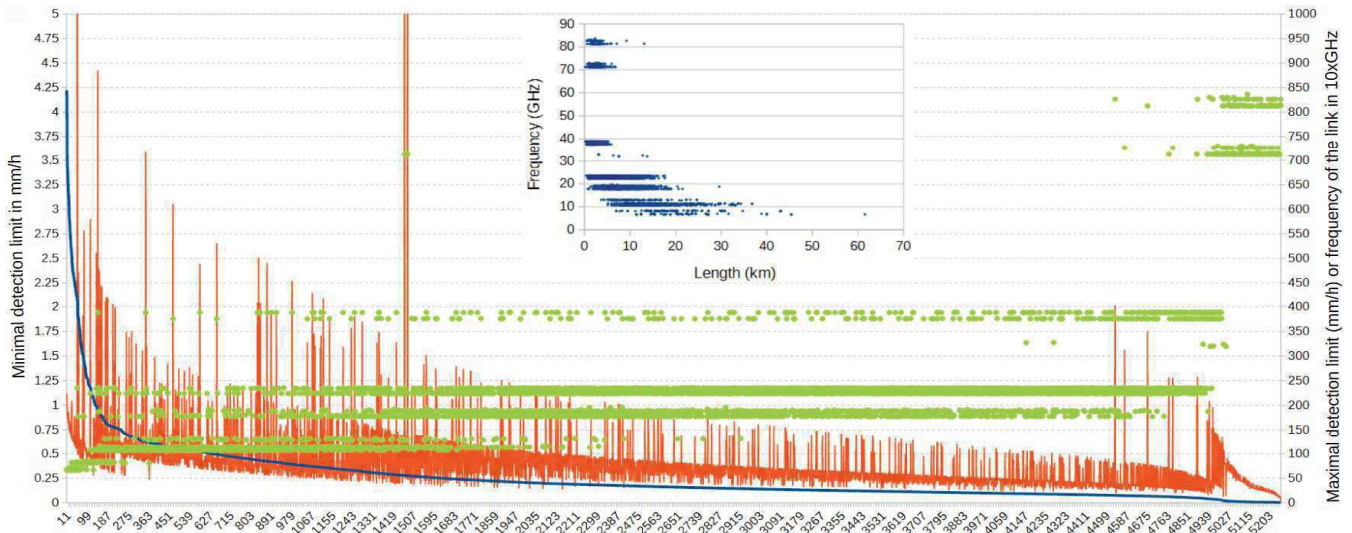


Figure 2: For each 5245 links: in blue curve, minimal detection (i.e. sensibility); in red maximal detection for a 40 dB maximal attenuation usable. In green, frequencies of the links. Ranked in descending order of the minimal detection limit. Insert: distribution of frequencies and lengths.



Figure 3: Before/after cleaning ice. Source/Copyright: Orange.

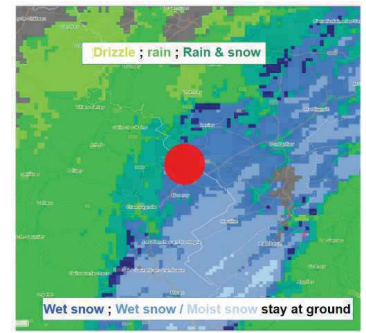
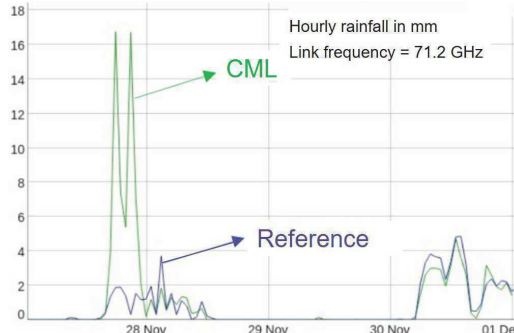


Figure 4: On the left, great over-estimation of CML vs reference estimations. On the right, HYDRE indicates wet snow in the air and staying at ground at the same time.

4 Validation results of classic CML estimations of rainfall

For all the validations, the reference was a 2D fused QPE product merging radar and rain gauges data (named Antilope), integrated on the path of each link, which is the best QPE available at Météo-France at 5-minutes and 1-hour time steps. All the data processing was made exactly as in real time, without knowing the future, and without possibility to modify the past estimates after the delivery of these estimates every minute. Every external data has to be available in real time.

4.1 Validations of the software

These validations over 5 months and for 180 chosen links (18-23 GHz), showed that the main improvements of the code between the different versions was (figure 6):

- the proposition of a new criterion, based uniquely on CML data, to define wet/dry periods (version V1.0),
- the utilisation of a radar QPE product, dated 5 minutes before real time, to define wet/dry periods (version V2.0). In this case, the reference using also radar data, some validation criteria become insignificant, like the probability of detection which is always close to 100% for the V2 CML estimates.

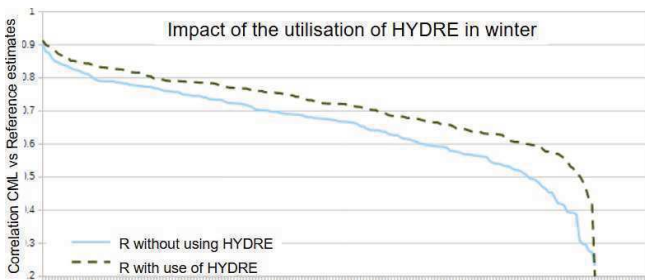


Figure 5: Improvement of the correlation R between 5mn CML estimates and reference, if HYDRE is used to invalidate CML data during short periods of time. Each curve represent 180 result values for 180 links, ranked by decreasing order, estimated from Dec. 2022 to Feb. 2023.

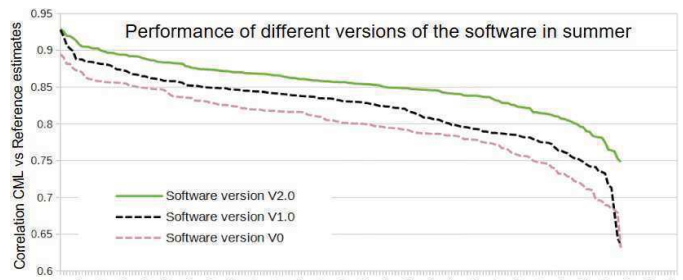


Figure 6: Correlation between CML 5mn estimates and reference, for 3 main versions of the CML data processing software. Ranked independently for each curve by decreasing order for 180 links, from April to August 2023.

4.2 Large validation of CML estimates

A validation of the V2 software estimates, without using HYDRE, has been realised over 1 year of data (Dec. 2022 to Nov. 2023) and for the summer and winter periods, for quite 4000 links available a long period of the time. A minority of links produce very bad rainfall estimates, with very important errors of estimation (figure 7, table 1): these links cannot be used and have to be invalidated. Other links can provide very interesting rainfall estimates, and in this case it is not always easy to determine which of the CML estimates of rainfall or the reference is better. Nevertheless, the data processing is not perfect, and for many links produces a number of false rainfall estimates, mainly small values, which have to be eliminated (red ellipse in figure 8).

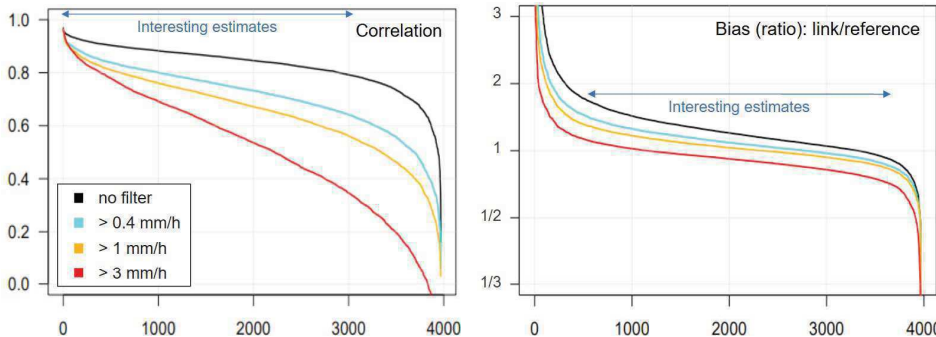


Figure 7: Validation of CML hourly estimates with reference, for about 4000 links, 1 year. Each curve presents all result values by link, ranked independently for each curve by decreasing order.

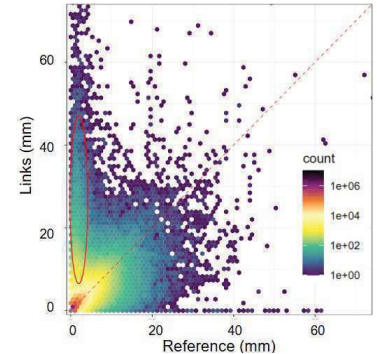


Figure 8: hourly CML and reference estimates, for about 4000 links, 1 year.

mean ± σ	25% closest to reference		50% closest to reference		75% closest to reference		25% the most distant to reference	
	r	bias	r	bias	r	bias	r	bias
No filter	0,89 ± 0,04	+8 % ± 12 %	0,87 ± 0,05	+11 % ± 18 %	0,85 ± 0,07	+17 % ± 27 %	0,75 ± 0,10	+98 % ± 166 %
ref ≥ 0,4 mm	0,80 ± 0,07	-2 % ± 11 %	0,77 ± 0,09	0 % ± 16 %	0,74 ± 0,11	+4 % ± 24 %	0,61 ± 0,14	+67 % ± 73 %
ref ≥ 1 mm	0,75 ± 0,09	-7 % ± 11 %	0,71 ± 0,12	-6 % ± 16 %	0,68 ± 0,13	-3 % ± 23 %	0,55 ± 0,16	+50 % ± 61 %
ref ≥ 3 mm	0,59 ± 0,21	-19 % ± 15 %	0,54 ± 0,23	-19 % ± 21 %	0,51 ± 0,24	-20 % ± 28 %	0,47 ± 0,26	+16 % ± 47 %

Table 1: Mean value and standard deviation (σ) of the correlation (r) and relative bias in % ((link-ref)/ref) between CML rainfall estimates and reference values, 1 year. Estimated for different filtering of the reference values, and for several sets of links function of distance between link estimates and reference, estimated with 3 criteria (r, bias, % of rainy time steps).

Figure 9 presents the impact of frequency and length of the links on results for all year: better results observed for lengths between 6 to 10 km; better results for 18 to 23 GHz, worst results for frequencies below 10 GHz (what was expected). No direct relation was found between the performance of the rainfall estimation and other metadata of the antennas or associated devices. A seasonal analysis also indicates that on average the performance is better in a large summer season (May to September) than in winter (December to February), but it is possible to improve the results in winter if we can eliminate periods of time not suitable for rainfall estimation by using external information (like HYDRE for example).

Remarks: 75% of lengths below 1 km are 38 GHz links, 76% of lengths between 1 and 2 km are 38 and 23 GHz links, 100% of lengths above 20 km are less than 13 GHz links. For lengths below 2 km, the overestimation increases when the frequency decreases (not shown), which could traduce the impact of an under-corrected WAA that impacts highly short links. The correlation is reduced in winter for short and long lengths.

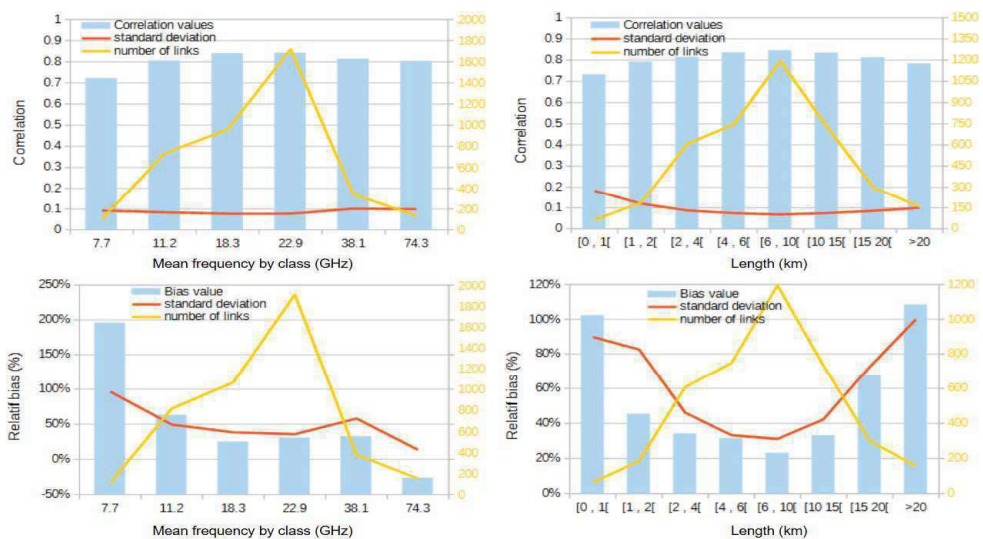


Figure 9: Validation of hourly CML estimates with reference, for 3983 links, 1 year, no use of HYDRE, no filtering. In blue, mean values of the criterion by class of frequency or length. In red, standard deviation of these values for each class. We can note that over-estimations are reduced in summer, and strongly increased in winter (not shown).

5 Preliminary Results for a Machine Learning CML-based QPE

5.1 Motivation

Both version V1 and V2 of the classic software are characterised by a sensible false detection rate. However, recent successes in machine learning (ML) for rain/no-rain (or wet/dry periods) segmentation using attenuation data suggest that ML approaches may improve accuracy of rainfall estimates [10]. Additionally, the classic methodology has limited performance to correct all the sources of errors in the QPE processing. Therefore, a deep learning approach was developed both for wet/dry segmentation and QPE estimation with a 5-minutes resolution. The first results confirm the good performance of ML for the segmentation, but also are encouraging concerning QPE performance.

5.2 Data

To build inputs, the two channelled attenuation data of a link were first centred by subtracting a sliding median and then normalised through a fixed multiplicative factor. For each link, the data series was segmented into 3-days intervals with a 6-hour overlap, except at month transitions, to ensure that entire months could be set aside for performance evaluation. As a result of the 15-seconds time step, the training inputs are arrays of size $2 \times 17,280$. To evaluate the outputs, the 3-days arrays are reassembled into monthly time series to minimise redundancy and edge effects.

The quantitative targets are generated from the 5-minutes reference product as the corresponding wet/dry masks, allowing to attempt both QPE through a time step-wise regression and wet/dry segmentation.

5.3 Methods

Details on loss functions, network architectures, data augmentation practices, may be found on the repository [github.com/nanopiero/CML_processing_by_ML].

Network design and supervision framework: The proposed approach combines a generic wet/dry segmentation with link-specific regression in a multi-task setting inspired from Moraux et al [11]. Attenuations are first passed to a fully convolutional network resembling U-Net [12].

To operate at the native resolution (15 seconds) while maintaining a large receptive field (8 hours), atrous convolution [13] is employed. Moreover, a limited amount of pooling layers and the use of left zero-padding ensure causality. The UNet-like network produces two temporal series: the first represents the estimated probability of rain while the second, representing QPE, feeds a small fully connected network whose weights are specific to the processed CML, allowing a proper calibration. For unknown CML, a non-specific version of this small network provides a generic QPE.

Finally, to address the temporal resolution gap between the 15-seconds outputs and the 5-minutes targets, masked versions of binary cross-entropy (for segmentation) and mean square error (for regression) were used.

Data Augmentation: To enhance generalisation performance, standard strategies are employed such as channel switching and random cropping. Additionally, an additive data augmentation process was implemented which consists in randomly summing attenuation signal to obtain a plausible new signal, notwithstanding the difference in terms of device characteristics (e.g. frequency).

Experimental setup: To evaluate performance on extrapolating to new data, three months of data from each of the 3264 CML in the training set have been set aside (“Test Intra” dataset). Additionally, to assess performance on unknown CML, a separate set of 654 CML has been reserved (“Test Inter” dataset).

Results: The results for the wet/dry classification are consistent with the literature. Figure 10 presents the QPE results for correlation and bias. QPE produced on the links used during training (“Test Intra”) have a quality comparable to the classic software V2 which uses radar data. On the reserved “Test Inter” dataset, the bias appears more variable around the median value. This is due to the fact that the non-specific ending network can hardly provide calibrated outputs.

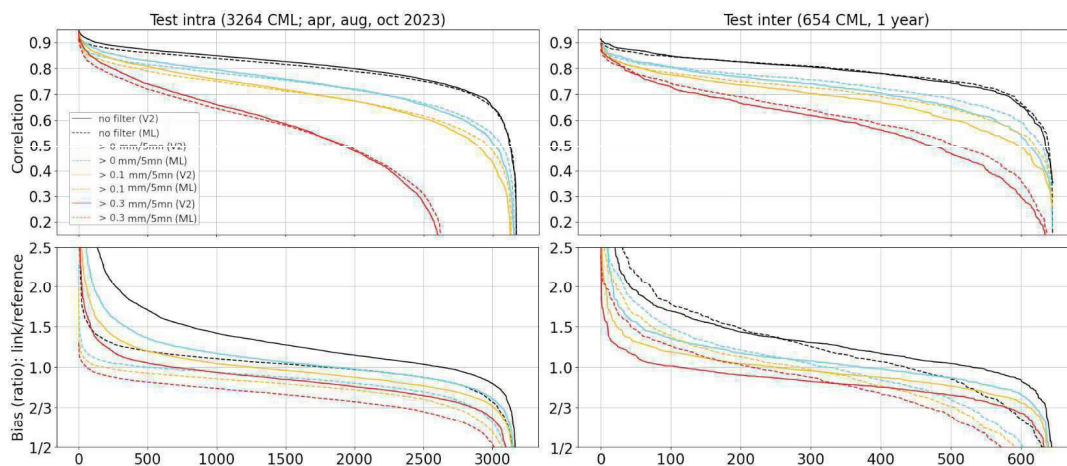


Figure 10: Validation of ML and classic software V2 5mn estimates with reference (“Test Intra” and “Test Inter”), for different filtering. Ranked independently for each curve by decreasing order.

6 Conclusion about a future operational utilisation

The last step of the data processing is to combine the CML estimates of rainfall with other sensor estimates in order to improve our current 2D fused QPE product merging radars and rain gauges data. This work, still on going, is realised by testing different methods, both for the classic CML estimates and the Machine Learning estimates. A specific challenge could be to better take into account the path integrated characteristic of the CML estimates, because this point could be improved. The final values of rainfall will be validated by cross validation with rain gauges measurements, in order to determine if the new fused product improves or not the quantitative precipitation estimation at ground level.

In complex terrain, particularly in mountain, the accuracy of QPE from radars and rain gauges data could be locally limited and the link measurements, realised close to the ground, could help to increase the density of valuable observations. But, as mentioned, this is also in mountain that CML estimates may have reduced performance, particularly in winter. So the improvement could be limited a part of the year, even if HYDRE could help to manage this limit.

In addition to data processing, for a future operational utilisation, other operational tasks need to be validated. In particular, the CML network evolves in time, and each incoming link will require to be evaluated before being used. A long and large validation in operational condition will probably be necessary to validate the introduction of CML estimates in a new operational fused product. Figure 11 shows that for a number of links it is possible to observe a very good agreement between CML estimates and the reference over one entire year.

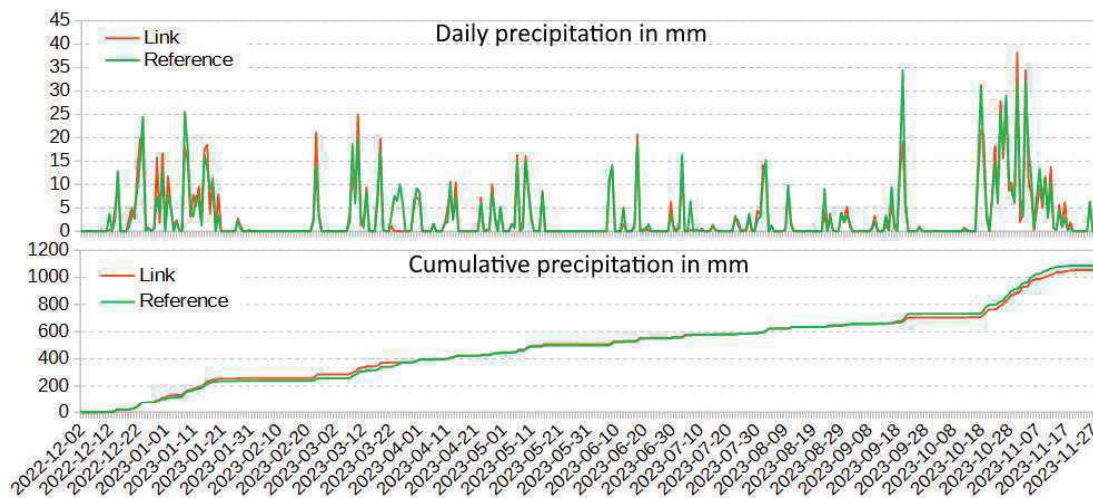


Figure 11: Example of series of CML (orange) and reference (green) estimates of rainfall for one link. Frequency: 38 GHz, length: 4 km, from December 2022 to November 2023.

7 References

- [1] Doumounia, A., Gosset, M., Cazenave, F., Kacou, M., and Zougmore, F.: Rainfall monitoring based on microwave links from cellular telecommunication networks: First results from a West African test bed: wireless networks for rainfall in Africa, *Geophys. Res. Lett.*, 41, 6016–6022, <https://doi.org/10.1002/2014GL060724>, 2014.
- [2] Uijlenhoet R, Overeem A, Leijnse H.: Opportunistic remote sensing of rainfall using micro- wave links from cellular communication networks. *WIREs Water* . 2018;e1289. <https://doi.org/10.1002/wat2.1289>
- [3] Chwala C, Kunstmann H.: Commercial microwave link networks for rainfall observation: Assessment of the current status and future challenges. *WIREs Water*. 2019;6:e1337. <https://doi.org/10.1002/wat2.1337>
- [4] Chwala, C., Gmeiner, A., Qiu, W., Hipp, S., Nienaber, D., Siart, U., Eibert, T., Pohl, M., Seltmann, J., Fritz, J., and Kunstmann, H.: Precipitation observation using microwave backhaul links in the alpine and pre-alpine region of Southern Germany, *Hydrol. Earth Syst. Sci.*, 16, 2647–2661, <https://doi.org/10.5194/hess-16-2647-2012>, 2012.
- [5] ITU-R. (2005). Specific attenuation model for rain for use in prediction meth347 ods (recommendation p.838-3).
- [6] van Leth, T. C., Overeem, A., Leijnse, H., and Uijlenhoet, R.: A measurement campaign to assess sources of error in microwave link rainfall estimation, *Atmos. Meas. Tech.*, 11, 4645–4669, <https://doi.org/10.5194/amt-11-4645-2018>, 2018.
- [7] Pastorek J., Fencel M., Rieckermann J. and Bareš V.: Precipitation Estimates From Commercial Microwave Links: Practical Approaches to Wet-Antenna Correction, in *IEEE Transactions on Geoscience and Remote Sensing*, vol. 60, pp. 1-9, 2022, Art no. 4104409, doi: <https://doi.org/10.1109/TGRS.2021.3110004>.
- [8] Minda, H. and Nakamura, K.: High temporal resolution path-average rain gauge with 50-GHz band microwave, *J. Atmos. Ocean. Tech.*, 22, 165–179, <https://doi.org/10.1175/JTECH-1683.1>, 2005.
- [9] Lian B, Wei Z, Sun X, Li Z, Zhao J.: A Review on Rainfall Measurement Based on Commercial Microwave Links in Wireless Cellular Networks. *Sensors*. 2022; 22(12):4395. <https://doi.org/10.3390/s22124395>.
- [10] Polz, J., Chwala, C., Graf, M., and Kunstmann, H.: Rain event detection in commercial microwave link attenuation data using convolutional neural networks, *Atmos. Meas. Tech.*, 13, 3835–3853, <https://doi.org/10.5194/amt-13-3835-2020>, 2020.
- [11] Moraux A, Dewitte S, Cornelis B, Munteanu A.: Deep Learning for Precipitation Estimation from Satellite and Rain Gauges Measurements. *Remote Sensing*. 2019; 11(21):2463. <https://doi.org/10.3390/rs11212463>.
- [12] Ronneberger O., Fischer P., Brox T.: U-Net: Convolutional Networks for Biomedical Image Segmentation, arXiv:1505.04597, <https://doi.org/10.48550/arXiv.1505.04597>.
- [13] Chen L.-C., Papandreou G., Kokkinos I., Murphy K., Yuille A. L., DeepLab: Semantic Image Segmentation with Deep Convolutional Nets, Atrous Convolution, and Fully Connected CRFs, arXiv:1606.00915, <https://doi.org/10.48550/arXiv.1606.00915>.

A STRAIGHTFORWARD ATMOSPHERIC-RADAR SIMULATOR FOR VERTICAL-AIR MOTION ANALYSIS FROM FREQUENCY-MODULATED CONTINUOUS-WAVE-RADAR RAIN MEASUREMENTS

A. Salcedo-Bosch¹, F. Rocadenbosch^{2,3,*}, A. García-García², S. Lolli¹, R. L. Tanamachi⁴, S. Frasier⁵



Andreu, Salcedo-Bosch

¹Consiglio Nazionale delle Ricerche, Istituto di Metodologie per l'Analisi Ambientale, C. da S. Loja, Tito Scalo, Potenza, 85050, Italy

²CommSensLab-UPC, Department of Signal Theory and Communications (TSC), Universitat Politècnica de Catalunya (UPC)

³Institut d'Estudis Espacials de Catalunya (Institute of Space Studies of Catalonia, IEEC), Barcelona, Spain

⁴Department of Earth, Atmospheric and Planetary Sciences (EAPS), Purdue University, West Lafayette, Indiana

⁵Microwave Remote Sensing Laboratory, University of Massachusetts, Amherst, MA 01003-9284

*francesc.rocadenbosch@upc.edu

1 Introduction

Ground-based S-band Frequency Modulated Continuous Wave (FMCW) radars have been used to assess atmospheric boundary layer precipitation microphysical processes for more than 40 years [1] because they are relatively unaffected by rain attenuation [2]; [3]. Derivation of key rain data products, namely, Drop Size Distribution (DSD) and rain rate (R) from vertically-pointed FMCW radar observations assume that raindrops are Rayleigh scatterers that fall at their terminal velocities, determined by the drop diameter [4]. In absence of Vertical Air Motion (VAM), the droplets' falling terminal velocity is directly related to the radar-measured Doppler frequency. However, in the presence of VAM, the radar-measured Doppler velocity is the superposition of the raindrop's terminal velocity and the corrupting VAM velocity. Even at a fixed measurement location, VAM is a complex phenomenon because it is height- and time-dependent. Storms can contain updrafts, downdrafts, and air turbulence at varying spatial scales (a few cm to a few km) and of varying intensity (0.1 - 80 m s⁻¹).

Different VAM estimation methods have been proposed in the literature [5], [6], [7], [8], [9]. Thus, in W-band ($\lambda = 3.2$ mm), [6] proposed a method to differentiate VAM and raindrops terminal velocity by exploiting Mie scattering. The VAM was determined by comparing the observed spectrum to a predicted spectrum assuming no VAM. However, this is only feasible for very short wavelengths. In UHF band, the so-called Sans Air Motion (SAM) model [7] uses the capabilities of UHF radar profilers to discriminate between Bragg and Rayleigh scattering. While the former type of scattering is prominently associated with fluctuations of the refractive index due with turbulence, the latter is associated to raindrops. During light precipitation, both scattering processes are present. However, during moderate-to-heavy precipitation, Rayleigh scattering dominates, and the SAM model is introduced to estimate the ambient vertical air motion, the spectral broadening, and the raindrop size distribution.

The present work is a continuation of results from the Ph.D. thesis at the CommSensLab by Dr. A. Salcedo (advisor Prof. Rocadenbosch) on VAM estimation, formerly presented in [9], which departs from the historic works of [5]. In [5], the authors proposed a fitting method in which the DSD was assumed to be with an exponential form characterized by two parameters (Marshall-Palmer distribution [10]). This methodology optimized the best fit between the theoretical spectrum retrieved from the DSD model (shifted by VAM) with respect to the experimental spectrum observations. However, it required exponentially distributed drop sizes and it is not suited for convective rain scenarios.

In [9], departing from the proposal by [5], a forward (FWD) method to estimate the VAM from stand-alone radar measurements was first presented. The foundations of this method are to parameterize the DSD as a Gamma distribution [11] and to project this parametric DSD through the radar processing chain up to the retrieved radar-measured reflectivity. Yet, the FWD method conceived in this preliminary form was not exempt from limitations: particularly, negative VAMs (i.e., updrafts) were wrongly corrected and velocity aliasing (i.e., Doppler velocities exceeding the maximum unambiguous radar velocity) were not appropriately taken into account (e.g., leading to complex number exceptions, refer to Sect. 3). The latter is to say that the radar-measured velocity is not the true atmospheric air velocity, but an aliased version of it, instead.

In the present work, in order to investigate and solve these issues, we present a basic atmosphere-to-radar simulator based on FWD modelling of the DSD, VAM and S-band FMCW radar parameters. This technique was conceived to study the impact of VAM on the retrieved radar products and, as a result, we propose an enhanced VAM correction method.

This paper is structured as follows: Sect. 1 summarizes basic state of the art on VAM correction. Sect. 2 presents the UMASS S-band FMCW radar in the context of VORTEX-SE 2017. Sect. 3 introduces the atmosphere-to-radar simulator based on forward modelling. Sect. 4 presents a simulation example. Additionally, a first application to real measurement cases from VORTEX is shown in companion poster. Lastly, Sect. 5 gives concluding remarks.

2 Materials

The S-band FMCW radar was developed by the Microwave Remote Sensing Laboratory (MIRSL), University of Massachusetts (UMASS) [1]. The UMASS radar is a truck-mounted vertical profiling 2.92-GHz FMCW radar using two 2.4-m diameter, 34-dB gain, vertically pointed antennas along with a 250-W transmitter [12]. The radar was operated at a rate of 256 frequency sweeps per 1.34-s interval. The reflectivity-velocity spectrum was measured with 1024 height bins and 256 velocity bins featuring 5-km maximum unambiguous range and $\pm 7.3\text{-m s}^{-1}$ unambiguous velocity (equivalently, $[0\text{-}14.6\text{ m s}^{-1}]$). Twelve such spectra, spanning 16.1-s temporal resolution and 5-m spatial resolution, were then averaged and sixth and third moments (i.e., reflectivity factor and rain rate, respectively) were calculated from the averaged spectra. Volume reflectivity (η , m^{-1}) was estimated from the radar equation radar equation ([4], Eq. (4.16)) and nominal system parameters. Reflectivity factor (Z , $\text{mm}^6\text{-m}^{-3}$) was calculated from volume reflectivity η .

During spring 2016 and spring 2017, the UMASS radar participated in two main measurement campaigns in northern Alabama as part of the Verification of the Origin of Rotation in Tornadoes Experiment-Southeast (VORTEX-SE) [13] [2]. In 2017, hardware upgrades increased the maximum unambiguous velocity from $\pm 4.9\text{ (m s}^{-1}\text{)}$ (2016) to $\pm 7.3\text{ (m s}^{-1}\text{)}$ (2017) [14]. The settings above have defined the instrument settings used in the simulator presented in Sect. 3.

3 Methodology

3.1 Radar-observed reflectivity-velocity spectrum

Central to the FWD-method atmosphere-to-radar simulator developed is formulation of the radar-observed volume reflectivity density of rainfall signals as a function of Doppler velocity, $\eta_{obs,a}(v_{Dop})$ (hereafter, the "reflectivity-velocity spectrum"), which is subject to the superposition of two effects: (i) aliasing by the radar instrument, and (ii) VAM. Detailed radar-retrieval equations are given in Appendix, [3].

We seek to express $\eta_{obs,a}(v_{Dop})$ as a function of the "true" atmospheric volume reflectivity density, $\eta_a(v)$. Subscript "a" is a reminder of "atmosphere", v is the terminal velocity of raindrops, and v_{Dop} is the radar-measured Doppler velocity due to VAM. These two velocities are related as follows:

$$v_{Dop} = v + v_{VAM} \quad (1)$$

where v_{VAM} is the VAM velocity. Because the radar points toward zenith, receding (negative) values of v correspond to upward vertical motion, while inbound (positive) values correspond to downward vertical motion.

The terminal velocity of raindrops follows from the empirical $v(D)$ relation for $0.109 \leq D \leq 6\text{ mm}$ put into analytical form by Atlas et al., [15] and rewritten next in reciprocal form, $D(v)$, for convenience:

$$D(v) = -\frac{1}{0.6} \ln\left(\frac{9.65}{10.3} - \frac{v}{10.3\delta_v(h)}\right), v \geq 0 \quad (2)$$

where $\delta_v(h) \approx 1$ is a second-order height-dependent air density correction. The log term mathematically expresses that D is only defined for $D \geq 0.109\text{ mm}$, as mentioned above.

The volume reflectivity with respect to velocity is computed as

$$\eta(v) = \eta(D) \frac{\partial D}{\partial v} \quad (3)$$

by using the physical relation $\eta(D) = N(D)\sigma(D)$, where $N(D)$ is the DSD and $\sigma(D) = \frac{\pi^5}{\lambda^4} |K_w|^2 D^6$ is the backscattering cross section assuming spherical raindrops ($|K_w|^2 \approx 0.92$) for water at the radar operating frequency, 2.94 GHz). $\frac{\partial D}{\partial v}$ and explicit dependency $D(v)$ are computed from Eq. 2 above.

In the absence of VAM, $v = v_{Dop}$ and reflectivity aliases only occur for high rainfall rates causing reflectivity factor integrand $D^6 N(D)$ (recall that $Z = \int_0^\infty N(D) D^6 dD$) to extend over the radar maximum unambiguous velocity, v_{max} . Under these circumstances, the radar-observed reflectivity-velocity spectrum is the periodized version of $\eta_a(v)$,

$$\eta_{obs,a}^{NO-VAM}(v_{Dop}) = \tilde{\eta}_a(v)|_{v=v_{Dop}}, \quad (4)$$

where

$$\tilde{\eta}_a(v) \approx \eta_a(v) + \eta_a(v - v_{max}) + \eta_a(v + v_{max}), \quad (5)$$

and where symbol \sim is the periodizing operator with period equal to the unambiguous maximum velocity, v_{max} . Retaining one period above and one below $v=0$ is more than sufficient approximation in practice.

In the presence of VAM, Eq. 1 holds and $\eta_{obs,a}(v_{Dop})$ is computed as

$$\eta_{obs,a}(v_{Dop}) \approx \tilde{\eta}_a(v)|_{v=v_{Dop}-v_{VAM,a}} = \tilde{\eta}_a(v_{Dop} - v_{VAM,a}), \quad (6)$$

3.2 Forward Simulator

FWD modeling is the use of a model (in the present case, a parameterized Gamma-model DSD) in order to simulate an observable or measurement (in the present case, the radar-observed reflectivity-velocity spectrum).

Towards this end, Eq. 6 FWD-formulates the radar-observed reflectivity-velocity spectrum as the aliased version (Eq. 5 of atmospheric volume reflectivity $\eta_a(v)$, which is computed from Eq. 3 departing from the atmospheric DSD, $N_a(D)$). The latter is parameterised by defining shape parameters (N_0 , μ and Λ) cast into state vector \mathbf{x}_a . The reader is referred to [9] for detailed formulation of the FWD model.

The FWD simulator operates in two main domains following identical computational procedure: the "atmosphere" domain and the "user" domain. In the "atmosphere" domain, the simulator synthesizes the dataset $\eta_{obs,a}(v_{Dop})$ in response to simulated atmospheric DSD state vector \mathbf{x}_a and atmospheric VAM velocity $v_{VAM,a}$. Alternatively, this dataset can be "switched" to "real data" in order to collect in variable $\eta_{obs,a}(v_{Dop})$ the real measured spectrum by the radar instrument. In the "user" domain the simulator synthesizes the user-estimated reflectivity-velocity spectrum, $\eta_{obs,u}(v_{Dop})$, in response to unknown, user-guessed, DSD state vector \mathbf{x}_u and VAM velocity $v_{VAM,u}$.

The simulator estimates the unknown DSD state-vector \mathbf{x}_u and unknown VAM velocity $v_{VAM,u}$ by either sweeping manually these parameters in a pre-defined multi-dimensional search space or by automatically solving the problem by means of constrained minimization so that $\eta_{obs,u}(v_{Dop}) \approx \eta_{obs,a}(v_{Dop})$ under a minimum least-squares error criterion. From the estimated \mathbf{x}_u and corresponding DSD, the estimated reflectivity factor, \hat{Z}_F , and estimated rain rate, \hat{R}_F , are derived as the 6th and 3rd moments of the DSD, respectively. For *validation and reference*, the solution found by the solver, \hat{Z}_F , is compared (in dBZ units) against different error indicators connected with standard Z-R model relations (e.g., WSR-88D) [4].

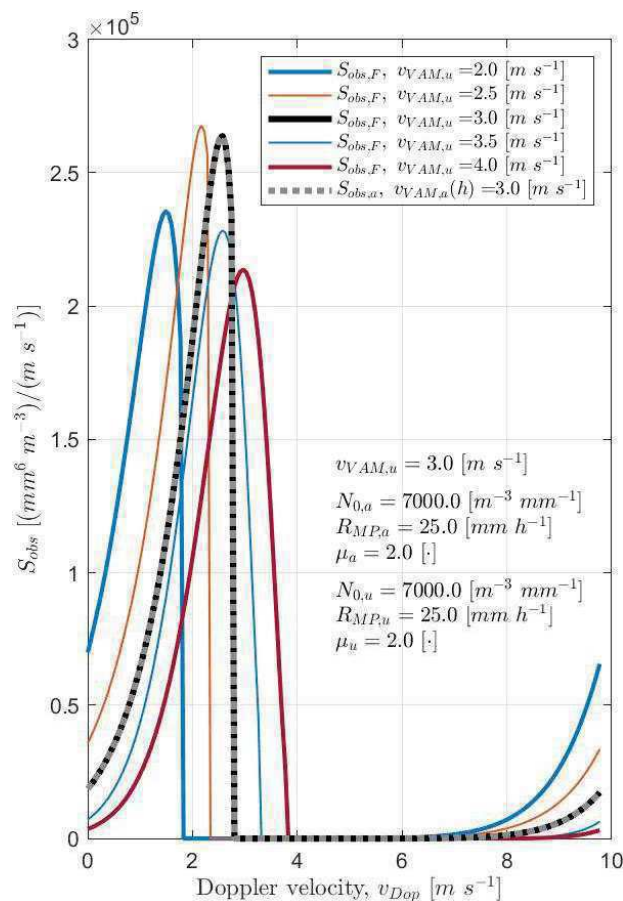


Figure 1: Radar products and VAM estimation analysis. Radar-observed reflectivity-velocity spectrum profile for different VAM velocities.

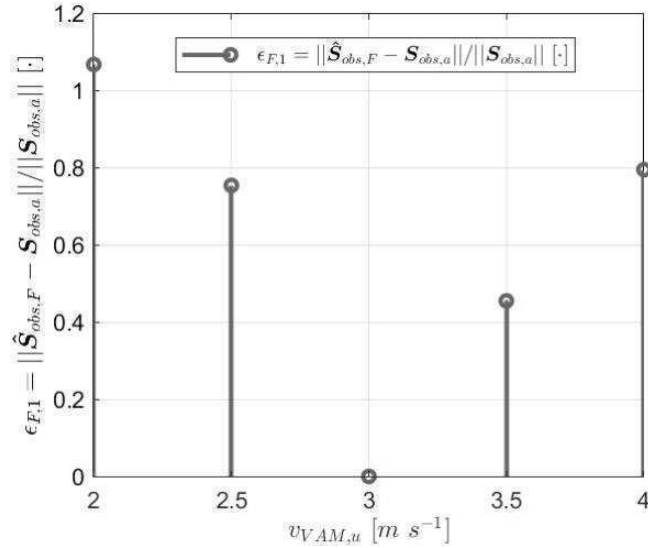


Figure 2: Radar products and VAM estimation analysis. Normalized error norm.

4 Results

The FWD simulator described in Sect. 3 was applied to the retrieval of the DSD, Z and R radar products from a synthetically-generated reflectivity-velocity spectrum in presence of VAM. DSD and VAM velocity parameters are summarized in Tab. 1. Column "atmosphere" domain lists the parameters used to generate the radar-observed atmosphere spectrum. Column "user" domain lists the search intervals used to estimate Gamma DSD shape parameters [9], $\mathbf{x}_u = (N_{0,u}, \mu_u, \Lambda_u)$. In order to best represent radar velocity aliasing, an unambiguous velocity interval $v_{max} = [0, 9.8] m s^{-1}$, as in VORTEX-SE 2016, was considered.

DSD and VAM parameters	ATMOSPHERE domain	User domain
$N_0 [m^{-3} mm^{-1}]$	8×10^3	10^3 to 10^4
$R_{MP} [mm h^{-1}]$	20	0.5 to 150
$\mu [·]$	2.9	-3 to 8
$v_{VAM} [m \cdot s^{-1}]$	2	1 to 3

Table 1: DSD and VAM estimation analysis: Simulation parameters.

Figs. 1-3 show the FWD-estimated results of the simulation. In Fig. 1 $S(v)$ stands for the reflectivity factor density, so that $Z = \int_0^\infty S(v) dv$. Equivalently, $S(v) = \frac{\lambda^4}{\pi^5 |K_w|^2} \eta(v)$.

In Fig. 1, the FWD-synthesized atmospheric reflectivity-velocity spectrum profile (i.e., the "true" one) is denoted $S_{obs,a}$ and plotted in grey dotted trace. The FWD-estimated profiles as function of estimated VAM velocity $v_{VAM,u}$ are denoted $S_{obs,F}$ and plotted in solid-colored traces. The same format applies to Fig. 3, which shows the retrieved DSDs.

Fig. 2 plots the normalized error norm, $\epsilon_{F,1}$, between the *estimated* radar-observed profile $S_{obs,F}$, which is a function of search parameters \mathbf{x}_u , $v_{VAM,u}$, and the "true" one, $S_{obs,a}$, which is generated synthetically. The minimum error norm is attained at $v_{VAM,u} = 2 m s^{-1}$, which is the solution estimated by the solver and which re-encounters the correct solution in perfect coincidence with the simulated atmospheric VAM ($v_{VAM,a} = 2 m s^{-1}$). This is also evidenced in Fig. 1 and Fig. 3 by the solid black trace overlapping the dotted one, which validates the FWD-solver algorithm.

Fig. 3 legend lists the FWD-estimated reflectivity factor, $\hat{Z}_F = 48.5$ dBZ, and estimated rain rate, $\hat{R}_F = 38.7 mm h^{-1}$ at the VAM solution along with the "atmospheric" reflectivity factor observed by the radar, $Z_{obs,a} = 48.6$ dBZ. For further comparison, the Marshall-Palmer Z-R estimate computed as $Z_{MP} = 200 R^{1.6}$ with $R = \hat{R}_F$ yields $\hat{Z}_{MP,F} = 48.4$ dBZ, which is only 0.1 dB below \hat{Z}_F , all of which shows good agreement of the retrieved results.

First application of the FWD-simulator for automatic VAM velocity estimation in real measurement cases is shown in companion ERAD-2024 poster.

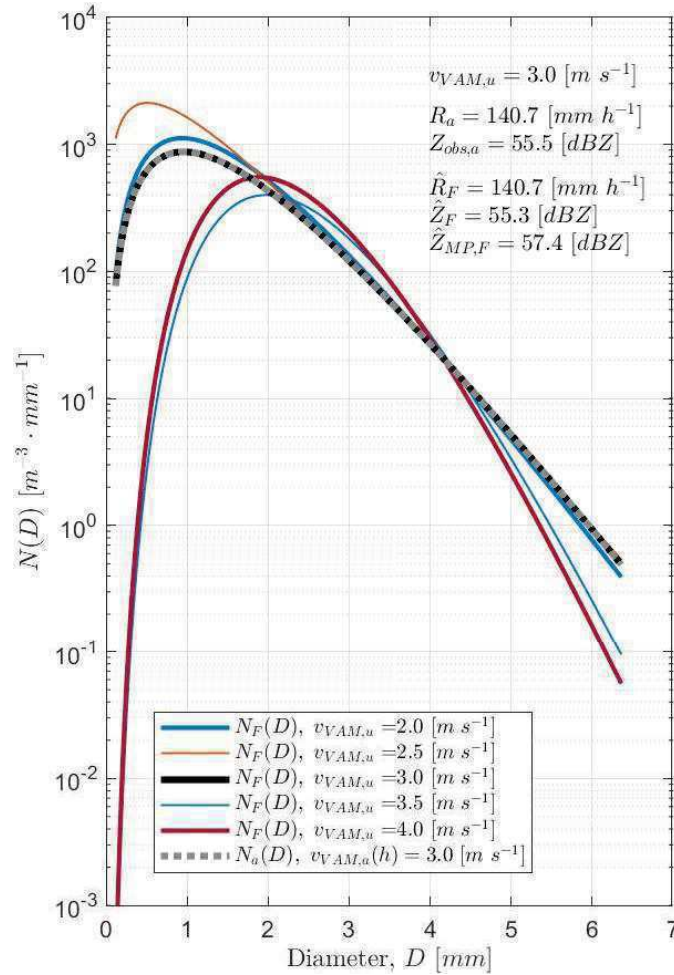


Figure 3: Radar products and VAM estimation analysis. Atmospheric (“true”) vs. FWD-estimated DSDs.

5 Conclusions

An atmosphere-to-radar simulator embedding both a FWD-retrieval method for VAM velocity estimation and a parametric simulator has been presented.

The enhanced FWD method shown, departing from the proposal of [5] and [16], computes second-order radar products DSD, Z and R in response to a Gamma-parameterized DSD and VAM velocity with unknown parameters which are estimated by the FWD-solver. The simulator also embeds simulation of the aliased reflectivity-velocity spectrum to realistically synthesize the “radar observable”. The mathematical formulation of the aliasing problem involved periodizing the volume-reflectivity density by the radar maximum unambiguous velocity.

The results shown pave the way for automatic VAM correction. However, application of the methodology presented to real-case scenarios during intensive observation periods in VORTEX-SE remains, particularly considering the height-dependent and time-dependent variability of VAM in convective scenarios, which makes difficult comparison with ground-based sensors (e.g., disdrometers). Additionally, microphysical processes such as differential sedimentation (size sorting) and drop shedding by melting hail, which can substantially modify DSDs in convective storms, are not accounted for in this parametric model.

6 Acknowledgements

This research is part of the projects PID2021-126436OB-C21 funded by Ministerio de Ciencia e Investigación / Agencia Estatal de Investigación / 10.13039/501100011033/FEDER “Una manera de hacer Europa” and part of the PRIN 2022 PNRR, Project P20224AT3W funded by Ministero dell’Università e della Ricerca”. The European Commission collaborated under projects H2020 ATMO-ACCESS (GA-101008004). The MIRSL contributed the mobile S-band radar. MIRSL and EAPS collected and provided the UMASS FMCW data under their respective VORTEX-SE NOAA grants (NA18OAR4590313).

7 References

- [1] T. Ince, S. J. Frasier, A. Muschinski, and A. L. Pazmany, “An S-band frequency-modulated continuous-wave boundary layer profiler: Description and initial results,” *Radio Sci.*, vol. 38, no. 4, 2003.
- [2] R. L. Tanamachi, S. J. Frasier, J. Waldinger, A. LaFleur, D. D. Turner, and F. Rocadenbosch, “Progress toward Characterization of the Atmospheric Boundary Layer over Northern Alabama Using Observations by a Vertically Pointing,

- S-Band Profiling Radar during VORTEX-Southeast,” *J. Atmos. Ocean. Technol.*, vol. 36, no. 11, pp. 2221–2246, 2019.
- [3] F. Rocadenbosch, R. Barragán, S. J. Frasier, J. Waldinger, D. D. Turner, R. L. Tanamachi, and D. T. Dawson, “Ceilometer-Based Rain-Rate Estimation: A Case-Study Comparison With S-Band Radar and Disdrometer Retrievals in the Context of VORTEX-SE,” *IEEE Trans. Geosci. Remote Sens.*, vol. 58, no. 12, pp. 8268–8284, 2020. [Online]. Available: <https://doi.org/10.1109/TGRS.2020.2984458>
- [4] R. J. Doviak and D. S. Zrnic, “8 - Rain Measurements,” in *Doppler Radar and Weather Observations*, R. J. Doviak and D. S. Zrnic, Eds. Academic Press, 1984, pp. 179–239. [Online]. Available: <https://www.sciencedirect.com/science/article/pii/B9780122214202500132>
- [5] D. Hauser and P. Amayenc, “A New Method for Deducing Hydrometeor-Size Distributions and Vertical Air Motions from Doppler Radar Measurements at Vertical Incidence,” *Journal of Applied Meteorology and Climatology*, vol. 20, no. 5, pp. 547–555, 1981.
- [6] R. M. Lhermitte, “Observation of rain at vertical incidence with a 94 GHz doppler radar: An insight on mie scattering,” *Geophysical Research Letters*, vol. 15, no. 10, pp. 1125–1128, 1988.
- [7] C. R. Williams, “Simultaneous ambient air motion and raindrop size distributions retrieved from UHF vertical incident profiler observations,” *Radio Sci.*, vol. 37, no. 2, pp. 1–22, 2002.
- [8] F. Tridon, J. Van Baelen, and Y. Pointin, “Aliasing in micro rain radar data due to strong vertical winds,” *Geophysical Research Letters*, vol. 38, 2011.
- [9] A. Salcedo, F. Rocadenbosch, S. Frasier, and P. Domínguez, “Forward method for vertical air motion estimation from frequency modulated continuous wave radar rain measurements,” in *11th European Conference on Radar in Meteorology and Hydrology*, Locarno, Switzerland: ERAD, 2022, 29th August–02nd September 2022.
- [10] J. S. Marshall and W. M. K. Palmer, “The distribution of raindrops with size,” *Journal of Meteorology*, vol. 5, no. 4, pp. 165–166, 1948.
- [11] C. W. Ulbrich, “Natural variations in the analytical form of the raindrop size distribution,” *Journal of Climate and Applied Meteorology*, vol. 22, no. 10, pp. 1764–1775, Oct. 1983.
- [12] J. Waldinger, T. Hartley, W. Heberling, S. Frasier, and R. Tanamachi, “S-band FMCW boundary layer profiler: System upgrades and results,” in *2017 IEEE International Geoscience and Remote Sensing Symposium (IGARSS)*, 2017, pp. 4526–4529.
- [13] The National Severe Storms Laboratory (NSSL). (2024) VORTEX–Southeast / VORTEX USA. [Online]. Available: <http://www.nssl.noaa.gov/projects/vortexse/>
- [14] J. Waldinger, T. Hartley, W. Heberling, S. J. Frasier, and R. L. Tanamachi, “S-band FMCW boundary layer profiler: System upgrades and results,” in *2017 IEEE International Geoscience and Remote Sensing Symposium (IGARSS)*, vol. 2017–July. Fort Worth, Texas: IEEE, 2017, p. TH4.L12. [Online]. Available: <http://www.igarss2017.org/Papers/viewpapers.asp?papernum=2567>
- [15] D. Atlas, R. C. Srivastava, and R. S. Sekhon, “Doppler radar characteristics of precipitation at vertical incidence,” *Reviews of Geophysics*, vol. 11, no. 1, pp. 1–35, 1973. [Online]. Available: <https://agupubs.onlinelibrary.wiley.com/doi/abs/10.1029/RG011i001p00001>
- [16] A. Salcedo-Bosch, “Artificial intelligence, lidar and co-operative remote sensing for atmospheric observation and off-shore wind energy,” Ph.D. dissertation, UPC, Departament de Teoria del Senyal i Comunicacions, 2023. [Online]. Available: <https://upcommons.upc.edu/handle/2117/402152>

Rainfall Estimation for Winter Events with Polarimetric VPR Applied to the German Radar Network

Raquel Evaristo¹, Ju-Yu Chen², Alexander Ryzhkov³, Silke Trömel¹

¹Institute for Geosciences, University of Bonn, Bonn, Germany

²Department of Geography, National Kaohsiung Normal University, Kaohsiung, Taiwan

³NOAA/NSSL, Norman, Oklahoma, USA



Evaristo, Raquel

1 Introduction

During the cold season when the freezing level is relatively close to the surface, radar measurements are often affected by the melting layer (ML), which is known for its enhanced reflectivity (Z_H) values comparatively to the rain below. This results in a prominent artificial ring of enhanced surface precipitation surrounding individual radars in the current precipitation products of the German weather service. Strategies to retrieve realistic rainfall at the surface for such cases include the estimation of a vertical profile of reflectivity (VPR; e.g. Seo *et al.*, 2000). These techniques correct the profile of Z_H from the effect of the ML eliminating not only the positive bias introduced by the ML, but also the underestimation caused by overshooting at longer distances to reconstruct the intrinsic profile of Z_H near the surface. The latter is subsequently used to calculate rain rates.

The new strategy proposed here is a polarimetric extension of VPR exploiting polarimetric observations of the ML, hence PVPR, and it was briefly mentioned in Ryzhkov *et al.*, 2022 (section 2.4). The main advantage relies on the detection of the ML edges and application of a correction independently for each radial. The detailed description of the method is presented in section 2. Results of the corrected Z_H field as well as the resulting rainfall are shown in section 3 for a few events occurring in Germany in January 2018.

2 Methodology

Systematic observations of the ML reveal a correlation between the maximum Z_H and the minimum cross-correlation coefficient ρ_{HV} values (Wolfensberger *et al.*, 2016, Griffin *et al.*, 2020). Taking advantage of this fact, the profile of Z_H , which is affected by the bias caused by the ML, is corrected based on the observed profile of ρ_{HV} . This is done through the use of lookuptables that are generated by modeling profiles of both variables for a range of elevation angles. It is considered here that two ML parameters are enough to characterize the ML: the height of the base of the ML (H_b) and the thickness of the ML (ΔH). Lookuptables are generated for a variety of values of H_b and ΔH .

For QPE applications low elevations are commonly used, and therefore the limits of the melting layer may not be very accurate due to beam broadening at long distances from the radar. Therefore an important part of this methodology is finding accurate values of H_b and ΔH , which is performed using the ML detection algorithm by Ryzhkov and Krause, 2022 (MLDA). It uses modelled radial profiles at low elevation and stores them in lookup tables. The observed radial profiles of ρ_{HV} and Z_H are used to determine the range at which the beam is first affected by the ML (r_b) and a new parameter that quantifies the drop of the ρ_{HV} , the ML strength (S). Figure 2 illustrates the process to determine r_b and S from one radial with ρ_{HV} . Once these are calculated, they are matched with the ones in the lookuptables and the MLDA outputs true values of H_b and ΔH , corrected for the effect of beam broadening.

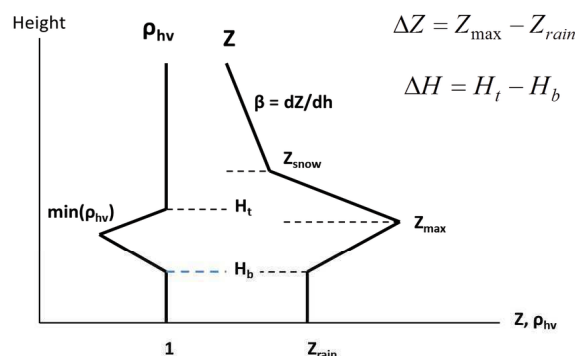


Figure 1: Idealized vertical profile of Z and ρ_{HV} showing the parameters used in the simulated profiles.

The correction of the Z_H profile is an extension of the MLDA. The modelled radials that were previously used to find true H_b and ΔH (given a specific elevation) also contain the information on the Z_H bias introduced by the ML (dz_{cor}), which is stored in separate lookuptables. So for each pair of H_b and ΔH there is a correction for Z_H along the whole beam that is applied to the observed Z_H profile. Profiles of dz_{cor} are shown in figure 3 for a 1° elevation and the whole range of H_b and ΔH . The corrected profile of Z_H ($Z_{H,cor}$) is calculated as:

$$Z_{H,cor} = Z_H - dzcor \quad (1)$$

It is clear from figure 3 that all dzcor curves show a positive bump within the ranges of the ML which decreases to negative values beyond the ML top. This shape ensures that the bias due to the ML is corrected, but also that the decrease of Z_H when the beam enters the snow above the freezing level is compensated (see the definition of β in Figure 1). For a fixed H_b (Figure 3 left panel), the dzcor positive bump increases as ΔH increases, and extends further into the far ranges. When ΔH is fixed location of the dzcor bump is displaced to farther ranges as the H_b increases, and its magnitude decreases. So radials with thicker MLs are subjected to more intense corrections in the Z_H profile, and for the same thickness the correction is more intense if the ML is low.

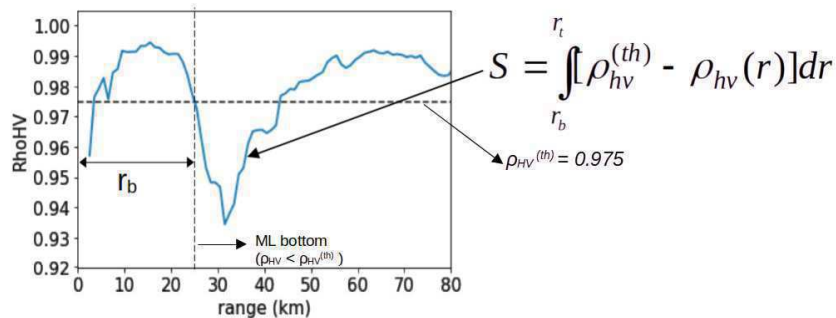


Figure 2: Observed radial profile of ρ_{HV} showing how r_b and S are determined. r_b and r_t are the ranges at which the beam encounters the lower and upper limits of the ML respectively.

2.1 Tests with parameters adjusted to the climate region of Germany

The profiles of dzcor are simulated with certain assumption on the parameters that characterize the profiles of Z_H and ρ_{HV} . The original lookup tables were generated with values based on statistics from several radars from the USA WSR-88D network (Griffin *et al.*, 2020, Ryzhkov and Krause, 2022). However, we are applying this method in a different climate region and with different radar stations, for which the initial assumptions may differ. Therefore new parameters were calculated from statistics based on one local radar (Julian Giles, University of Bonn, personal communication). New lookup tables were first generated using 2 differences from the original in Ryzhkov and Krause (2022): adding $H_b = 0$ for cases where the melting layer is very close to the ground, and a lower Z_{max} (from 36 to 30 dBZ) according to the local statistics. This run was called the default run. Several other parameters were subsequently changed. In order to understand the impact of each of the parameters, only one was changed for the different runs, so that it could be compared with the default run. The parameters that were adapted according to the local climatological values were the value of the maximum Z_H in the melting layer, the rate of change of Z_H with height above the freezing level (β) and the range of ML thicknesses (ΔH). A few other were changed since there doesn't seem to be a consensus about the actual values they should have, as for example the coefficient of attenuation (α) within the ML. The default run applies a multiplicative factor of 2.0 to the value of α in the rain to represent the enhanced attenuation inside the ML, and that multiplicative factor was altered in the test runs. The negative slope of the dzcor curve after the peak was also changed from the default value to better represent the upper edge of the ML, which is usually observed as a relatively abrupt drop in Z_H . Looking at any of the curves in figure 3, this coefficient impacts how fast dzcor decreases with range after it reaches the maximum value.

The parameters used in the different runs are presented in Table 1.

Table I. Z_H profile parameters used in the default and test runs

	Default	Runs
Max ΔH	0.55 km	0.65 km
β	4 dB/km	3.5 dB/km
		5 dB/km
Zmax	30 dBZ	28 dBZ
Multiplicative factor to α within the ML	2.0	2.5
		3
		4
Decreasing slope after the ML peak	1.25	1.5
		1.75

The influence of the varied parameters in the profile of the dzcor is shown in Figure 4, as well as the differences with respect to the default run. The differences are in general low (mostly less than 1 dB, for the fixed values represented). The

largest differences are observed for the runs where β and the decreasing slope are changed from the default. The impact of varying β is mostly observed at far ranges, beyond the melting layer. It also affects affects more intensely profiles that have a low ML height or profiles with thinner MLs (not shown). The effect of varying the decreasing slope has the most impact after the ML peak, and it is stronger in profiles with thicker MLs. The value of the multiplicative factor used for the ML attenuation had an imperceptible impact.

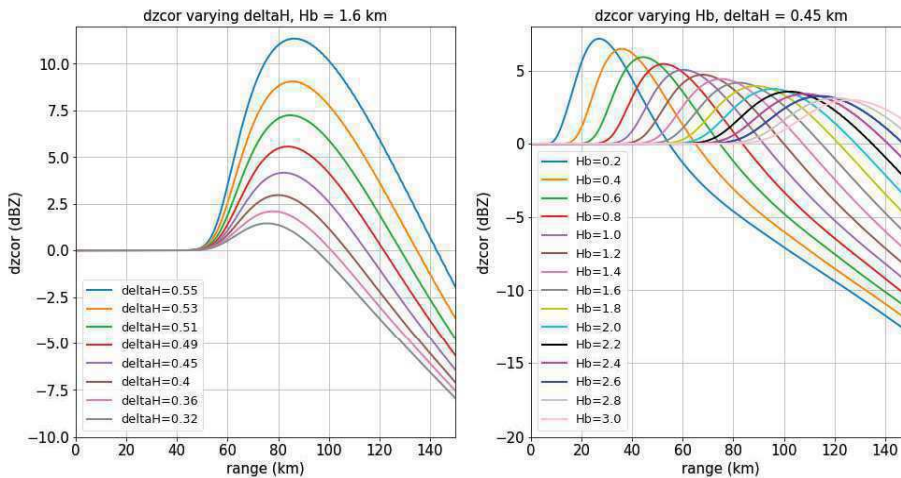


Figure 3: dzcor at 1° elevation for varying ΔH (left panel), and varying H_b (right panel).

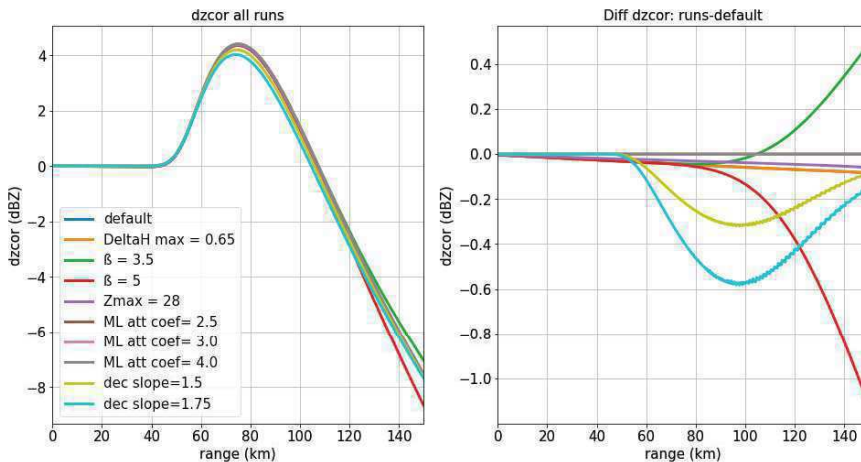


Figure 4: dzcor at 1° elevation for the different runs (left panel) and difference between the default and the other runs (right panel). H_b and ΔH are fixed at 1.6 km and 0.45 km respectively.

3 Results of PVPR application

3.1 Impact on ZH

The application of PVPR to one PPI of Z_H is shown in Figure 5, along with ρ_{HV} . The ML determined with QVP is located between 1000 and 1300 m heights. The drop in ρ_{HV} associated with the ML is observed at a distance of about 30 km from the radar and a ring of enhanced Z_H is observed in the original data at a slightly longer range distance (~50 km, depending on the azimuthal direction). The corrected Z_H shows no sign of the ML ring and enhances certain precipitation features like a line of weak convection to the west of the radar. This line is observed both in previous and subsequent images moving west to east and is a genuine feature that was imperceptible due to the effect of the ML. The effect of the adjustments made to the PVPR in the other runs are too small to be visible on single PPIs. However, the cumulative effect on several hours of QPE can be significant and will be shown in the next section.

3.2 Impact on accumulated rainfall

Using the original and different PVPR runs with the corrected Z_H , the rain rate was derived with 3 different relations that were adjusted to the local climatology: $R(Z_H)$, $R(Z_H, A_h)$, $R(Z_H, K_{DP})$ (Chen *et al.*, 2021). The corresponding rainfall accumulation over 8h is shown in Figure 6 for the relation $R(Z_H, K_{DP})$. The validation is performed by comparing the radar retrievals with rain gauges, also represented in Figure 6 by the small colored circles, and using the same metrics as in Chen *et al.* (2021): normalized root mean square error (NRMSE), normalized mean bias (NMB) and the correlation coefficient

(CC). The effect of the melting layer is obvious when the original Z_H is used, with a circle of extreme rainfall values surrounding the radar, resulting in a large overestimation of the rainfall at intermediate ranges. At far ranges, especially towards the south, the rainfall is underestimated. When the PVPR correction is applied the overestimation ring vanishes, which greatly improves the overall appearance of the rain retrieval. However, there is a generalized underestimation, confirmed by the value of the NMB of about -30% for the default PVPR. The region to the south that is underestimated with the original Z_H is greatly improved with the application of the PVPR. The validation metrics show that the NRMSE decreases from 182% with the original Z_H to 138% when the default PVPR is used. The rainfall calculated with the modified PVPR shown in Figure 6 (right panel) is very similar to the one using the default PVPR, with only slight differences observed. The metrics are slightly improved with the NRMSE decreasing to 128%, NMB decreasing to -23%, and the CC increasing from 0.18 to 0.25.

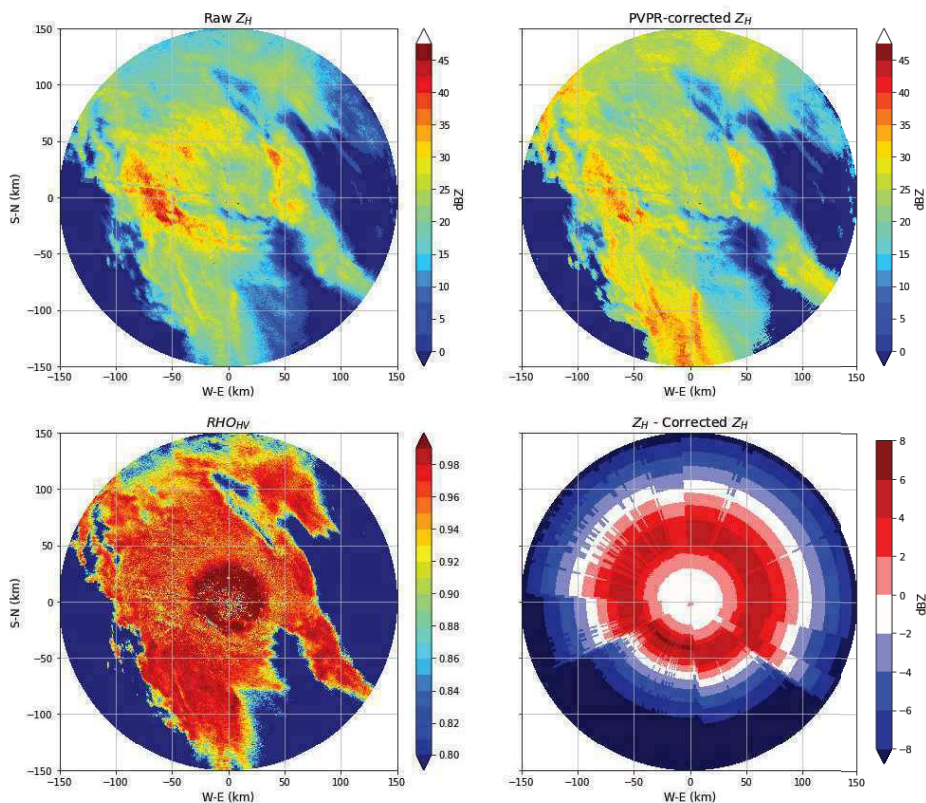


Figure 5: PPI for the Hannover radar on 20180103 at 0150 UTC showing the original Z_H (top left), the PVPR corrected with the default scheme Z_H (top right), ρ_{HV} (bottom left) and the difference between original and corrected Z_H (bottom right). The elevation of the precipitation scan for this radar varies between $\sim 0.8^\circ$ in the north and $\sim 1.4^\circ$ in the south.

The effect of the different PVPR runs is summarized in Figure 7, where the NRMSE is shown for the different runs (horizontal axis) and for a number of cases or radars (colored lines). As expected according to Figure 4, the main differences with respect to the default run are observed for the runs where β and was changed. For most cases reducing the value of β from 4 to 3.5 dB/km contributed to a slight decrease in the value of the NRMSE while increasing it to 5 dB/km increased it. However, for one event the opposite happened with 3 of the radars (20180103 fld, hnr and boo), where a higher value of β resulted in a decrease in NRMSE. Detailed analysis of QVPs for this event show an average β close to 5 dB/km, in contrast to others which show values closer to 3.5 dB/km. This suggests that a universal value for β may not be ideal to correct the profile of Z_H , and that the statistics may need to be adjusted depending on the vertical profile of Z_H above the ML retrieved from QVP. The impact of all the other runs seems to be very small in terms of NRMSE. However, the decreasing slope after the melting layer does show in some cases an impact in either the NMB or the CC, or both (not shown).

4 Conclusions

The application of the PVPR technique for QPE shows great improvement in removing the effect of the ML and the low Z_H at far ranges associated with the beam overshooting the ML. When the default parameters of the PVPR are modified from the default value, there is only a very limited impact on the resulting QPE. Of all the parameters that were changed (see table I) the one that shows the greatest impact was the change in β . However, for some cases the metrics showed an improvement when β was increased to 5 dB/km while for other cases the performance was better when β was decreased to 3.5 dB/km. This suggests that β may need to be adjusted on a case by case basis in order to obtain the most accurate estimate of

rainfall. Most other parameters showed only small changes in the validation metrics, with only the decreasing slope of dzcor after the melting layer showing some visible improvement in NMB and/or CC.

So far the parameters were tested independently from each other. It is possible that the combination of some of the parameters further improves the final rainfall retrievals. Future work includes the use of some machine learning techniques to test the combinations that produce the best results.

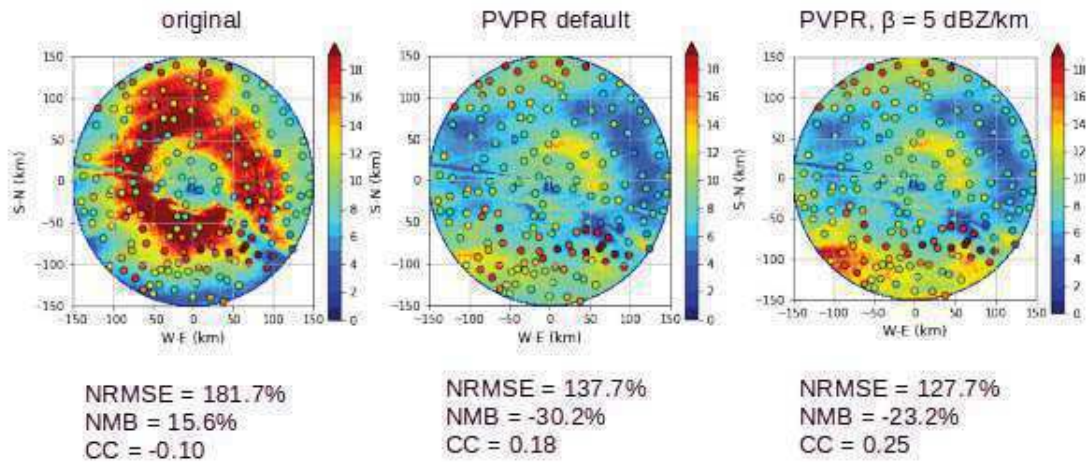


Figure 6: Accumulated rainfall calculated from the $R(Z_H, K_{DP})$ relation for the Hannover (hnr) radar on 20180103 between 00 and 08UTC. Left uses the original Z_H , center the default PVPR correction and right the PVPR correction for the run with β modified to 5 dBZ/km. The small colored circles indicate the accumulation measured by the surrounding rain gauges. Below each panel the validation statistics (NRMSE, NMB, CC) with respect to the rain gauges are shown.

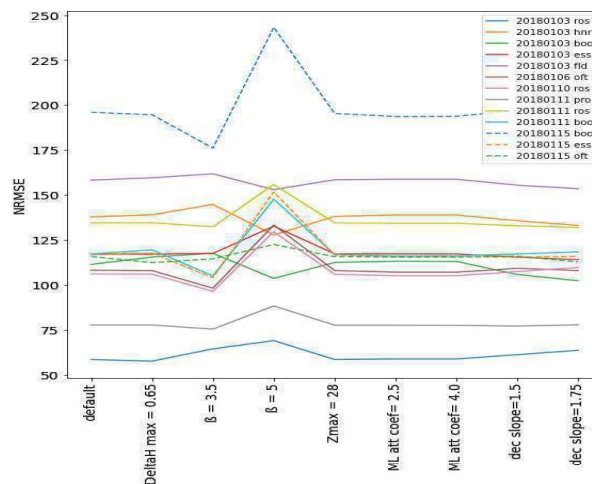


Figure 7: NRME for varying parameters within the Z_H model applied to different events and radars.

5 Acknowledgements

A special thank is due to Julian Giles from the University of Bonn for providing the vertical profile statistics for Germany.

6 References

Chen, J., S. Trömel, A. Ryzhkov, and C. Simmer, 2021: Assessing the Benefits of Specific Attenuation for Quantitative Precipitation Estimation with a C-Band Radar Network. *J. Hydrometeor.*, **22**, 2617–2631, <https://doi.org/10.1175/JHM-D-20-0299.1>.

Griffin, E. M., T. J. Schuur, and A. V. Ryzhkov, 2020: A Polarimetric Radar Analysis of Ice Microphysical Processes in Melting Layers of Winter Storms Using S-Band Quasi-Vertical Profiles. *J. Appl. Meteor. Climatol.*, **59**, 751–767, <https://doi.org/10.1175/JAMC-D-19-0128.1>.

Ryzhkov, A., and J. Krause, 2022: New Polarimetric Radar Algorithm for Melting-Layer Detection and Determination of Its Height. *J. Atmos. Oceanic Technol.*, **39**, 529–543, <https://doi.org/10.1175/JTECH-D-21-0130.1>.

Ryzhkov, Alexander, Pengfei Zhang, Petar Bukovčić, Jian Zhang, and Stephen Cocks, 2022: Polarimetric Radar Quantitative Precipitation Estimation. *Remote Sensing* **14**, no. 7: 1695. <https://doi.org/10.3390/rs14071695>

Seo, D., J. Breidenbach, R. Fulton, D. Miller, and T. O’Bannon, 2000: Real-Time Adjustment of Range-Dependent Biases in WSR-88D Rainfall Estimates due to Nonuniform Vertical Profile of Reflectivity. *J. Hydrometeor.*, **1**, 222–240, [https://doi.org/10.1175/1525-7541\(2000\)001<0222:RTAORD>2.0.CO;2](https://doi.org/10.1175/1525-7541(2000)001<0222:RTAORD>2.0.CO;2).

Wolfensberger, D., Scipion, D. and Berne, A., 2016: Detection and characterization of the melting layer based on polarimetric radar scans. *Quarterly Journal of the Royal Meteorological Society*, **142**, pp.108–124.

The Mean Diameter Update Approach for Ensemble-Based Dual-Polarimetric Radar Data Assimilation

Kao-Shen Chung¹, Bing-Xue Zhuang¹, Wei-Yu Chang¹, Chih-Chien Tsai²

¹Department of Atmospheric Sciences, National Central University, Taoyuan City, Taiwan

²National Science and Technology Center for Disaster Reduction, New Taipei City, Taiwan



Kao-Shen Chung

1 Introduction

For the past decades, Doppler weather radars have been gradually upgraded to dual-polarization radars, which can measure dual-polarimetric (dual-pol) parameters, such as differential reflectivity (Z_{DR}), specific differential phase (K_{DP}), and co-polar correlation coefficient (ρ_{hv}). Dual-pol parameters has been widely used in quantitative precipitation estimation (QPE; Ryzhkov and Zrnić 1996; Brandes et al. 2002) and hydrometeor classification algorithm (Park et al. 2009). With additional information related to hydrometeors, assimilating dual-pol parameters is expected to improve the microphysical states and rainfall forecasts. Studies assimilating dual-pol parameters via the variational method modified the formula for rainwater content estimation (Wu et al. 2000; Li and Mecikalski 2010, 2012). The dual-pol observation operator converting model variables to dual-pol parameters (Jung et al. 2008, 2010) enables model validation with dual-pol parameters and direct assimilation of dual-pol parameters with ensemble Kalman filter. Putnam et al. (2019) first attempted to assimilate Z_{DR} observations with the operator proposed by Jung et al. (2010) in the real case. The mesocyclone structure was well captured in the analysis field with the assimilation of Z_{DR} . Tsai and Chung (2020) revealed that assimilating dual-pol parameters achieves further improvement in short-term forecasts.

The aforementioned studies update rainwater mixing ratio (q_r) and total number concentration (N_{Tr}) with the assimilated Z_{DR} observations. The mean diameter of raindrops is consequently updated implicitly since it is the ratio between q_r and N_{Tr} . A hypothesis is raised that leveraging the relationship between Z_{DR} and the mean diameter of raindrops in the DA procedure may have the capability to further improve microphysical states. Therefore, this study attempts to develop a novel approach to updating the mean diameter of raindrops explicitly with the assimilated Z_{DR} observations, which is expected to result in more precise microphysical states than updating q_r and N_{Tr} separately. In order to prove the feasibility of this novel approach, the observations system simulation experiment (OSSE) is conducted. Moreover, three different high-impact weather systems are selected to execute the novel approach in reality.

2 Methodology

2.1 Radar Data Assimilation System

The radar DA system employed in this study couples the Weather Research and Forecast (WRF) model and local ensemble transform Kalman filter (LETKF), named WRF-LETKF radar assimilation system (WLRAS; Tsai et al. 2014). The observation operator introduced by Jung et al. (2008) is integrated in WLRAS. Based on the bulk microphysics parameterization (MP) schemes and T-matrix simulation, model variables can be converted to simulated dual-pol parameters. The horizontal reflectivity factor (Z_h) and vertical reflectivity factor (Z_v) are calculated as

$$Z_{h,x} = \frac{4\lambda^4}{\pi^4 |K_w|^2} \int N_x(D) (A |f_{a,x}(\pi)|^2 + B |f_{b,x}(\pi)|^2 + 2C |f_{a,x}(\pi)| |f_{b,x}(\pi)|) dD, \quad (4)$$

$$Z_{v,x} = \frac{4\lambda^4}{\pi^4 |K_w|^2} \int N_x(D) (B |f_{a,x}(\pi)|^2 + A |f_{b,x}(\pi)|^2 + 2C |f_{a,x}(\pi)| |f_{b,x}(\pi)|) dD, \quad (5)$$

where λ is the wavelength, and K_w is the dielectric factor of water. Inside the integration are the hydrometeor size distribution ($N_x(D)$), major and minor scattering amplitudes ($f_{a,x}$ and $f_{b,x}$) simulated by T-matrix, and coefficients related to the canting angle of hydrometeors (A , B , and C). Subscript x can be r , s , and g which represent rain, snow, and graupel, respectively. After transforming the all the hydrometeor variables to $Z_{h,x}$ and $Z_{v,x}$ and taking the decibel scale of the linear combination, simulated Z_H and Z_V are obtained. Subsequently, the simulated Z_{DR} can be calculated by the following equation,

$$Z_{DR} = Z_H - Z_V. \quad (6)$$

Since the axis ratio of ice-phased hydrometeors is a fixed value, the difference between Z_H and Z_V is limited, leading to the simulated Z_{DR} close to 0 above the melting layer.

2.2 Mean Diameter Update Approach

The same value of Z_H can correspond to various values of Z_{DR} , indicating that Z_{DR} is independent of Z_H to a certain degree. Assimilating Z_{DR} in addition to Z_H can provide external correction in microphysical states. Consequently, previous studies assimilated Z_{DR} observations to update the common prognostic variables in double-moment MP schemes, q_r and N_{Tr} . The mass weighted mean diameter (D_m) can be diagnosed via the following equations,

$$\Lambda = \left[\frac{\pi \rho_w N_{Tr} \Gamma(\mu+4)}{6 \rho_a q_r \Gamma(\mu+1)} \right]^{\frac{1}{3}}, \quad (7)$$

$$D_m = \frac{4+\mu}{\Lambda}, \quad (8)$$

where Λ and μ are the slope and shape parameters of the three-parameter gamma distribution; ρ_w and ρ_a are the density of water and air, respectively. Updating q_r and N_{Tr} with the radar observations implicitly updates D_m based on Eq. (9) and (10). The joint frequency of D_m and Z_{DR} simulated by WRF double-moment 6-category (WDM6) MP scheme is shown in Figure 1a. The one-to-one relationship aligns with the principle of dual-polarimetric parameters that larger raindrops lead to larger Z_{DR} values. Leveraging this one-to-one relationship may be able to enhance the correction in the D_m analysis. Therefore, this study attempts to develop a mean diameter update (MDU) approach to update D_m explicitly in WLRAS.

According to Eq. (7) and (8), D_m can be recognized as mass evenly distributed to every raindrop. Therefore, the D_m value could be extremely large if the N_{Tr} value is small. To prevent unrealistic D_m values, a threshold is essential when executing the MDU approach. Since D_m is proportional to the reciprocal of Λ , the Λ minimum can be recognized as the D_m maximum. Based on the Λ minimum in WDM6 scheme, the D_m maximum is 2.5 mm correspondingly. The D_m value in Figure 1a can actually be higher than 2.5 mm; therefore, the D_m value smaller than 3.0 mm is set as the threshold to execute the MDU approach. The complete procedure of the MDU approach is summarized in Figure 1b. First, D_m is diagnosed via Eq. (7) and (8). If all the ensemble members at a certain grid point have D_m values smaller than 3.0 mm, the MDU approach is executed to update D_m with assimilated Z_{DR} observations explicitly; otherwise, Z_{DR} observations are assimilated to update q_r and N_{Tr} as the previous studies did. After obtaining the q_r , N_{Tr} , and D_m analyses, q_{r_new} and N_{Tr_new} are subsequently diagnosed via the following equations,

$$q_{r_new} = \left[\frac{D_m}{(4+\mu)} \right]^3 \frac{\rho_w \pi \Gamma(\mu+4) N_{Tr}}{6 \rho_a \Gamma(\mu+1)}, \quad (9)$$

$$N_{Tr_new} = \left[\frac{(4+\mu)}{D_m} \right]^3 \frac{6 \rho_a q_r \Gamma(\mu+1)}{\pi \rho_w \Gamma(\mu+4)}. \quad (10)$$

Updating D_m explicitly with Z_{DR} observations is expected to generate more correction in the D_m analysis through the relationship between Z_{DR} and D_m . Via Eq. (9) and (10), the external correction in the D_m analysis can feed back into the q_r and N_{Tr} analyses, resulting in additional correction in the microphysical states of rainwater.

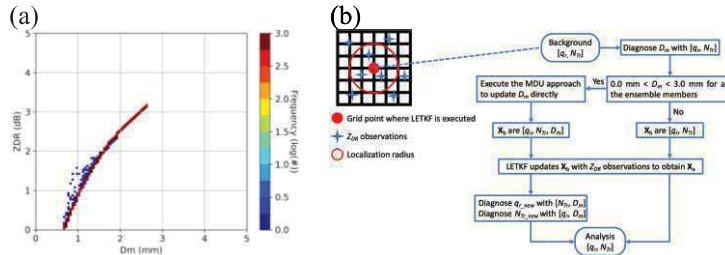


Figure 1: (a) The joint frequency of D_m and simulated Z_{DR} ; (b) Flow chart of the mean diameter update approach.

3 Experimental Design

3.1 Case Overview

Three common high-impact weather systems are selected in this study, including a squall line, a typhoon, and a Mei-Yu front. The joint frequency of Z_H and Z_{DR} observations reveal the microphysical characteristics of these three cases. The squall line and Mei-Yu front cases have the similar distribution pattern of the joint frequency. The frequency concentrates in the region of $30 \text{ dBZ} < Z_H < 40 \text{ dBZ}$ in the typhoon case. In all three cases, the high frequency concentrates in the area with Z_{DR} smaller than 1.0 dB, indicating the intense precipitation systems are formed by relatively small raindrops in these heavy rainfall events.

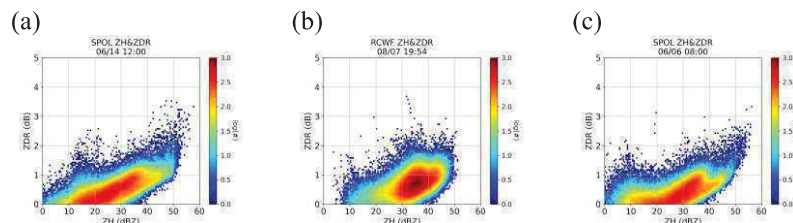


Figure 2: The joint frequency of Z_H and Z_{DR} observations below 4 km in the (a) squall line, (b) typhoon, and (c) Mei-Yu front cases.

3.2 Assimilation Procedure

The WRF model version 3.9.1 is employed as the numerical weather prediction model for all the three cases. The initial and boundary conditions are made from National Centers for Environmental Prediction (NCEP) 0.25° reanalysis field. Figure 3 describes the whole DA procedure in all three cases. In the beginning, 50 ensemble members are generated by perturbing the initial condition with the statistical background error covariance. Secondly, the ensemble members are integrated for the model spin-up to obtain the mesoscale background field. After the model spin-up, radar data are assimilated during a 2-hour assimilation period. V_r , Z_H , and Z_{DR} are assimilated sequentially at each cycle. Three constraints are employed for the assimilation of Z_{DR} observations. First of all, negative Z_{DR} observation data are eliminated since they are against the fact that larger raindrops should be oblate and have positive Z_{DR} values. Second, the Z_{DR} observations are only

assimilated if the altitude lower than 4 km in order to ignore the uncertainty of simulated Z_{DR} above the melting layer. The final constraint is that Z_{DR} is assimilated in latter half of the assimilation period to guarantee that assimilating V_r and Z_H already construct reasonable precipitation system to assimilate Z_{DR} observations. When the cycling DA is finished, a short-term is initiated with the final analysis. Table 1 lists all the experiments conducted in these three cases. The VrZ experiment assimilates only V_r and Z_H observations. The VrZZdr experiment assimilates V_r , Z_H , and Z_{DR} observations. The VrZZdr_MDU experiment also assimilates V_r , Z_H , and Z_{DR} observations but utilizes the MDU approach implemented to explicitly update D_m with the Z_{DR} observations.

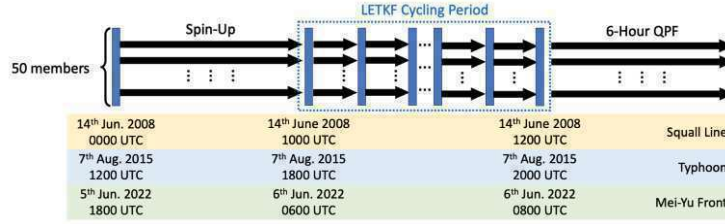


Figure 3: The flow chart of the assimilation procedure including a model spin-up period, a 2-hour assimilation period, and a 6-hour short term forecast after assimilation.

Experiment Names	Assimilated Observations	MDU Approach
VrZ	V_r , Z_H	No
VrZZdr	V_r , Z_H , and Z_{DR}	No
VrZZdr_MDU	V_r , Z_H , and Z_{DR}	Yes

Table 1: All the experiments conducted in this study.

4 Results

4.1 OSSE in the Mei-Yu Front Case

The Mei-Yu front case is used to conduct the OSSE to evaluate the feasibility of the MDU approach. Figure 4a shows the max composite Z_H in the background field of VrZ at 0700 UTC on 6th June 2022. The linear rainband is captured in after 5 assimilating cycles. The cross section of the correlation between simulated Z_{DR} at the reference point (grey star) and rainwater variables (q_r , N_{Tr} , and D_m) are shown in Figure 4b. The correlation between simulated Z_{DR} and D_m near the reference point exceeds 0.95, corresponding to the one-to-one relationship in Figure 1a. The high correlation reveals the capability to propagate more correction from the observation space to the model grid. A pseudo Z_{DR} observation is placed on the reference point to conduct a simplified assimilation experiment. Assimilating the Z_{DR} observation on the reference point to update q_r and N_{Tr} leads to the positive q_r increment and negative N_{Tr} increment. Consequently, the D_m increment is positive based on the adjustment in q_r and N_{Tr} . When the MDU approach is employed to assimilate the Z_{DR} observation, there is more positive D_m increment near the reference point, proving the hypothesis of updating D_m explicitly to generate more correction in D_m . The additional D_m increment can feed back to q_r and N_{Tr} through Eq. (9) and (10), leading to more positive q_r increment and negative N_{Tr} increment. This single-pseudo-observation assimilation observation proves the feasibility of the MDU approach to generate more correction in the microphysical states of rainwater.

Figure 6 shows the root-mean-square error (RMSE) of Z_{DR} , q_r , and N_{Tr} and the analysis error improvement in the latter half of the assimilation period. The analysis error improvement is defined as

$$\text{Improvement} = \left(1 - \frac{\text{Analysis RMSE}}{\text{Analysis RMSE of VrZ}}\right) \times 100\%, \quad (10)$$

where VrZ is the benchmark to evaluate the impact on the analysis field caused by assimilating Z_{DR} observations. Implementing the MDU approach to update D_m explicitly generates more Z_{DR} analysis error improvement at each cycle. Correspondingly, VrZZdr_MDU shows more analysis error improvement in both q_r and N_{Tr} analyses. These results proves that the MDU approach is able to take advantage of the high correlation between Z_{DR} and D_m to further improve the microphysical states.

The performance of the short-term rainfall forecast is shown in Figure 7. The 6-hour rainfall forecast is divided to two periods. In the 1st period, all three experiments present similar performance. As for the 2nd period, assimilating Z_{DR} observations increases the success ratio while implementing the MDU approach shows the highest success ratio. Regarding the overall performance of the 6-hour rainfall forecast, VrZZdr_MDU has the highest fraction skill score (FSS) under every threshold, especially for the threshold of rainfall higher than 40 mm. With additional improvement in the microphysical states, assimilating Z_{DR} observations through the MDU approach is able to enhance the accuracy of short-term forecast.

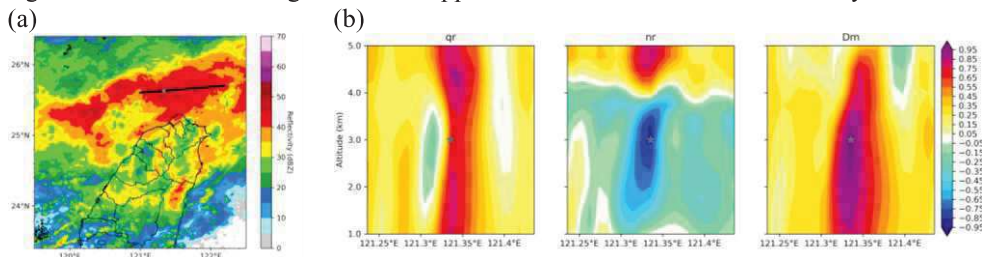


Figure 4: (a) The composite Z_H of the background at 0700 UTC 6th June 2022 obtained by assimilating V_r and Z_H for an hour; (b) the vertical cross-section along the black line in Figure 4a of the correlation between simulated Z_{DR} at the reference point (grey star) and rainwater variables (q_r , N_{Tr} , and D_m) at 0700 UTC 6th June 2022.

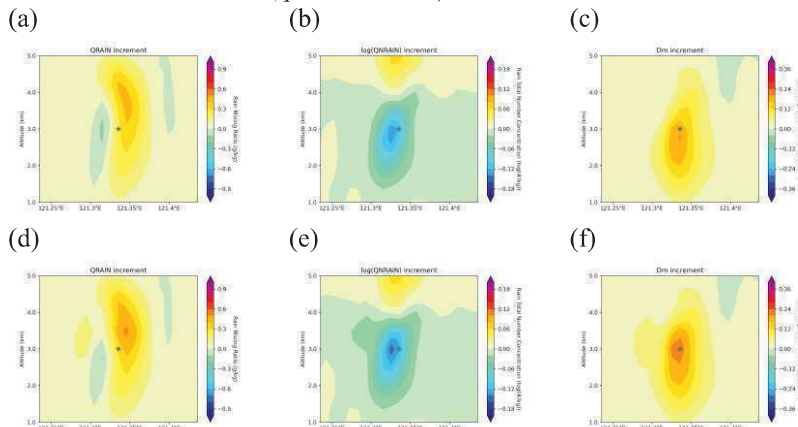


Figure 5: Increment of rainwater variables resulting from assimilating a pseudo Z_{DR} observation on the reference point (grey star) with (the upper row) and without the MDU approach (the lower row).

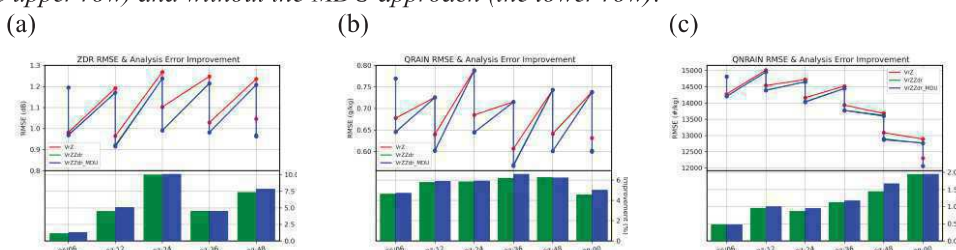


Figure 6: The RMSE and analysis error improvement of Z_{DR} , q_r , and N_{Tr} during the latter half of the assimilation period in the Mei-Yu front OSSE. The line chart displays the RMSE while the bar chart illustrates the analysis error improvement of the experiments assimilating Z_{DR} in comparison with the experiment only assimilating V_r and Z_H .

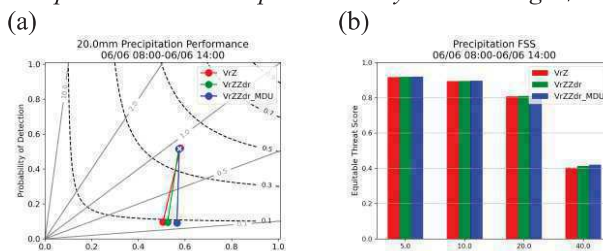


Figure 7: The verification of the short-term rainfall forecast in the Mei-Yu OSSE. (a) Performance diagram of 3-hour accumulated rainfall (the white cross indicates the scores of the 1st period from 0800 UTC to 1100 UTC). (b) Fraction skill scores of the 6-hour accumulated rainfall under different thresholds. The scores of all the experiments are the average scores of the forecasts initiated at each cycle in the latter half of the assimilation period.

4.2 Impacts in Three Real Cases

Figure 8 shows the RMSEs of Z_{DR} in the latter half of the 2-hour assimilation period in all three cases, as well as the analysis error improvement of VrZZdr and VrZZdr_MDU in comparison with VrZ. Consistent with the result in the OSSE, implementing the MDU approach to assimilate Z_{DR} observations reduces more Z_{DR} analysis errors at each cycle in all three cases. Therefore, it is proved that the MDU approach can leverage the relationship between Z_{DR} and D_m to generate more correction in various cases. The performance diagrams of 2-hour rainfall accumulation in the 6-hour rainfall forecast in all three cases are shown in Figure 9a-c. Assimilating Z_{DR} observations through the MDU approach outperforms the experiment without using the MDU approach. As for the overall performance of the 6-hour rainfall accumulation, assimilating Z_{DR} observations to update q_r and N_{Tr} reduces the FSSs of higher rainfall. Implementing the MDU approach to assimilate Z_{DR} observations alleviates the degradation of rainfall forecast and can even performs better than VrZ (Figure 9d-f).

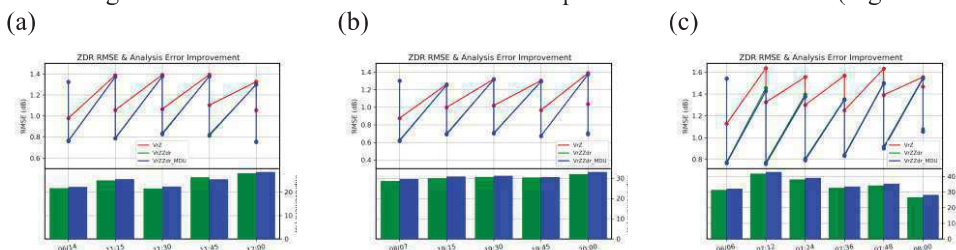


Figure 8: Same as Figure 6 but for Z_{DR} RMSEs in the (a) squall line, (b) typhoon, and (c) Mei-Yu front cases.

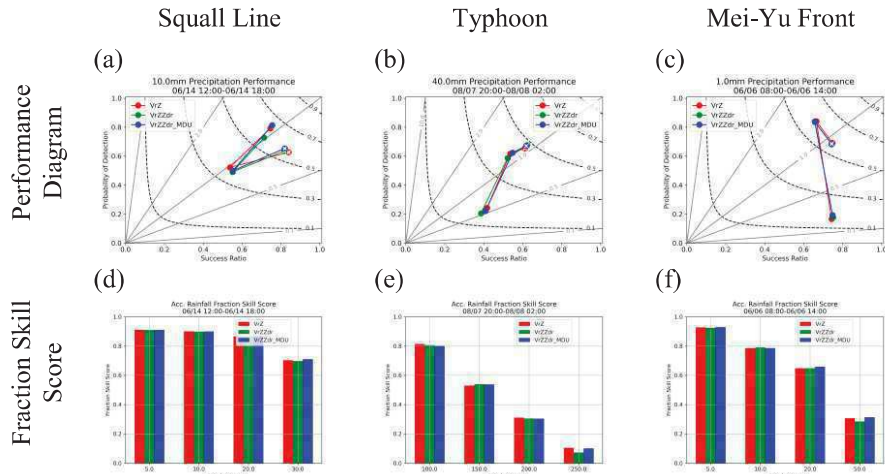


Figure 9: Same as Figure 7 but for the performance diagrams of 2-hour rainfall accumulation and FSSs of 6-hour rainfall accumulation in all three real cases.

5 Conclusions

In order to make use of the high correlation between Z_{DR} and D_m in the ensemble-base DA, the MDU approach updating D_m explicitly with Z_{DR} observations is developed in this study. Through the high correlation between Z_{DR} and D_m , the MDU approach is expected to further improve the microphysical states. The OSSE is conducted to evaluate the feasibility of the MDU approach. Implementing the MDU approach to assimilate Z_{DR} observations generates more D_m correction than updating q_r and N_{Tr} respectively. Subsequently, the accuracy of q_r and N_{Tr} analyses is improved. Initiated with more accurate microphysical states, the performance of the short-term forecast is also improved.

As for real cases, the results of the analysis field are consistent with the OSSE. The MDU approach extract more correction from the assimilated Z_{DR} observations to further reduce Z_{DR} analysis error. Assimilating Z_{DR} observations in real cases may degrade the performance of the rainfall forecast. Utilizing the MDU approach to assimilate Z_{DR} in reality can suppress the deterioration and even improve the performance of rainfall forecast in comparison with the experiment only assimilating V_r and Z_H . Based on the results of the OSSE and real cases, converting the background variable to leverage the physical relationship in the DA system is able to obtain more precise analyses and forecasts.

6 Acknowledgements

The authors are grateful to the National Center of High-Speed Computing and Data Bank for Atmospheric and Hydrologic Research for providing the computational resources and data of Central Weather Administration weather stations.

7 References

- Brandes, E. A., G. Zhang, and J. Vivekanandan, 2002: Experiments in Rainfall Estimation with a Polarimetric Radar in a Subtropical Environment. *Journal of Applied Meteorology and Climatology*, **41**, 674-685, doi: 10.1175/1520-0450(2002)041<0674:Eirewa>2.0.Co;2.
- Jung, Y., G. Zhang, and M. Xue, 2008: Assimilation of Simulated Polarimetric Radar Data for a Convective Storm Using the Ensemble Kalman Filter. Part I: Observation Operators for Reflectivity and Polarimetric Variables. *Monthly Weather Review*, **136**, 2228-2245, doi: 10.1175/2007mwr2083.1.
- Jung, Y., M. Xue, and G. Zhang, 2010: Simulations of Polarimetric Radar Signatures of a Supercell Storm Using a Two-Moment Bulk Microphysics Scheme. *Journal of Applied Meteorology and Climatology*, **49**, 146-163, doi: 10.1175/2009jame2178.1.
- Li, X., and J. R. Mecikalski, 2010: Assimilation of the dual-polarization Doppler radar data for a convective storm with a warm-rain radar forward operator. *Journal of the Geophysical Research*, **115**, doi: 10.1029/2009JD013666.
- Li, X., and J. R. Mecikalski, 2012: Impact of the Dual-Polarization Doppler Radar Data on Two Convective Storms with a Warm-Rain Radar Forward Operator. *Monthly Weather Review*, **140**, 2147-2167, doi: 10.1175/mwr-d-11-00090.1.
- Park, H. S., A. V. Ryzhkov, D. S. Zrnić, and K.-E. Kim, 2009: The Hydrometeor Classification Algorithm for the Polarimetric WSR-88D: Description and Application to an MCS. *Weather and Forecasting*, **24**, 730-748, doi: 10.1175/2008waf2222205.1.
- Putnam, B., M. Xue, Y. Jung, N. Snook, and G. Zhang, 2019: Ensemble Kalman Filter Assimilation of Polarimetric Radar Observations for the 20 May 2013 Oklahoma Tornadoic Supercell Case. *Monthly Weather Review*, **147**, 2511-2533, doi: 10.1175/mwr-d-18-0251.1.
- Ryzhkov, A., and D. Zrnić, 1996: Assessment of Rainfall Measurement That Uses Specific Differential Phase. *Journal of Applied Meteorology and Climatology*, **35**, 2080-2090, doi: 10.1175/1520-0450(1996)035<2080:Aormtu>2.0.Co;2.
- Tsai, C.-C., S.-C. Yang, and Y.-C. Liou, 2014: Improving quantitative precipitation nowcasting with a local ensemble transform Kalman filter radar data assimilation system: observing system simulation experiments. *Tellus A*, **66**, 21804, doi: 10.3402/tellusa.v66.21804.
- Tsai, C.-C., and K.-S. Chung, 2020: Sensitivities of quantitative precipitation forecasts for Typhoon Soudelor (2015) near landfall to polarimetric radar data assimilation. *Remote Sensing*, **12**, 3711, <https://doi.org/10.3390/rs12223711>.
- Wu, B., J. Verlinde, and J. Sun, 2000: Dynamical and Microphysical Retrievals from Doppler Radar Observations of a Deep Convective Cloud. *Journal of the Atmospheric Sciences*, **57**, 262-283, doi: 10.1175/1520-0469(2000)057<0262:Damrfd>2.0.Co;2.

Assimilation of radar data in ICON at very high resolution - the GLORI Project

Virginia Poli^{1,2}, Xu Xu³, Claire Merker⁴, Klaus Stephan³, Arianna Valmassoi³, Thomas Gastaldo^{1,2}, Alina Yapparova⁴, Pier Paolo Alberoni², Chiara Marsigli^{1,3}

¹*Agenzia ItaliaMeteo, Bologna, Italy*

²*Arpae Emilia-Romagna, Bologna, Italy*

³*Deutscher Wetterdienst, Offenbach, Germany*

⁴*MeteoSwiss, Zurich, Switzerland*



Virginia Poli

1 Introduction

Numerical weather prediction is an essential tool for producing forecasts for a wide range of weather phenomena at different spatial scales. However, the challenges posed by high-impact weather events, often associated with extremes, need to be addressed by pushing the weather forecasting tools beyond their current limits and by strengthening the link with the end-users of the forecasts.

The GLORI (Global-to-Regional ICON Digital Twin) project is the result of a trilateral collaboration between German, Italian and Swiss institutions. The aim of this project is to develop a global-to-regional digital twin based on the prediction capability of the ICON modeling system (Zängl et al., 2015), improving, in particular, forecasts at different scales by exploiting the knowledge and capabilities known about high resolution.

In this work, we focus on the Alpine region, and we aim to assimilate data from the Italian, German and Swiss radar networks, for both reflectivity volumes and radial winds. Radar volumes over Germany are operationally assimilated at DWD (Bick et al., 2016), while radar volumes over Italy are assimilated at Arpae (Gastaldo et al., 2018; Gastaldo et al., 2021). At MeteoSwiss the assimilation of radar volume is in experimental phase (Claire Merker, personal communication). The GLORI project provides the framework where radar data from the three partner countries will be used in combination, permitting a better description of the precipitating systems over the Alpine area and therefore improving the forecasts of intense precipitation.

The experiments presented here are related to the flooding events in Southern Germany in May 2022, but will be replicated and investigated for the flooding episodes that hit the Emilia-Romagna Region, in Northern Italy, in May 2023. In particular, the results will show the improvement of forecasts initialized with analysis including the assimilation of radar data, with respect to the control run in which no radar data are assimilated. The impact of adding data from different networks (German and Italian) will also be evaluated.

2 The GLORI Digital Twin

The GLORI DT is a configurable on-demand global-to-regional short-range high-resolution digital twin of the Earth's weather system. GLORI is developed in a trilateral collaboration between Germany, Italy, and Switzerland, including operational centers as well as research institutes of these three countries, and with support by computing centers, to improve availability of and access to cutting-edge weather and extremes forecasting data for decision-making. GLORI provides more timely information needed for decision making and early warnings, such as short-range global and European storm-resolving km-scale (~3 km horizontal) predictions, as well as regional very high-resolution predictions (~500 m horizontal) on selected prototype-domains, the Alpine area and the Italian peninsula. The GLORI DT runs on different HPC systems, available for the different project partners, thanks to a distributed infrastructure.

The chain described here is based on the BACY system. BACY stands for Basic Cycling and consists of a variety of shell scripts designed to perform the analyses (atmosphere, soil moisture, snow, etc.) and model runs for full NWP data assimilation and forecasting. It has been developed at DWD for running experiments in a fast and modular way and it is portable to different architectures.

The DACE data assimilation package and the ICON model with its components, including the icontool package, are included in the BACY implementation. The system is complemented by the MEC (Model Equivalent Calculator), which generates the files where observations and forecasts are paired, prepared for the verification.

2.1 Implementation

For this work, the chain has started with an ICON global run with data assimilation at 13 km with a 6.5 km refinement over Europe (2-way nesting), run on the Horeka machine at Karlsruhe Institute of Technology (KIT). The global data assimilation is performed with a hybrid assimilation using 3d-Var and LETKF with a 40-members ensemble. Then, an ICON-LAM data assimilation cycle, receiving boundary conditions from ICON-EU, is performed on the Alpine domain shown in Figure 1, at a horizontal resolution of 2 km, with two refinements (two-way nesting) at 1 km and 500 m. The LAM

data assimilation cycles are based on a LETKF scheme with a 40 member ensemble, assimilating conventional observations and radar volumes. LHN is also applied, for the assimilation of surface instantaneous precipitation (Figure 1).



Figure 1: GLORI Digital Twin model chain and used domains.

2.2 Test case

In the first phase of the work, as the assimilation of the Swiss radar volumes is still in the experimental phase, only the German and Italian radar volumes will be used (the two networks are shown in Figure 2). In order to understand the impact of the use of the different networks, several tests were performed, which are summarized in Table 1. One of the crucial points is also the assimilation of radar-derived precipitation by the LHN, which is tested in combination or not with the assimilation of volumes. In the test case LHN is applied using only German composite, in a second step we will also add composite from the Italian side. The control run is the one in which no assimilation is performed.

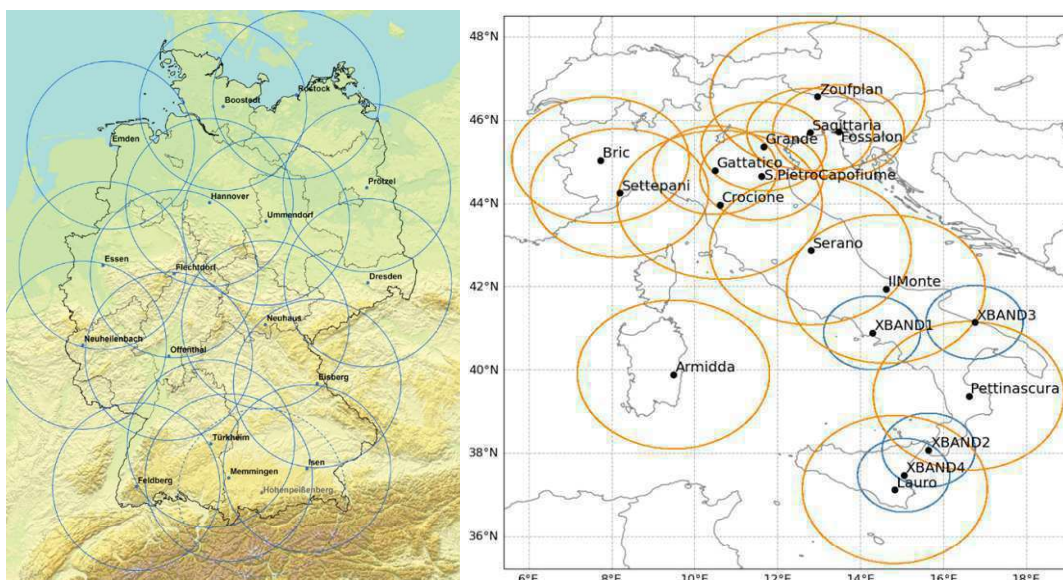


Figure 2: German and Italian radar networks.

Table 1: Experiments performed on the Alpine domain. D stands for German radar volumes, I for Italian ones.

	D	I	LHN
DI_radar_LHN	T	T	T
DI_radar	T	T	F
LHN	F	F	T
none	F	F	F
D_radar_LHN	T	F	T

The first case study analyzed was a flood in Southern Germany for which an alert was issued (Figure 3). Assimilation runs were performed from the 04/05/2022 00 UTC to 05/05/2022 00 UTC.



Figure 3: Alert issued for the case study.

Next figures demonstrate how the forecast varies by changing the input data, i.e. using only the German radar composite (left-hand columns) or the German and Italian composite together (right-hand columns). Observed precipitation from German composite and German+Italian composite is shown as a reference (Figure 4).

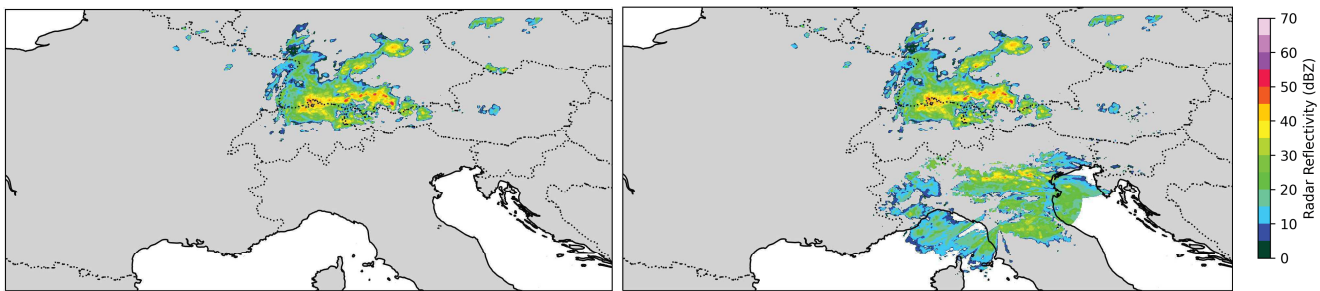


Figure 4: German (left) and German+Italian (right) radar reflectivity composite for the 05/05/2022 19:00 UTC.

For the forecast run of 05/05/2022 initialized at 19:00 UTC, for the experiment with LHN, the difference between simulated and observed reflectivity fields is shown in Figure 5, while in Figure 6 is the forecasted precipitation. In particular, as can be observed in forecasted precipitation fields, the use of information on a larger domain increases precipitation over southern Germany.

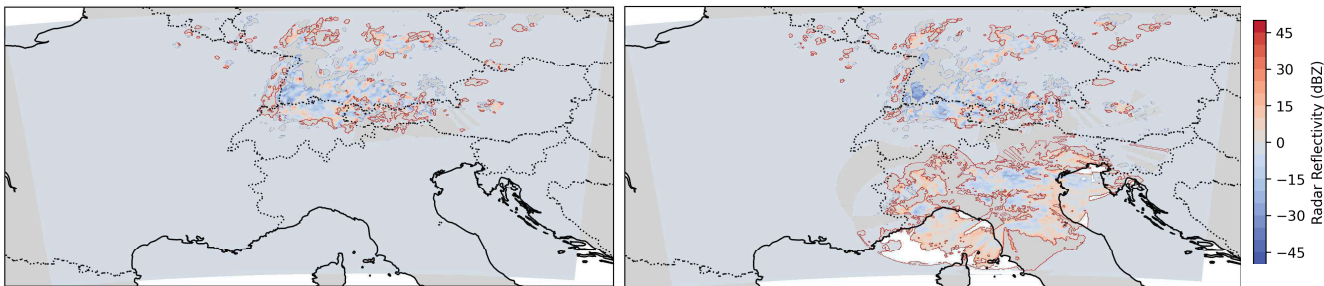


Figure 5: Difference between simulated and observed reflectivity fields for the run initialized on 05/05/2022 19:00 UTC with the analyses obtained using German radar + LHN (left) and German + Italian radar + LHN (right).

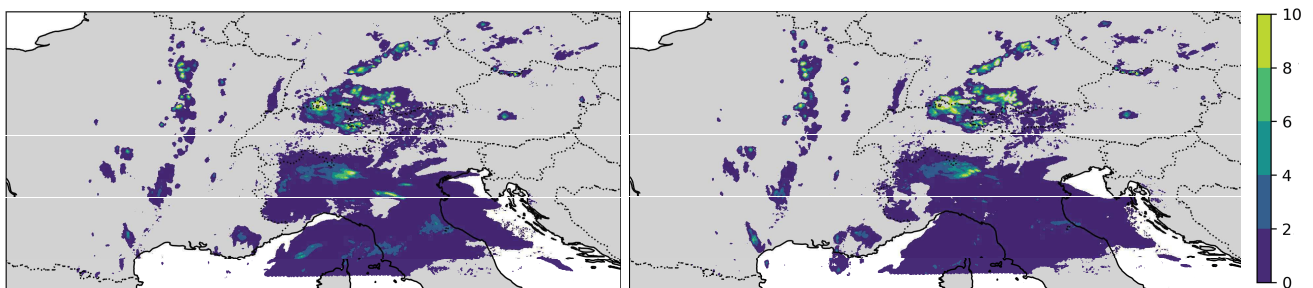


Figure 6: Total forecasted precipitation (in kg/m²) for the run initialized on 05/05/2022 19:00 UTC with the analyses obtained using German radar + LHN (left) and German + Italian radar + LHN (right).

3 Future work

The aim of the GLORI Digital Twin project is to study in depth the impact of forecasts at very high-resolution, in particular by paying attention to the needs of end-users.

The research is in its early stages and is ongoing. Initial experiments have been carried out to verify the functionality of the chain: from global to limited area assimilation runs. The first results already show the difference in using information over a larger domain, combining all available data. Particularly when dealing with areas where the orography is complex. When these results are confirmed, including data from the Swiss radar network, the horizontal resolution will be doubled by switching the global ensemble from 13 to 6.5 km, with nesting from 6.5 to 3.25 km. We will then proceed with multi-nesting to direct assimilation at 1 km with nesting at 500 m. This will mean that all configurations used operationally in the assimilation cycles will have to be re-evaluated. In particular, for the assimilation of radar volumes, the resolution used for superobbing and the horizontal and vertical localisation will have to be evaluated in order to define the errors to be associated with the observations.

4 Acknowledgements

The authors would like to acknowledge the KNMI EMADDC for the use of MODE-S data in the GLORI project.

5 References

- Bick, T., Simmer C., Trömel S., Wapler K., Hendricks Franssen H.-J., Stephan K., Blahak U., Schraff C., Reich H., Zeng Y. and Potthast R. (2016): Assimilation of 3D radar reflectivities with an ensemble Kalman filter on the convective scale. *Q. J. R. Meteorol Soc.*, 142, 1490–1504. <https://doi.org/10.1002/qj.2751>
- Gastaldo, T., Poli V., Marsigli C., Cesari D., Alberoni P.P. and Paccagnella T. (2021): Assimilation of radar reflectivity volumes in a pre-operational framework. *Q. J. R. Meteorol Soc.*, 14, 1031- 1054. <https://doi.org/10.1002/qj.3957>
- Gastaldo, T., Poli V., Marsigli C., Alberoni P. P., Paccagnella T. (2018): Data assimilation of radar reflectivity volumes in a LETKF scheme. *Nonlin. Processes Geophys.*, 25, 747-764, <https://doi.org/10.5194/npg-25-747-2018>
- Zängl, G., Reinert D., Rípodas P. and Baldauf M. (2015), The ICON (ICOsahedral Non-hydrostatic) modelling framework of DWD and MPI-M: Description of the non-hydrostatic dynamical core. *Q.J.R. Meteorol. Soc.*, 141 563-579. <https://doi.org/10.1002/qj.2378>

Impact of Latent Heat Nudging on ICON model forecasts

Virginia Poli^{1,2}, Thomas Gastaldo^{1,2}, Chiara Marsigli^{1,3}, E. Minguzzi², D. Cesari² and P. P. Alberoni²

¹*Agenzia ItaliaMeteo, Bologna, Italy*

²*Arpae Emilia-Romagna, Bologna, Italy*

³*Deutscher Wetterdienst, Offenbach, Germany*



Virginia Poli

1 Introduction

At the HydroMeteorological Service of the Regional Agency for the Environment and Energy of Emilia-Romagna (Arpae Emilia-Romagna, Italy), the ICOSahedral Nonhydrostatic model (ICON; Zangl et al., 2015) provides deterministic and probabilistic weather forecasts over Italy at a horizontal resolution of 2.2 km.

The modeling chain comprises hourly assimilation cycles that determine the analyses from which the forecasts are initialized. In order to obtain the current operational configuration, the two components of the assimilation system were tested: the kilometre-scale ensemble data assimilation (KENDA; Schraff et al., 2016) system, in which the Local Ensemble Transform Kalman Filter (Hunt et al., 2007) scheme is implemented and which is employed for the assimilation of conventional observations and radar volumes of reflectivity and radial wind, and the Latent Heat Nudging (LHN, Jones and Macpherson, 1997) scheme, used to assimilate radar-estimated precipitation (Gastaldo et al., 2018; Gastaldo et al., 2021).

The focus of this work is on the use and on the impact of the LHN on forecasts. The LHN assimilates the precipitation derived from radar data exploiting the high horizontal resolution and high temporal frequency of these data. It scales the model temperature and humidity profiles according to the assumption that the precipitation rate at one point is proportional to the latent heat integrated along the vertical column above it. The adjustment of the profiles is proportional to the ratio between the modeled and observed precipitation and it differs according to the model precipitation type (stratiform or convective). The LHN has a direct impact on the forecasted fields as it acts run-time during the assimilation cycle. It is successfully used in different operational frameworks at DWD (Stephan et al., 2008), at MeteoSwiss (Leuenberger and Rossa, 2004; Leuenberger and Rossa, 2007) and Arpae Emilia-Romagna (Gastaldo et al., 2018; Gastaldo et al., 2021, Gastaldo et al., 2022). In the implementation of ICON over the Italian domain (ICON-2I), the surface rainfall intensity (SRI) fields used as input to the LHN are provided by the Italian Civil Protection Department.

The impact of LHN on the forecasts is evaluated over a long period of time, characterized by different types of phenomena, in order to have a significant sample. Runs with different pre-processing of the input data are performed and then compared with a reference run in which no data assimilation is done. The verification of the forecasts is carried out taking into account precipitation as well as upper air and near surface variables. In particular, the impact of considering the quality of the assimilated radar data is shown.

2 Implementation

In the operational implementation of the ICON-2I model, the LHN is applied during the hourly assimilation cycles, together with the assimilation through LETKF of conventional and radar data. In this work, focusing on the impact of the LHN, deterministic 24-hour forecasts were made, with initial conditions from IFS high resolution analyses, applying the LHN throughout the whole forecast. In the control run, no assimilation was made.

Forecasts were made for the period from 00 UTC on 01/04/2023 to 18 UTC on 21/05/2023. They were initialized every 6 hours for a total of 204 forecasts per experiment. This period was characterized by intense and persistent rainfall, which led to two flooding episodes (2-3 May and 16-17 May) in Emilia-Romagna region, alternating with convective episodes typical of the spring season. The total precipitation for the selected period, estimated from the hourly accumulated precipitation product, is shown in Figure 1. This image highlights some of the problems affecting the radar network, i.e. beam blocking.

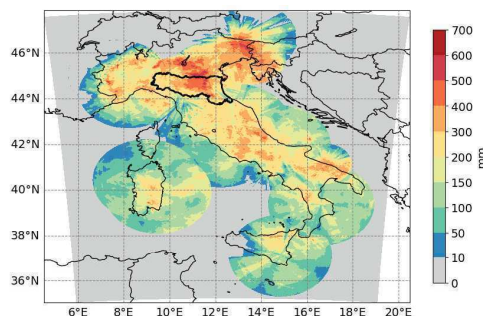


Figure 1: Total precipitation accumulated from 01/04/2023 00 UTC to 22/05/2023 18 UTC. Emilia-Romagna region is highlighted by the bold black outline.

2.1 Dataset

The estimated SRI fields are used with a frequency of 10 minutes. These data are associated with a quality value ranging from 0 (low quality) to 100 (high quality). The quality is calculated on the basis of several parameters: clutter, beam blocking, distance from the radar, height of measurement and attenuation (Rinollo et al., 2013).

Analyzing the quality of the SRI composites as an average of the qualities associated with each individual acquisition (Figure 2), we observe that there is poor quality in Northern Italy, along the Alps where the orography is very complex, and where coverage is not optimal, e.g. in Southern Italy.

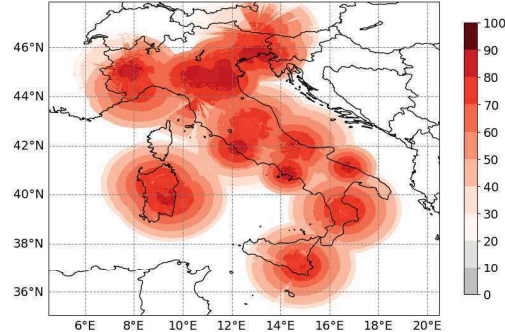


Figure 2: Mean quality of the SRI composites from 01/04/2023 00 UTC to 22/05/2023 18 UTC.

2.2 Experimental set-ups

As the assimilation of reliable and good quality data is expected to provide a more precise analysis, it was decided to test latent heat nudging by selecting increasingly higher quality values in the SRI fields.

Figure 3 shows an example of how many data are assimilated by taking all data regardless of their quality (left), in a run where only points with quality greater than 50 (center) and with quality greater than 70 (right) are selected.

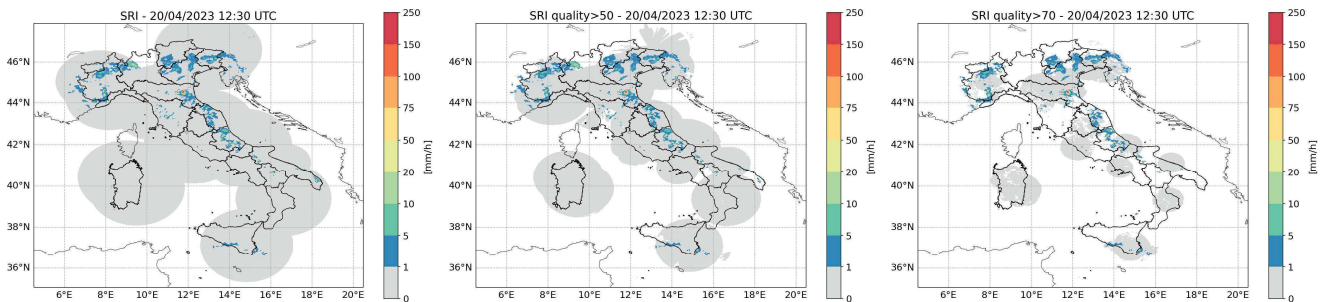


Figure 3: SRI product of 20/04/2023 12:30 UTC (left), with quality greater than 50 (center) and with quality greater than 70 (right).

Four different experiments were carried out:

- *w/o KENDA*: 24-hour forecasts initialized from IFS analyses, without any assimilation
- *w/o KENDA + LHN*: as without KENDA, but using all available SRI data for all the forecast length
- *w/o KENDA + LHN $q > 50$* : as without KENDA + LHN, but using only SRI data with quality higher than 50
- *w/o KENDA + LHN $q > 70$* : as without KENDA + LHN, but using only SRI data with quality higher than 70

3 Results

Verification was performed for precipitation, temperature at 2 m, relative humidity at 2 m, pressure at the surface and u and v wind components at 10 m and; for upper-levels, it was limited to temperature, relative humidity and wind speed.

For precipitation, the verification was carried out against rain gauge observations (almost 3000) of hourly precipitation within the warning areas defined by the Civil Protection Department (Figure 4). Different thresholds were chosen for average and maximum precipitation accumulations. Plots were obtained by combining the values of all time scales from +2 to +24 h. The results are presented in performance diagrams summarizing the calculated dichotomous scores (success ratio, SR, on the x-axis; probability of detection, POD, on the y-axis; critical success index, CSI, on hyperbolic curves and frequency bias on lines centered in the lower left-hand corner), in which the horizontal and vertical bars associated with each symbol represent 95% confidence levels estimated by bootstrapping. The first hour was discarded as the forecasts initialized by IFS give a strongly underestimated precipitation forecast and the reason is being investigated (Figure 5).



Figure 4: Italian warning areas. Black dots are rain gauges.

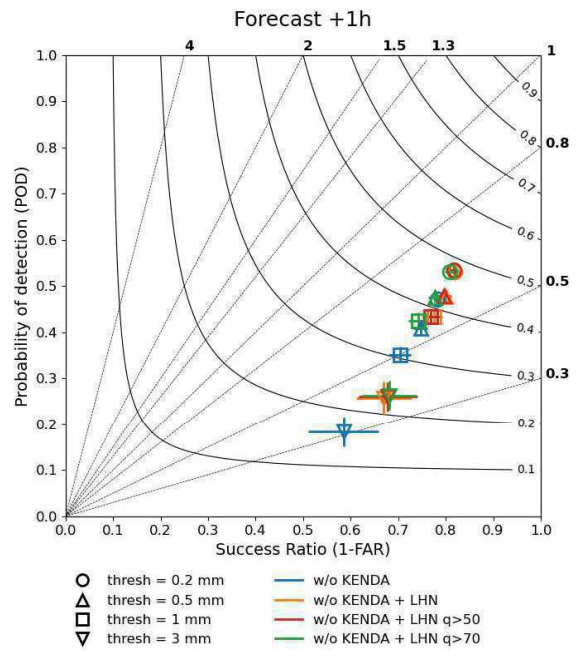


Figure 5: Performance diagram for average precipitation for 1-hour forecasts.

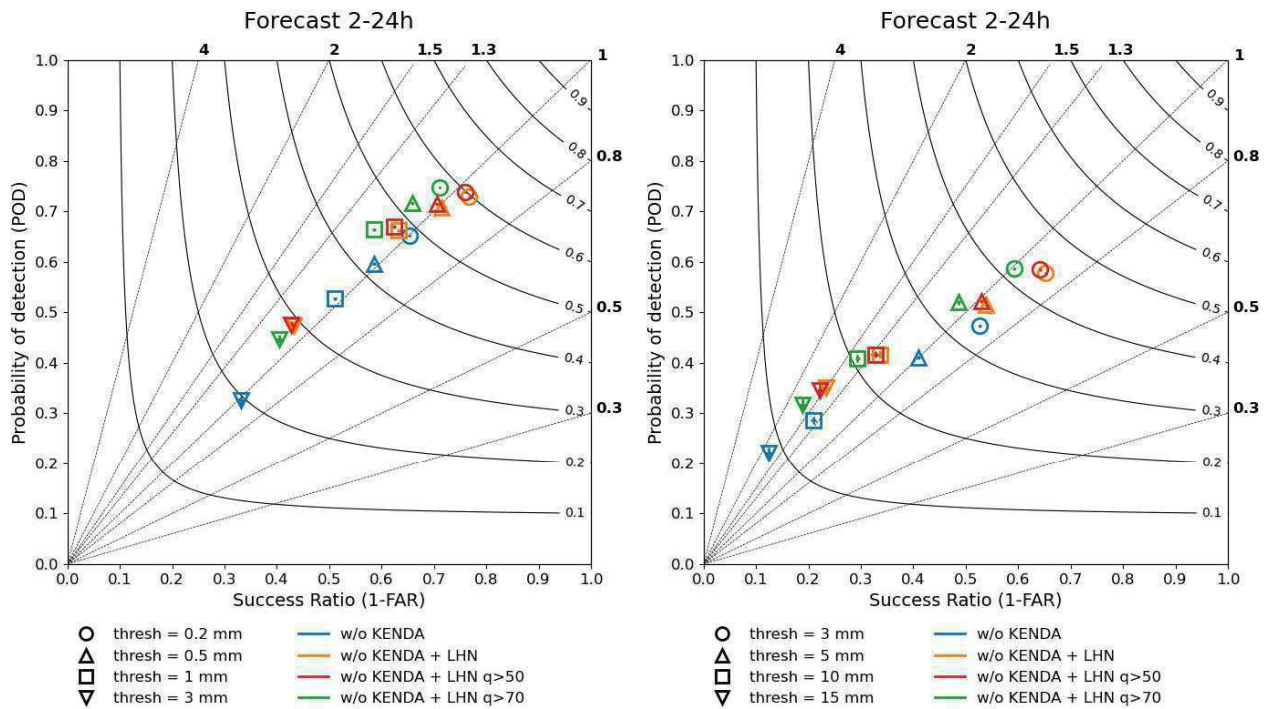


Figure 6: Performance diagrams for average (left) and maximum (right) precipitation from +2h to +24h forecasts. The different thresholds in use are represented by symbols, while the different experiments have different colors (blue: w/o KENDA, yellow: w/o KENDA + LHN, red: w/o KENDA + LHN q>50, green: w/o KENDA + LHN q>70).

It is evident from the performance diagrams (Figure 6) that the use of the LHN significantly improves the forecast accuracy compared to the control run (w/o KENDA, in blue), although it leads to overestimation of the frequency of occurrence of precipitating events. The results for the different thresholds show very little difference between the w/o KENDA + LHN (in yellow) and w/o KENDA + LHN q>50 (in red) runs. The use of a higher quality (w/o KENDA + LHN q>70, in green), on the other hand, leads to an overestimation of the frequency of occurrence of precipitation and lower CSI.

Verification for the surface and upper air variables is calculated as described in Gastaldo et al. (2021) using aircraft measurements (AIREP) for temperature and horizontal wind, radiosonde data (TEMP) for relative humidity and surface station observations (SYNOP) for 2 m temperature, 2 m relative humidity, 2 m dew point temperature, 10 m horizontal wind and surface pressure.

For surface parameters, the root mean square error (RMSE) as a function of the forecast lead time shows better values for the w/o KENDA + LHN q>70 run (green line) although the improvement is small (Figure 7, top row). For 2m relative

humidity *w/o KENDA + LHN* (yellow line) is slightly worse than the control run (blue line) and for 2m dew point both *w/o KENDA + LHN* and *w/o KENDA + LHN $q>50$* (red line) runs are slightly worse than the control run. In terms of bias (Figure 7, bottom row), the only relevant differences are again only for 2m relative humidity and 2m dew point where the *w/o KENDA + LHN* run performs slightly worse than the other runs.

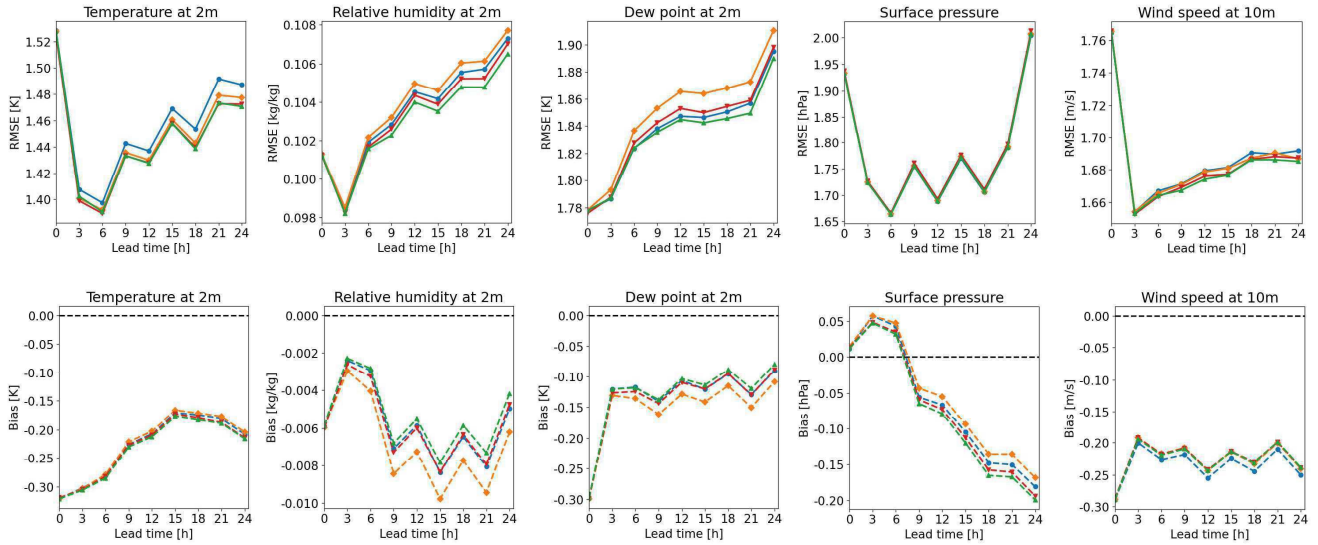


Figure 7: RMSE (top row) and bias (bottom row) of 2 m temperature, 2 m relative humidity, 2 m dew point, surface pressure, and 10 m wind speed. Different experiments have same colors of Figure 6 (blue: *w/o KENDA*, yellow: *w/o KENDA + LHN*, red: *w/o KENDA + LHN $q>50$* , green: *w/o KENDA + LHN $q>70$*).

Figure 8 shows the difference between the RMSE of the control run and each experiment (*w/o KENDA + LHN* in the left column, *w/o KENDA + LHN $q>50$* in the middle column and *w/o KENDA + LHN $q>70$* in the right column) for each atmospheric layer (y-axis) and for forecast time intervals (x-axis). Different rows are for the different parameters verified. Green values indicate an improvement of the experiment with respect to the control. Missing boxes (white boxes) are for the levels and the lead times for which there are not enough observations.

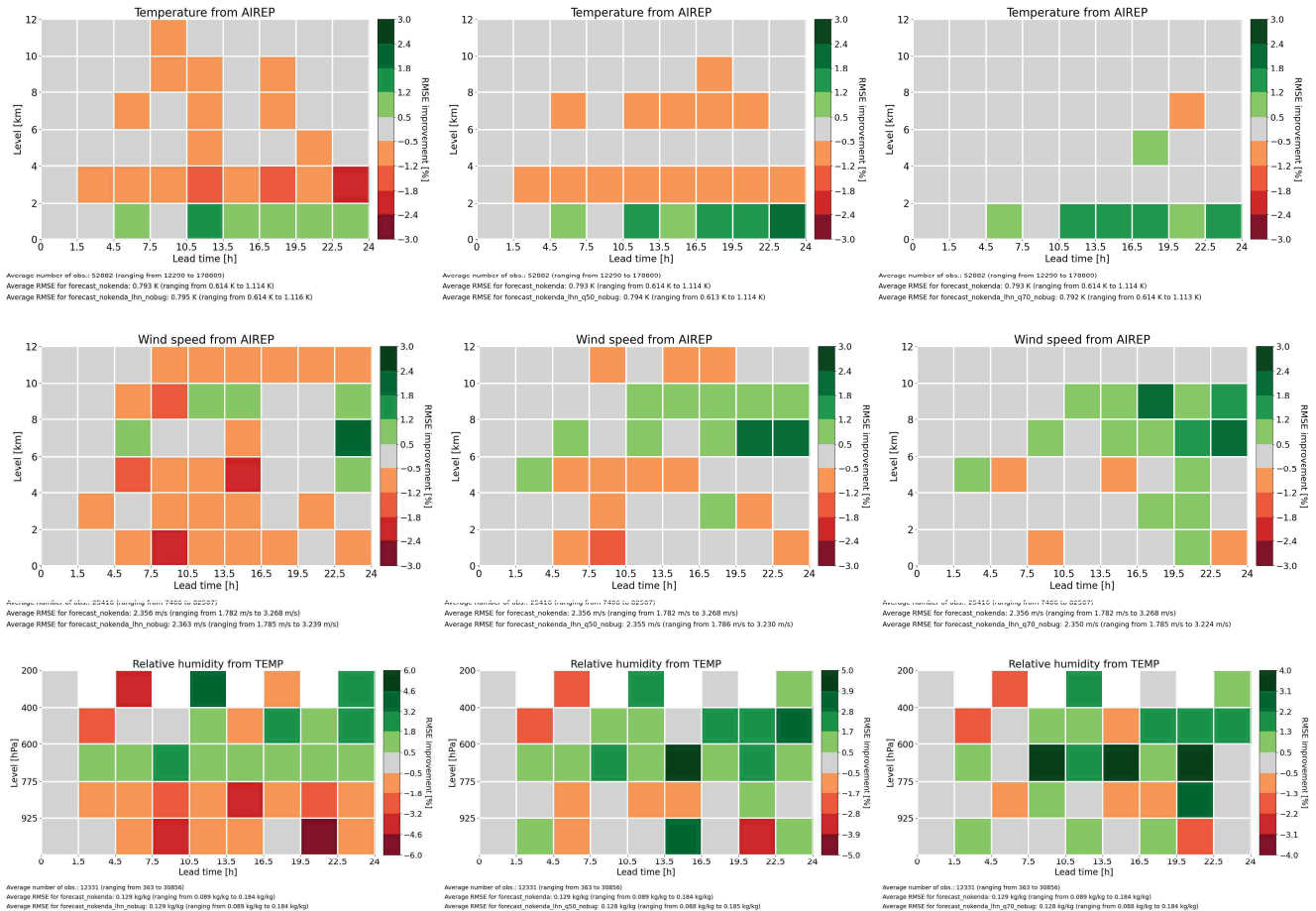


Figure 8: Difference (in percentage) between the RMSE of the control run and the different LHN experiments (w/o KENDA + LHN in the left column, w/o KENDA + LHN $q > 50$ in the middle column and w/o KENDA + LHN $q > 70$ in the right column) for AIREP temperature (top row), AIREP horizontal wind speed (middle row) and TEMP relative humidity (bottom row) observations. For each coloured square, the values on the y-axis indicate the vertical levels defining the corresponding layers while the values on the x-axis are the lead times defining the forecast intervals.

For temperature and wind speed from AIREP, an improvement in forecast accuracy is observed with increasing quality of assimilated SRI data. Similarly, a consistent positive improvement is observed for relative humidity, which increases with lead time. The improvement is stronger at lower levels (up to 775 hPa), but is also noticeable at the highest levels.

For temperature and wind speed from AIREP, the difference between the absolute value of the bias of the experiments and the control run is very small with a slight worsening as the quality of the assimilated SRI data increases, especially in the middle atmosphere levels. For temperature this happens after 4.5 hours of forecast, for wind speed 3 hours later. For relative humidity the impact of the experiments is neutral. Due to the small values of the differences, these plots are not shown.

4 Conclusions

In this work, the impact of the assimilation of instantaneous precipitation data by the LHN on the ICON forecasts was tested. In particular, the results were analyzed by increasing the quality value associated with these data.

For precipitation, the use of the LHN improves the results compared to the control run. The score values are similar whether all the data are used or only those with a quality greater than 50. The use of higher quality thresholds, greater than 70, worsens the results. This is probably due to the reduction in the number of assimilated data. As far as the other variables are taken into account, however, the verification shows an improvement for the upper air variables in proportion to the increase in SRI quality, but associated with a slight worsening of the bias.

In the future, attempts will be made to further improve the impact of the LHN by modifying the various namelist parameters during the assimilation cycles.

5 References

- Gastaldo, T., Poli V., Paccagnella T. and Alberoni P. P. (2022): Chapter 24 - direct assimilation of radar reflectivity volumes in COSMO-LETKF. In Silas Michaelides, editor, *Precipitation Science*, pages 757-786. Elsevier
- Gastaldo, T., Poli V., Marsigli C., Cesari D., Alberoni P.P. and Paccagnella T. (2021): Assimilation of radar reflectivity volumes in a pre-operational framework. *Q. J. R. Meteorol. Soc.*; 147: 1031- 1054. <https://doi.org/10.1002/qj.3957>
- Gastaldo, T., Poli V., Marsigli C., Alberoni P. P., Paccagnella T. (2018): Data assimilation of radar reflectivity volumes in a LETKF scheme. *Nonlin. Processes Geophys.*, 25, 747-764, <https://doi.org/10.5194/npg-25-747-2018>
- Hunt, B. R., Kostelich, E. J., and Szunyogh, I. (2007): Efficient data assimilation for spatiotemporal chaos: A local ensemble transform Kalman filter, *Physica D: Non-linear Phenomena*, 230, 112–126, <https://doi.org/10.1016/j.physd.2006.11.008>
- Jones, C. D. and Macpherson B. (1997): A latent heat nudging scheme for the assimilation of precipitation data into an operational mesoscale model. *Meteorological Applications*, 4, 269–277, <https://doi.org/10.1017/S1350482797000522>
- Leuenberger, D. and Rossa A. (2007): Revisiting the latent heat nudging scheme for the rainfall assimilation of a simulated convective storm. *Meteorology and Atmospheric Physics*, 98, 195–215.
- Leuenberger, D. and Rossa A. (2004): Revisiting the latent heat nudging scheme for the rainfall assimilation in convective system, in: *Proc. of 3th European Radar Conference on Radar Meteorology and Hydrology (ERAD)*, pp. 162–167, Visby, Gotland, Sweden, 6–10 September, 2004.
- Rinollo, A., Vulpiani G., Puca S., Pagliara P., Kanák J., Lábó E., Okon L., Roulin E., Baguis P., Cattani E., Laviola S., and Levizzani V. (2013): Definition and impact of a quality index for radar-based reference measurements in the h-saf precipitation product validation. *Nat. Hazards Earth Syst. Sci.*, 13, 1–11
- Schraff, C., Reich H., Rhodin A., Schomburg A., Stephan K., Perianez A., and Potthast R. (2016): Kilometre-scale ensemble data assimilation for the COSMO model (KENDA), *Quarterly Journal of the Royal Meteorological Society*, 142, 1453–1472, <https://doi.org/10.1002/qj.2748>
- Stephan, K., Klink S. and Schraff C. (2008): Assimilation of radar-derived rain rates into the convective-scale model COSMO-DE at DWD. *Q. J. R. Meteorological Society*, 134, 1315–1326. <https://doi.org/10.1002/qj.269>
- Zängl, G., Reinert D., Rípodas P. and Baldauf M. (2015), The ICON (ICOsahedral Non-hydrostatic) modelling framework of DWD and MPI-M: Description of the non-hydrostatic dynamical core. *Q.J.R. Meteorol. Soc.*, 141: 563-579. <https://doi.org/10.1002/qj.2378>

Radar and society

Proposal of Hail Forecast Method and Performance Evaluation Utilizing SNS Post Data

Yuta Ozawa¹, Takahisa Wada¹, Satoshi Kida², Masakazu Wada²,
Yasunori Nakagawa², Osamu Yamanaka¹

¹ *Infrastructure Systems Research and Development Center, Toshiba Infrastructure Systems & Solutions Corporation*

² *Toshiba Digital Solutions Corporation*



Yuta Ozawa

1 Introduction

In recent years, hail-related damage has rapidly increased worldwide due to climate change, making the development of hail forecast technology urgent. In the development of hail forecast technology based on conventional meteorological radar data, there has been a lack of a sufficient number of fixed observation points capable of detecting hail, which is a short-term and localized weather phenomenon. This limitation has made it difficult to evaluate and improve the accuracy of hail forecasts. Therefore, we propose a method (T-SHIBA: Two-Stage, Hydrometeor classification and forecasting Induced By SNS, Algorithm), which utilizes the rapidly expanding use of social media platforms (SNS) in recent years. Through SNS posts by the general public about hail events, we identified approximate hail locations and times, enabling the evaluation and improvement of hail forecast technology. This method consists of two stages: the first stage involves hydrometeor classification in three dimensions based on observations from meteorological radar, and the second stage forecasts hail locations in two dimensions (latitude and longitude) based on the results of the first stage.

This report presents the method for forecasts hail in the second stage. The hydrometeor classification method for the first stage will be reported separately. In hail forecast, the hail locations are forecasted using hydrometeor classification results for hail and the movement direction of rain cloud which is predicted using the advection vector of VIL (VIL: Vertically Integrated Liquid water) estimated from the three-dimensional observations of meteorological radar. However, numerical evaluation of forecast method for such weather phenomena was an issue because fixed observation data of localized weather phenomenon such as hail is often fragmented information. In this situation, we evaluated the hail forecast method by utilizing the locations and times of SNS posts about hail events. In this paper, we report the results of hail forecast for the hail cases in the Kanto region from June to October 2023.

2 Methodology

In hail forecasting, meteorological radar is widely used to monitor the structure and development of thunderstorms. For example, dual-polarization radar technology is employed to identify the presence of hail within thunderstorms. Radar-derived products such as radar reflectivity and VIL are also used to detect and predict hail. Numerous hail prediction techniques have been developed, utilizing meteorological data and models to assess the risk and scale of hailstorms. These prediction techniques include those based on meteorological radar observation data and point observation data, that utilize weather simulation models such as convection-allowing models (CAM) and the weather research and forecasting (WRF) model in conjunction with observational data, and hybrid approaches that combine these methods to enhance prediction accuracy. A representative method involves combining a one-dimensional coupled cloud model with a time-dependent hail growth model[1]. This method generates vertical profiles of cloud velocity, liquid water content, and temperature, and estimates the probability of hail occurrence and hail size. Additionally, hybrid methods include that utilize CAM outputs and gridded radar observation data[2]. In this method, by matching hailstorms identified from CAM and radar observation data with observed hailstorms, distribution parameters for hail size are predicted, and the probability of hail size and hailfall is estimated. In addition to these studies, numerous studies employing machine learning have been conducted, and it has been reported that the performance of hail forecasting improves. A mainstream evaluation method involves utilizing report information from meteorological observation sites and meteorologists, often gathered through large-scale hail projects. These reports are primarily based on observations made at specific locations, including information about the actual hail occurrence locations and severity, recorded by observation stations or local observers. There is also hail size information derived empirically from a hail index based on radar observation data and observed hail events. This information is used in evaluations as data with excellent spatial and temporal coverage[3]. On the other hand, obtaining observational data that could indicate potential hail damage on the ground is limited, and there are challenges in acquiring such data at short intervals. Furthermore, when updating hail prediction methods based on newly obtained observation data, it is necessary to not only manually review the observational data but also to adjust the parameters with expert input. As a result, adding observational data and updating hail prediction methods impose a high workload, leading to certain limitations.

In this context, our study proposes a new hail prediction method using SNS post data, called T-SHIBA: Two-Stage, Hydrometeor classification and forecasting Induced By SNS, Algorithm (Figure 1). The purpose of this method is to utilize hail-related SNS post data from the general public to identify approximate hail occurrence locations and times, and to evaluate and improve hail prediction technology online. In general, the quality of hail forecasts is expected to vary

depending on the intended use of the forecast. For example, in cases where users take evasive actions based on hail forecasts, frequent false alarms can reduce user response rates and lead to significant losses. In such cases, minimizing false alarms becomes a high priority. As a method for improving the performance of hail prediction technology while allowing performance adjustments according to the intended use of the forecast, this method adopts a two-stage structure consisting of a common module and an individual module. In the first stage, three-dimensional observation data from X-band polarized radar are used as input to output three-dimensional hydrometeor classification results. In the second stage, the two-dimensional position (latitude and longitude) of hail is predicted based on these three-dimensional hydrometeor classification results. By clearly separating the common module and the individual module for three-dimensional hydrometeor classification, this approach aims to improve the accuracy of different hydrometeor classification models, such as those for rain, snow, and hail, and enables the adjustment and updating of forecast models according to the intended use.

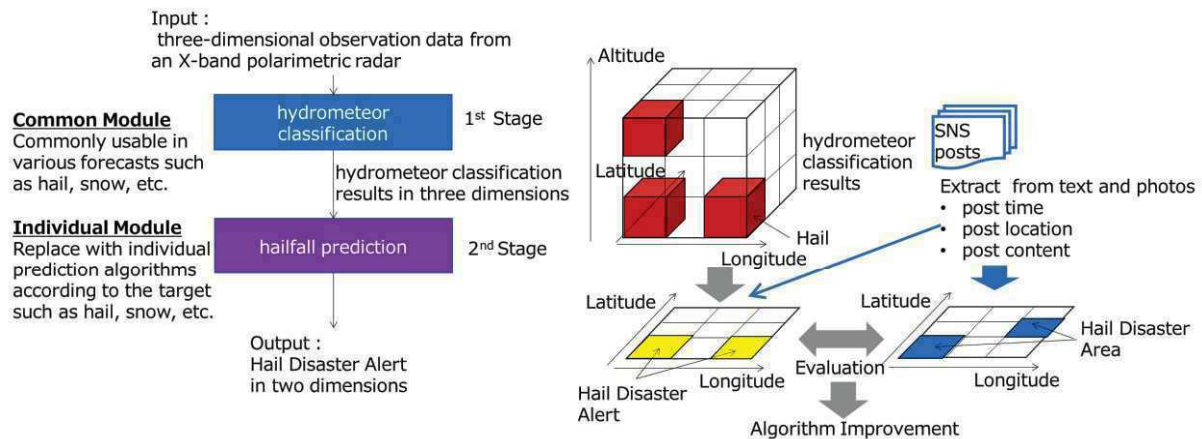


Figure 1: Our proposed new hail forecasting method (T-SHIBA)

2.1 Hydrometeor classification

The hydrometeor classification method used in the first stage of T-SHIBA improves upon traditional methods by using X-band polarimetric radar to classify hydrometeor into 11 categories based on fuzzy logic, including torrential rain: 1) drizzle, 2) rain, 3) wet snow, 4) dry snow, 5) ice crystals, 6) dry graupel, 7) wet graupel, 8) small hail, 9) large hail, 10) rain and hail, 11) torrential rain. Our objective is to establish a method for reducing the false alarm rate in hail forecasting. The three-dimensional hydrometeor classification model used in this method is trained using data from SNS post data specifically for torrential rain cases where no hail was reported and applies a Gaussian Mixture Model with Bayesian inference to classify categories including rain, hail, and torrential rain. This approach improves upon the issue where torrential rain without hail was previously classified as "rain and hail" leading to a high false alarm rate even in the absence of actual hail. The specific details of this method will be reported separately [4].

2.2 Hail forecasting based on hydrometeor classification results

In the second stage of hail prediction, two-dimensional hail prediction results are output based on the three-dimensional hydrometeor classification results (Figure 2). Specifically, it can be broadly divided into two steps: hail detection and expansion of the detection area. In hail detection step, three-dimensional hydrometeor classification results and three-dimensional observation data from X-band polarimetric radar are used to detect hail at ground level. This detected data is then converted and output as two-dimensional information. In the step of expanding the detection area, we predict hail locations by extending the hail detection areas based on advection vector, which indicate the future movement direction and speed of the rain cloud. The outputs of hail detection and forecasting are defined by a two-stage alert system consisting of caution and warning levels to notify users. The caution alert is information that indicates that hail has been detected in the sky and that there is a possibility of hailfall or torrential rain. The warning alert provides information with higher confidence, using details such as hydrometeor size and signs that hail may fall to the ground, in addition to the caution alert. Therefore, the two-dimensional hail prediction results consist of three categories: no alert, caution alert, and warning alert.

In this study, we present numerical evaluation results of a prediction method that focuses specifically on large hail, aiming to reduce hail damage. The criteria for hail detection can be adjusted based on hydrometeor size derived from radar observation data, as well as hydrometeor information obtained from three-dimensional hydrometeor classification. To effectively reduce hail damage, it is beneficial to exclude smaller particles, such as graupel or those associated with localized torrential rain, and to focus on predicting larger hydrometeors. By reducing false alarms in this manner, it is expected that a decline in user response rates and an increase in losses will be prevented.

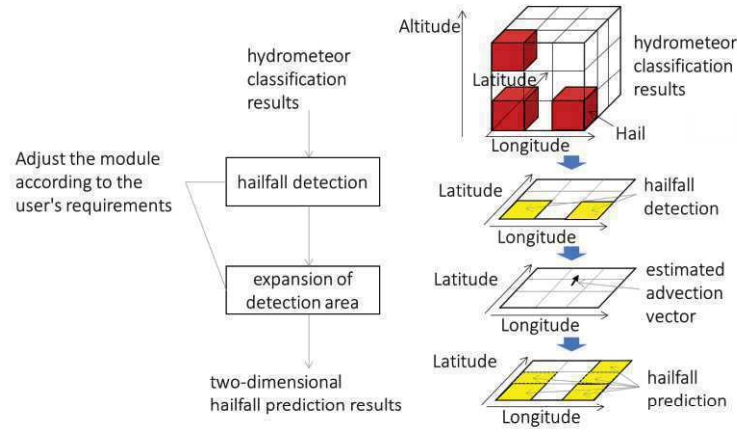


Figure 2: Hailfall prediction process flow

2.3 Numerical evaluation method using SNS post data

In a numerical evaluation of hail predictions, when comprehensive ground truth data for hail is available, evaluation metrics commonly used in machine learning, such as precision and recall, can be employed by comparing the actual hail locations with the predicted hail locations. However, for rare weather phenomena such as hail, these indices cannot accurately assess performance because they occur infrequently and in a localized area. To address the lack of accessible ground truth data for hail, we developed a numerical evaluation method utilizing SNS post data. An issue when using SNS posted data as hail observation data is that the time and location information of the posting is not necessarily accurate. This is because SNS post data are not necessarily made in real-time and can be posted at the user's convenience. Additionally, users may post after moving away from the observation location, leading to discrepancies in the timing and location of the actual hail events. To deal with this, we implemented a strategy to introduce spatial and temporal margins during evaluation. Specifically, we established a certain allowable range between the location and time of SNS posts and the predicted location and time of hail, using this range as the basis for evaluation. For example, we defined a spatial margin where SNS posts within 5 km of the predicted location are considered successful predictions, and a temporal margin where posts within one hour after the predicted hail time are considered matches. Additionally, it is expected that regions with lower population density will have fewer SNS post data, leading to variability in data availability depending on population density. To ensure more accurate evaluation, it is desirable to include a large number of SNS post data, so we carefully selected the evaluation areas. Specifically, we focused on areas with high population density, such as metropolitan regions, and conducted evaluations based on case studies from these areas. To evaluate data with these characteristics, we defined three original evaluation metrics. The evaluation metrics are prediction success rate(PSR), over-prediction rate(OPR), and lead time(LT).

The PSR is a metric that evaluates whether a specific hail event was successfully predicted without missing any SNS post data, and it is defined by Equation (1).

$$PSR = \frac{s}{n} \times 100 \quad (1)$$

Where, s represents the number of SNS posts judged as successful predictions, and n represents the total number of SNS post data considered. A higher PSR indicates fewer missed predictions. Here, a prediction is considered successful if it was output up to one hour before the SNS post data time and within a 5 km radius of the post location. This value reaches 100% when all SNS post data are predicted accurately, indicating that the higher the value, the better the prediction performance. We evaluate the missed detection performance by focusing on whether an alert is provided. Therefore, if a prediction is deemed successful at the first warning, any subsequent caution is also considered successful.

The OPR is the ratio of the number of grids where hail was predicted for a specific hail case to the number of grids predicted in areas inferred to be hail-free. This index used to evaluate whether an alert was predicted in an area close to the time and location of the SNS post data and defined by Equation (2).

$$OPR = \frac{\sum_t^T o_t}{\sum_t^T m_t} \times 100 \quad (2)$$

Where, t represents the target prediction time, T is the number of target prediction times, m_t is the number of grids predicted to have hail at time t , and o_t is the number of grids incorrectly predicted to have hail when there was none at time t . A lower value of this metric indicates that alerts were limited to areas surrounding the SNS post data. Grids without hail are determined by allowing a certain margin in both time and location relative to each SNS post. Here, grids that are more than two hours before the SNS post time and beyond a 20 km radius from the post location are considered as grids without hail. The OPR takes a value of 0% when there are no false predictions for grids distant from the SNS post data, indicating better performance when the value is low. It is important to note that this metric is based on SNS post data and does not necessarily reflect all actual weather phenomena. The metric may be high when hail is predicted in areas without corresponding SNS post data. However, this does not necessarily indicate an incorrect prediction, as actual hail may still be occurring in those areas.

LT is a metric used to evaluate how far in advance an alert was predicted relative to the time of a SNS post, or if the alert was predicted after the fact, as defined by Equation (3).

$$LT_p^i = time_{pred}^i - time_p \tag{3}$$

Where, LT_p^i represents the lead time for grid i corresponding to SNS post p (in minutes), $time_{pred}^i$ is the first time hail was predicted in grid i , and $time_p$ is the posting time of the targeted SNS post p . Grids used to calculate lead time are those that fall within a 5 km radius of each SNS post location. Lead time is calculated from the first predicted alert time for both caution and warning alerts.

3 Dataset

3.1 Data used for hydrometeor classification

To classify hydrometeor types, we used the data observed by conventional radars in Japan include the X- and C-band parabolic dual-polarization radars that comprise the Ministry of Land, Infrastructure, Transport and Tourism’s eXtended Radar Information Network (XRAIN) (Figure 3(a)). In this study, we used observational data from five X-band parabolic dual-polarization radars deployed in the Kanto region of Japan (Kanto, Shinyokohama, Funabashi, Ujiie, Yattajima) (Figure 3(b)). We performed a three-dimensional synthesis of each radar data (Zh, Zdr, Kdp and ρhv) using Cressman interpolation and converted it into orthogonal coordinates with a resolution of 250m. Furthermore, for temperature and relative humidity, we used values extracted from MesoScale Model(MSM) data that are numerical weather forecasting data using the Japan Meteorological Agency (JMA) meso-scale model.

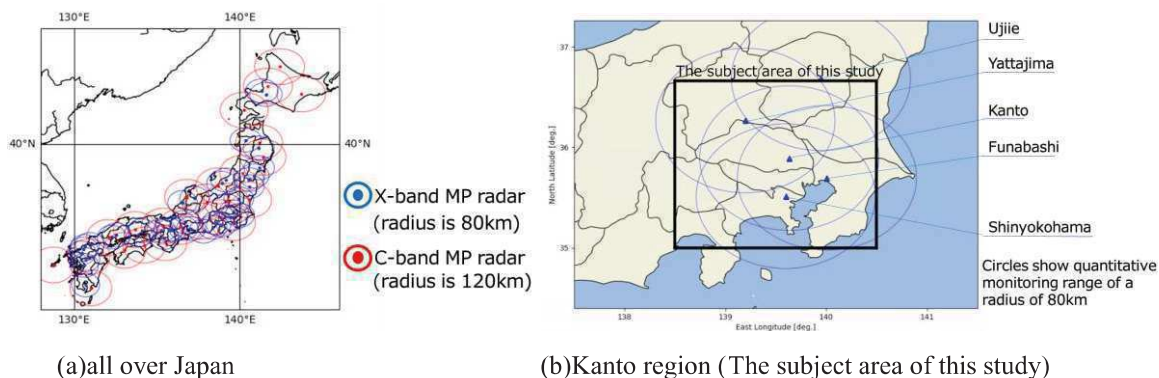


Figure 3: Locations of XRAIN MP radars

3.2 Evaluation hail cases

The evaluation data focused on 11 cases of hail and torrential rain that occurred in the Kanto region between June and November 2023 (Table 1). The Kanto region, which includes the densely populated capital city of Tokyo, provides a relatively large amount of SNS post data. To evaluate the over-prediction rate of torrential rain cases in hail prediction, the analysis includes nine cases of hail and two cases of torrential rain without hail. The evaluation period was determined by the time span covering the initial and final timestamps of the SNS post data.

Table 1: Hail cases

No	Case	Time	Number of SNS post data
1	Hail	2023-06-28 13:00~19:00	23
2	Hail	2023-07-03 19:00~23:59	30
3	Hail	2023-07-04 14:00~18:00	10
4	Hail	2023-07-10 14:00~20:00	16
5	Hail	2023-07-11 17:00~19:00	6
6	Hail	2023-07-12 16:00~18:00	1
7	Hail	2023-07-31 16:00~22:00	54
8	Hail	2023-08-01 09:00~17:00	21
9	torrential rain	2023-08-09 10:00~16:00	0
10	torrential rain	2023-08-15 17:00~23:00	0
11	Hail	2023-10-25 15:00~23:59	71

3.3 SNS post data

The SNS post data utilizes disaster-related analysis information from social media (X). This data provides more accurate and real-time information by analyzing SNS posts related to disasters such as hail, based on the location of the posts and images. The main information used includes the post date and time, analysis date and time, text, URL, and post location (prefecture, city/ward/town, district, latitude, longitude).

4 Results

Figure 4 shows the visualization results for the top six hail cases and two sudden downpour cases with the most evaluation SNS post data in the Kanto region from June to November 2023. In the visualization, the highest level of alert predicted for each grid is displayed to observe the overall trends across all time periods for each case. In the hail cases shown in Figure 4(a)-(e), (h), it was confirmed that alerts were predicted for localized areas where SNS post data were concentrated. The alert area shown in red is displayed within the area where SNS post data are distributed, indicating that this method captures the area around the location where the hail occurred. Next, in the sudden downpour cases shown in Figure 4(f) and (g), This result indicates that the proposed method effectively suppresses the issuance of alerts in torrential rain cases without hail, thereby reducing the false alarm rate for hail. This suggests that the method has the potential to provide information that reduces the likelihood of decreased user responsiveness and associated losses due to frequent false alarms.

Figure 5 shows the numerical evaluation results for the nine hail cases. In Figure 5(a), the prediction success rate achieved over 80% accuracy, with 89.2% for caution alerts and 80.2% for warning alerts. Simultaneously, the over-prediction rate was kept at around 50%, indicating that this method tends to detect hail without issuing excessive alerts. Figure 5(b) shows the evaluation results for lead time. The average lead time was 16.9 minutes for caution alerts and 13.6 minutes for warning alerts. Both cases showed that hail could be predicted in advance with a lead time of over 13 minutes. This indicates the possibility for users to prepare for and respond to hail events.

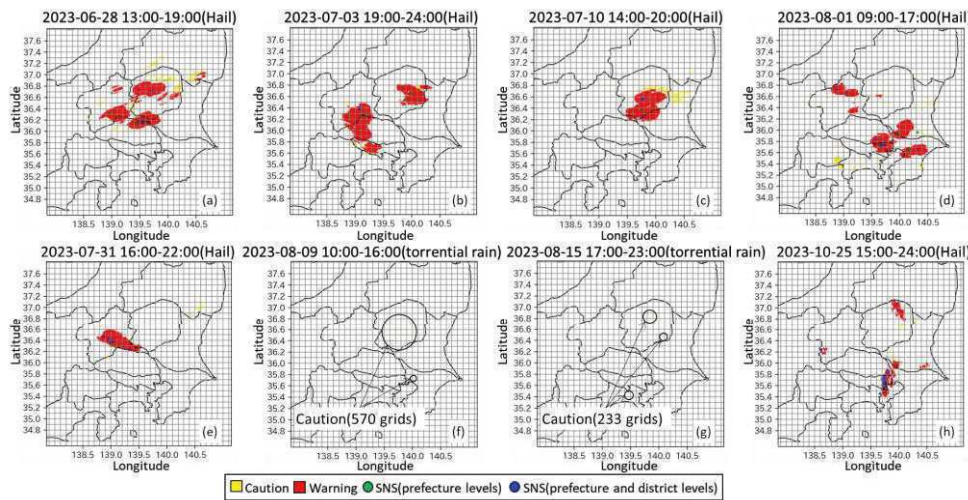


Figure 4: Hail Forecast visualization results

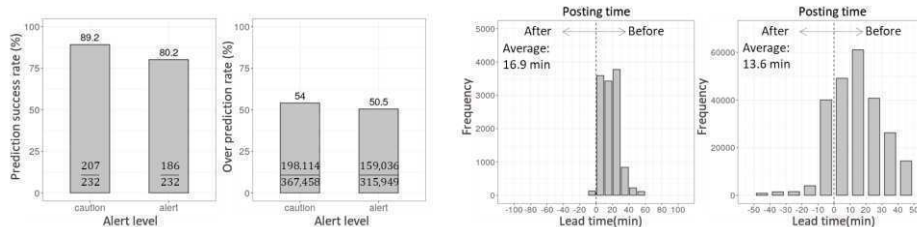


Figure 5: Numerical evaluation results for nine hail cases

5 Conclusions

In this study, we proposed methods for evaluating and improving hail prediction techniques using SNS post data. We conducted numerical evaluations on hail prediction methods aimed at reducing hail damage, focusing on 11 cases of hail and sudden localized torrential rain. The results confirmed that the proposed method effectively predicts alerts in areas with high concentrations of SNS post data, suppresses alerts in cases of torrential rain without hail, and ensures a lead time of more than 13 minutes. These findings suggest that the method is effective for early detection of hail, indicating its potential use as a tool for preventing hail damage and facilitating prompt response actions.

6 References

[1]. Brimelow, J. C., Reuter G. W., and Poolman E. R., “Modeling maximum hail size in Alberta thunderstorms”, Wea. Forecasting, 17, 1048–1062(2002)
 [2]. Gagne, D. J., II, A. McGovern, S. E. Haupt, R. A. Sobash, J. K. Williams, and M. Xue, “Storm-based probabilistic hail forecasting with machine learning applied to convection-allowing ensembles”, Wea. Forecasting, 32, 1819–1840(2017)
 [3]. Cintineo, J. L., T. M. Smith, V. Lakshmanan, H. E. Brooks, and K. L. Ortega, “An objective high-resolution hail climatology of the contiguous United States”, Wea. Forecasting, 27, 1235–1248(2012)
 [4]. T. Wada et al., “A Hydrometeor Classification Method for Dual Polarization Weather Radar Based on Gaussian Mixture Model using Bayesian Inference”, European Conference on Radar in Meteorology and Hydrology (ERAD2024)